Prompt Fission Neutron Spectra of Actinides

Capote, R.; Chen, Y.-J.; Hambsch, F.-J.; Jurado, B.; Kornilov, N.;
Lestone, John Paul; Litaize, O.; Morillon, B.; Neudecker, Denise;
Oberstedt, S.; Ohsawa, T.; Otuka, N.; Pronyaev, V.G.; Saxena, A.;
Schmidt, K.-H.; Serot, O.; Shcherbakov, O.A.; Shu, N.-C.; Smith, D.L.;
Talou, Patrick; Trkov, A.; et al.

To be published in: Nuclear Data Sheets, Vol.131, pp.1-106, January 2016.

DOI to publisher's version: 10.1016/j.nds.2015.12.002

Permalink to record: http://permalink.lanl.gov/object/view?what=info:lanl-repo/lareport/LA-UR-15-26188

DOI of formal publication: http://dx.doi.org/10.1016/j.nds.2015.12.002

Prompt Fission Neutron Spectra of Actinides

R. Capote,[1, *] Chen Y.-J.,[2] F.-J. Hambsch,[3] N. V. Kornilov,[4] J. P. Lestone,[5] O. Litaize,[6] B. Morillon,[7] D. Neudecker,[5] S. Oberstedt,[8] T. Ohsawa,[9] N. Otuka,[1] V. G. Pronyaev,[10] A. Saxena,[11] O. Serot,[6] O. A. Shcherbakov,[12] Shu N.-C.,[2] D. L. Smith,[13] P. Talou,[5] A. Trkov,[1] A. C. Tudora,[14] R. Vogt,[15, 16] and A. S. Vorobyev[12]

[1] *NAPC–Nuclear Data Section, International Atomic Energy Agency, Vienna, A-1400 Austria*
[2] *China Institute of Atomic Energy, China Nuclear Data Center, Beijing, China, 102413*
[3] *European Commission, Joint Research Centre - IRMM, Retieseweg 111, B-2440 Geel, Belgium*
[4] *Physics and Astronomy Department Ohio University, Athens, OH 45701, USA*
[5] *Los Alamos National Laboratory, Los Alamos, NM 87544, USA*
[6] *CEA, DEN, DER, SPRC, F-13108 Saint-Paul-lez-Durance, France*
[7] *CEA, DAM, DIF, F-91297 Arpajon, France*
[8] *European Commission, Joint Research Centre - IRMM, Retieseweg 111, B–2440 Geel, Belgium*
[9] *School of Science and Engineering, Kinki University, Higashi-osaka, Osaka-fu 577-8502, Japan*
[10] *Institute of Physics and Power Engineering, Obninsk, Russian Federation*
[11] *Nuclear Physics Division, Bhabha Atomic Research Centre, Mumbai 400 085, India*
[12] *Neutron Research Department, Petersburg Nuclear Physics Institute*
of NRC "Kurchatov Institute", Gatchina, 188300, Russian Federation
[13] *Argonne National Laboratory, 1710 Avenida del Mundo #1506, Coronado, CA 92118, USA*
[14] *University of Bucharest, Faculty of Physics, Magurele, POB MG-11, RO-077125, Romania*
[15] *Nuclear and Chemical Sciences Division, Lawrence Livermore National Laboratory, Livermore, CA 94551, USA*
[16] *Physics Department, University of California, Davis, CA 95616, USA*

The energy spectrum of prompt neutrons emitted in fission (PFNS) plays a very important role in nuclear science and technology. A Coordinated Research Project (CRP) "Evaluation of Prompt Fission Neutron Spectra of Actinides" was established by the IAEA Nuclear Data Section in 2009, with the major goal to produce new PFNS evaluations with uncertainties for actinide nuclei. The following technical areas were addressed: **(i) experiments and uncertainty quantification (UQ):** New data for neutron-induced fission of ^{233}U, ^{235}U, ^{238}U, and ^{239}Pu have been measured, and older data have been compiled and reassessed. There is evidence from the experimental work of this CRP that a very small percentage of neutrons emitted in fission are actually *scission* neutrons; **(ii) modeling:** The Los Alamos model (LAM) continues to be the workhorse for PFNS evaluations. Monte Carlo models have been developed that describe the fission phenomena microscopically, but further development is needed to produce PFNS evaluations meeting the uncertainty targets; **(iii) evaluation methodologies:** PFNS evaluations rely on the use of the least-squares techniques for merging experimental and model data. Considerable insight was achieved on how to deal with the problem of too small uncertainties in PFNS evaluations. The importance of considering that all experimental PFNS data are "shape" data was stressed; **(iv) PFNS evaluations:** New evaluations, including covariance data, were generated for major actinides including 1) non-model GMA evaluations of the ^{235}U(n_{th},f), ^{239}Pu(n_{th},f), and ^{233}U(n_{th},f) PFNS based exclusively on experimental data ($0.02 \leq E \leq 10$ MeV), which resulted in PFNS average energies $\overline{E}$ of 2.00±0.01, 2.073±0.010, and 2.030±0.013 MeV, respectively; 2) LAM evaluations of neutron-induced fission spectra on uranium and plutonium targets with improved UQ for incident energies from thermal up to 30 MeV; and 3) Point-by-Point calculations for ^{232}Th, ^{234}U and ^{237}Np targets; and **(v) data testing:** Spectrum averaged cross sections (SACS) calculated for the evaluated ^{235}U(n_{th},f) PFN field agree within uncertainties with evaluated SACS experimental data. Despite the observed reduction of the PFNS $\overline{E}$ by about 30 keV for neutron-induced fission of ^{233}U, ^{235}U, and ^{239}Pu, the criticality benchmark outcomes suggested that new evaluations can achieve the same (or better) integral performance with respect to existing evaluations, but the strong compensating effects observed need to be addressed. Summarizing, this project has significantly improved PFNS evaluations and evaluation methodology, provided new PFNS data for applications, and also highlighted the areas for future research.

---

*Corresponding author, electronic address: r.capotenoy@iaea.org

CONTENTS

I. INTRODUCTION

"Trust is the greatest incentive. If trust is missing, everything is missing." [Maria Theresia (1717–1780), Empress of Austria]

If nuclear data users do not trust the data provided by data evaluators, then their evaluation effort is of little practical value. Consequently, it is of paramount importance that the data available in evaluated libraries (e.g., ENDF/B, JEFF, JENDL, CENDL, BROND, TENDL) adequately reflect the best knowledge of these physical quantities available at the time the libraries were produced, and that these data were derived using state-of-the-art statistical and mathematical tools. Fulfilling this expectation from data users is the responsibility of all data evaluators, and it also presents their greatest challenges.

The energy spectrum of prompt neutrons emitted in neutron-induced fission (PFNS) plays an important role in many applications in nuclear science and technology. In particular, accurate predictions of nuclear criticality using neutron transport codes are dependent on the underlying nuclear data, especially the fission spectrum. For example, it has been demonstrated that for certain ^{239}Pu solution thermal-critical assemblies with high neutron leakage, where the criticality parameter k_{eff} is particularly sensitive to the PFNS average energy $\overline{E}$, differences in obtained values of k_{eff}, corresponding to observed variations of $\overline{E}$ of 1–2% (corresponding approximately to 20–40 keV) for the evaluated PFNS generated by different evaluators, can approach 1000 *pcm* (= 1%) [1, 2]. This is a huge effect. Validation of important neutron dosimetry reactions is also heavily reliant on the availability of accurate PFNS data [3]. On the other hand, validated dosimetry cross sections (e.g., from the IRDFF library [3]) can be used to check the PFNS evaluations [4]. In general, the high sensitivity of calculated integral quantities to fission-neutron data has been emphasized recently by researchers in many groups around the world who are working on conventional as well as advanced reactors, criticality safety, waste management, and non-proliferation applications.

This paper has been prepared to serve as the final documentation of an International Atomic Energy Agency (IAEA) Coordinated Research Project (CRP) that began in 2010 and terminated in 2014. Section II reviews some of the significant events in the history of this topic and the origins of this particular CRP. The main body of the paper discusses more recent technical work and accomplishments associated with this project in the following categories: Section III (Experiments), Section IV (Deterministic Models), Section V (Monte Carlo Models and Codes), Section VI (Evaluation Methodologies), Section VII (Evaluations), and Section VIII (Data Testing). The overall objective of this document is to provide a comprehensive picture of the contemporary status of knowledge concerning the PFNS in each of these technical categories.

The work reported in this paper involves efforts by the CRP participants and, in many instances, by other investigators as reported in published documents. Therefore, numerous references are provided to guide the reader toward relevant sources dealing with this subject. In those cases where adequate documentation of the present CRP work is available elsewhere (or will be available soon) in readily accessible literature, many of those details are omitted here and only brief summaries are offered to provide the reader with an overview of the work that has been accomplished without having to refer constantly to other references. More detailed expositions are provided here in specific areas where experimental documentation is lacking or limited. Extensive use is made of figures and tables to provide useful information, to illustrate key concepts, and to highlight problem areas. The extent to which this CRP has generated meaningful improvements with respect to contemporary knowledge of the PFNS for the studied actinides is also discussed. Finally, some remaining problem areas are identified and specific suggestions for future work are offered.

II. BACKGROUND

Fission neutron spectra have been studied experimentally since 1939 [5], shortly after the discovery of fission [6, 7]. If isotropy of neutron emission is assumed, then it was shown by Feather [8] that at low emission energies E the fission neutron spectrum must be proportional to $\sqrt{E}$. A number of earlier microscopic measurements by a Los Alamos laboratory group [9–13] confirmed the predicted behavior. They also showed that the energy spectrum of these neutrons was an "evaporation" spectrum with an average energy close to 2 MeV. This observation was consistent with the theoretical concept of neutron emission from a highly excited and rapidly moving fission fragment, as pointed out by Terrell [14].

Today, 76 years later, one is amazed at how a basic understanding of many of the properties of fission neutron spectra achieved in pioneering fission studies, as reported, e.g., in the papers by Bohr and Wheeler [15], Turner [16], and Peierls [17], has been validated by many investigations during the intervening years. Also, many problems raised by investigators at that time are still open questions, e.g., "whether neutrons are emitted during scission" [15]. Simple theoretical descriptions based on either Watt [12] or Maxwellian [18] spectra were proposed at that time and continue to play useful roles in some applications to this day.

In recognition of significant developments in nuclear fission, the IAEA convened the *First International Symposium on the Physics and Chemistry of Fission* at Salzburg, Austria from 22–26 March, 1965 [19]. Session VI of this symposium was devoted to the study of prompt neutrons from fission, with a review presented by Terrell [20] and PFNS measurements in the thermal neutron-induced fission of ^{233,235}U and spontaneous fission of ^{240}Pu and ^{252}Cf reported by Condé [21]. Fission research developed rapidly after this symposium, and the *Second International Symposium on the Physics and Chemistry of Fission* was organized in the summer of 1969 in Vienna, Austria [22]. Session F of that symposium was devoted to the study of prompt neutrons and photons from fission, with a paper by Weinstein et al. [23] showing the measured energy dependence of the prompt neutron multiplicity ($\overline{\nu}$) in the thermal and resonance regions of ^{233,235}U and ^{239}Pu nuclei.

Following a recommendation from the International Nuclear Data Committee (INDC), the IAEA held its first Consultants' Meeting on the status of "Prompt Fission Neutron Spectra" on 25–27 August 1971 in Vienna [24]. This meeting discussed both differential and integral measurements. It proved to be extremely important in defining the direction of future studies. The meeting participants reached a consensus on a number of points, which are reflected in the following specific recommendations [24]:

- High priority should be given to experimental determination, with the best possible precision, of the ^{252}Cf(sf) spectrum, with the goal of making it a "standard" fission neutron spectrum.
- It is recognized that a simple Maxwellian form does not satisfactorily fit all observed fission spectra.
- The shape of the fission spectra of ^{233,235}U and ^{239}Pu should be studied as a function of incident neutron energy. Techniques that specifically identify the observed neutrons as being of fission origin should be used.
- Multiple-scattering corrections in differential experiments are important and should be considered.
- Angular distribution measurements of fission neutrons relative to the direction of the incident neutron seem necessary, as anisotropies might arise from different causes.
- Particular attention should be paid to measurements of the low-energy region of ^{252}Cf(sf), the ^{235}U PFNS, and other PFNS.
- A theoretical understanding of the shape of fission spectra and that of the energy dependence of the neutron multiplicity are very desirable in the long term.
- Several recommendations on spectrum average cross section measurements in well-characterized reactor fields are also proposed.

New experimental and model-development research activities were undertaken by many groups worldwide in response to this meeting's recommendations. Additional IAEA meetings that discussed prompt fission neutron emission (among other topics) were held in 1973 [25], 1976 [26], 1979 [27], 1988 [28] and 1990 [29]. Three important developments that emerged from this work are highlighted here:

- Experiments were undertaken by NIIAR researchers led by Starostov [30–33] to measure the PFNS ratio in thermal neutron-induced fission of fissile elements relative to ^{252}Cf(sf) down to neutron emission energies around 20 keV. These high-accuracy data are still unique. A similarly-designed experiment (for fast neutrons) was undertaken in 1979 by Smith et al. [34, 35], but unfortunately their goal was solely to estimate the average energy of the PFNS $\overline{E}$ and most of their measured ratio data sets were lost, see Sec. VI for details.
- High-precision measurements of the neutrons emitted in the spontaneous fission of ^{252}Cf were undertaken, thereby enabling Mannhart to perform a non-model evaluation of this important reference spectrum based on measured data alone [36, 37].
- A milestone in theoretical investigations of the shape of prompt fission neutron spectra was the publication by Madland and Nix, in 1982, of their fission spectrum model which nowadays is commonly referred to as the Los Alamos model (LAM) [38]. It has become the workhorse underlying modern PFNS data evaluations.

A comprehensive review of all spectra measurements undertaken up to 1985 was presented by Holden [39] at the *Meeting of the International Committee for Radionuclide Metrology*, held in Grenoble, France on June 3–7, 1985. Holden's goal was to evaluate the average energy of emitted fission neutrons $\overline{E}$. Holden pointed out that for most of the actinide nuclides, the neutrons detected in the spectral range $0.010 < E < 10$ MeV comprise about 99.9% of the emitted neutrons.. He noted that there had been much concern about deviations of measured spectra from the Maxwellian or Watt shape at low or high energies, but this has little impact on the mean neutron energy because so few of the neutrons are emitted in these energy regions. Holden also attempted to estimate the systematic error as well as the precision in each of the considered experiments. Holden's recommended values for the PFNS average energies $\overline{E}$ of ^{233,235}U(n$_{\mathrm{th}}$,f), ^{239}Pu(n$_{\mathrm{th}}$,f) and ^{252}Cf(sf) were 2.02 ± 0.03, 1.98 ± 0.03, 2.06 ± 0.04, and 2.14 ± 0.03 MeV, respectively [39].

In 1998, almost 30 years after the 1971 IAEA Consultants' Meeting, a Working Party Subgroup 9 on International Evaluation Co-operation (WPEC SG-9) was established by the OECD/NEA Nuclear Science Committee. The WPEC SG-9 goal was to investigate discrepancies found between microscopic and macroscopic data for the ^{235}U fission neutron spectrum (e.g., see [40]) and to review and improve the existing PFNS of ^{235}U [41]. This re-evaluation work included theoretical calculations of new spectral values using the latest models (e.g., the Los Alamos Model (LAM) [38]), along with comparisons of these calculations with both differential and integral experimental data. The most recent differential measurement results available at the time were those published by NIIAR researchers [30–33] and Wang et al. [42]. The spectrum average cross sections (SACS) in the ^{235}U(n_{th},f) PFNS evaluated by Mannhart [41] served as integral measurements to be compared with the selected differential data. WPEC SG-9 found that differential thermal PFNS reproduced the SACS within 10% up to about 8–11 MeV but failed at the higher energies. A similar behavior was observed for the ENDF/B-VI spectrum evaluated using the LAM. Therefore, no calculated thermal spectrum has been found that simultaneously reproduces either of the two latest (at that time) thermal differential measurements [33, 42], as well as the SACS cross-section set evaluated by Mannhart, to within an acceptable level of accuracy. It was concluded by WPEC SG-9 that, given the importance of the thermal ^{235}U fission neutron spectrum, this contradiction should be resolved. Further experimental and theoretical studies were recommended but no meaningful change in the evaluated spectrum emerged as a consequence of subsequent investigations.

While the accuracy of evaluated fission cross sections and neutron multiplicities, $\overline{\nu}$, in the relevant energy range has improved steadily in recent years, the nuclear science community continues to face the situation that existing measured PFNS are in many cases discrepant and that different PFNS theoretical models, as well as various PFNS data evaluation procedures, yield predictions that differ significantly. This is clearly unacceptable from the scientific point of view and is a challenge for nuclear data users.

With this historical context in mind, in November 2008 the IAEA Nuclear Data Section organized another Consultants' Meeting in Vienna to review and discuss the adequacy and quality of the recommended prompt fission neutron spectra to be found in existing nuclear data applications libraries. These prompt fission neutron spectra were judged by the consultants to be inadequate. They strongly recommended to the IAEA that it initiates a new CRP on PFNS evaluations [43]. The proposed goal of this activity would be to determine the prompt fission neutron spectra and covariance matrices for actinides in the energy range from thermal to 20 MeV, including validation against integral critical assembly, k_{eff}, and dosimetry data. The following nuclei were recommended for study, in descending order of priority: (i) major actinides ^{235,238}U and ^{239}Pu; (ii) ^{232}Th and ^{233}U of relevance to the Th-U fuel cycle; and (time permitting) (iii) minor actinides such as ^{237}Np, ^{241}Am, $^{242\mathrm{m}}$Am, ^{240}Pu and ^{245}Cm. The focus of this endeavor would be solely on the emitted-neutron spectral shapes, not on absolute neutron yields, i.e., a detailed consideration of $\overline{\nu}$ was to be avoided. This approach would be consistent with the fact that $\overline{\nu}$ and PFNS shape information are archived as different categories in evaluated nuclear data libraries, using distinct formats [44]. In practice, actual neutron yield values are generated for applications by multiplying unit-normalized spectral shapes by $\overline{\nu}$. Evaluated values of $\overline{\nu}$ are considered to be known to rather high accuracy based on independent experiments (e.g., Gwin et al. [45] and the thermal $\overline{\nu}$ evaluations [46–48]). Therefore, it was perfectly reasonable to launch a CRP that focused solely on the PFNS shape.

This proposed project was endorsed by the INDC and approved by the IAEA. Therefore, a CRP labeled *Prompt Fission Neutron Spectra for Actinides* commenced in 2010. Several experts from IAEA Member States with experience in measurements, theoretical modeling, and data evaluation methodologies relevant to PFNS were invited to participate in this project. The major task areas adopted for this endeavor were defined in general terms as follows:

- Experiments: The available experimental PFNS data relevant to the selected isotopes, including any results that might be generated during the course of the CRP, would be collected, organized, and archived. This information would be accessible to all the CRP participants. The data would then be critically reviewed for quality issues (e.g., adequacy of the data corrections, availability of uncertainty information, consistency of calibration standards, etc.). Adjustments would be made and uncertainty quantification would be undertaken as required to prepare these data for evaluation.

- Modeling: The status of theoretical modeling of the PFNS (both deterministic and stochastic) would be examined and work would be undertaken to improve the predictive power of these models, including their capabilities to generate covariances. Also, effort would be devoted to developing enhanced variants of the existing models, as needed to generate reliable supplementary PFNS data in energy regions where experimental data are limited, nonexistent, or otherwise inadequate.

- Evaluation Methodologies: PFNS data evaluation methods would be examined for their capacities to incorporate

TABLE 1. Measured differential PFNS data sets for thermal neutron-induced fission of ^{235}U. The EXFOR No., first author, year of publication and main reference, outgoing neutron energy E, and comments that include the quality of the information for the purposes of uncertainty quantification (UQ) are given.

EXFOR No.	First Author & Year	Type of data	E (MeV)	Comments
14400002	Bonner (1952) [9]	shape	0.05–0.7	+delayed FNS
14134002	Nereson (1952) [10]	shape	0.39–7.02	+delayed FNS
13810002	Hill (1952) [11]	shape	0.4–6.44	+delayed FNS
14099003	Watt (1952) [12]	shape	3.30–17.22	+delayed FNS
13824002	Cranberg (1956) [13]	shape	0.35–12.	+delayed FNS
20616003	Werle (1972) [57]	shape	0.104–9.495	+delayed FNS
41502002	Batenkov (2004) [58]	shape, ratio to Cf	0.12–17.5	preliminary, uncorrected
41597002	Vorobyev (2013) [59]	absolute, ratio to Cf	0.221–16.65	Detailed UQ
31692002	Kornilov (2010) [60]	absolute	0.7–11.8	Detailed UQ, use 31692006
31692006	Kornilov (2011) [61]	absolute, ratio to Cf	0.7–11.8	Detailed UQ
32587002	Wang (1989) [42]	shape	0.56–15.0	Incomplete UQ
30704003	Lajtai (1985) [62]	absolute, ratio to Cf	0.03–3.855	Detailed UQ for ^{252}Cf(sf) [63]
40871011	Nefedov (1983) [30]	absolute, ratio to Cf	0.084–0.91	Detailed UQ
40871012	Nefedov (1983) [30]	absolute, ratio to Cf	1.0–7.8	Detailed UQ
40872007	Starostov (1983) [31]	absolute, ratio to Cf	4.115–12.06	Detailed UQ
40873004	Boytsov (1983) [32, 33]	absolute, ratio to Cf	0.021–4.5	Detailed UQ

both model-generated and experimental data in consistent ways, as well as to generate evaluated covariances. Improvements in existing procedures would be sought and implemented where feasible and practical.

- Evaluations and Covariances: The work of this CRP would generate ENDF-6 formatted PFNS evaluations [44] for the selected actinide isotopes (including covariances) that could eventually be included in evaluated nuclear data libraries used for applications for as many of the selected actinide isotopes as time and available reliable physical information would allow.
- Data Testing: The performance of the generated PFNS evaluations would be tested in various neutronics and dosimetry benchmark applications.

There were three Research Coordination Meetings (RCM) of this CRP during its five years of existence, each with the objective of reviewing the status of technical progress in the project: RCM-1 (April 2010) [49]; RCM-2 (December 2011) [50]; and RCM-3 (October 2013) [51]. The CRP formally terminated in December 2014.

III. EXPERIMENTS

Although considerable progress has been made in recent years in developing theoretical models that can provide descriptions of PFNS (see Secs. IV and V), it is widely acknowledged within the nuclear data community that there are deficiencies in these models because of the difficulty of modeling the complex physical processes associated with prompt emission of neutrons from fission of actinide nuclei. Furthermore, it is pointed out in Sec. VI that certain mathematical features of contemporary nuclear models can actually impact in negative ways on the evaluation of PFNS data, especially with respect to estimating uncertainties in the evaluated results. Consequently, owing to the strong sensitivity encountered in nuclear applications to the detailed behavior of the PFNS, as well as to estimated uncertainties in their evaluated representations, there remains a compelling need for good quality experimental PFNS data to compensate for limitations in these nuclear models.

PFNS are difficult to measure at energies below a few hundred keV (due to neutron scattering effects) and above 8 MeV (due to very low neutron yields). Detector calibration also presents obstacles that are difficult to overcome at these energies. Furthermore, for a variety of reasons, it is difficult for laboratories to acquire and utilize samples of actinide materials with sufficient masses to enable these experiments to be performed. Therefore, at the mentioned above (low and high) energy ranges is necessary to rely, to a great extent, on nuclear models in generating evaluated numerical representations of PFNS. However, at the intermediate energies, where favorable experimental conditions enable measurements to be performed, and some decent quality PFNS data are available, evaluators of PFNS data should rely, to the extent possible, on these data rather than relying solely on values from nuclear models. This point is discussed further in Sec. VI.

A survey of the literature and the experimental neutron reaction database, EXFOR [52][1], reveals that while consid-

---

[1] a retrieval from the EXFOR database is a complex task for PFNS as many different ways of coding the relevant data have been used by

erable neutron-induced PFNS data are available for three major actinides, ^{235,238}U and ^{239}Pu, at a few mostly lower than 2 MeV incident neutron energies, the experimental data base for ^{233}U and ^{232}Th is more limited. The data base for minor actinides is relatively sparse to nonexistent.

Progress in expanding the existing experimental databases of PFNS for all the actinide isotopes is likely to proceed rather slowly in the near term as a consequence of the above-mentioned technical and logistical factors. Therefore, evaluators will need to make use of whatever experimental information is available for the foreseeable future.

The existing PFNS experimental data have been assembled and examined for quality and relevance under the auspices of this CRP. The status of these data, and the experiments used to acquire them, are discussed in some detail in the present section. A few very recent experiments were undertaken within the CRP activities and they are described briefly at the end of this Section. All the data compiled during this project were reviewed and vetted, and this collection is available online [53] at *www-nds.iaea.org/pfns/*. As discussed above, the best known PFNS spectrum is that of spontaneous fission of ^{252}Cf [36, 37]. In fact, it is sufficiently well known to be treated as a standard. Consequently, it is widely used for calibrating neutron detectors and for measuring PFNS ratios. For this reason, and due to lack of new high-quality measurements[2], further investigation of ^{252}Cf(sf) PFNS has not been included in the scope of work for the present CRP.

A. Neutron-Induced Fission of ^{235}U

Assessment of the experimental PFNS data for ^{235}U(n,f) was divided into two separate sub-tasks. One is comprised of data for thermal neutron-induced fission. The second is comprised of data pertaining to all other incident neutron energies, E_n. The reason for this separation is that the thermal data were assembled for use in a non-model evaluation, with the idea that the resulting ^{235}U($n_{\rm th}$,f) evaluation could be considered as a reference standard. A number of integral measurements of nuclear reactions, especially dosimetry reactions, have been made in the ^{235}U($n_{\rm th}$,f) PFN field (and related neutron reactor fields), and they serve to complement similar integral measurements performed using ^{252}Cf(sf) neutrons.

1. *Thermal Neutron-Induced Fission of ^{235}U*

The differential data sets that are available for the thermal neutron-induced PFNS of ^{235}U are listed in Table 1. These data sets were reviewed and vetted for their quality and appropriateness for evaluation purposes, and they were checked for repeated data in Refs. [55, 56]. A brief summary of this review is as follows: The data of Bonner et al. [9], Nereson [10], Hill [11], Watt [12], Cranberg et al. [13], and Werle [57] were rejected from consideration, as these data include delayed neutron contributions[3]. However, to their credit, most of these data were measured using track detectors and the subsequent analysis was based on the use of the H(n,p) cross section as standard. The track-detection accuracy is higher for higher energies of nuclear recoils. Therefore, it could be possible to use the high energy region in these measurements (above 3–4 MeV) by updating the quoted H(n,p) cross sections to the current standard values. This task is left for future work. The data of Batenkov et al. [58] were rejected as these are preliminary raw (uncorrected) data; the final data were never published.

Ultimately, only 8 experimental data sets were viewed as sufficiently reliable for evaluation purposes, over either all or some portions of the emitted-neutron energy ranges [55, 56]. The data sets retained for evaluation purposes were those of Vorobyev et al. [59], Kornilov et al. [60, 61], Wang et al. [42], Lajtai et al. [62], Nefedov et al. [30] (two sets), Starostov et al. [31], and Boytsov et al. [32, 33]. Portions of some of these retained data sets still needed to be excluded for evaluation purposes for the following reasons: Four data points above 2.7 MeV in the data by Boytsov [32] were discarded, as they were also discarded in a subsequent journal publication by the authors (see Starostov et al. [33]). The rest of the data of Boytsov [32] were taken because they were provided to EXFOR by the authors in numerical form, while the data from Ref. [33] in EXFOR were digitized from a graph in a publication. The data were measured as ratios to ^{252}Cf(sf), but they were provided to EXFOR (and compiled) as a ratio to a Maxwellian with temperature 1.418 MeV (i.e., representing the ^{252}Cf(sf) spectrum as a Maxwellian with that temperature). In the fits, the data were converted to ratios to a Maxwellian with temperature 1.313 MeV, and they were subsequently corrected for the standard ^{252}Cf(sf) spectrum [36, 37]. The Lajtai data [62] above 0.2 MeV were deemed unreliable because of very

---

compilers over several decades [52].

[2] At the time of submission, the authors are aware of on-going ^{252}Cf(sf) PFNS measurements at RPI (Y. Danon et al.) and PNPI (Vorobyev et al.), and planned new measurements by the Chi-Nu team at Los Alamos National Laboratory. Kornilov published a new measurement of ^{252}Cf(sf) PFNS [54], which is in excellent agreement with Mannhart evaluation [36, 37] for E=2–20 MeV.

[3] Note that Kornilov assessed delayed-neutron corrections for Cranberg et al. data [13], and found a fairly small correction on the PFNS shape and $\overline{E}$ (5 keV on the latter).

large corrections (more than ∼50% at some energies) that had to be applied due to the use of a thick Li-glass detector in the measurements [63]. The Wang data [42] below 1.3 MeV were excluded due to the non-physical shape of the measured spectrum, which seems to be caused by the employed detector efficiency (the efficiency at those energies was extrapolated, not measured). Also, the uncertainties on the last two points in the latter data set were doubled and tripled, respectively, for statistical consistency with other data. The uncertainties on the last two data points from Refs. [60, 61] were doubled for the same reason. Even after these uncertainty modifications, Fig. 1 shows that the experimental data above 10 MeV are discrepant, therefore those data were discarded in the least-squares analysis. The ^{235}U(n_{th},f) PFNS can not be defined on the basis of existing differential data above 10 MeV due to mentioned discrepancies.

The question is which of the data corrections in the TOF measurements is extremely sensitive and may define the validity of the measured spectral shape at emitted neutron energies higher than 10 MeV. One of the possible candidates is the background correction in the measured time spectra (see Sec. III M). The main part of this background originates from random coincidences (uncorrelated stop events) and is strongly time dependent. A minor part is time independent. Both components must be calculated, based on a few parameters of the experiment, and require the knowledge of the "true" spectrum. Thus, iterative steps are necessary before subtracting the composed background in the time spectra. If one considers the small number of counted neutron events at high energies, then it is obvious that any mistake in the background correction can easily result in a wrong shape of the high-energy portion of the measured spectra. This may explain the observed discrepancies in the data above 10 MeV as shown in Fig. 1.

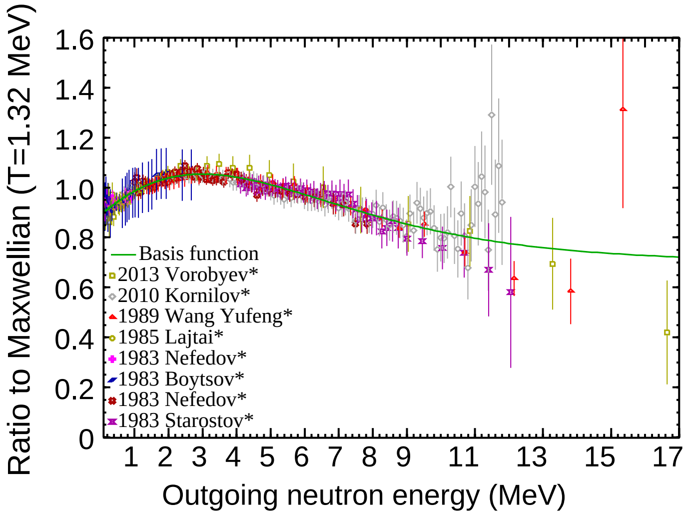

FIG. 1. (Color online) The basis function (green solid line) used as an anchor for rescaling in comparison with rescaled "shape" PFNS data (symbols) for ^{235}U($\mathrm{n_{th}}$,f) presented as ratios to a Maxwellian. The basis function, Eq. (102), and parameters are discussed in Sec. VII B 1 [55].

To begin the uncertainty quantification (UQ) the uncertainty analysis prepared by Pronyaev was adopted. Further details on the data and the selection process can be found on the present CRP web page [53]. A comprehensive discussion on the selection of differential data from the EXFOR database is available on the IAEA CIELO web page [64] of the OECD/NEA-coordinated CIELO project [65].

2. *Fast Neutron-Induced Fission of ^{235}U*

The available ^{235}U(n,f) PFNS data corresponding to incident neutron energies above thermal were compiled as one of the sub-tasks of the present CRP. An inventory of the measurements appears in Table 2. The experimental values have been tabulated and they are available from the CRP website [53].

Some of the major challenges that are encountered in these PFNS experiments are: characterization of the incident neutron spectrum, sample characterization, generation of timing signals needed for measuring fission-neutron energies by time-of-flight, calibration of the neutron detector response, and corrections for unwanted perturbations to measured PFNS spectra by neutron scattering. The measurement approaches employed in these experiments have been grouped into five categories:

- *Method 1*: Constant mono-energetic neutron beams are used, and the time-of-flight condition that is imposed to measure fission-neutron energies is satisfied by obtaining the start signals from fission-fragment events in ionization chambers. The PFNS yields are measured relative to ^{252}Cf spontaneous fission.

TABLE 2. Experimental PFNS for fast neutron-induced fission of ^{235}U. The incident neutron energy E_n, EXFOR No., first author, year of publication and main reference, type of data, outgoing neutron energy E, and comments that include the quality of the information for the purposes of UQ are given.

E_n (MeV)	EXFOR No.	First Author & Year	Type of data	E (MeV)	Comments
1.5	–	Lestone (2014) [66, 67]	shape	1.5–11.5	Detailed UQ
Spectrum, 0.5–10	14350002	Enqvist (2012) [68]	shape	0.55–7.9	Broad incident spectrum
1–8 (ΔE_n=1)	14290002	Noda (2011) [73]	shape	1.5–9.5	Incomplete UQ
0.5	23056	Kornilov (2007) [69]	shape	0.7–11.0	Data not available
0.5	13982002	Staples (1995) [74]	shape	0.596–16.772	Incomplete UQ
1.5				1.696–16.772	
2.5				2.808–14.485	
3.5				4.088–15.193	
0.5	41162003	Trufanov (1994) [77]	shape	0.38–10.51	Detailed UQ
5.0				0.539– 14.41	Detailed UQ
2.9	41110009	Boykov* (1991,1994) [78, 79]	absolute, ratio to Cf	0.232–11.885	Detailed UQ
14.7			absolute, ratio to Cf	0.225–11.77	Detailed UQ
0.55	14418002	Sugimoto (1987) [70, 71]	shape, ratio to Pu	1.–10.	Incomplete UQ
0.525	10911003	Smith (1980) [34, 35]	shape, ratio to Cf	0.559–7.72	Incomplete UQ
0.01-0.058	20997003	Abramson (1977) [80, 81]	shape	0.5–13.946	Incomplete UQ
0.53	20175003	Johansson (1977) [81, 82]	shape	0.625–14.45	Incomplete UQ
0.1	40358004	Alexandrova (1975) [83]	shape	1.5–14.	Insufficient UQ
0.52	20996003	Adams (1975) [81, 84]	shape	0.62–15.6	Incomplete UQ
0.4	20385003	Islam (1973) [81, 85]	shape	0.58–6.9	Incomplete UQ
1.5	20394008	Knitter (1972) [86]	shape	1.8–6.7	Incomplete UQ
0.04	20575003	Condé (1965) [87, 88]	shape	0.3–7.5	Insufficient UQ
1.5	20575004		shape	0.3–5.5	Insufficient UQ

* G.S. Boykov name has been often transliterated as G.S. Boikov (see a note in EXFOR entry 41110).

- *Method 2*: Neutron energy spectra from small samples of fissile material exposed to constant mono-energetic neutron beams are deduced by detector pulse-height unfolding techniques, using calibrated neutron detectors. This method is limited to incident neutron energies below 0.5 MeV to minimize complications due to elastic and inelastic neutron scattering.

- *Method 3*: This approach is similar to Method 2 except that pulsed neutron beams are used to generate signals for neutron time-of-flight determinations.

- *Method 4*: A double time-of-flight approach is used that employs pulsed white-source incident neutrons, as well as signals from fission fragments in ionization chambers, for timing purposes.

- *Method 5*: This approach is similar to Method 1 but it uses relatively large samples in the fission chamber. It is suitable only for neutrons with high incident energies (e.g., 5 to 14 MeV).

A few comments on some of these experiments are provided below. The data of Lestone et al. [66, 67] derived from Nevada test site measurements are discussed in Sec. III K. The data of Enqvist [68] are excluded from the following discussion because they correspond to broad incident neutron spectrum measurements that cannot be readily incorporated into an evaluation. The data of Kornilov [69] were not available for consideration during the duration of the CRP. The work of Smith et al. [34, 35] is discussed separately in Sec. VI E. Recently, Lestone discovered a PFNS ^{239}Pu(n,f)/^{235}U(n,f) ratio measurement at E_n =0.55 MeV by Sugimoto et al. [70, 71] that was not compiled in EXFOR. The resulting Sugimoto-Lestone ^{235}U(n,f) spectrum [71, 72] was derived from the Sugimoto ratio [71] using the accurate ^{239}Pu(n,f) fission spectrum derived by Lestone from the NUEX experiment [66, 67] (see Sec. III K), and is given in Table 3.

Other individual data sets considered are identified by their assigned EXFOR numbers [52]. In the following, when the data are introduced, the first author's name and the EXFOR number are given in square brackets, then the incident neutron energy, E_n, while the limits on the outgoing neutron energy E are given in parentheses.

[Noda:14290002] Incident neutron energies (measured PFNS energy range) in MeV: 1–2, 2–3, 3–4, 4–5, 5–6, 6–7, and 7–8 (all 1.5–9.5) [73]. The experiment measured shapes using Method 4. The data are not corrected for scattering of the fission neutrons from components of the fission chamber (estimated correction between 6–7%). Statistical uncertainty is given. Uncertainty in the detector efficiency is about 5%.

[Staples:13982002] Incident neutron energies (measured PFNS energy ranges) in MeV: 0.5 (0.596–16.772), 1.5 (1.696–16.772), 2.5 (2.808–14.485), and 3.5 (4.088–15.193) [74]. Measured shapes using Method 2, but Staples used a large sample of 107.5 g. Multiple scattering and neutron attenuation corrections were not performed. The absolute liquid scintillator detector efficiency was calculated using the Monte Carlo code SCINFUL [76], and it was compared with a ^{235}U(n,f) fission chamber with known efficiency (see recent work by Lestone [75]). Large energy-dependent uncertainty

TABLE 3. Inferred prompt fission neutron spectrum values for $E_n = 1.5$ MeV neutron-induced fission of ^{235}U from Sugimoto et al. ^{239}Pu/^{235}U ratio measurement [70, 71] using the NUEX data [66, 67] (see Table 17). The Sugimoto et al. ratios at $E_n = 0.55$ MeV are corrected to $E_n = 1.5$ MeV using ratios of ratios from the ENDF-B/VII.1 PFNS evaluation [148].

E (MeV)	^{239}Pu-NUEX [66] / (^{239}Pu/^{235}U ratio [71]) Probability (1/MeV)
1.5	0.2974 ± 0.0077
2.5	0.1917 ± 0.0042
3.5	0.1047 ± 0.0027
4.5	0.0552 ± 0.0016
5.5	0.0278 ± 0.0011
6.5	0.01415 ± 0.00058
7.5	0.00711 ± 0.00043
8.5	0.00329 ± 0.00040
9.5	0.00155 ± 0.00020

TABLE 4. Experimental PFNS for neutron-induced fission of ^{239}Pu. The incident neutron energy E_n, EXFOR No., first author, year of publication and main reference, type of data, outgoing neutron energy E, and comments that include the quality of the information for the purposes of UQ are given.

E_n (MeV)	EXFOR No.	First Author & Year	Type of data	E (MeV)	Comments
thermal	20616005	Werle (1972) [57]	shape	0.104–9.495	+delayed FNS
thermal	41502003	Batenkov (2004) [58]	shape, ratio to Cf	0.12–19	preliminary, uncorrected
thermal	40137004	Belov (1969) [91]	shape	0.3–7	Incomplete UQ
thermal	40871009	Nefedov (1983) [30]	absolute, ratio to Cf	0.084–1.8	Detailed UQ
thermal	40871010			1.2–9.1	
thermal	40872006	Starostov (1983) [31]	absolute, ratio to Cf	3.007–11.16	Detailed UQ
thermal	40873006	Boytsov (1983) [32]	absolute, ratio to Cf	0.021–4.5	Incomplete UQ
thermal	40930	Starostov (1985) [33]	absolute, ratio to Cf	0.020658–11.287	Incomplete, duplicate
thermal	30704004	Lajtai (1985) [62]	absolute, ratio to Cf	0.03–3.855	Detailed UQ for ^{252}Cf(sf) [63]
thermal	–	Vorobyev, this work, Sec. III I	absolute, ratio to Cf	0.241–10.86	Detailed UQ
1.5	–	Lestone (2014) [66, 67]	shape	1.5–11.5	Detailed UQ
1–200	14379	Chatillon (2014) [92, 93]	shape	0.3–8.25	Detailed UQ
1–8 ($\Delta E_n = 1$)	14290	Noda (2011) [73]	shape	1.5–9.5	Incomplete UQ
0.5	13982003	Staples (1995) [74]	shape	0.596–15.952	Incomplete UQ
1.5				1.696 - 15.192	Missing mult. scatt. corr.
2.5				2.808 - 14.485	
3.5				4.088 - 13.828	
0.525	10911004	Smith (1980) [34, 35]	shape, ratio to Cf	0.79–9.86	Not all data available
0.01–0.058	20997004	Abramson (1977) [80, 81]	shape	0.55–14.253	Incomplete UQ
0.53–2.0	–	Johansson (1975) [81, 90]	shape	0.325–14.4	Incomplete UQ
0.215	20576003	Knitter (1975) [81, 94]	shape	0.28–13.87	Incomplete UQ
0.04	20575006	Condé (1965) [87, 88]	shape	0.7–7.5	Insufficient UQ

in outgoing neutron energy (2–8%) and detector efficiency (up to 8%). The total uncertainty does not appear to include the uncertainty in the energy determination.

[Trufanov:41162003] Incident neutron energies (measured PFNS energy ranges) in MeV: 0.5 (0.38–10.51), 5 (0.539–14.415) [77]. Absolute ratios of the ^{235}U(n,f) to ^{252}Cf(sf) spectra were measured using Method 1, but they were provided to EXFOR (and compiled) as absolute data normalized to unity. The standard ^{252}Cf(sf) spectrum from the Mannhart evaluation [36], with wide energy groups, was used to calculate the reported absolute PFNS. The efficiency of fission-fragment detection was 80%. Thickness of the sample was 1 mg/cm^2. No information is provided about corrections and partial uncertainties; only the total uncertainty is given. The data presented in EXFOR [52] appear to be too smooth in the high-energy tail where statistical uncertainties are huge.

[Boykov:41110009] Incident neutron energies (measured PFNS energy ranges) in MeV: 2.9 (0.232–11.885), 14.7 (0.225–11.77) [78, 79]. Absolute neutron yields were measured using Method 1. The reported PFNS was normalized to unity. Values of the ^{252}Cf(sf) standard used in the experiment can be deduced from ratios of PFNS data of this set to those of the following set. The absolute neutron yields can be renormalized to correspond to the ^{252}Cf(sf) standard spectrum by Mannhart [36]. The total uncertainties are the same for the absolute ratios and the absolute values, and they account for statistics, detector efficiency uncertainties, sample mass uncertainties, and correction uncertainties. The uncertainties of the ^{252}Cf(sf) standard spectrum values should be added for the absolute value specifications.

[Abramson:20997003] Incident neutron energies (measured PFNS energy range) in MeV: 0.010–0.058 (0.5–13.946) [80, 81]. The experiment measured shapes using Method 2. A broad neutron spectrum was produced using the ^{7}Li(p,n) reaction near threshold with a 6 keV resolution proton beam. Neutron detectors were installed at 30 and 60 degrees relative the proton beam. A correction for finite sample size was determined by H.-H. Knitter [81]. No correction was made for the time spread of incident neutrons over the sample.

[Johansson:20175003] Incident neutron energy (measured PFNS energy range) in MeV: 0.53 (0.625–14.45) [81, 82]. Measured shape data using Method 3. The n-p standard was used for detector efficiency determination (shape). The data are corrected for a contribution from elastic scattering. Detailed values of the uncertainty components are given. See corrections in Appendix A, Ref. [81].

[Alexandrova:40358004] Incident neutron energy (measured PFNS energy ranges) in MeV: 0.1 (1.511–14.188 and 1.5–10.5) [83]. The experiment measured shapes using Method 2. A ^{252}Cf source was used in place of ^{235}U to check instrumental stability.

[Adams:20996003] Incident neutron energy (measured PFNS energy range) in MeV: 0.52 (0.625–15.629) [81, 84]. Measured shape data using Method 3. The n-p standard was used for detector efficiency determination (shape). The most important sources of error are the relative detector efficiency and the detector energy scale calibration. See corrections in Appendix A, Ref. [81].

[Islam:20385003] Incident neutron energy (measured PFNS energy range) in MeV: 0.4 (0.575–6.87) [81, 85]. Measured shape data using Method 3. Two different detectors were used (for the 0.07–1.1 MeV and 0.07–6.0 MeV neutron energy ranges, respectively). Uncertainties are given to account for counting statistics, background separation, and energy change of the outgoing fission neutrons by inelastic scattering and fission processes. See corrections in Appendix A, Ref. [81].

[Knitter:20394008] Incident neutron energy (measured PFNS energy range) in MeV: 1.5 (1.75–6.98) [81, 86]. Measured shape data using Method 3. The n-p standard was used for detector efficiency determination (shape). The total uncertainty is given, with inclusion of about 2% uncertainty for the detector efficiency. Data are divided by the square root of the neutron spectrum energy. See corrections in Appendix A, Ref. [81].

[Condé:20575] Incident neutron energies (measured PFNS energy range) in MeV: 0.04 and 1.5 (0.3–7.5) [87, 88]. Measured shape data using Method 3. Neutrons were produced by the ^{7}Li(p,n) source reaction using proton beams from a pulsed 2.5-MV Van de Graaff accelerator. The fission neutrons were detected with a plastic scintillator. Thick ^{235}U foil samples were mounted in a xenon gas scintillation chamber that was used to measure the fission fragments. Pb and/or Cd shielding were employed to measure the background fission events resulting from scattered neutrons (the number of fissions attributed to thermal neutrons was estimated to be less than 1% of the fast-neutron fission contributions). Corrections were also applied for detector efficiency variations, secondary neutron events, and uranium sample-thickness effects. The information provided regarding UQ is limited. Relative spectral yield values (shape) are given in the EXFOR entry #20575, and the acquired data were fitted with Maxwellian functions to extract effective temperature values.

B. Neutron-Induced Fission of ^{239}Pu

The existing measurements of the ^{239}Pu PFNS are described in detail in a companion publication in the same volume and journal as this manuscript [89] so they will not be repeated here. See Table 4 for a list of ^{239}Pu PFNS measurements (e.g., see exclusive ^{239}Pu PFNS measurements in Refs. [90–94]). The data of Lestone et al. derived from Nevada test measurements are discussed in Sec. III K. It should be noted that the Johansson 1975 data [81, 90] are not compiled in EXFOR. A brief summary of this work is provided here:

[Johansson: No EXFOR entry] Incident neutron energy (measured PFNS energy range) in MeV: 0.1 (0.1–3.0), 0.18 (0.3–3.0), 0.53 (0.625–14.45), and 2.07 MeV (2.5–10) [81, 90]. This experiment measured shape data using Method 3. The corresponding ^{239}Pu/^{235}U PFNS ratio could be easily derived from measured data. Unfortunately, the measured fission spectra of each incident energy were combined into a single spectrum extending from 0.16 MeV up to 15 MeV [90] for each target. The n-p standard was used for detector efficiency determination (shape). These data were corrected for a contribution from elastic scattering. Detailed values of the uncertainty components are provided. The corrections are given in Appendix A, Ref. [81].

C. Neutron-Induced Fission of ^{233}U

The available ^{233}U(n,f) PFNS data were compiled and 11 relevant references were retrieved from EXFOR [52], 9 of them for the thermal incident neutron energy. An inventory of the measurements appears in Table 5. Data for the evaluation at the thermal neutron point were selected from the same experiments as selected for ^{235}U. The data sets retained for evaluation purposes were those of Starostov et al. [31], Nefedov et al. [30], Boytsov et al. [32, 33], Lajtai

TABLE 5. Measured differential PFNS data sets for neutron-induced fission of ^{233}U. The incident neutron energy E_n, EXFOR [52] accession number, first author, year of publication and main reference, type of data, outgoing neutron energy E, and comments that include the quality of the information for the purposes of UQ are given.

E_n (MeV)	EXFOR No.	First Author & Year	Type of data	E (MeV)	Comments
thermal	–	Vorobyev, this work, Sec. III I	absolute, ratio to Cf	0.221–16.65	Detailed UQ
thermal	30704002	Lajtai (1985) [62]	absolute, ratio to Cf	0.03–3.9	Detailed UQ for ^{252}Cf(sf) [63]
thermal	40872008	Starostov (1983) [31]	absolute, ratio to Cf	4.8–9.3	Detailed UQ
	40872005		absolute	4.9–10.2	Duplicate, use 40872008
thermal	40871013	Nefedov (1983) [30]	absolute, ratio to Cf	0.85–4.7	Detailed UQ
thermal	40873002	Boytsov (1983) [32, 33]	absolute, ratio to Cf	0.02–4.5	Detailed UQ, use below 3.3
thermal	40930004	Boytsov (1983) [32, 33]	absolute, ratio to Cf	0.1–1.7	Detailed UQ
	40930010			1.6–4.5	
	40930011			3.8–9.4	
	40930012			0.02–3.3	Duplicate, use 40873002
0.55	22688002	Miura (2002) [95]	shape	0.7–12.	Detailed UQ
0.525	10911002	Smith (1980) [34, 35]	shape, ratio to Cf	0.58–7.7	Not all data available

et al. [62], and Vorobyev et al. (see Sec. III I). The experimental values have been tabulated and are available from the CRP website [53].

The measurement techniques used in these experiments fall into the same categories mentioned above for the ^{235}U PFNS experiments at energies other than thermal. The reader is referred to the descriptions of these techniques in Sec. III A 2 of this paper. As in the case for the ^{235}U PFNS experiments mentioned earlier, the contributions below are identified by their EXFOR [52] entries.

[Vorobyev: Sec. III I] Incident neutron energy (measured PFNS energy range): Maxwellian with $T = 0.0363$ eV (0.2–16.65 MeV). Measured shape data using Method 1. Measured coincidences between prompt fission neutrons registered by the detectors (covering 2π solid angle) and light or heavy fission fragments. PFNS are obtained by integration over angle and summation of fragment events after introducing all needed corrections to the primary observables.

[Lajtai:30704002] Incident neutron energy (measured PFNS energy range) in MeV: thermal (0.03–3.855) [62]. Measured shape data using Method 1. A thick lithium glass detector was used for the neutron measurements (see corrections in Ref. [63]). A Maxwellian with $T = 1.418$ MeV was employed to represent ^{252}Cf(sf) as a standard. These data can be recalculated using the Mannhart standard [36, 37] to yield the shape of the ratio of ^{252}Cf(sf) to ^{233}U PFNS.

[Starostov:40872008] Incident neutron energy (measured PFNS energy range) in MeV: thermal (4.777–9.27) [31]. The experiment measured the absolute ratio of ^{252}Cf(sf) to ^{233}U PFNS using Method 1. The experimental setup was optimized for measurements of spectra in various energy ranges. Statistical uncertainties and uncertainties in the energy scale determination are given.

[Starostov:40872005] Incident neutron energy (measured PFNS energy range) in MeV: thermal (4.91–10.2) [31]. Measured absolute neutron yields using Method 1. The experimental setup was optimized for measurements of the high-energy part of spectra. Detailed components of the uncertainties are presented. A Maxwellian with $T = 1.418$ MeV for ^{252}Cf(sf) was used as the standard spectrum. These data can be recalculated using the Mannhart standard [36, 37] to yield the shape of the ratio of ^{252}Cf(sf) to ^{233}U PFNS. This data set corresponds to the same experiment as compiled in subentry 40872008 described in the preceding paragraph, so it is not used in the evaluation.

[Nefedov:40871013] Incident neutron energy (measured PFNS energy range) in MeV: thermal (0.847–4.71) [30]. The experiment measured the absolute ratio of ^{252}Cf(sf) to ^{233}U PFNS using Method 1. The experimental setup was optimized for measurements of spectra in various energy ranges. Statistical uncertainties and uncertainties in the energy determination are given.

[Boytsov:40873002] Incident neutron energy (measured PFNS energy range) in MeV: thermal (0.021–4.5) [32, 33]. Absolute ratios of the ^{233}U to ^{252}Cf spectra were measured using Method 1, but they were provided to EXFOR (and compiled) as absolute ^{233}U ratios to a Maxwellian with $T = 1.34$ MeV. The experimental setup was optimized for measurements of spectra at low energy. A Maxwellian with $T = 1.418$ MeV was employed to represent ^{252}Cf(sf) as a standard. These data can be recalculated using the Mannhart standard [36, 37] to provide the absolute ratio of ^{252}Cf(sf) to ^{233}U PFNS and then used as primary data in the evaluation.

[Boytsov:40930004, 40930010, 40930011, 40930012] Incident neutron energy (measured PFNS energy ranges) in MeV: thermal (0.1–1.7, 1.6–4.5, 3.769–9.37, 0.02–3.3) [32, 33]. Measured absolute ratio data relative to a Maxwellian with $T = 1.34$ MeV using Method 1. The experimental setup was optimized for measurements of spectra in various energy ranges. A Maxwellian with $T = 1.418$ MeV was employed to represent ^{252}Cf(sf) as a standard. The data have been digitized. These data should be replaced by data compiled as absolute ratios to ^{252}Cf if they are available (e.g., data in 40930012 should be dismissed and replaced by data in 40871013).

[Boytsov:40873008–40873013] Incident neutron energy (measured PFNS energy ranges) in MeV: thermal (0.0182–

3.942, 0.080–1.445, 0.0945–1.398, 0.024–0.3158, 0.107–0.612, 0.675–0.948). Measured shape data using Method 1. The experimental setup was optimized for measurements of spectra in various energy ranges. A Maxwellian with T = 1.418 MeV was employed to represent ^{252}Cf(sf) as a standard. The data have been digitized. This set seems to be a duplicate one but further investigation is required. As they are, these data cannot be recommended for use in an evaluation.

[Miura:22688002] Incident neutron energy (measured PFNS energy range) in MeV: 0.53 (0.7–11.6) [95]. Measured shape data using Method 3. Corrections were made for time resolution, flux attenuation, and multiple scattering within the samples. The spectra were measured at 135° for 1.9 MeV incident neutrons and 115° for 4.1 MeV incident neutrons (EXFOR = 22688008).

[Smith:10911002] Incident neutron energy (measured PFNS energy range) in MeV: 0.53 (0.58–7.72) [34, 35]. Measured the ratio of ^{233}U PFNS to ^{252}Cf(sf) using neutron time-of-flight techniques, scintillation detectors, and a fission chamber with Method 1. Timing signals were generated from the scintillation detectors (for neutrons), from fission fragments (for the Cf measurements), and pulsed-neutron beams (for the uranium measurements). Plotted sets of the experimental data were digitized since the original data are unavailable. The total uncertainty varies between 100% at low energy, to 10% at 1–2 MeV, and up to 30% at higher energies. This experiment is described in more detail in Sec. VI E of the present paper.

TABLE 6. Experimental PFNS for fast neutron-induced fission of ^{238}U. The incident neutron energy E_n, EXFOR [52] accession number, first author, year of publication and main reference, type of data, outgoing neutron energy E, and comments that include the quality of the information for the purposes of UQ are given. Method 1 was used in all measurements.

E_n (MeV)	EXFOR No.	First Author, Year	Type of data	E (MeV)	Comments
14.3	40740002	Baryba (1979) [99, 100]	shape	0.6–9.96	Incomplete UQ
6.01	40631	Kornilov (1980) [99, 101]	shape	0.72–8.8	Incomplete UQ
7.02				0.62–8.14	
8.01				0.7–8.63	
8.94				0.61–9.73	
2.0	22112003	Baba (1989) [102]	shape	2.3–12.87	Incomplete UQ
2.9	41110010	Boykov* (1991) [78, 79, 103]	shape, ratio to Cf	0.232–11.885	Incomplete UQ
14.7			shape, ratio to Cf	0.225–11.77	
16.0	41461004	Smirenkin (1996) [98]	shape, ratio to Cf	0.39–11.95	Incomplete UQ
17.7				0.39–13.36	
5.0	41450003	Trufanov (2001) [97]	shape, ratio to Cf	0.28–12.27	Incomplete UQ
13.2			shape, ratio to Cf	0.45–12.36	
6.0	41447003	Lovchikova (2004) [96]	shape, ratio to Cf	0.13–13.77	Incomplete UQ
7.0			shape, ratio to Cf	0.14–15.17	
2.0	–	Desai (2015) [104] and Sec. III J	shape	0.75–8.75	Incomplete UQ
2.5	–		shape	0.75–6.75	
3.0	–		shape	0.75–8.25	

* G.S. Boykov name has been often transliterated as G.S. Boikov (see a note in EXFOR entry #41110).

D. Fast Neutron-Induced Fission of ^{238}U

Seven data sets relevant to ^{238}U PFNS are available and listed in Table 6. The quality of the experimental data, as reflected in the corresponding uncertainties, was assessed by analyzing the information provided by the authors of the publication regarding their estimates of the various sources of experimental uncertainty. In instances where such information is not available in that particular publication, assessments could be made by comparing their results with those obtained from similar experiments that utilized different experimental setups. In some cases it is not clear whether data from a previous experiment were simply re-analyzed or whether the results were actually new but acquired using the same experimental setup described in an older reference.

In the following a brief summary is given of the different instrumentations used in the evaluated experiments together with the identified sources of uncertainty. It is indicated in which cases the information provided appears unsatisfactory, eventually leading to the uncertainty quantification quality statements that appear in Table 6.

In all cases except one, multi-section ionization chambers with active layers up to 2 mg/cm^2 in thickness were used. Each section is a parallel-plate chamber and the uranium layer is fixed on the cathode plate. The fission fragment detection efficiency varies in the different experiments between 70% [78, 96–98] and 90% [99] with a reported uncertainty of 5%. From the contained information about the chamber design, it appears that the small inter-electrode gap did not allow for measuring the fission axis relative to the neutron beam. In Ref. [78] a correction for angular anisotropy of fission fragment emission was applied. However, uncertainty quantification is lacking.

Prompt fission neutrons were measured by means of time-of-flight relative to the fission event time trigger. The distance between the fission source and the neutron detector ranged between 1.7 m [97, 98] and 2.05 m [78]. The time-of-flight was measured with a timing resolution of 1.5–3.0 ns. Stilbene-type scintillation detectors of size 7 cm × 4 cm (diameter × length) were typically used as neutron detectors.

The neutron detection efficiency was measured relative to the spontaneous fission of ^{252}Cf. In some cases the γ-background was reduced by employing the pulse-shape discrimination technique [96–98]. γ-ray suppression factors of 80 [97], at 250 keV prompt fission neutron energy, and 10, at 80 keV [96], were reported. In the latter case a paraterphenyl detector was employed, with the neutron detection threshold given to be 100 keV. However, all specified values are not traceable, because no spectra were provided in the documentation. Therefore, the influence on the shape of the prompt fission neutron spectrum cannot be quantified.

As a general statement it should be noted that all low-energy thresholds given in the above mentioned papers appear to be too low, considering the known efficiency of the neutron detectors employed. Nowadays even paraterphenyl detectors do not allow measuring neutrons below an energy of 400 to 500 keV with reasonable uncertainty. For the future this might impose the largest problem when considering whether to perform validation measurements.

[Baryba:40740002] [99, 100] and [Kornilov:40631002–40631005] [101]: PFNS data are reported for incident neutron energies between 6.01 and 14.3 MeV. A multi-section ionization chamber (IC) was used as a fission detector. A ^{252}Cf(sf) source (in a gas scintillator detector or in a fast ionization chamber) was used for detector efficiency estimation in a separate experiment. The fission fragment detection efficiency was 75%. The uncertainty in this value is around 5%, as determined from similar experiments mentioned below. The contribution from background neutrons produced in the target structure is specified to be 5% at most. The samples were made from highly depleted material (99.999% ^{238}U), which limits the spectral contamination due to ^{235}U from thermalized source neutrons to a negligible level. A stilbene crystal of size 7 cm × 5 cm (diameter × length) coupled to a a FEU-30 PMT served as the neutron detector. This detector was placed at 90° relative to the direction of the incident neutron beam. The total mass of the highly depleted ^{238}U loaded is 2.69 g, distributed over a 5.5 cm diameter circular deposits. There are 34 electrodes in the chamber. The efficiency was determined relative to the spectrum from spontaneous fission of ^{252}Cf approximated by a Maxwellian with $T = 1.42$ MeV. The combined effect of neutron attenuation and multiple scattering in the target was estimated for the prompt neutron energy range between 0.6 and 8 MeV to be smaller than 2%. The PFN energy was determined by means of time-of-flight (TOF), with a timing resolution of 1.5–3.0 ns and a TOF distance of 210 cm. Pulse shape discrimination (PSD) was apparently used in the experiment but there was no further specification of the method.

[Boykov(a):41110010] Incident neutron energies (measured PFNS energy ranges) in MeV: 2.9 (0.232–11.885) and 14.7 (0.225–11.77) [78]. This paper describes spectral neutron measurements at two different incident neutron energies, 2.9 and 14.7 MeV. The corresponding EXFOR entry is #41110, as indicated in Table 6. The fission trigger consists of a multi-section IC. With an inter-electrode gap that is only equal to 0.35 cm, it is not possible that the fission fragments will be stopped in the IC filler gas. Therefore, no information on the emission angle relative to the neutron beam is available. A correction for angular anisotropy of the fission fragment emission relative to the incident neutron beam was applied, but no uncertainty is specified. Instrumental anisotropy was eliminated through a measurement relative to the reference reaction ^{252}Cf(sf).

The total mass of the highly depleted ^{238}U loaded per chamber section is 1.87 g, distributed over a 10 cm diameter circular deposits. There are 12 active films in each of the three chamber sections, i.e., a total of 36 active layers. The detection efficiency is given as 70% with a quoted uncertainty of 5%. The IC was made from 0.01 cm of stainless steel. The whole chamber was surrounded by 0.2 cm cadmium to eliminate fission events induced by thermal neutrons. A stilbene crystal of size 7 cm × 5 cm (diameter × length) coupled to a a FEU-30 PMT served as the neutron detector. This detector was placed at 90° relative to the direction of the incident neutron beam. A PSD technique, with a threshold of 250 keV, was employed, and a γ-ray suppression factor of 180 is reported. The neutron detection efficiency was measured relative to ^{252}Cf, with uncertainty of 3% over the entire energy range of the PFNs. The PFN energy was determined by means of time-of-flight (TOF), with a timing resolution of 2.5 ns and a TOF distance of 205 cm.

For the spectral data, average PFN energy and the Maxwellian parameter T, only a total uncertainty is given. In #41110 the total uncertainty in percent is quoted for each spectral energy bin, and it ranges between 3 and 25%. Contributions to the uncertainty are, at the very least, due to counting statistics, detection efficiency and the uncertainty in determining the TOF.

[Boykov(b):41110010] Incident neutron energies (measured PFNS energy ranges) in MeV: 2.9 (0.232–11.885) and 14.7 (0.225–11.77) [103]: This paper describes spectral neutron measurements at two different incident neutron energies, 2.9 and 14.7 MeV. The description of experimental setup resembles that of the entry in the preceding paragraph [78], and it seems that the same experimental data were exploited. At least, Fig. 2 is identical to Fig. 1 in Ref. [78]. However, from the setup shown in the paper it appears that there were a few differences:

- the timing resolution of the IC is quoted as 1.5 ns, and the total TOF resolution was 2.5 ns, as in the preceding entry,
- the orientation of the neutron detector relative to the incident neutron beam axis is quoted to be 90°, however

TABLE 7. Experimental PFNS for fast neutron-induced fission of ^{232}Th. The incident neutron energy E_n, EXFOR [52] accession number, first author, year of publication and main reference, type of data, outgoing neutron energy E, and comments that include the quality of the information for the purposes of UQ are given.

E_n (MeV)	EXFOR No.	First Author (Year)	Type of data	E (MeV)	Comments
2.0	22112004	Baba (1989) [102]	shape	2.3–10.87	Stat. uncert.
2.9	41110008	Boykov (1991) [78]	shape, ratio to Cf	0.232–11.885	Incomplete UQ
14.7			shape, ratio to Cf	0.225–11.77	
14.6	41446004	Lovchikova (2004) [105]	shape, ratio to Cf	0.4–10.14	Incomplete UQ
17.7				0.55–13.75	

the sketch indicates an angle of 110°.

[Smirenkin: 41461004] Incident neutron energies (measured PFNS energy ranges) in MeV: 16.0 (0.39–11.95) and 17.7 (0.39–13.36) [98]. This work was a follow-up of the measurements reported in Ref. [78]. PFNS for incident neutron energies of 16 and 17.7 MeV were measured, as indicated in Table 6. The setup is the one previously reported by Boykov(a). However the TOF distance was 170 cm and the timing resolution is quoted to be between 2.5 and 3 ns. The stilbene neutron detector is somewhat smaller than the one used in a previous experiment [103], i.e., 6.3 cm × 3.9 cm (diameter × length). Uncertainties for the spectral data may be assumed as quoted/deduced in Ref. [78]. We note that the stated sample mass of 5 g is compatible with the description of the IC configuration.

[Trufanov:41450003] Incident neutron energies (measured PFNS energy ranges) in MeV: 5.0 (0.28–12.27) and 13.2 (0.45–12.36) [97]. The work reports spectral prompt neutron measurements at incident neutron energies of 5.0 and 13.2 MeV, as indicated in Table 6. The energies were chosen to confirm results obtained at $E_n = 2.9$ MeV and to get more precise information about the contribution of the $(n,2nf)$ reaction infringing on the spectrum at higher incident neutron energies. The experiment setup is based on the same components used in previous measurement campaigns [78, 98]. The neutron detector was embedded in sandwich-like shielding consisting of ^{6}LiH, Pb, Fe and Cu, arranged sequentially in this order. However, no thicknesses for the layers are given. PSD is applied. At a pulse height threshold corresponding to 200 keV, a γ suppression factor of 80 was achieved. This information is not traceable because no spectrum is given.

According to the authors, and (again) in contradiction with the experimental sketch in Ref. [103], secondary neutrons were measured at 90° relative to the axis of the primary neutron beam. The TOF distance is 170 cm and the detector is the same as in Ref. [98]. The assumption about point-wise uncertainties may, therefore, be made as in the previous reference(s).

There were 20 layers reported for the IC, with a total fissionable mass of 5.5 g. The given thickness of the layers and the total mass do not match. The efficiency of fission fragment detection and of the neutron detector were determined relative to the spontaneous fission of ^{252}Cf. The corresponding target thickness is stated to be 2 mg/cm^2.

[Lovchikova:41447003] Incident neutron energies (measured PFNS energy ranges) in MeV: 6.0 (0.13–13.77) and 7.0 (0.14–15.17) [96]. The authors measured the PFNS for incident neutron energies of 6.0 and 7.0 MeV, as indicated in Table 6. Secondary neutrons were measured between 140 keV and 15 MeV. Primary neutrons were produced with a proton beam on a gaseous tritium target. This kept the contribution of low-energy neutrons below 1% for proton energies up to 9 MeV. A paraterphenyl crystal of size 5 cm × 5 cm (diameter x length) coupled to a FEU-143 photomultiplier (PM) was used as the neutron detector. A low-energy threshold of 100 keV was reported. The absolute neutron detection efficiency was 50%. PSD with a neutron energy threshold of 80 keV was employed and a γ suppression factor of 80 was achieved. The neutron detector was placed in shielding, which was configured like that detailed in Ref. [103]. Additionally, the detector was surrounded by 10 cm of Pb, and a 0.5 cm thick lead shield was used in the detector face to attenuate the γ-background.

The multi-section IC chamber described in an earlier section was used for this work. It was loaded with a total amount of 5.61 g ^{238}U (99.999%). Therefore, the uncertainty on the detection efficiency may be assumed to be 5%. The IC was oriented at an angle of 45° relative to the axis of the incident neutron beam. A neutron fluence monitor was placed 300 cm away at an angle of 90°. No further uncertainty discussion is presented. From the measured spectra, depicted as the ratio to a Maxwellian, a point-wise total uncertainty of 3% at 2 MeV up to 10% at 100 keV may be extracted from Fig. 1 of Ref. [96]. The corresponding total uncertainty from 2 MeV upward in energy increases to at least 20% at 16 MeV for $E_n = 7.0$ MeV. For the extracted spectral characteristics, no uncertainties are given in the Table on page 1254 of Ref. [96] (English translation).

[Baba:22112] Incident neutron energy (measured PFNS energy range) in MeV: 2.0 (2.3–12.87) [102]. ^{238}U PFNS for 2-MeV incident neutrons were measured using the time-of-flight technique and massive ^{238}U samples (Method 5). The primary neutrons were produced via the $t(p,n)$ reaction using a tritium-loaded titanium target. A 4.5 MV Dynamitron accelerator provided the pulsed proton beam. The energy spread was about 50 to 70 keV (FWHM). The average neutron pulse width was found from the width of the prompt γ-flash to be (1.7 ± 0.1) ns. The repetition rate was 2 MHz. The average beam current was 4 to 6 μA and it was monitored with a detector of same type, but of smaller size, which was well shielded from the fission target. The monitor data were used to normalize the sample-in and sample-out data. The fission sample was placed about 10 cm from the neutron producing target and suspended by a remotely-controlled sample changer. The time-of-flight distance was 3.9 m.

The neutron detector was housed in a massive hydrogenous shield with tight collimation to reduce time-dependent backgrounds. The detector was a 14 cm diameter by 10 cm thick NE-213 scintillator coupled to a 12.7 cm diameter photomultiplier (Hamamatsu R1250). Pulse shape discrimination was applied, but no spectrum is shown in the reference. The relative efficiency of the neutron detector was determined from Monte Carlo calculations and measurements of ^{252}Cf(sf) and of hydrogen-scattered neutrons. The authors quote an uncertainty band of 5% throughout the range of the efficiency curve. The background due to elastically scattered source neutrons was investigated using a Pb target. Statistical background was determined in a sample-out measurement. The low-energy threshold of the PFNS was set at 2 MeV. The effect of multiple neutron scattering was quantified to "a few percent" above 2 MeV by means of Monte-Carlo simulations. A correction to the PFNS was made for the tail of elastically scattered neutrons that affected the spectrum by examining the spectrum for the Pb target. The effects of time resolution and time shift due to the length of the scintillator were negligible. The PFNS were obtained from 2–12 MeV. Ultimately, these data were fitted with Maxwellian and Watt [12] functions in order to derive $\overline{E}$ value for the ^{238}U PFNS.

E. Fast Neutron-Induced Fission of ^{232}Th

The experimental data base for ^{232}Th PFNS consists of results from only three experiments. See Table 7 for a list of these measurements. Brief descriptions of the experiments are provided here.

TABLE 8. Experimental PFNS for neutron-induced fission of ^{237}Np and ^{240}Pu. The target, incident neutron energy E_n, EXFOR accession number, first author, year of publication and main reference, type of data, and outgoing neutron energy E are given.

Isotope	E_n (MeV)	EXFOR No.	First Author & Year	Type of data	E (MeV)
^{237}Np	0.620	22112	Baba (1988) [102]	fitted Maxwellian	0.8–12
^{237}Np	0.620	22481	Win (1999) [106]	fitted Maxwellian	0.8–12
^{237}Np	4.9	41132003	Trufanov (1992) [107]	shape, ratio to Cf	0.79–12
	7.8	41132004			1.5–12
^{237}Np	6.0	–	Trufanov (1991) [108]	shape, ratio to Cf	0.79–12
^{237}Np	0.52	41332002	Kornilov (2000) [109]	shape	0.71–12
^{240}Pu	0.85	10911005	Smith (1980) [34, 35]	shape, ratio to Cf	1.0–7.6
^{240}Pu	sf	40250004	Alexandrova (1974) [110]	shape	2.4–14
^{240}Pu	sf	40250005		shape	1.9–5.9
^{240}Pu	sf	41421002	Gerasimenko (2002) [111]	absolute, ratio to Cf	0.13–11

[Baba:22112] [102] Incident neutron energy (measured PFNS energy range) in MeV: 2.0 (2.3–10.87) [102]. This experiment measured ^{232}Th PFNS for 2 MeV incident neutrons using the time-of-flight technique and solid thorium samples (Method 5). The primary neutrons were produced via the t(p, n) reaction using a tritium-loaded titanium target. A 4.5 MV Dynamitron accelerator provided the pulsed proton beam. The energy spread was about 50 to 70 keV (FWHM). The fission sample was placed about 10 cm from the neutron producing target and suspended by a remotely-controlled sample changer. The neutron detector was housed in a massive hydrogenous shield with tight collimation to reduce time-dependent backgrounds. The detector was a NE-213 scintillator whose relative efficiency was determined from Monte Carlo calculations and measurements of spontaneous-fission neutrons from ^{252}Cf and of hydrogen-scattered neutrons. The PFNS were obtained from 2–10 MeV. Ultimately, these data were fitted with Maxwellian and Watt [12] functions in order to derive values for ^{232}Th PFNS average energy.

[Boykov:41110] [78] Incident neutron energies (measured PFNS energy ranges) in MeV: 2.9 (0.232–11.885) and 14.7 (0.225–11.77) [78]. Sufficient information is available from the EXFOR entry to provide a brief description of the experiment (Method 1). The measurements utilized neutrons of 2.9 and 14.7 MeV generated by pulsed deuteron beams from a NG-400 neutron generator incident on deuterium and tritium targets (D-D and D-T source reactions). A TOF procedure was used for fission neutron spectrum determinations, with a total time resolution of 2.5 ns. A four-section ionization chamber filled with methane and covered with 0.2 mm thick Cd was used to measure fission fragments from ^{232}Th fissions as well as from a ^{252}Cf fission deposit which was used for detector efficiency calibration. The calibration uncertainty was estimated to be 3%. The fission neutrons were detected with a 40 mm high × 100 mm diameter stilbene crystal that was attached to a FEU-30 photo-multiplier tube. Corrections were applied for TOF path differences for the various deposits in the ionization chamber for neutron energies above 0.25 MeV. The total error in the reported data was based on consideration of statistics, detector efficiency uncertainty, and uncertainties in the corrections.

TABLE 9. Experimental PFNS for neutron-induced or spontaneous fission of other actinides. The incident neutron energy E_n, EXFOR number, first author, year of publication and main reference,type of data, and outgoing neutron energy E are given.

Isotope	E_n (MeV)	EXFOR No.	First Author & Year	Type of data	E (MeV)
^{229}Th	thermal	40064028	Kroshkin (1970) [112]	shape	0.52–6.2
^{238}Pu	thermal	40064029	Kroshkin (1970) [112]	shape	0.42–6.2
^{241}Pu	0.53	10911	Smith (1980) [34, 35]	shape, ratio to Cf	1.0–7.6
^{242}Pu	sf	40137003	Belov (1969) [91]	shape	0.37–4.8
^{242}Pu	sf	41421003	Gerasimenko (2002) [111]	absolute, ratio to Cf	0.13–11
^{241}Am	2.9,4.5,14.6	41589	Drapchinsky (2004) [113]	absolute, ratio to Cf	0.43–13
^{242m}Am	thermal	41421008	Gerasimenko (2002) [111]	absolute, ratio to Cf	0.12–14
^{243}Am	2.9,4.5,14.6	41589	Drapchinsky (2004) [113]	absolute, ratio to Cf	0.43–13
^{243}Cm	thermal	41589008	Drapchinsky (2004) [113]	absolute, ratio to Cf	0.27–13
^{244}Cm	sf	40064025	Kroshkin (1970) [112]	shape	0.33–6.0
^{244}Cm	sf	40137002	Belov (1969) [91]	shape	0.29–6.2
^{244}Cm	sf	40250002	Alexandrova (1974) [110]	shape	2.0–13
^{244}Cm	sf	41340004	Boykov* (1997) [114]	absolute, ratio to Cf	0.10–14
^{245}Cm	thermal	40064026	Kroshkin (1970) [112]	shape	0.44–5.9
^{245}Cm	thermal	41421009	Gerasimenko (2002) [111]	absolute, ratio to Cf	0.10–11
^{246}Cm	sf	41340005	Boykov* (1997) [114]	absolute, ratio to Cf	0.12–14
^{248}Cm	sf	32726002	Bao (2001) [116]	absolute, ratio to Cf	1.2–11
^{248}Cm	sf	41113004	Batenkov (1991) [115]	absolute, ratio to Cf	0.14–15
^{249}Cf	thermal	40064030	Kroshkin (1970) [112]	shape	0.40–6.5

* G.S. Boykov name has been often transliterated as G.S. Boikov (see a note in EXFOR entry 41110).

[Lovchikova:41446] [105] Incident neutron energies (measured PFNS energy ranges) in MeV: 14.6 (0.4–10.14) and 17.7 (0.55–13.75) [105]. Sufficient information is available from the EXFOR entry to provide a brief description of the experiment. The experiment was performed using a KG-2.5 Van de Graaff accelerator to produce pulsed 14.6 and 17.7 MeV neutrons via the D-T source reaction (Method 1). The TOF method was used to measure the fission neutron spectra. The flight path was 1.7 m, and it was situated at 90° to the incident neutron beam. A three-section ionization chamber was used to measure the fragments from ^{232}Th fissions as well as those from a ^{252}Cf deposit which was used for efficiency calibration purposes. The total weight of the thorium was 5.65 g. The neutron detector was a 63 mm diameter × 39 mm high stilbene crystal. The minimum neutron detection energy was 250 keV. Total uncertainties in the neutron spectrum values are given in percent. They range from 2.4 to 84%.

F. Fast Neutron-Induced Fission of ^{237}Np and ^{240}Pu and Spontaneous Fission of ^{240}Pu

Table 8 catalogs PFNS measurements for ^{237}Np from four authors and ^{240}Pu data from three authors. All these data are available in EXFOR [52]. Brief summaries of each of these experiments are given below.

a. ^{237}Np Measurements. [Baba:22112] Incident neutron energy (measured PFNS energy range) in MeV: 0.620 (0.8–12) [102]. This experiment was undertaken to determine the PFNS average energy for 0.620 MeV incident neutrons. The measurements were carried using the time-of-flight technique (Method 5). The Tohoku University 4.5 MV Dynamitron accelerator was employed to produce the pulsed neutron beam. A heavily shielded NE-213 scintillation detector was used to measure the ^{237}Np PFNS neutrons over the emitted neutron-energy range 0.8–12 MeV. These measurements were made relative to ^{252}Cf(sf). The original spectral data were not made available. Instead, the authors fitted their measured spectra with Maxwellian and Watt-type distribution functions that were chosen to approximate the fission-neutron spectrum shapes. The Maxwellian temperature deduced from this work was 1.28 ± 0.04 MeV.

[Win:22481] Incident neutron energy (measured PFNS energy range) in MeV: 0.620 (0.8–12) [106]. Although this experiment was carried out a decade later than the work of Baba [102], the measurements were performed in the same facility (Method 5), and it is apparent from the documentation that the procedures used in the measurement and data analysis are basically the same for the two experiments. In fact, the authors of the present work state that this is the case, with the exception of a few improvements related to the sample and ^{252}Cf deposit used in the later work. The derived Maxwellian temperature and its uncertainty are identical to the earlier results of Win [106].

[Trufanov:41132003,41132004] Incident neutron energies (measured PFNS energy ranges) in MeV: 4.9(0.79–12) and 7.8(1.5–12) [107]. A brief description of these experiments is available from EXFOR [52]. More detailed documentation is available in the reference cited in the Table. A Van de Graaff accelerator was used to produce the incident pulsed-neutron beams. Stilbene detectors were used to measure the PFNS neutrons. These detectors were calibrated using ^{252}Cf(sf) neutrons. The ^{252}Cf deposit was placed in an ionization chamber that was used to measure the fission fragments. The ^{237}Np deposit weighed 500 milligram, and it was deposited on fission chamber electrodes. The experiments yielded PFNS shape data rather than an absolute yield determinations. No uncertainty analysis was specified. It is noted that there is an additional experiment at E_n=6 MeV reported by the same group [108], but those data are not compiled in EXFOR.

[Kornilov:41332002] Incident neutron energy (measured PFNS energy range) in MeV: 0.52(0.71–12) [109]. A summary of this experiment is provided in the indicated EXFOR [52] entry. Further details are available from published documentation [99, 101]. Pulsed-neutron beams were generated using a Van de Graaff accelerator and the p-^{7}Li source reaction. The flight path was 2 m. The PFNS neutrons were measured using a 70 mm dia x 50 mm high stilbene detector. A long counter and plastic scintillator were employed for incident neutron yield and TOF monitoring purposes. A carbon sample was also used in these measurements. The PFNS neutron detector was calibrated using ^{252}Cf(sf) neutrons. A cylindrical Np-oxide powder sample weighing 189.1 g was used in these measurements. The ^{252}Cf deposit was placed in a fission chamber that was employed to measure fission fragments. The measured data were corrected for scattering from oxygen and from the iron in the Np-deposit container. PFNS values are provided in units of particles per fission per MeV. The given spectrum uncertainties range from $2.5-57\%$.

b. ^{240}Pu Measurements. [Smith:10911005] Incident neutron energy (measured PFNS energy range) in MeV: 0.85 (1.0–7.6) [34, 35]. This measurement formed part of a collection of PFNS measurements on several isotopes using Method 1. The procedure was the same for all of them, as described in Sec. VI E. The spectral data measured in this experiment were used to derive a PFNS average temperature of 2.054 ± 0.029 MeV based on the assumed value of 2.13 MeV for the ^{252}Cf(sf) spectrum-average temperature. Plots for the measured spectra are shown in the original documentation [35]. However, numerical values were not given, nor were they provided for EXFOR [52].

[Alexandrova:40250004,40250005] Incident neutron energies (measured PFNS energy ranges) in MeV: sf (2.4–14) and sf(1.9–5.9) [110]. A brief description of this experiment was obtained from the indicated EXFOR [52] entries. This experiment measured spontaneous fission (sf) neutrons from ^{240}Pu rather than neutron-induced fission. These measurements were made using a fission ionization chamber to detect fission fragments from a Pu-oxide sample. A stilbene crystal of 3 cm dia x 3 cm high placed 3 cm from the Pu sample in the ionization chamber was employed to detect the sf neutrons from ^{240}Pu. The spectrum energy scale was calibrated at an accelerator using mono-energetic neutrons from the *p-t*, *d-d*, and *d-t* reactions. A lead plate was placed between the sample and neutron detector to suppress photons. Measurements of ^{252}Cf(sf) were also made with this experimental setup. The spectral data were provided to EXFOR [52] as yield values relative to the square root of the emitted neutron energy (arbitrary units). No uncertainties were provided. However a statement appears in EXFOR indicating that there were uncertainties that resulted from digitizing both the spectral data and spectral energies.

[Gerasimenko:41421002] Incident neutron energy (measured PFNS energy range) in MeV: sf (0.13–11). A brief summary follows based on information provided in the EXFOR [52] entry. Additional information can be found in Ref. [111]. This experiment measured both ^{240}Pu and ^{242}Pu(sf) neutron spectra by using a coincidence method. Two detectors were employed to measure the fission neutrons, a NE-213 scintillation detector and a B-105A detector. Fission fragments were measured with a fission ionization chamber. Measurements were also made of ^{252}Cf(sf), serving as a monitor, with this experimental setup. Neutrons and fission fragments were detected in coincidence. The data were corrected for random coincidence background, neutron capture background photons, finite time resolution, and spontaneous fission of other actinide nuclides. The measured spectral data represent absolute ratios to ^{252}Cf(sf). The numerical values as a function of emitted neutron energy (lab system) that were provided for EXFOR [52] include ratio values to Cf, derived PFNS values in arbitrary units, based on assuming a Maxwellian with $T = 1.42$ MeV for ^{252}Cf(sf), and uncertainties for both of these quantities in the corresponding units. These data can be recalculated using the Mannhart standard [36, 37] to yield the shape of the ratio of ^{252}Cf(sf) to ^{240}Pu(sf) PFNS.

G. Spontaneous and Neutron-Induced PFNS for Remaining Actinides

Table 9 catalogs all available PFNS measurements not discussed above, including several spontaneous fission datasets. This data compilation is provided for completeness, but these data were not used in evaluations or compared to model calculations in this work. Consequently, no descriptions of these tabulated experiments are provided.

H. IRMM Experiments for Thermal Neutron-Induced Fission of ^{235}U

PFNS of ^{235}U(n,f) were measured at the incident neutron energies 0.5 MeV [69] and the thermal point [60, 61]. Results and experimental details for 0.5 MeV were presented at the conference ND2007 [69], however the data presented there were preliminary and final results are not yet available. The thermal point measurements are described briefly in this section and they were published in Refs. [60, 61]. Further experimental and data analysis details, as well as final results, will be published at a future time when all the experimental data have been analyzed.

PFNS were measured at 100 K incident neutron energy by the time of flight method at the cold-neutron PGAA facility of the Budapest Nuclear Research Reactor. The experimental procedure was similar to that used in a previous experiment [117]. A ^{235}UF$_4$ (97.7% enrichment in ^{235}U, diameter = 30 mm) layer of 112 μg/cm^2 thickness evaporated onto a thin (24 μg/cm^2) gold (40 μg/cm^2) coated polyimide foil served as the target. This target was placed in the center of a conventional multiple-plate ionization chamber that was used to count fission fragments. A ^{252}Cf layer (diameter = 10 mm) was placed in the same chamber, but it was shifted by 5 cm from the ^{235}U layer and also situated out of the neutron beam. The fast current signal at a cathode of a particular component of a chamber was used to produce the start signal. The corresponding anode was used for measurement of neutron spectra emitted from fission fragments with fixed mass and emission angle. The fission fragment counting efficiency was 98% for both neutron sources. It was determined as described in Ref. [117].

Three identical cylindrical scintillation detectors (diameter = 101.6 mm and height = 50.8 mm) were each coupled to a XP4312 photomultiplier tube. The organic scintillator was NE213-equivalent LS301. These neutron detectors were placed at different angles relative to the neutron beam, with slightly different flight paths. The uncertainties in flight path length and angle were ±0.5 cm and ±1°, respectively. Each individual detector was placed in its own massive shielded collimator arrangement. A more detailed description of the experimental setup can be found in Ref. [60, 117]. The anode signal of the photomultiplier tube was used for the pulse height and pulse shape analysis employed in the neutron-gamma discrimination circuitry. Each amplitude and pulse shape output was connected to a separate ADC. The "start" signal of the TAC modules used in the time of flight measurements originates from the dynode of the neutron detectors while the cathode pulses from the ionization chamber for both sources provided the "stop" signals. The data were collected in list mode using the data acquisition software GENDARC [118]. Several independent runs were made.

The raw data were sorted off-line into various combinations to optimize the data reduction process. Adjustments were made for time width of the bins, etc. After discriminating between neutron and γ-ray events, and correcting for the time shift as a function of pulse height, the data acquired for each detector were organized as a three column array of values: energy E, counts $N(E)$, and uncertainty $\Delta N/N$. The γ-ray suppression factor was about 200. The threshold for usable data from the detectors was determined to be approximately 0.6 MeV neutron emission energy. In the first stage of data analysis, separate data runs were examined to check for instabilities of the electronic units and the detectors. No significant instabilities were observed. In the final stage of data analysis, all list mode data were analyzed as one single file. Time independent and time correlated background [117] were also subtracted.

The experimental spectra $N_{\rm x}(E)$ are related to the investigated ones $S_{\rm x}(E)$ by the following general equation

$$N_{\rm x}(E) = Y_{\rm x}\, S_{\rm x}(E)\, \frac{\overline{\nu}_{\rm x}}{4\pi}\, \Omega\, \epsilon(E)\, \alpha_{\rm x}(E), \tag{1}$$

where x=U5,Cf; $Y_{\rm x}$ is the FF yield during the run, $\overline{\nu}_{\rm x}$ – the neutron multiplicity, Ω – detector solid angle, $\epsilon(E)$ – detector efficiency, and $\alpha_{\rm x}(E)$ – correction for neutron scattering in the chamber materials.

The experimental spectra taken with the ^{252}Cf(sf) source could be used for detector efficiency estimation. A comparison of the experimental results with the calculated efficiency provided an additional verification of the experimental method. In reality, the ^{235}U($n_{\rm th}$,f) spectrum $S_{\rm U5}(E)$ may be estimated directly from the measured ratio $S_{\rm U5}(E)/S_{\rm Cf}(E)$ [61]. So knowledge of the detector efficiency is not a crucial factor. More important is the correction due to neutron multiple scattering. The fission fragment yields $Y_{\rm x}$ were measured during the same experimental runs, therefore the present data are normalized to the neutron multiplicity. Since both values $\overline{\nu}_{\rm U5}$ and $\overline{\nu}_{\rm Cf}$ are known with high accuracy from many other investigations, a comparison with the present experimental results offers some measure of experimental consistency. However, the "experimental" $\overline{\nu}$ obtained in this work corresponds only to the measured emitted neutron energy range above 0.6 MeV and does not cover the energies below 0.6 MeV where the fission yield may be still significant.

TABLE 10. Partial uncertainties for spectrum measurement at different emitted neutron energies.

E (MeV)	δ_1, %	δ_2, %	δ_3, %	δ_4, %	δ_5, %
1	0.5	1.6	< 0.1	0.1	< 0.1
5	1.6	1.4	1.3	0.9	0.5
10	15	2.7	3.9	3.8	1.2

Correction factors for neutron multiple scattering and attenuation were calculated as a ratio of a neutron spectrum emitted from the source surrounded by the real chamber to a spectrum calculated without chamber materials. The MCNP code [119] was used for this purpose. The neutron spectra were calculated separately for the ^{235}U and ^{252}Cf sources, and for each individual detector. The experimental data for each detector were then multiplied by these correction factors so as to cancel the contributions from the scattered neutrons on the fission chamber materials. All three neutron spectra after incorporation of these corrections were found to be in good agreement, as shown in Fig. 2.

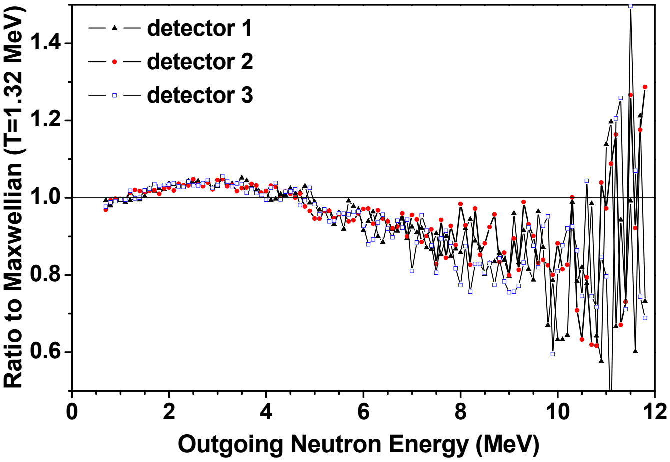

FIG. 2. (Color online) PFNS measured by 3 neutron detectors after correction for multiple scattering.

The partial uncertainties for the measured spectra are given in Table 10: δ_1 is the statistical uncertainty for one detector, δ_2 is the uncertainty of the ^{252}Cf(sf) PFN standard, δ_3–δ_5 are systematic uncertainties due to the shift of the zero time (±2 channels), flight path ($\Delta L = 0.5$ cm), and the channel width (0.1%), respectively. It may be assumed that $\delta_4 = \Delta L$ is not important for this "ratio to ^{252}Cf" experiment.

I. PNPI Experiments for Thermal Neutron-Induced Fission of ^{233,235}U and ^{239}Pu

The energy and angular distributions of prompt fission neutrons associated with light (L) and heavy (H) groups of fission fragments (FF) from ^{252}Cf(sf) and from fission of ^{233,235}U and ^{239}Pu induced by 0.0363 eV neutrons were measured at the WWR-M research reactor in PNPI (Gatchina, Russia). ^{233,235}U fissile targets were deposited on a self-supported backing which is transparent to FFs. Therefore, ^{233,235}U$(n$,f) PFNS were measured simultaneously with the time-of-flight of both FFs allowing to obtain the average number of neutrons $\overline{\nu}_i$ per fission event as a function of the FF (pre-neutron) mass A_i and the FF total kinetic energy (TKE), and the average energy per nucleon $\overline{E_i}$ for the light ($i = L$) and heavy ($i = H$) fragments for each fission event. The ^{239}Pu fissile target and the ^{252}Cf(sf) source were deposited on a backing opaque to FFs, therefore only the angular distribution of one FF was measured simultaneously with fission neutrons in these cases. The fission neutrons were detected using two stilbene crystal detectors while the fragments were detected by multiwire proportional detectors. The emitted neutron detection threshold was 150–200 keV. A pulse shape analysis procedure was applied to distinguish neutron from γ-events in the detectors. The neutron energy and fission fragment characteristics were both obtained by the time-of-flight (TOF) method. The timing resolution of the neutron detectors (FWHM of the "fragment-γ" coincidence curve) was 1.0–1.2 ns. The PFNS was measured simultaneously for 11 angles between the neutron and the fission fragment directions of motion: 0°, 18°, 36°, 54°, 72°, 90°, 108°, 126°, 144°, 162° and 180°. In the geometry of the experimental setup, these angles were 8.9°, 19.8°, 36.9°, 54.5°, 72.2°, 90°, 107.8°, 125.5°, 143.1°, 160.2° and 171.2°, respectively. The spectra were measured over a wide prompt fission neutron energy interval, reducing the need for model assumptions when extrapolating the measurements to the full spectral range.

The experimental setup guarantees identical conditions of the magnitude and composition of the background as well as neutron rescattering off the detectors for the measured PFNS at the given angles relative to the fission fragment's direction. A detailed description of the experimental setup and some preliminary results have been presented in Ref. [120]. A subsequent analysis of these data [121], concluded that additional corrections and improved data processing were required to improve the quality of the results. The following effects need to be considered: a correction for the neutron detector efficiency, a normalization correction arising from the fact that experimental angular histograms were used in the measurements instead of continuous distributions, a neutron energy resolution correction, and a correction for neutron detector background due to accidental coincidences between fission fragments and neutrons attributed to different fission events. In order to determine the neutron spectra from measured time-of-flight data, relativistic kinematics were employed and the angular resolution correction was applied in a more consistent manner than was the case in the earlier stages of the experiment [120].

TABLE 11. The measured PFNS ratios of ^{233}U(n,f) and ^{239}Pu(n,f) to the ^{252}Cf(sf) reference spectrum. Here E is the emitted neutron energy in the lab frame. All uncertainties are relative uncertainties, given in %. R and ΔR are the PFNS ratio of the given isotope to the ^{252}Cf(sf) spectrum and the corresponding uncertainty, respectively. For isotope x, $\delta^2_{\mathrm{SM}} = \delta^2_{\mathrm{Cf}} + \delta^2_{\mathrm{x}}$ is the total uncertainty including statistical and "time zero" mark uncertainties as well as uncertainties due to the stability of the detector electronics. The uncertainties of the normalization and resolution corrections, determined independently for each measurement cycle, are also included. δ_{bkg}, δ_{BW}, δ_E are the uncertainties related to the background determination, bin-width correction, and neutron-energy grid. $\Phi(E)$ and $\Delta\Phi$ are the absolute PFNS of the given isotope and the corresponding uncertainty derived from the ratio considering the uncertainty of the ^{252}Cf(sf) reference spectrum [3, 36].

^{233}U(n,f)									^{239}Pu(n,f)									
E (MeV)	R	ΔR (%)	δ_{SM} (%)	δ_{bkg} (%)	δ_{BW} (%)	δ_E (%)	$\Phi \times 10^4$ (neut/MeV)	$\Delta\Phi$ (%)	E (MeV)	R	ΔR (%)	δ_{SM} (%)	δ_{bkg} (%)	δ_{BW} (%)	δ_E (%)	$\Phi \times 10^4$ (neut/MeV)	$\Delta\Phi$ (%)
16.65	0.3793	33.1	21.1	23.1	2.7	37.6	.25833	36.6	–	–	–	–	–	–	–	–	–
13.29	0.4655	22.6	12.6	15.6	2.3	28.4	3.0781	23.0	–	–	–	–	–	–	–	–	–
10.86	0.4339	16.0	9.0	5.9	1.9	22.1	14.846	16.3	–	–	–	–	–	–	–	–	–
9.043	0.4691	12.6	7.2	2.7	1.5	17.7	54.140	12.8	10.86	0.558	22.4	18.1	5.9	1.8	22.1	19.130	22.6
7.647	0.5313	9.7	5.1	1.5	1.3	14.3	155.58	9.9	9.043	0.712	15.9	12.1	2.7	1.5	17.7	82.200	16.1
6.552	0.5614	7.9	3.9	1.0	1.0	11.8	339.32	8.1	7.647	0.671	11.8	8.4	1.5	1.2	14.3	196.50	12.0
5.677	0.5988	6.7	3.6	0.7	0.8	9.8	638.37	6.9	6.552	0.710	9.3	6.3	1.0	1.0	11.8	428.90	9.5
4.967	0.6074	5.4	2.6	0.4	0.7	8.2	1014.9	5.6	5.677	0.734	7.6	5.0	0.7	0.8	9.8	783.00	7.7
4.383	0.6433	4.6	2.3	0.3	0.6	6.9	1547.5	4.8	4.967	0.769	6.2	4.0	0.4	0.7	8.2	1284.6	6.4
3.896	0.6501	3.9	2.0	0.2	0.5	5.8	2099.4	4.1	4.383	0.767	5.2	3.3	0.3	0.6	6.9	1845.1	5.3
3.486	0.6495	3.3	1.7	0.2	0.4	4.9	2666.2	3.5	3.896	0.755	4.4	2.8	0.2	0.5	5.8	2438.6	4.5
3.137	0.6550	3.0	1.8	0.1	0.4	4.2	3277.0	3.3	3.486	0.785	3.9	2.6	0.2	0.4	4.9	3221.0	4.0
2.839	0.6585	2.7	1.8	0.1	0.3	3.5	3871.4	2.9	3.137	0.785	3.4	2.4	0.1	0.4	4.2	3925.1	3.6
2.581	0.6745	2.4	1.7	0.1	0.3	3.0	4525.8	2.7	2.839	0.768	3.1	2.3	0.1	0.3	3.5	4513.2	3.3
2.357	0.6903	2.2	1.7	0.1	0.2	2.5	5174.1	2.5	2.581	0.785	2.7	2.1	0.1	0.3	3.0	5268.4	3.0
2.161	0.6735	1.9	1.4	0.1	0.2	2.1	5537.1	2.2	2.357	0.812	2.6	2.1	0.1	0.2	2.5	6086.5	2.8
1.988	0.6938	1.9	1.6	0.1	0.2	1.7	6167.8	2.2	2.161	0.785	2.4	2.1	0.1	0.2	2.1	6457.0	2.7
1.835	0.6882	1.7	1.5	0.1	0.2	1.4	6529.2	2.1	1.988	0.798	2.3	2.1	0.1	0.2	1.7	7091.3	2.6
1.699	0.6960	1.6	1.4	0.1	0.2	1.1	6987.9	2.0	1.835	0.760	2.2	2.0	0.1	0.2	1.4	7210.8	2.5
1.578	0.6864	1.8	1.7	0.1	0.1	0.9	7203.9	2.2	1.699	0.759	2.2	2.1	0.1	0.1	1.1	7622.9	2.6
1.469	0.6635	1.7	1.7	0.1	0.1	0.7	7233.0	2.1	1.578	0.775	2.2	2.1	0.1	0.1	0.9	8133.6	2.5
1.372	0.6929	2.0	2.0	0.1	0.1	0.5	7801.3	2.3	1.469	0.788	2.1	2.1	0.1	0.1	0.7	8587.3	2.5
1.283	0.6861	1.4	1.3	0.1	0.1	0.3	7930.2	1.8	1.372	0.783	2.1	2.1	0.1	0.1	0.5	8815.5	2.4
1.203	0.6771	1.7	1.7	0.1	0.1	0.2	8009.8	2.1	1.283	0.785	2.2	2.2	0.1	0.1	0.3	9069.4	2.5
1.130	0.6943	1.5	1.5	0.1	0.1	0.1	8349.3	1.9	1.203	0.775	2.3	2.3	0.1	0.1	0.2	9164.6	2.6
1.064	0.6847	1.9	1.9	0.1	0.1	0.1	8346.4	2.3	1.130	0.774	2.3	2.3	0.1	0.1	0.1	9305.6	2.6
1.003	0.6778	2.1	2.1	0.1	0.1	0.1	8365.0	2.6	1.064	0.768	2.4	2.4	0.1	0.1	0.1	9359.4	2.7
0.948	0.6848	1.7	1.7	0.1	0.1	0.1	8523.4	2.4	1.003	0.742	2.5	2.5	0.1	0.1	0.1	9151.5	3.0
0.896	0.6761	2.4	2.4	0.1	0.1	0.1	8470.3	3.0	0.948	0.788	2.5	2.5	0.1	0.1	0.1	9809.4	3.0
0.849	0.6873	2.0	2.0	0.1	0.1	0.1	8659.7	2.7	0.896	0.778	2.6	2.6	0.1	0.1	0.1	9741.8	3.2
0.806	0.6888	2.4	2.3	0.1	0.1	0.1	8700.3	3.0	0.849	0.771	2.6	2.6	0.1	0.1	0.1	9711.6	3.2
0.766	0.6748	2.4	2.4	0.1	0.1	0.2	8522.9	3.0	0.806	0.777	2.7	2.7	0.1	0.1	0.1	9814.4	3.2
0.728	0.7021	2.1	2.1	0.1	0.1	0.3	8868.0	2.8	0.766	0.786	2.9	2.9	0.1	0.1	0.2	9926.7	3.4
0.694	0.6946	2.5	2.5	0.1	0.0	0.4	8772.8	3.1	0.728	0.770	3.1	3.1	0.1	0.1	0.3	9719.0	3.6
0.661	0.6922	2.6	2.6	0.1	0.0	0.6	8725.0	3.1	0.694	0.790	3.1	3.1	0.1	0.0	0.4	9978.5	3.6
0.631	0.6733	2.4	2.3	0.1	0.0	0.8	8455.9	2.9	0.661	0.761	3.2	3.2	0.1	0.0	0.6	9588.5	3.6
0.603	0.6939	2.7	2.7	0.1	0.0	1.0	8683.1	3.2	0.631	0.724	3.3	3.3	0.1	0.0	0.8	9091.9	3.7
0.577	0.6943	2.9	2.8	0.2	0.0	1.2	8659.9	3.4	0.603	0.743	3.5	3.5	0.1	0.0	1.0	9302.7	3.9
0.553	0.6986	3.0	2.9	0.2	0.0	1.5	8660.3	3.5	0.577	0.747	3.7	3.6	0.2	0.0	1.2	9317.7	4.1
0.530	0.7045	3.3	3.1	0.2	0.0	1.7	8686.6	3.7	0.553	0.734	4.0	3.9	0.2	0.0	1.5	9103.1	4.4
0.488	0.7064	2.2	1.8	0.2	0.1	2.3	8573.7	2.8	0.530	0.749	3.9	3.8	0.2	0.0	1.7	9234.5	4.3
0.434	0.6953	2.7	1.9	0.2	0.1	3.3	8269.2	3.2	0.488	0.782	3.1	2.8	0.2	0.1	2.3	9496.9	3.5
0.388	0.6677	3.5	2.5	0.2	0.1	4.4	7720.0	3.9	0.434	0.757	3.3	2.7	0.2	0.1	3.3	8998.7	3.7
0.349	0.7084	4.4	3.0	0.3	0.0	5.5	7983.4	4.7	0.388	0.731	4.8	4.1	0.2	0.1	4.4	8452.6	5.1
0.316	0.7179	4.7	2.6	0.3	0.0	6.7	7882.1	5.0	0.349	0.797	5.8	4.9	0.3	0.0	5.5	8981.4	6.1
0.287	0.6859	5.7	3.4	0.3	0.0	7.9	7322.5	6.0	0.316	0.741	6.4	5.1	0.3	0.0	6.7	8133.7	6.6
0.263	0.7040	6.7	4.2	0.3	0.0	9.0	7290.6	6.9	0.287	0.711	9.5	8.3	0.3	0.0	7.9	7589.3	9.6
0.241	0.6558	7.5	4.7	0.7	0.0	10.1	6594.0	7.8	0.263	0.708	10.9	9.6	0.3	0.0	9.0	7328.3	11.1
0.221	0.7289	9.4	6.5	2.9	0.0	11.3	7118.3	9.6	0.241	0.767	12.6	11.2	0.7	0.0	10.1	7707.4	12.8

TABLE 12. The PFN angle-integrated multiplicities $\overline{\nu}$ and average energies $\overline{E}$ with uncertainties in parentheses. The prompt neutron multiplicities, $\overline{\nu}$, are compared to the evaluated thermal standard values, $\overline{\nu}^{\rm STD}$ [46, 47], by subtracting the delayed neutron multiplicity $\nu_{\rm del}^{\rm STD}$ estimated by Divadeenam and Stehn [122] from the evaluated total multiplicity $\overline{\nu}_{\rm tot}^{\rm STD}$ [46, 47].

	^{233}U($n_{\rm th}$,f)	^{235}U($n_{\rm th}$,f)	^{239}Pu($n_{\rm th}$,f)	^{252}Cf(sf)
$\overline{E}$ (MeV), angle-integrated, this work	2.03 (0.03)	2.01 (0.03)	2.08 (0.03)	2.13 (0.03)
$\overline{\nu}$, angle-integrated, this work	2.5400 (0.0600)	2.4400 (0.0500)	2.8900 (0.0500)	3.7700 (0.0300)
$\overline{\nu}^{\rm STD}$ [46, 47]	2.4904 (0.0040)	2.4184 (0.0021)	2.8778 (0.0050)	3.7610 (0.0051)
$\overline{\nu}_{\rm del}^{\rm STD}$ [122]	0.0066 (0.0003)	0.0166 (0.0005)	0.0062 (0.0003)	0.0080 (0.0010)
$\overline{\nu}_{\rm tot}^{\rm STD}$ [46, 47]	2.4970 (0.0040)	2.4350 (0.0020)	2.8840 (0.0050)	3.7690 (0.0050)

1. *Absolute PFNS Ratio Measurements*

Additional measurements and analyses of the acquired data, following procedures described in Ref. [59], were undertaken to derive the absolute PFNS ratios of thermal neutron-induced fission of ^{233,235}U and ^{239}Pu to spontaneous fission of ^{252}Cf. Measuring ratios made it possible to eliminate uncertainties related to neutron detection efficiency. The required corrections to the measured ratios, which are nearly independent of the detailed experimental setup, were found to not exceed 3% for $0.2 < E < 10$ MeV. The corrected ratios of ^{233}U($n_{\rm th}$,f) and ^{239}Pu($n_{\rm th}$,f) PFNS to the ^{252}Cf(sf) PFNS are listed in Table 11. The corrected ratio of ^{235}U($n_{\rm th}$,f) PFNS to the ^{252}Cf(sf) PFNS was given in Ref. [59].

The PFNS calculated from these ratios using the Mannhart evaluation of the ^{252}Cf(sf) PFNS [36, 37] are shown in Fig. 3 by red symbols. The angle-integrated measured neutron multiplicities $\overline{\nu}$ and average energies $\overline{E}$ are shown in Table 12. There is good agreement within uncertainties between the measured $\overline{\nu}$ and those evaluated in the Standards Project, $\overline{\nu}^{\rm STD}$ [46, 47].

2. *PFNS Derived from Measured Data at Small Angles Relative to the Fragments' Direction of Motion*

Considerable information on the PFNS in the center-of-mass system (cm) may be obtained from the more accessible fission neutron spectrum in the laboratory frame (lab) as proposed by Terrell [123]. As Terrell pointed out, even if some fraction of the neutrons in low-energy fission are emitted from the fissioning nuclide (i.e., *scission* neutrons), the results obtained should be approximately correct if this fraction is small.

The cm PFNS can be obtained by using neutron data measured at small angles (less than 45°) relative to the one fragment direction of motion in the lab (8.9°, 19.8°, 36.9° for the light fragment L, and 143.1°, 160.2° and 171.2° for the corresponding heavy fragment H), assuming binary fission (and averaging over all fragments, so only one "average" fragment pair is considered). This approximation was shown by Madland [124] to be very good, as it has a minor influence on the calculated total energy spectrum. For neutrons emitted by fragment i, ($i = L, H$), the neutron cm energy ε, the neutron energy in the lab E, the fragment energy per nucleon E_i, and the neutron emission angles in the cm θ and lab $\theta_{\rm lab}$ are related by [120]

$$\begin{aligned} &\varepsilon = E + E_i - 2\sqrt{E\,E_i}\,\cos\theta_{\rm lab} \\ &E_i = \mathrm{TKE}\,[1/A_i - 1/A] \\ &\sqrt{\varepsilon}\cos\theta = \sqrt{E}\cos\theta_{\rm lab} - \sqrt{E_i}\,, \end{aligned} \tag{2}$$

where A is the mass of the fissioning nucleus, A_i is the fragment mass and TKE is the total kinetic energy[4].

The distribution of neutrons with energy E in angle $\theta_{\rm lab}$, $d^2n(E,\theta_{\rm lab})/dEd\theta_{\rm lab}$ can be written as a sum of the distributions for emission from light, $d^2n_L(E,\theta_{\rm lab})/dEd\theta_{\rm lab}$, and heavy, $d^2n_H(E,180° - \theta_{\rm lab})/dEd\theta_{\rm lab}$ fragments. Furthermore, the number of neutrons per energy and angle in the lab frame is related to the number of cm neutrons per corresponding energy and angle, $d^2n_i/d\varepsilon d\theta$ by [120]

$$\begin{aligned} &\frac{d^2n_i}{dEd\theta_{\rm lab}} = \sqrt{\frac{E}{\varepsilon}}\,\frac{d^2n_i}{d\varepsilon d\theta} = \sqrt{\frac{E}{\varepsilon}}\,\varphi(\varepsilon,\theta)\,\frac{dn_i}{d\varepsilon}\,, \\ &\varphi(\varepsilon,\theta) = \frac{1}{4\pi}\left[1 + A_2\,\varepsilon\,\frac{3\cos^2\theta - 1}{2}\right]\,, \end{aligned} \tag{3}$$

---

[4] The same equation holds for the average quantities, e.g., E_i is replaced by the average fragment energy per nucleon $\overline{E_i}$, and TKE – by the average total kinetic energy $\overline{\mathrm{TKE}}$.

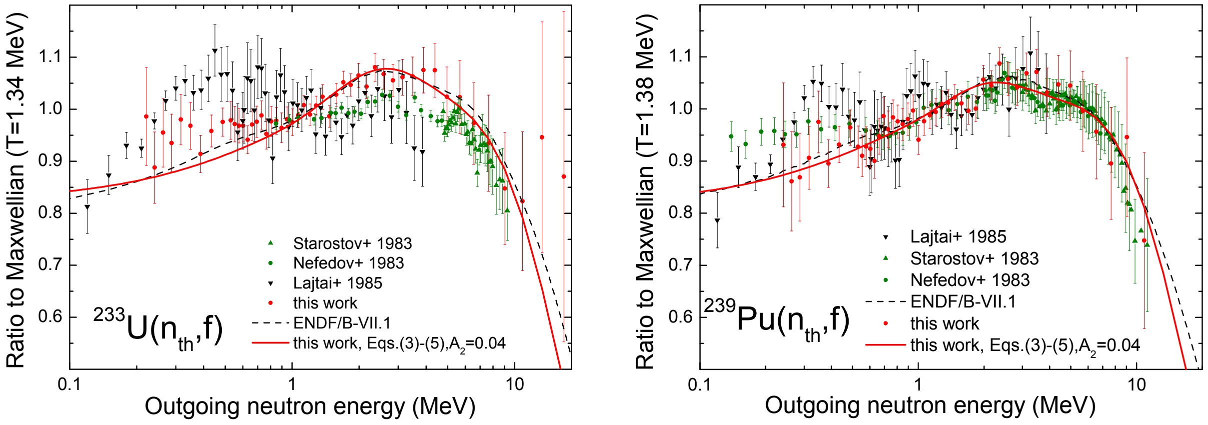

(a) Measured PFNS of ^{233}U($n_{\rm th}$,f) vs. ENDF/B-VII evaluation. All data are normalized to $\overline{\nu} = 2.49$.

(b) Measured PFNS of ^{239}Pu($n_{\rm th}$,f) vs. ENDF/B-VII evaluation. All data are normalized to $\overline{\nu} = 2.89$.

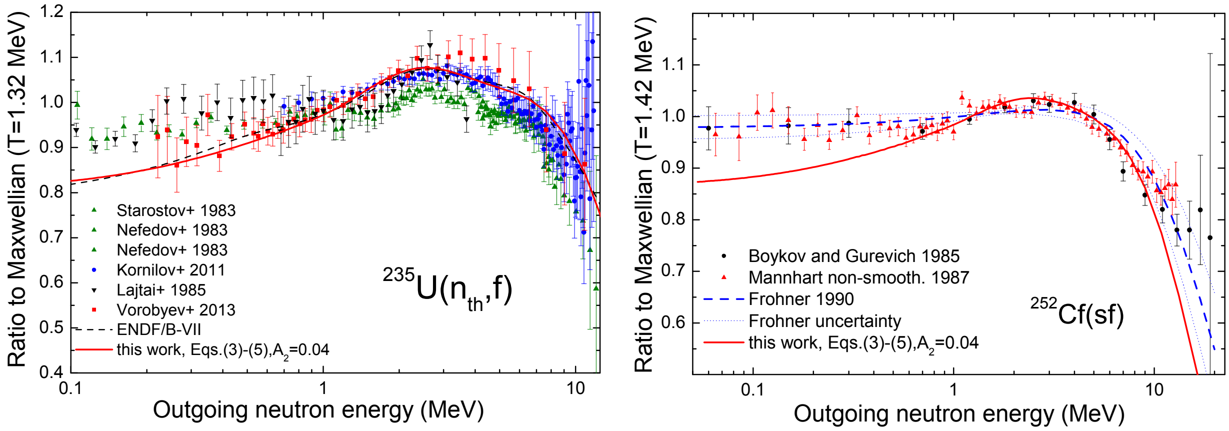

(c) Measured PFNS of ^{235}U($n_{\rm th}$,f) vs. ENDF/B-VII evaluation. All data are normalized to $\overline{\nu} = 2.42$.

(d) Evaluated PFNS of ^{252}Cf(sf) [36, 125, 126]. All data are normalized to $\overline{\nu} = 3.759$.

FIG. 3. (Color online) The solid curve is the PFNS calculated from prompt neutron spectra measured at small angles relative to the fission fragment direction of motion, assuming that all neutrons are emitted by accelerated fragments.

where the function $\varphi(\varepsilon,\theta)$ is the normalised angular distribution of neutrons in the cm, $dn_i/d\varepsilon$ is the angle-integrated PFNS in the cm, and $A_2 = 2b/(3+b)$ is the neutron angular anisotropy in the cm frame, being b given as a function of the ratio at $\varepsilon = 1$ MeV of forward ($\theta = 1°$) to perpendicular ($\theta = 90°$) PFNS angular distribution in the cm as,

$$b = \frac{d^2 n_i}{d\varepsilon d\theta}(1, 0°)/\frac{d^2 n_i}{d\varepsilon d\theta}(1, 90°) - 1 \geq 0. \tag{4}$$

The only inputs needed for cm PFNS calculations with Eqs. (2) and (3) are the average energies per nucleon for the light $\overline{E}_L$ and the heavy $\overline{E}_H$ fragments, and the average total kinetic energy of the fragments $\overline{\rm TKE}$ given in Table 13. The $\overline{E}_i$ values were obtained as suggested by Terrell (see Eq. (A8) in Ref. [123]). Those values are in excellent agreement with the directly measured $\overline{E}_i$ values for neutron-induced fission of ^{233}U and ^{235}U targets (derived from measured pre-neutron FF mass A_i and TKE distributions at the same time of neutron detection). Such agreement validates

TABLE 13. Input average fragment energies per nucleon used to calculate the PFNS estimated by the equations proposed by Terrell [123] are compared with results obtained from FF distributions measured simultaneously with PFN for ^{233}U($n_{\rm th}$,f) and ^{235}U($n_{\rm th}$,f) reactions. The last line is the result weighted over fitted FF multiplicities $\overline{\nu}_{L,H}$ listed in Table 14.

$\overline{\rm TKE}$ and $\overline{E}_i$ (MeV)	^{233}U($n_{\rm th}$,f)	^{235}U($n_{\rm th}$,f)	^{239}Pu($n_{\rm th}$,f)	^{252}Cf(sf)
$\overline{\rm TKE}$	170.5(0.5)	171.0(0.6)	177.5(0.7)	185.3(0.9)
$\overline{E}_L$, using eq.(A8) [123]	1.033 (0.007)	1.012 (0.007)	0.995 (0.007)	0.949 (0.007)
$\overline{E}_L$, this experiment	1.035 (0.005)	1.015 (0.003)	–	–
$\overline{E}_H$, using eq.(A8) [123]	0.471 (0.004)	0.474 (0.004)	0.511 (0.004)	0.540 (0.004)
$\overline{E}_H$, this experiment	0.470 (0.002)	0.472 (0.002)	–	–
$\overline{E}_f$, following Ref.[123]	0.79	0.77	0.77	0.76

both the data processing used in this experiment, and the method to calculate $\overline{E}_i$ suggested by Terrell [123]. Terrell's method was used to derive the $\overline{E}_{L,H}$ for all nuclei of interest which are listed in Table 13.

TABLE 14. Characteristics of prompt fission neutron spectra and estimated uncertainties (in parentheses) based on Eq. (5) and assuming the anisotropy parameter $A_2 = 0.04$ [120, 127]. The prompt neutron multiplicity $\overline{\nu}$ obtained is compared to the angle-integrated value and the Standards value.

Fit values from Eq. (5)	^{233}U($n_{\rm th}$,f)	^{235}U($n_{\rm th}$,f)	^{239}Pu($n_{\rm th}$,f)	^{252}Cf(sf)
$\overline{\nu}_L$	1.47 (0.02)	1.43 (0.03)	1.62 (0.02)	2.04 (0.02)
ω_L	0.173 (0.014)	0.170 (0.015)	0.153 (0.018)	0.108 (0.017)
T_{1L}	0.316 (0.008)	0.289 (0.010)	0.266 (0.019)	0.293 (0.015)
T_{2L}	0.896 (0.018)	0.890 (0.016)	0.945 (0.028)	0.980 (0.026)
$\overline{\nu}_H$	1.02 (0.02)	1.02 (0.02)	1.23 (0.2)	1.69 (0.03)
ω_H	0.024 (0.015)	0.029 (0.016)	0.024 (0.009)	0.019 (0.008)
T_{1H}	0.294 (0.024)	0.286 (0.027)	0.222 (0.026)	0.146 (0.029)
T_{2H}	0.861 (0.021)	0.868 (0.022)	0.918 (0.017)	0.916 (0.024)
$\overline{\nu} = \overline{\nu}_L + \overline{\nu}_H$, from the fit	2.49 (0.03)	2.45 (0.03)	2.85 (0.03)	3.73 (0.04)
$\overline{\nu}$, angle-integrated (Table 12)	2.54 (0.06)	2.44 (0.05)	2.89 (0.05)	3.77 (0.03)
$\overline{\nu}^{\rm STD}$ [46, 47]	2.4904 (0.0040)	2.4184 (0.0021)	2.8778 (0.0050)	3.7610 (0.0051)
$\overline{\varepsilon}_L$ (MeV)	1.23 (0.02)	1.20 (0.02)	1.28 (0.02)	1.38 (0.02)
$\overline{\varepsilon}_H$ (MeV)	1.28 (0.03)	1.28 (0.03)	1.35 (0.03)	1.36 (0.03)
$\overline{\varepsilon}$ (MeV)	1.25 (0.03)	1.23 (0.03)	1.31 (0.03)	1.37 (0.03)
$\overline{E} = \overline{\varepsilon} + \overline{E}_f$ (MeV), $\overline{E}_f$ from Table 13	2.04	2.00	2.08	2.13
$\overline{E}$ (MeV), angle-integrated (Table 12)	2.03 (0.03)	2.01 (0.03)	2.08 (0.03)	2.13 (0.03)

The obtained cm PFNS were used to calculate the corresponding neutron energy and angular distributions in the lab frame [120]. Additionally, the agreement with experimental data may be improved by introducing the anisotropy of the fission neutron angular distribution in the cm of the fission fragments. The best value of the anisotropy parameter is $A_2 = 0.04 \pm 0.02$ ($b = 0.061$) [120, 127]. It is noteworthy that the calculation performed by Bunakov et al. [128], as well as a recent study by Randrup and Vogt [129], explained the anisotropy of the neutron emission in the CMS due to the rotation of the fissioning nucleus.

The calculations described above have several advantages: they are very simple to perform and are free from any model parameters (numbers of neutrons emitted by the light and heavy fragments, the neutron spectrum shape, etc.). It is possible to deduce the PFNS in the cm frame that extend to the lowest cm neutron energies ε. It is therefore possible to determine the average neutron multiplicity $\overline{\nu}$ as well as the PFNS average energy $\overline{E}$ without any approximations or interpolation. The analysis and data processing were performed exactly the same way for all nuclei studied. Analyses of the experimental data revealed that the angle-integrated PFNS in the cm frame of each fission fragment, $dn_i/d\varepsilon$ ($i = L, H$), can be fit by

$$\begin{aligned} \frac{dn_i}{d\varepsilon} &= \overline{\nu}_i\,\omega_i\,\frac{\varepsilon}{T_{1i}^2}\,\exp\left[-\frac{\varepsilon}{T_{1i}}\right] \\ &+ \overline{\nu}_i\,(1-\omega_i)\,\frac{2}{\sqrt{\pi}T_{2i}}\sqrt{\frac{\varepsilon}{T_{2i}}}\,\exp\left[-\frac{\varepsilon}{T_{2i}}\right]. \end{aligned} \tag{5}$$

The fitted values of parameters $\overline{\nu}_i$, ω_i, T_{1i}, and T_{2i} for all nuclei are presented in Table 14. The angle-integrated measured neutron multiplicities $\overline{\nu}$ in Table 12 are in good agreement within uncertainties with those obtained from the fit with Eq.(5) as well as with the evaluated values in the Standards Project $\overline{\nu}^{\rm STD}$ [46, 47].

The PFNS average energies $\overline{E}$ obtained from the sum of $\overline{\varepsilon}$ and $\overline{E}_f$ [123] are also shown in Table 14. They are in excellent agreement, within uncertainties, with angle-integrated values $\overline{E}$, first row of Table 12. Comparison of $\overline{\nu}$ and $\overline{E}$ calculated using different methods with values from the literature and evaluated data demonstrates good agreement between them. Therefore, it can be concluded that, on average, the proposed two-fragment model reproduces the observed data.

The lab PFNS are calculated as an integral over $\theta_{\rm lab}$ of the $d^2n_i/dEd\theta_{\rm lab}$ given by Eq. (3), where the angle-integrated PFNS $dn_i/d\varepsilon$ in the cm frame are calculated with Eq. (5) using the parameter values from Table 14. Calculated PFNS in the lab frame are given by the solid curves in Fig. 3 There is good agreement of calculated spectra with spectra obtained from measured PFNS ratios (see Sec. III I 1 and Ref. [59]) in the energy range $0.6 < E < 10$ MeV, which covers most of the neutron yield. Therefore, it is possible to conclude that the contribution from the *scission* neutrons to the total PFNS is rather small. Note that the results in this section depend on model assumptions.

The angular and energy distributions of prompt fission neutrons studied in the previous section assumed that the neutrons are emitted only by two fully accelerated fragments. However, a systematic difference between the calculated PFNS in the lab frame (as an integral over θ_{lab} of the $d^2n_i/dEd\theta_{\mathrm{lab}}$ given by Eq. (3)) and those measured by different groups is evident for $E < 0.6$ MeV, see Fig. 3. For example, in Fig. 4 the absolute difference between the Mannhart pointwise evaluation [36] and the calculated ^{252}Cf(sf) spectrum is shown. This difference might be interpreted as a manifestation of *scission* neutrons and, therefore, the average energy of the *scission* neutrons $\overline{E}_{\mathrm{sc}}$ would be ∼0.4-0.6 MeV with a yield ∼1–3% of the total prompt fission neutron yield (depending on the fissioning nucleus). This result agrees with conclusions of earlier investigations [130–134]. It is worth noting that this conclusion is based on the use of angle-integrated spectral data. However, larger differences reaching up to 10% have been observed at certain angles if we compare the measured double-differential neutron emission with calculated values of the $d^2n_i/dEd\theta_{\mathrm{lab}}$ given by Eq. (3). Similar larger variations at selected angles were also seen in measurements of the angular dependence of the neutron-neutron coincidence curves by Sokolov et al. [134]. Further investigation of the angular dependence of the *scission* neutron yield is warranted.

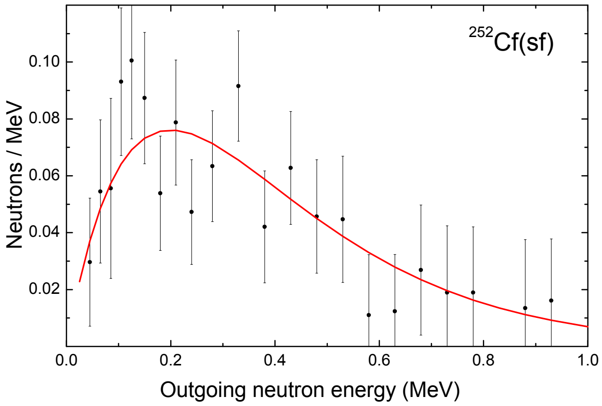

FIG. 4. (Color online) *Scission* neutron contribution to the ^{252}Cf(sf) PFNS. The difference spectrum (points) between the Mannhart evaluation [36, 37] and the PFNS calculated assuming neutron emission by two accelerated fragments with Eq. (5) using the parameter values from Table 14. The difference plotted in this figure can be easily seen also in Fig. 3(d). The full line represents a least square fit to a Weisskopf distribution with $T = 0.20$ MeV. The integrated *scission* neutron contribution is about 1% of the total neutron multiplicity.

J. BARC Experiments for Fast Neutron-Induced Fission of ^{238}U

A preliminary report of this work has been provided to the CRP 3^{rd} Research Coordination Meeting [51], and an article has been recently published [104]. Thus, only a brief description of this experiment is provided here.

TABLE 15. The BARC experimental PFNS $N(E)$ with total δN_{tot}, statistical δN_{stat}, and systematic δN_{syst} uncertainties (all in units of MeV^{-1}) for the ^{238}U(n,f) reaction at $E_n = 2.0$, 2.5 and 3.0 MeV.

		E$_n$ = 2.0 MeV				E$_n$ = 2.5 MeV				E$_n$ = 3.0 MeV			
E(MeV)	δE(MeV)	$N(E)$	δN_{tot}	δN_{stat}	δN_{syst}	$N(E)$	δN_{tot}	δN_{stat}	δN_{syst}	$N(E)$	δN_{tot}	δN_{stat}	δN_{syst}
0.75	0.053	1.0110	0.0569	0.0290	0.0490	1.017	0.094	0.0270	0.09030	1.1100	0.1218	0.0210	0.1200
1.25	0.089	0.8960	0.0340	0.0300	0.0160	0.918	0.047	0.0250	0.03940	0.8690	0.0470	0.0230	0.0410
1.75	0.125	0.7410	0.0269	0.0250	0.0100	0.711	0.034	0.0240	0.02480	0.7700	0.0320	0.0200	0.0250
2.25	0.160	0.4940	0.0280	0.0270	0.0074	0.476	0.027	0.0190	0.01850	0.6230	0.0269	0.0200	0.0180
2.75	0.196	0.4480	0.0257	0.0250	0.0058	0.438	0.023	0.0180	0.01460	0.4540	0.0220	0.0170	0.0140
3.25	0.232	0.2810	0.0235	0.0230	0.0049	0.273	0.020	0.0140	0.01460	0.3270	0.0208	0.0170	0.0120
3.75	0.267	0.2120	0.0283	0.0280	0.0041	0.232	0.017	0.0140	0.01050	0.2270	0.0172	0.0140	0.0100
4.25	0.303	0.1700	0.0253	0.0250	0.0036	0.174	0.015	0.0120	0.00912	0.1470	0.0175	0.0150	0.0090
4.75	0.339	0.1030	0.0242	0.0240	0.0031	0.116	0.014	0.0120	0.00807	0.1110	0.0143	0.0120	0.0078
5.5	0.392	0.0570	0.0182	0.0180	0.0026	0.070	0.012	0.0100	0.00753	0.0810	0.0119	0.0100	0.0065
6.5	0.464	0.0260	0.0110	0.0110	0.0023	0.027	0.012	0.0096	0.00659	0.0390	0.0126	0.0120	0.0039
7.5	0.535	0.0120	0.0068	0.0064	0.0022	–	–	–	–	0.0270	0.0083	0.0079	0.0025
8.5	0.606	0.0084	0.0075	0.0072	0.0019	–	–	–	–	0.0082	0.0052	0.0051	0.0011

The experiment was performed at the 6MV Folded Tandem Ion Accelerator (FOTIA) facility [135], Bhabha Atomic Research Centre (BARC), Mumbai. The primary monoenergetic neutrons were obtained via the ^{7}Li$(p,n)^7$Be reaction

TABLE 16. Parameters obtained from the fit by Maxwellian and Watt parametrizations to BARC PFNS data for n+^{238}U PFNS. The extracted values of neutron multiplicity $\overline{\nu}$ and average neutron energy $\overline{E}$ are also given.

	Watt Fit				Maxwellian Fit			$\overline{E}$ (MeV)
E $_n$(MeV)	a(MeV^{-1})	b(MeV^{-1})	$\overline{\nu}$	$\overline{E}$ (MeV)	T(MeV)	$\overline{\nu}$	$\overline{E}$ (MeV)	($0.75 \leq E \leq 7.5$)
2.0	0.819± 0.005	1.200± 0.002	2.590± 0.020	2.280± 0.017	1.24± 0.01	2.590± 0.025	1.860± 0.015	2.240± 0.034
2.5	0.784± 0.003	0.994± 0.002	2.620± 0.020	2.300± 0.018	1.27± 0.01	2.620± 0.025	1.900± 0.015	2.260± 0.028
3.0	0.751± 0.005	0.892± 0.002	2.720± 0.025	2.310± 0.020	1.29± 0.01	2.620± 0.025	1.920± 0.015	2.270± 0.041

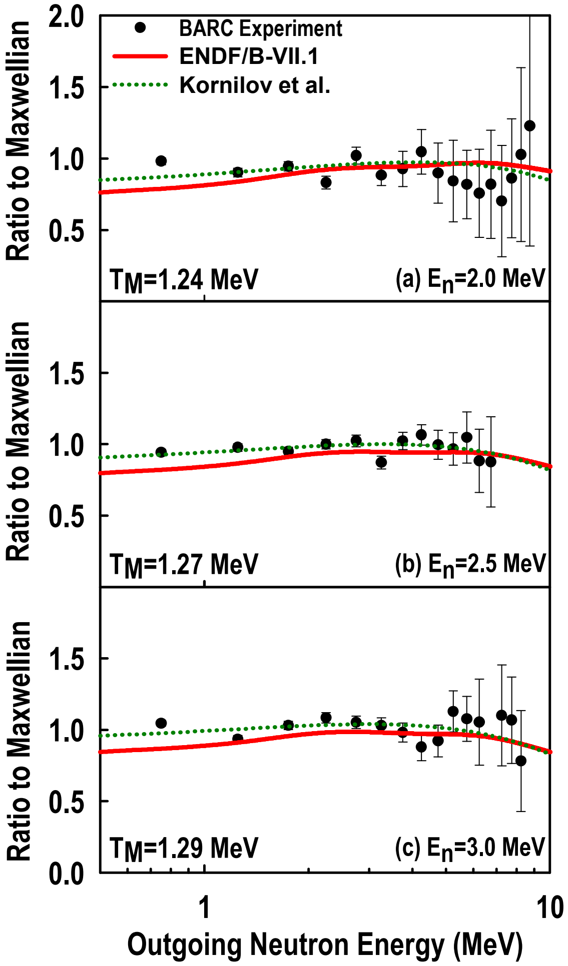

FIG. 5. (Color online) The BARC experiment (solid circles), ENDF/B-VII.1 evaluation (solid line), and Kornilov parametrization (dotted line) for n+^{238}U PFNS plotted as a ratio to a Maxwellian (temperature indicated as T$_{\mathrm{M}}$) for $E_n = 2.0, 2.5,$ and 3.0 MeV.

by bombarding a thin natural lithium metallic target with protons. The produced neutrons impinged on a ^{238}U target that was mounted on a cathode plate of a conventional parallel-plate fission chamber. The fission chamber was aligned at 0° with respect to the neutron beam direction. Electronic pulses indicating a fission event provided start signals for time-of-flight (TOF) measurements. Excellent discrimination was achieved between fission fragments events, α particles (^{238}U is a weak α-emitter), and electronic noise. A fission-fragment detection threshold was also applied off-line during the data analysis process so as to discard any random coincidences that might arise from α-particles and the electronic noise in the fission chamber.

Two EJ301 liquid organic scintillator detectors (12.7 cm diam. and 5 cm thick) were used to detect fission neutrons. They were placed at a distance of about 70 cm from the fission chamber, making an angle of 60° with respect to the incident neutron beam direction on either side of the beam. Electronic pulses initiated in these detectors by neutrons (or γ-rays) were used as TOF stop signals. The EJ301 detector exhibits good n-γ pulse shape discrimination properties. Consequently, neutrons and γ-rays could be discriminated by pulse shape analysis as well as by their TOF characteristics. The detection efficiency of each neutron detector was experimentally determined in a separate TOF experiment using a

^{252}Cf(sf) neutron source. The measured spectrum was then compared with the evaluated standard ^{252}Cf(sf) spectrum shape provided by Mannhart [36]. The measured neutron TOF spectra, after correcting for background and detector efficiency, were used to generate PFNS energy distributions at E_n=2.0, 2.5 and 3.0 MeV incident neutron energies. Corresponding data from both detectors were summed so as to provide better statistical precision. The numerical results are given in Table 15. To obtain an estimate of the complete PFNS and neutron yield, the measured spectral data (which covered a limited emitted neutron energy range) were fitted with both a Watt formula [12] (see Eq. (16)) and a Maxwellian distribution [14] (see Eq. (15)) using a χ^2 minimization procedure (see Sec. IV). The values obtained from the fit of the Watt (a and b) and Maxwellian (T) parameters are given in Table 16. The best fit values of the $\overline{\nu}$, and the calculated average energy $\overline{E}$, obtained in the present work for incident neutron energies 2.0, 2.5 and 3.0 MeV, are also presented in Table 16. PFNS average energies $\overline{E}$ derived from the Watt and Maxwellian fits agree within estimated uncertainties if we limit the fit to the range of outgoing neutron energies $0.75 \leq E \leq 7.5$ MeV. The Kornilov model (see Sec. IV A and Ref. [136]) was used to calculate the PFNS as implemented in the EMPIRE code [137, 138]. In Fig. 5, ratios of calculated and experimental data with respect to the equivalent Maxwellian distribution are shown for comparison. The present experimental PFNS data are seen to agree very well both with calculations based on the Kornilov parameterization [136], and with the ENDF/B-VII.1 evaluation.

K. NUEX Experiments for Fast Neutron-Induced Fission of ^{235}U and ^{239}Pu

Diagnostic neutron experiments (NUEX) have been performed at the Nevada Test Site by Los Alamos National Laboratory, by studying the proton recoils induced by the neutrons produced from a device. The time dependence of the current recorded in a Faraday cup is a measure of the spectrum of those neutrons. By accurately modeling the device and performing accurate neutron transport calculations, one can use these data to infer the PFNS for different materials for emitted neutron energies from ~1 to ~11 MeV.

TABLE 17. Inferred prompt fission neutron spectrum values for $E_n = 1.5$ MeV neutron-induced fission of ^{235}U and ^{239}Pu from NUEX experiments [66].

E (MeV)	^{235}U Probability (1/MeV)	^{239}Pu Probability (1/MeV)
1.5	0.2947 ± 0.0065	0.2905 ± 0.0073
2.5	0.1884 ± 0.0041	0.1945 ± 0.0041
3.5	0.1063 ± 0.0023	0.1110 ± 0.0027
4.5	0.0559 ± 0.0013	0.0607 ± 0.0016
5.5	0.0277 ± 0.0010	0.0318 ± 0.0011
6.5	0.0144 ± 0.0006	0.0166 ± 0.0005
7.5	0.00638 ± 0.00068	0.00853 ± 0.00035
8.5	0.00292 ± 0.00060	0.00421 ± 0.00022
9.5	0.00091 ± 0.00061	0.00224 ± 0.00019
10.5	-	0.00135 ± 0.00023

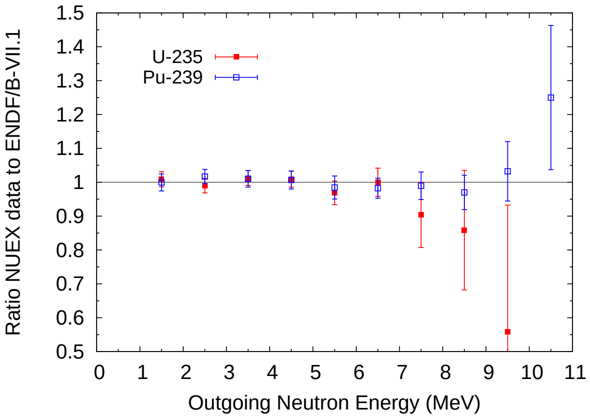

FIG. 6. (Color online) Ratio of the ^{235}U-NUEX and ^{239}Pu-NUEX inferred PFNS data at $E_n = 1.5$ MeV to the ENDF/B-VII.1 PFNS evaluation based on the LAM.

This study was performed for several events, enabling data to be inferred for n+^{239}Pu and n+^{235}U PFNS. The fission neutrons in these devices were produced by fission events induced by neutrons over a broad range of energies. We have listed the inferred PFNS at an incident neutron energy of 1.5 MeV. The complete results have been published in [66, 67], and are only summarized here in Table 17 and Fig. 6. Note that the NUEX results are in very good agreement with the ENDF/B-VII.1 PFNS evaluations for both isotopes at the selected $E_n = 1.5$ MeV, up to an outgoing energy of ∼8.5 MeV, for ^{239}Pu and ∼6.5 MeV for ^{235}U. Discrepancies, as well as inferred uncertainties, increase beyond those energies.

L. On-going Chi-Nu Experiments at LANSCE

A significant experimental effort to measure the prompt fission neutron spectrum of neutron-induced fission of ^{239}Pu and ^{235}U has been initiated at the Los Alamos Neutron Science Center (LANSCE). The most important goals of this effort are twofold: (1) significantly improve the experimental accuracy of the measured PFNS over previous data, in particular in the low- and high-energy tails of the spectrum; (2) produce PFNS data as a function of incident-neutron energy for which very little experimental data exist to date. The stated target accuracies for this measurement are as follows: 5% in the 0.1–1.0 MeV outgoing neutron energy range, 3% for 1−5 MeV, 5% for 5−9 MeV, 15% for 9−12 MeV, and 30% above.

The experimental approach is based on a double time-of-flight technique employed to measure the energies of the incident and outgoing neutrons. The WNR/LANSCE facility provides spallation neutrons ranging from a few hundreds of keV to more than 200 MeV. The incident neutron energy is derived experimentally by time-of-flight measurement over a flight path of over 21.5 meters. Outgoing neutrons are measured by an array of neutron liquid scintillator detectors of the type EJ309, as well as ^{6}Li-glass detectors, to cover a wide range of energies from about 50 keV- lower limit based on noise due to room return background, to over 12 MeV- higher limit of liquid scintillators and the limited number of neutrons emitted at this energy.

For all outgoing neutron energies, except perhaps at the highest energies above 10 MeV, systematic uncertainties are by far the dominant source of uncertainties compared to statistical uncertainties. At least 50 possible sources of systematic uncertainties have been identified as part of this effort: beam profile, target impurities, PPAC response, neutron detector efficiencies, multiple scattering, time resolution, TOF length, cross-talk between adjacent detectors, etc. Due to the complexity of the experimental setup and the challenging target accuracies of the project, significant effort has been devoted to the simulation of those effects through Monte Carlo transport simulations using the MCNPX-PoliMi [119] and GEANT-4 [139] transport codes. Measurements of the ^{252}Cf(sf) standard neutron spectrum have been used to calibrate the responses of the detectors.

Data have been taken recently (Jan. 2015) and they are now being analyzed. The α-activity of Pu sources renders the PFNS measurement especially challenging for this nucleus. Consequently, the Chi-Nu program focus shifted to measuring the $n+^{235}$U PFNS instead.

Note that during the course of this experimental effort, the Monte Carlo transport simulations were extended to analyze various previous experimental PFNS data sets. This investigation has revealed much larger uncertainties and errors than often reported in the original publications. Most of this work has been documented in Ref. [140], and it will be the subject of a separate publication in the current journal issue [89].

M. Guideline on PFNS Uncertainty Quantification

In this Section, a guideline is presented for determining what information is needed by an evaluator to generate an adequate uncertainty quantification, and how the experimental covariances can be prepared based on this information. In Appendix I, a brief definition of "uncertainty", "covariances" and related terms is provided.

1. *Information needed for a proper uncertainty estimate*

It is of high importance for a proper uncertainty estimate that a measurement can be unambiguously identified as a "absolute", "absolute ratio", "absolute ratio calibration", "shape", "shape ratio" or "shape ratio calibration" measurement. Because the ENDF-6 [44] format requires the PFNS to be normalized over its outgoing neutron energy range to one, absolute measurements can be treated as a "shape" type of measurement[5]. This distinction relates to a decision that

---

[5] The distinction "shape" and "absolute" measurement is of less importance, as the information needed for a PFNS evaluation is essentially about the shape of the PFNS. The absolute normalization of the measured PFNS is of interest for the estimate of the prompt neutron $\overline{\nu}$, which is measured to a higher accuracy and precision in different types of experiments [55, 141].

have to be made by the experimentalists regarding how to quantify or avoid quantifying their neutron detector efficiency and background contributions. Based on this decision, in some cases certain uncertainty sources can cancel, whereas in other situations they must be included in an uncertainty analysis. The associated uncertainty quantification procedures differ, thus leading to different estimated uncertainties. In a “shape” measurement, the neutron detector efficiency is either measured, e.g., relative to several neutron product cross-sections or it is calculated directly. In a “shape ratio” measurement, a reference measurement is performed in *exactly* the same geometry, and the final data are given as a ratio of the desired PFNS to the reference PFNS, or vice versa. The data of a “shape ratio calibration” measurement are also often given as a ratio of desired and reference PFNS in EXFOR [52]. However, contrary to “shape ratio” data, the reference measurement to obtain the detector efficiency was obtained in a different geometry: for instance, with different fission event detectors, different sample size or even in a different experimental facility location. Therefore, background and multiple scattering effects might not cancel as in a “shape ratio” measurement.

It is also vital that the experimental setup be documented in sufficient detail so that the measurement can be reasonably well simulated with neutron-transport codes. Also, corrections made to the measured raw data should be retained following completion of the experiment, and also be well-documented. If both these requirements are met, the experimental data can be corrected at a later time if the need arises, and they will be available for future analysis by evaluators at a future time, perhaps using newer methods. In situations where original data are reduced by analysis, and the original information is discarded, this option is not possible. Valuable information can be lost forever. Several of the earlier data sets mentioned in this paper suffer from this deficiency. However, it is worth noting that above mentioned Monte Carlo transport calculations were often not possible before. Simulations have greatly improved due to the availability of extremely well validated and optimized codes running in powerful multi-tasking computers.

The prerequisite for being able to perform a detailed uncertainty quantification is the knowledge of partial uncertainties and associated correlations [142, 143]. These partial uncertainties quantify uncertainty information for distinct parts of the measurement or analysis procedures, e.g., uncertainties related to the neutron detector efficiency determination or background subtraction. Special care should be taken by the experimentalists to identify and provide good estimates for the *major* uncertainty sources of the experiment. Partial uncertainty components can be most reliably calculated by applying the error propagation method to the reduction formulas used in the experimental analysis to determine the specific component (e.g., background, detector efficiency) of the uncertainty. But in general, this is impossible due to absence of all needed information and we rely on the experimentalists to provide the partial uncertainties. Below, partial uncertainty contributions typically encountered in PFNS experiments are listed based on information in Refs. [143–146], including a few general suggestions concerning the estimation of associated correlations.

- **Counting statistics** uncertainties with standard deviation Δs stemming from the finite number of prompt fission neutron counts are of a random, uncorrelated nature and their off-diagonal correlations Cor_s are zero.

- **Background** uncertainties with standard deviation Δb quantify possible ambiguities in the correction of background events. While the background events due to random coincidence, room return or scattering in air can be of random nature, the uncertainties associated to their correction might not be. If, for instance, a computer program with uncertain underlying nuclear data was used to calculate the background, or the impact of shielding material was incorrectly estimated, correlated systematic uncertainties arise. The underlying uncertainty sources can be used to estimate the non-zero off-diagonal correlations Cor_b associated to Δb.

- Uncertainties related to the **detector efficiency** determination with standard deviation Δd can be either or both of statistical and systematic nature, and their often non-zero off-diagonal correlations Cor_d need to be estimated according to the uncertainty components that comprise Δd. Possible underlying uncertainty sources are uncertain reference cross sections, uncertain cross sections in a simulation program, or extrapolations and interpolations employed to obtain the detector efficiency curve.

- If the PFNS is measured as a **ratio** to the PFNS of a **reference material**, e.g., ^{252}Cf(sf), the final PFNS is obtained by multiplying the ratio with an accepted numerical representation of the reference PFNS. Standard deviations Δr and correlations Cor_r are usually known for the standard and reference nuclear data, see e.g., [36, 37].

- The standard deviation Δt of the **time resolution** is often given in units of time and it needs to be transformed into uncertainties pertaining to the PFNS. In double-time-of-flight experiments, where a fission detector provides the start signal (called “t_0”) and the neutron detector the end signal, the time resolution can be partitioned into contributions, one due to the finite channel width and one due to an uncertainty in the determination of t_0. Usually Δt applies equally to all values in the same measurement, however if several neutron or fission detectors are used in a measurement, the off-diagonal correlations Cor_t might be smaller than 1 for the different detectors.

- An uncertainty in the **time-of-flight length** with standard deviation Δl usually applies to the whole measurement. It is often given in units of length, consequently it needs to be transformed into uncertainties pertinent to the PFNS. The correlation which is encountered in the PFNS space results from this transformation.

- Corrections for **multiple scattering and attenuation** in the sample and surrounding material are obtained for many PFNS experiments via computer simulations or analytical considerations. Due to simplifying assumptions in these procedures, and use of uncertain nuclear data, uncertainties with standard deviation Δm and non-zero off-diagonal correlations Cor_m apply to the PFNS spectrum.

- The **detector response** function is not a delta-function in energy, and thus the spectrum should be obtained through a de-convolution procedure. This is a complex process, and simplifying assumptions (e.g., assuming a delta-function) lead to a systematic bias of the spectrum at high outgoing energies with standard deviation Δc and non-zero off-diagonal correlation Cor_c.

- The geometry of some fission detectors can lead to an **angular distortion** of the spectrum that requires corrections. The correction might be subject to an uncertainty with standard deviation $\Delta\Omega$ and correlations Cor_Ω that depend on the specific method used to estimate the corrections.

- Sometimes, experimental **uncertainties relative to the outgoing neutron energy** with standard deviations ΔE are provided by the experimentalists. For instance, these might stem from the uncertainty in energy calibration, time resolution or time-of-flight length, and the correlations Cor_E can be estimated according to their underlying sources. The uncertainties relative to energy need to be transformed into uncertainties relative to the PFNS.

While it is of course desirable to have such detailed uncertainty information, it is often missing. In particular, correlation information is often not available and it has to be estimated using expert judgment by the evaluator. It is obsolete practice in nuclear data evaluations of cross-sections to assume full correlations for systematic partial uncertainties, which can be interpreted as an uncertainty on the scaling of the PFNS. However, when the integral of the evaluated PFNS is normalized to unity, as required for PFNS recorded in evaluated data libraries, the scaling is fixed and uncertainties on the scaling drop out during the normalization of the evaluated covariances [141, 147]. A global assumption of full correlation for systematic uncertainties would consequently lead to a reduction of the evaluated uncertainty which might not be applicable to the nature of the specific partial uncertainty. Special care must be taken by the evaluator to assume a distinct shape for the correlation matrix associated with systematic partial uncertainties. The underlying sources of the uncertainties can provide helpful guidelines for estimating this correlation pattern.

It is obvious that detailed information for partial uncertainties, the experimental setup and analysis technique are needed for a reasonable uncertainty quantification. If this information is not available, the evaluator might choose to reject an experimental data set for the evaluation, as unknown, and hence potentially not well estimated, associated uncertainties might lead to an improper weight of a specific data set and introduce a bias in the evaluated mean values as well as the covariances. If only information about fully correlated systematic uncertainties is missing, the data can be used as a shape type of measurement.

2. *Estimating experimental covariances*

This section describes the procedures used to estimate covariances of total uncertainties from partial uncertainty information for "shape", "shape ratio" and "shape ratio calibration" measurements.

a. Shape measurements. The detector efficiency is determined directly without relying on one specific reference isotope, but, for instance, it is derived relative to several neutron production cross sections or via a program computing the detector efficiency. The covariance matrix elements $\mathrm{Cov}\,(N_i, N_j)$ of the total uncertainties associated with the PFNS N_i and N_j are obtained by the sum of all partial uncertainty contributions, as follows

$$\begin{aligned}
&\mathrm{Cov}\,(N_i, N_j) = \Delta s_i \Delta s_j \delta_{ij} \\
&+ \Delta b_i \Delta b_j \mathrm{Cor}_b\,(N_i, N_j) + \Delta d_i \Delta d_j \mathrm{Cor}_d\,(N_i, N_j) \\
&+ \mathrm{Cov}_t\,(N_i, N_j) + \mathrm{Cov}_l\,(N_i, N_j) \\
&+ \Delta m_i \Delta m_j \mathrm{Cor}_m\,(N_i, N_j) + \Delta c_i \Delta c_j \mathrm{Cor}_c\,(N_i, N_j) \\
&+ \Delta\Omega_i \Delta\Omega_j \mathrm{Cor}_\Omega\,(N_i, N_j) + \mathrm{Cov}_E\,(N_i, N_j)\,. \qquad (6)
\end{aligned}$$

Use is made in this formula of the Kronecker delta $\delta_{ij} = 1$ for $i = j$ and $\delta_{ij} = 0$ for $i \neq j$. The indexes i and j for a variable x indicate that x is given for the outgoing neutron energies E_i and E_j. It is implicitly assumed that the correlations between different uncertainty contributions are zero. It is straightforward to add other uncertainty contributions as long as they are independent of each other. No PFNS of a reference isotope is employed to obtain the PFNS in Case 1, hence no associated uncertainty Δr needs to be considered.

The outgoing neutron energy covariances $\mathrm{Cov}_E\left(N_i, N_j\right)$ are already transformed into covariances for the PFNS N_i and N_j. To obtain those from ΔE_i and $\mathrm{Cor}(E_i, E_j)$ in outgoing neutron energy space, linear error propagation is used,

$$\mathrm{Cov}_E\left(N_i, N_j\right) = \left.\frac{\partial N}{\partial E}\right|_{E_i} \Delta E_i \mathrm{Cor}(E_i, E_j) \Delta E_j \left.\frac{\partial N}{\partial E}\right|_{E_j} . \tag{7}$$

The expression $N_i = C\sqrt{E_i}\exp\left(-E_i/T\right)$, a Maxwellian distribution with a normalization constant C and temperature T, is used to estimate the partial derivative $\partial N/\partial E|_{E_i}$, thus

$$\left.\frac{\partial N}{\partial E}\right|_{E_i} = \frac{N_i}{E_i}\left(\frac{1}{2} - \frac{E_i}{T}\right) . \tag{8}$$

For N_i the actual experimental data can be used. Of course, this approach suffers from (a) the shortcomings of a Maxwellian to describe actual experimental data, and (b) neglecting higher-order uncertainty terms. Issue (a) becomes substantial once the resulting relative uncertainty in PFNS space exceeds 10% and can be addressed by replacing Eq. (8) with the numerical derivative following Eq. (43) of Ref. [143].

The covariances $\mathrm{Cov}_t(N_i, N_j)$ in terms of the PFNS associated with the finite time resolution Δt are obtained from a two-step process. First, time resolution uncertainties Δt given relative to the time-of-flight are transformed into uncertainties relative to the outgoing neutron energy by using linear error propagation and a non-relativistic approximation of the energy-time relationship, $\mathrm{Cov}_t(E_i, E_j) = 4\Delta t^2 E_i E_j/(t_i t_j)$. It is assumed implicitly that the time resolution uncertainty Δt is constant for all times-of-flight t_i, and it is thus a fully correlated uncertainty component. In a second step, the covariances $\mathrm{Cov}_t(E_i, E_j)$ are transformed into covariances associated to the PFNS using again linear error propagation (see Eq. (7)):

$$\mathrm{Cov}_t\left(N_i, N_j\right) = 8\frac{\sqrt{E_i E_j}}{m_{\mathrm{n}} l^2} N_i N_j \left(\frac{1}{2} - \frac{E_i}{T}\right)\left(\frac{1}{2} - \frac{E_j}{T}\right)(\Delta t)^2 , \tag{9}$$

using the neutron mass m_{n}.

Analogously, a time-of-flight length uncertainty Δl is transformed into covariances associated with the outgoing neutron energy by $\mathrm{Cov}_l(E_i, E_j) = 4(\Delta l)^2 E_i E_j/l^2$, and then into corresponding covariances relative to the PFNS by:

$$\mathrm{Cov}_l\left(N_i, N_j\right) = \frac{4}{l^2} N_i N_j \left(\frac{1}{2} - \frac{E_i}{T}\right)\left(\frac{1}{2} - \frac{E_j}{T}\right)(\Delta l)^2. \tag{10}$$

Of course, Eq. (6) can be generalized to estimate covariances between two different experiments that need not be undertaken for the same isotope. Statistical uncertainties will not appear in covariances between two experiments k and h, hence the covariances between experiments read:

$$\begin{aligned}
&\mathrm{Cov}\left(N_i^k, N_j^h\right) = \Delta b_i^k \Delta b_j^h \mathrm{Cor}_b\left(N_i^k, N_j^h\right) \\
&+ \Delta d_i^k \Delta d_j^h \mathrm{Cor}_d\left(N_i^k, N_j^h\right) + \mathrm{Cov}_t\left(N_i^k, N_j^h\right) \\
&+ \mathrm{Cov}_l\left(N_i^k, N_j^h\right) + \Delta m_i^k \Delta m_j^h \mathrm{Cor}_m\left(N_i^k, N_j^h\right) \\
&+ \Delta c_i^k \Delta c_j^h \mathrm{Cor}_c\left(N_i^k, N_j^h\right) \\
&+ \Delta\Omega_i^k \Delta\Omega_j^h \mathrm{Cor}_\Omega\left(N_i^k, N_j^h\right) \\
&+ \mathrm{Cov}_E\left(N_i^k, N_j^h\right) .
\end{aligned} \tag{11}$$

It is often difficult to assess correlations between different experiments. It is recommended to compare the uncertainty sources of two experiments as well as their underlying sources, and from that to infer their correlations.

b. Shape ratio measurements. For a "shape ratio" measurement, the PFNS of an isotope A is given as a ratio to a reference PFNS B, $\rho_i = N_i^A/N_i^B$. For both measurements, the same neutron detectors are used, and thus the neutron detector efficiency and the associated uncertainties Δd cancel. In addition, major components of the background counts cancel each other, for instance part of the room-return background. If the isotope B is measured with beam off and A with beam on, the background contribution caused by incoming neutrons does not cancel, and non-zero, but reduced, background uncertainties apply. Also, the uncertainty due to an angular distortion $\Delta\Omega$, due to biases in the multiple scattering correction Δm and the deconvolution correction Δc reduce significantly, while statistical uncertainties Δs still apply. Outgoing neutron energy uncertainties ΔE, uncertainties due to the finite time resolution Δt and time-of-flight length Δl uncertainties are reduced in ratio measurements[6]. This reduction can be demonstrated if one represents the PFNS N_A and N_B by Maxwellian distributions for the ratio, $\rho_i = C_\rho \exp\{E_i\,(1/T_B - 1/T_A)\}$, with Maxwellian temperatures T_A and T_B and $C_\rho = C_A/C_B$. The first partial derivative of ρ with respect to E is given by $\partial\rho/\partial E|_{E_i} = \rho_i\,(1/T_B - 1/T_A)$, where one can use again the actually measured value ρ_i. Consequently, $\mathrm{Cov}_E(\rho_i, \rho_j)$, $\mathrm{Cov}_t(\rho_i, \rho_j)$ and $\mathrm{Cov}_l(\rho_i, \rho_j)$ read:

$$\begin{aligned}
&\mathrm{Cov}_E(\rho_i,\rho_j) = \\
&\rho_i\rho_j\left(\frac{1}{T_B}-\frac{1}{T_A}\right)^2 \Delta E_i \Delta E_j \mathrm{Cor}(E_i,E_j), \\
&\mathrm{Cov}_t(\rho_i,\rho_j) = \\
&8\rho_i\rho_j\left(\frac{1}{T_B}-\frac{1}{T_A}\right)^2 \frac{(\Delta t)^2}{m_\mathrm{n} l^2} (E_i E_j)^{3/2}, \\
&\mathrm{Cov}_l(\rho_i,\rho_j) = 4\rho_i\rho_j\left(\frac{1}{T_B}-\frac{1}{T_A}\right)^2 E_i E_j \frac{(\Delta l)^2}{l^2}.
\end{aligned} \tag{12}$$

The experimental PFNS are obtained by multiplication of the measured ratio data ρ_i with N^R, the nuclear data for the reference isotope B (usually, this would be the ^{252}Cf(sf) PFNS of [36, 37]), $N_i^A = \rho_i N_i^R$. The covariances $\mathrm{Cov}\left(N_i^A, N_j^A\right)$ associated with the values N_i^A are derived from linear error propagation,

$$\begin{aligned}
\mathrm{Cov}\left(N_i^A, N_j^A\right) = {} & N_i^R N_j^R \mathrm{Cov}\left(\rho_i, \rho_j\right) \\
& + \rho_i\rho_j \Delta r_i \Delta r_j \mathrm{Cor}_r(N_i^R, N_j^R),
\end{aligned} \tag{13}$$

using the standard deviations Δr and correlation matrix Cor_r associated with the nuclear data N^R of the reference PFNS. The covariance matrix elements for the total uncertainties of the ratio data $\mathrm{Cov}\left(\rho_i, \rho_j\right)$ are given by summing up the non-zero uncertainties following Eq. (6).

c. Shape ratio calibration measurements. This section considers the case in which the detector efficiency ε is calibrated by the PFNS measurement with values C^B of a reference isotope B, using a known numerical representation N^R of the reference PFNS, $\varepsilon_i = C_i^B/N_i^R$. The experimental PFNS of the isotope in question A can then be derived using the formula $N_i^A = C_i^A N_i^R / C_i^B$. The covariances of the total uncertainties,

$$\begin{aligned}
\frac{\mathrm{Cov}(N_i, N_j)}{N_i^A N_j^A} = {} & \frac{\mathrm{Cov}\left(C_i^A, C_j^A\right)}{C_i^A C_j^A} + \frac{\mathrm{Cov}\left(C_i^B, C_j^B\right)}{C_i^B C_j^B} \\
& + \frac{\Delta r_i \Delta r_j \mathrm{Cor}_r(N_i^R, N_j^R)}{N_i^R, N_j^R},
\end{aligned} \tag{14}$$

comprise covariances $\mathrm{Cov}_A \equiv \mathrm{Cov}\left(C_i^A, C_j^A\right)$, $\mathrm{Cov}_B \equiv \mathrm{Cov}\left(C_i^B, C_j^B\right)$ and $\Delta r_i \Delta r_j \mathrm{Cor}_r(N_i^R, N_j^R)$ of the actual measured values C_i^A, C_i^B and the nuclear data N_i^R of the reference PFNS.

In Cov_A as well as Cov_B, Δs, Δb, Δt, Δl, Δm, $\Delta\Omega$ and ΔE enter for each measurement separately, while detector efficiency and deconvolution uncertainties cancel. This entails a detailed uncertainty analysis of measurements A and B. Another way to represent this is to consider the uncertainties Cov_B and $\Delta r_i \Delta r_j \mathrm{Cor}_r(N_i^R, N_j^R)$ in the covariances associated with the detector efficiency determination $\Delta d_i \Delta d_j \mathrm{Cor}_\mathrm{d}(N_i^A, N_j^A)$ and then use Eq. (6) instead. This is formerly correct, however it might be less transparent than a detailed analysis of measurement B.

N. Uncertainty analysis of PFNS data for ^{232}Th(n,f) and ^{238}U(n,f) as UQ examples

This section summarizes the available uncertainty information for neutron-induced fission of ^{232}Th and ^{238}U, and it illustrates the concepts and procedures discussed in the previous section III M 2 by means of these two representative examples. In addition, information is provided regarding where partial uncertainties can be found to facilitate the uncertainty quantification for future evaluations. The estimation of covariances for the suitable experimental data of the ^{239}Pu(n,f) PFNS is described in detail in a companion publication [89] and therefore will not be treated here.

---

[6] We assume that Δt and Δl are the same for N_A and N_B to derive $\mathrm{Cov}_t(\rho_i, \rho_j)$ and $\mathrm{Cov}_l(\rho_i, \rho_j)$ in Eq. (12).

1. ^{232}*Th PFNS*

TABLE 18. The uncertainty sources explicitly provided in the EXFOR [52] entry and described in the literature are listed here for experimental data sets of ^{232}Th(n,f) and ^{238}U(n,f) where sufficient experimental information is available to estimate a covariance matrix. The different uncertainty sources are named following the notation in Section III M 2, namely Δs for statistical uncertainties, Δb for background uncertainties, Δd for detector efficiency uncertainties, Δr for uncertainties of a reference PFNS, Δt for time resolution, Δl for TOF length uncertainties, Δm for multiple scattering uncertainties, Δc for uncertainties due to the deconvolution of the PFNS, $\Delta\Omega$ for angular correction uncertainties and ΔE for uncertainties relative to the outgoing neutron energy. An unspecified component of uncertainty interpreted to contain statistical uncertainties is marked with *.

Experiment	Literature to assess correlations	Uncertainty in EXFOR	Uncertainty in literature
Boykov [78], ^{232}Th	[36, 37, 78, 79, 103]	$(\Delta s + \Delta d' + ...)$, Δt, Δr	Δt, Δd Δr
Lovchikova [105], ^{232}Th	[36, 37, 78, 98, 103, 105]	$(\Delta s + ...)$	Δs,Δt, Δd, Δr
Baba [102], ^{232}Th	[102]	Δs, Δt	Δt, Δd
Boykov [78, 103], ^{238}U	[36, 37, 78, 79, 103]	$(\Delta s + \Delta d' + ...)$, Δt, Δr	Δt, Δd Δr
Baba [102], ^{238}U	[102]	Δs, Δt	Δt, Δd
Trufanov [97], ^{238}U	[36, 37, 78, 97, 98, 103]	$(\Delta s + ...)$	Δt, Δd, Δr
Lovchikova [96], ^{238}U	[36, 37, 78, 96, 103]	$(\Delta s + ...)$, Δs, Δt	Δs, Δt, Δd, Δr
Kornilov [99, 101], ^{238}U	[36, 37, 99, 101]	$(\Delta s + ...)^*$, Δm, $\Delta\Omega$	Δm,Δt, Δb, Δr
Baryba [99, 100], ^{238}U	[36, 37, 99, 100]	Δs, Δm, Δt	Δb, Δr, $\Delta\Omega$
Smirenkin [98], ^{238}U	[36, 37, 78, 98, 103]	$(\Delta s + ...)$	Δs,Δt, Δd, Δr

In Table 18, the available partial uncertainty sources for the experimental data of [78, 102, 105] are listed.

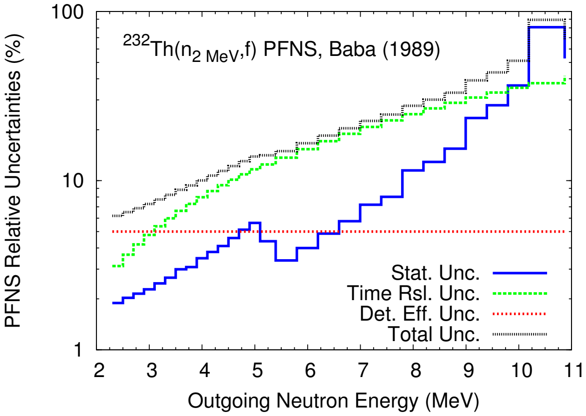

FIG. 7. Partial and total relative uncertainties are shown for the ^{232}Th(n,f) PFNS data of Ref. [102].

For the data set of [102] sufficient uncertainty information is available to estimate a covariance matrix. It is shown for this particular example how the covariances were estimated following the procedure described in Section III M 2. The detector efficiency was determined on the basis of Monte-Carlo calculations, and it was verified via experiments with the ^{252}Cf(sf) PFNS and hydrogen-scattered neutron yields. Hence, these data are interpreted as "shape" data. Statistical uncertainties Δs, detector efficiency uncertainties $\Delta d = 5\%$ and the time resolution $\Delta t = 1.5 - 1.8$ ns are provided in EXFOR and Ref. [102], and are also shown in Fig. 7. The time resolution relative uncertainties in PFNS space are shown in Fig. 7, and associated correlations were obtained following Eq. (9). The off-diagonal correlations for statistical uncertainties are set to zero. For the detector efficiency uncertainties, correlations between different energies were defined by $\mathrm{Cor}_d(N_i, Nj) = \exp\left\{-\left[(E_i - E_j)/\max(E_i, E_j)\right]^2\right\}$. This correlation function was estimated by expert judgment based on the fact that nuclear data are used for Monte Carlo simulations and the nuclear data uncertainties are often strongly correlated for neighboring energy bins and less so for energy bins far apart.

The total correlation matrix in Fig. 8 corresponds to a covariance matrix that is the sum of all the partial covariances according to Eq. (6). No uncertainties are given for the background correction, the TOF length, multiple scattering in the sample, and deconvolution and angular distortion of the PFNS. The TOF length uncertainty is usually a small contribution compared to total uncertainties[7]. The measured PFNS was corrected for multiple scattered neutrons in the sample. These neutrons were a small contribution to the total PFNS in the energy range of the present experiment. Hence, the associated uncertainty contribution is expected to be small. However, the background uncertainties due to neutrons scattering in the shielding material surrounding the neutron detector could be a non-negligible uncertainty

---

[7] If no TOF length uncertainty is provided, a reasonable estimate would be 1 mm.

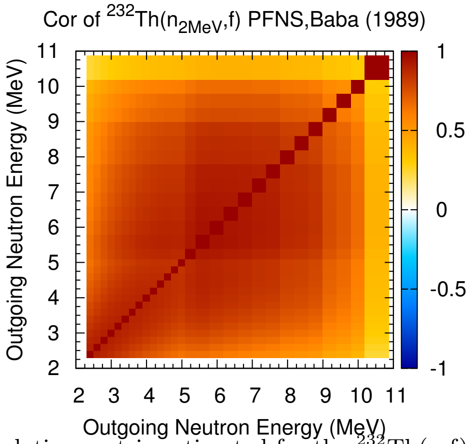

FIG. 8. (Color online) The correlation matrix estimated for the ^{232}Th(n,f) PFNS data of Ref. [102] is shown.

source. The influence of angular distortions and deconvolution on the PFNS could lead to additional uncertainties, but they are expected to be smaller than the given uncertainties. The detector efficiency and time resolution uncertainties for the ^{232}Th(n,f) and ^{238}U(n,f) PFNS data of Ref. [102] are correlated, as shown in Table 19, because both data sets were measured in the same setup.

TABLE 19. The correlated uncertainty sources of different ^{232}Th(n,f) and ^{238}U(n,f) PFNS measurements are provided. The superscript * in Δt^* indicates that the correlation for the time resolution uncertainties should be reduced between the two measurements because the associated neutron detector was probably not the same, while the same neutron detector type and the same method to determine the time resolution were used.

Experiment	[78], ^{232}Th	[105]	[102], ^{238}U	[78], ^{238}U	[97]	[96]	[101]	[100]	[98]
Baba [102], ^{232}Th	0	0	Δt,Δd	0	0	0	0	0	0
Boykov [78], ^{232}Th	-	Δd, Δr, Δt^*	0	Δd, Δr, Δt	Δd, Δr, Δt^*	Δd, Δr	Δr	Δr	Δd, Δr, Δt^*
Lovchikova [105]		-	0	Δd, Δr, Δt^*	Δd, Δr, Δt	Δd, Δr	Δr	Δr	Δd, Δr, Δt
Baba [102], ^{238}U			-	0	0	0	0	0	0
Boykov [78], ^{238}U				-	Δd, Δr, Δt^*	Δd, Δr	Δr	Δr	Δd, Δr, Δt^*
Trufanov [97]					-	Δd, Δr	Δr	Δr	Δd, Δr, Δt
Lovchikova [96]						-	Δr	Δr	Δd, Δr
Kornilov [101]							-	Δr, Δm, $\Delta\Omega$	Δr
Baryba [100]								-	Δr

Estimation of experimental covariances for the experimental data of Boykov et al. [78, 79, 103] is also considered here to give an example of uncertainty quantification for a ratio measurement. In addition, the fission detectors for this measurement series of ^{232}Th, ^{235}U and ^{238}U were re-used for the experiments of Refs. [96–98, 105]. In the measurements of Refs. [97, 98, 105], the same neutron detector type, if not the same instrument, was used, and it is assumed that the time resolution was estimated in a similar manner. Therefore, the procedure to estimate the covariances for ^{232}Th PFNS of Ref. [78] can be applied to the data of Refs. [96–98, 105]. The data of Boykov et al. were measured as a ratio to the ^{252}Cf(sf) PFNS, using a multi-layered ionization chamber, with three sections containing ^{232}Th and one monitor section containing ^{252}Cf. Thus, neither the neutron detector efficiency nor the deconvolution uncertainties apply to these data. Instead, the uncertainties related to the reference PFNS need to be considered. In the literature and the EXFOR entry, an overall uncertainty of 3% is given, which should be replaced by the detailed reference uncertainties Δr and associated correlations of Refs. [36, 37] if those standard data are used to convert the ratio data to PFNS space. Multiple-scattered and background neutron contributions to the PFNS should also largely cancel due to the fact that the data are measured as a ratio to reference material values. Only, background and multiple scattering contributions stemming from incoming neutrons do not cancel because the reference PFNS was not determined in-beam. No uncertainty is provided for this contribution. Also, no uncertainty is provided for the TOF length which often leads to a minor uncertainty component. In Ref. [78], it is described in detail how the angular distortion of the PFNS due to the angular correlation between prompt fission and incident neutrons is corrected, and it is shown how an angle between fission and neutron detector was chosen to minimize distortions of the PFNS due to lost fission fragment counts at small angles to the plane. Hence, the uncertainty component due to the angular distortion that is not included should be small. The covariance contribution due to the time resolution of 2.5 ns can be calculated following Eq. (12).

To interpret and understand the total uncertainties tabulated in EXFOR, some assumptions must be made. These total uncertainties contain statistical, detection efficiency, and correction uncertainties. The EXFOR entry lists corrections for the TOF path difference between different sections of the fission detector, neutrons induced by fission of ^{252}Cf, and the normalization of the PFNS. In the literature, one can find specified an accuracy of the fission fragment detection efficiency of 5% which is higher than part of the total uncertainties in EXFOR. Therefore, it is to be assumed that they are to be excluded from the total uncertainties, albeit the latter should contain unspecified "detection efficiency" uncertainties. A conservative approach to estimating the uncertainties would be to assume that the total uncertainties are of statistical nature only and then add the 5% uncertainty for the fission fragment detection efficiency. As no information is provided for the latter uncertainty component, correlations have to be assigned based on expert judgment. The total covariances are obtained in two steps: In the first step, the partial relative uncertainties pertinent to the ratio data are summed. The procedure is analogous to the one described for the ^{232}Th data of Ref. [102], so it is not discussed here. The only difference is that Eq. (12) is used to transform the time resolution uncertainty contribution into PFNS space since ratio data are involved. In the second step, ratio uncertainties are combined with those of the reference PFNS, in accordance with Eq. (13), to provide total covariances. The relative uncertainties of the ratio data in Fig. 9 are distinctly larger than those of Refs. [36, 37], and therefore they dominate the total relative uncertainties in Fig. 9 and correlations in Fig. 10. As ^{232}Th and ^{238}U PFNS ratio data were measured in the experiments of Refs. [96–98, 105] with the same fission fragment detector and a somewhat similar neutron detector, correlations arise between partial uncertainties of those data sets.

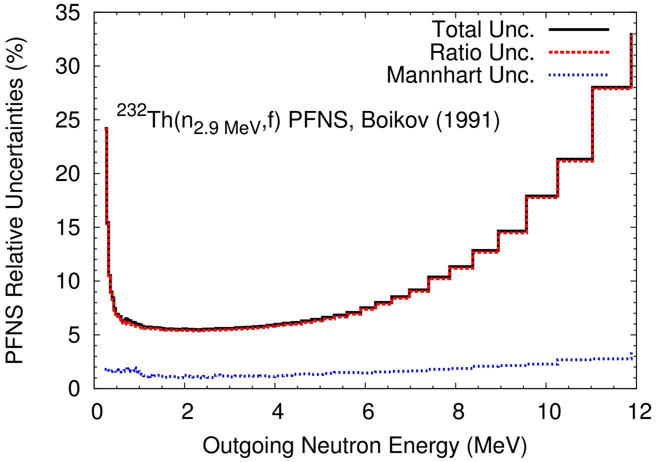

FIG. 9. Total relative uncertainties for the ^{232}Th(n,f) PFNS data of Boykov et al. [78, 103] are compared to the ratio relative uncertainties and those related to the ^{252}Cf(sf) PFNS data of Mannhart [36, 37].

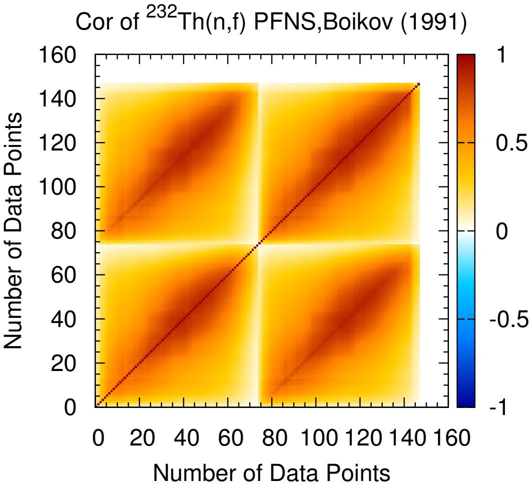

FIG. 10. (Color online) The correlation matrix estimated for the ^{232}Th(n,f) PFNS data of Boykov et al. [78, 103] is shown. The first 74 data points were measured for E_n=2.9 MeV, the data points above for E_n = 14.7 MeV.

These correlated partial uncertainties are listed in Table 19. It is difficult to estimate reasonable experimental covariances for the PFNS of Ref. [105]. In EXFOR, unspecified total uncertainties are tabulated. In Ref. [105], statistical uncertainties of 1.5% at around 1 MeV and 30% at the highest measured outgoing neutron energy are quoted. It is also stated that the total uncertainty is larger due to various, but unspecified, corrections. No further uncertainties are provided. However, the same ionization chamber as in Ref. [78] was used, and the same neutron detector as in Refs. [97, 98] was employed. Hence, one could use the time resolution Δt = 2.5 -3 ns of Ref. [98] and fission fragment detection efficiency uncertainty given in Refs. [78, 103]. Inferring uncertainties from other measurements leads to correlations between the concerned partial uncertainties of this measurement and those of Refs. [78, 98], as specified in Table 19. The time resolution uncertainty between Ref. [78] and Refs. [97, 98, 105] measurements is assumed to be not fully positively correlated because a neutron detector of the same type, but with different dimensions of the stilbene crystal, was used. The data of Ref. [105] are measured as a ratio to the ^{252}Cf(sf) PFNS, hence one can also employ the data and covariances of Refs. [36, 37] to obtain PFNS data and estimate uncertainties. Experimental covariances can be estimated following the procedure outlined for the Boykov et al. ^{232}Th data. It should be noted that covariances estimated from the considerations above are just an educated guess, so some sources of uncertainty might be missing.

2. ^{238}U PFNS

The ^{238}U PFNS data of Boykov et al. [78] were measured in the same setup as the ^{232}Th PFNS data using a very similar fission counter with ^{238}U instead of ^{232}Th. Hence, the procedure to estimate the uncertainties are identical, and the specific uncertainty values are the same except for the statistical uncertainties. Therefore, they are not repeated here. The same is true for the ^{238}U data of Baba et al. [102]. However, different TOF path lengths were used for ^{232}Th and ^{238}U data, namely 3.2 m and 3.9 m, leading to a difference in the uncertainties associated with the time resolution in PFNS space.

Similarly to the ^{232}Th PFNS measurement of Ref. [105], the ^{238}U measurements of Trufanov et al. [97] and Smirenkin et al. [98] as a ratio to the ^{252}Cf(sf) PFNS, were performed with the same fission detector as in Ref. [78]. Hence, detector related uncertainties Δd can be inferred from Ref. [78]. A time resolution of $\Delta t = 2.5-3$ ns is provided in Ref. [98], and this applies to both measurements. The uncertainties of the ^{252}Cf(sf) reference PFNS of Mannhart [36, 37], which are used to convert the ratio data to PFNS, need to be considered for the uncertainty estimation for both measurements. For both data sets, total uncertainties are provided in EXFOR. They are comprised of statistical and unspecified correction uncertainties. In the case of Smirenkin et al. data, statistical uncertainties, according to Ref. [98], amount to $1-40\%$. These statistical uncertainties can be separated approximately from the total uncertainties stored in EXFOR. The total covariances can be calculated following the procedure outlined for the ^{232}Th data of Ref. [78]. The issues related to missing uncertainty contributions for the data of Ref. [78] are also valid for the data of Refs. [97, 98, 105].

The same fission fragment detector as was used in Ref. [78] was also used for measuring the ^{238}U/^{252}Cf(sf) ratio data of Ref. [96], and therefore Δd from Ref. [78] can be used. However, a different neutron detector with time resolution $\Delta t = 2.5$ ns was employed. Therefore, non-zero correlations for Δd and Δr of Mannhart [36, 37] arise between the measurements of Ref. [96] and Refs. [78, 97, 98, 105], while no correlations for Δt to other measurements are listed in Table 19. In the EXFOR entry, total uncertainties are provided. For the most part they are of a statistical nature. The covariances can be estimated following the procedure shown for the ^{232}Th data of Ref. [78].

Unfortunately, Refs. [100, 101] could not be consulted for the uncertainty estimate of the ^{238}U data of Kornilov et al. and Baryba et al. Recourse had to be taken to apply the corresponding information in the associated EXFOR entries, as well as to consulting Ref. [99]. The latter literature source describes both measurements, but it is currently not listed in the EXFOR entries. Furthermore, some ambiguities exist with the information in Ref. [99] and the EXFOR entries (e.g., concerning time resolution, sample mass or TOF length). The data of Kornilov et al. and Baryba et al. are interpreted as "ratio calibration" data, as it is mentioned in Ref. [99] that the neutron detector efficiency was determined from the ^{252}Cf(sf) PFNS while no mention of a ^{252}Cf(sf) source in the fission chamber is made. Statistical uncertainties are provided in the EXFOR entry for the data of Baryba et al. while only unspecified uncertainties are listed in the EXFOR entry pertaining to the data of Kornilov et al. The latter uncertainties are interpreted as of statistical nature based on their magnitude. Of course, this assumption might be incorrect. In Ref. [99], a time resolution $\Delta t = 1.5-2$ ns is provided which is used for the present purposes. In the EXFOR entry for the Baryba et al. data, a distinctly higher Δt of 3 ns is documented. Therefore, that value is assumed for these data. Otherwise, the assumed uncertainty is based on information in Ref. [99], and in the corresponding EXFOR subentry. This is comprised of a multiple scattering and attenuation uncertainty $\Delta m = 1-2\%$, an angular correction uncertainty of $\Delta\Omega = 2.6\%$, background uncertainties $\Delta b = 5\%$, and reference material uncertainties of Mannhart [36, 37]. In Table 1 of Ref. [99], uncertainties associated with corrections of a $\overline{\nu}$ measurement are given. Items (3), (4), (5) and (10) of this table could also apply to the PFNS measurement, but their contribution is small compared to, e.g., Δb or Δs of Baryba et al. The experimental covariances can be estimated according to Eq. (14) by summing up the uncertainty contributions of the ^{238}U measurement, the ^{252}Cf measurement, and the reference PFNS. Information from the ^{252}Cf(sf) calibration measurement is missing, and it could be estimated based on information from the ^{238}U measurement, although it might not be consistent with the calibration measurement.

It is obvious from Table 19 that the uncertainties of ^{232}Th and ^{238}U experimental data are strongly correlated with each other. Three distinct measurement series exist, Baba et al. [102], measurements performed with the fission fragment detectors of Ref. [78], and those described in Ref. [99]. This strong interdependence simplifies the uncertainty estimation process if partial uncertainties are missing, but one should also bear in mind that a systematic bias, such as, for instance,the one involving the fission fragment detectors of Ref. [78] might affect many data sets in the same way.

IV. DETERMINISTIC MODELS

Models have long served a practical role in describing the emission of neutrons in neutron-induced fission (PFNS), and the spontaneous fission of actinide nuclides, in an approximate way. Madland [124] offered a brief overview of the early history of PFNS modeling at the *IAEA Consultants' Meeting on Nuclear Data for Neutron Emission in the Fission Process*, held in Vienna, 22-24 October 1990. A portion of the introductory material appearing in the following three paragraphs is taken from that reference.

The earliest and simplest model of the PFNS [18], and one still employed for some applications, is the single-parameter Maxwell-Boltzmann distribution (generally referred to simply as a "Maxwellian") that depends on a temperature parameter, T, which is taken to correspond to the nuclear temperature at the time of neutron emission,

$$\chi_{_M}(E,T) = \frac{2\sqrt{E}}{\sqrt{\pi T^3}} \exp(-E/T) \ . \tag{15}$$

being E the energy of the emitted neutron. The mean energy of the emitted neutron is $\overline{E} = \frac{3}{2}T$. With T in units of MeV, the spectrum has units of MeV^{-1}. This function has an analytical form that is easy to code for computational purposes. However, for this model to be physically applicable, the neutron-emitting actinide nucleus must be in thermal equilibrium at temperature T and that neutrons "boil off" with a statistical energy distribution consistent with this assumption, much like the distribution of particle energies for a heated perfect gas (non-interacting particles) or for electrons emitted from a heated cathode by thermionic emission [124]. Of course, this is far from the true physical situation here since the neutrons are emitted as a consequence of the fission process. A nucleus that undergoes either spontaneous or neutron-induced fission is clearly not in thermal equilibrium in any traditional sense of the concept.

The Maxwellian model of the PFNS neglects the fission fragment excitation energy distribution; the energy dependence of the inverse process of compound nucleus formation; and the center-of-mass motion of the neutron-emitting fragments. Thus, in the Maxwellian, the single temperature parameter must simultaneously account for all of these physical effects. Accordingly, this approach has no predictive power. Given the severe limitations inherent in this model, it is surprising that it replicates the broad general features of the PFNS as well as it does.

The Watt spectrum [12], with two parameters, is based on a center-of-mass Maxwellian spectrum for neutron emission from an average fission fragment with average kinetic energy E_f after transformation to the laboratory frame,

$$\chi_{_W}(E,a,b) = \frac{2}{\sqrt{\pi a^3 b}} \sinh\sqrt{bE} \exp\left[-\frac{ab}{4} - \frac{E}{a}\right] , \tag{16}$$

where E is the energy of emitted neutrons and the parameters a and b depend on the fissile material. The mean neutron energy is $\overline{E} = 3a/2 + a^2b/4$. The physical meaning of the parameters can be better understood by expressing them in terms of T and E_f,

$$a = T \ \ , \ \ b = \frac{4E_f}{T^2} \ \ , \ \ \overline{E} = \frac{3T}{2} + E_f \ . \tag{17}$$

Using Eq. (17), the Watt spectrum can be rewritten as

$$\chi_{_W}(E,T,E_f) = \frac{1}{\sqrt{\pi T E_f}} \sinh\sqrt{\frac{4E_f E}{T^2}} \exp\left[-\frac{E_f + E}{T}\right] . \tag{18}$$

In the limit $E_f \to 0$, the Watt formula, Eq. (18), reduces to a Maxwellian, Eq. (15). A Watt spectrum with $a = 0.988$ MeV and $b = 2.249$ MeV^{-1} was used for the ^{235}U($n_{\rm th}$,f) PFNS evaluation in ENDF/B-V that corresponds to the PFNS average energy $\overline{E}$ of 2.03 MeV.

While the Watt formulation also neglects the fragment excitation energy and the energy dependence of compound nucleus formation, it does account for the center-of-mass motion of an average fragment. Therefore, the Watt distribution, while more physical than a Maxwellian, still has little predictive power. If a Watt representation is desirable, it may be preferable to use separate Watt spectra for the light and heavy fragments, as done by, e.g., Kornilov et al. [131, 132] and discussed later.

In the more than 60 years since introduction of the Watt spectrum [12], a great deal of both theoretical and experimental effort has been devoted to gaining a better physical understanding of fission, and in particular, the PFNS.

The models developed during this period have become quite sophisticated. While some are microscopic physics models, parameterized analytical models continue to play an important role for most practical evaluation purposes. In the remainder of this section, model development work along both lines, with an emphasis on work done during this CRP, is discussed.

Experimental data provide important constraints on model predictions which can vary widely even if the model parameters are varied within reasonable limits. However, experimental data are often limited to specific reactions and incident energies. In addition, the experimental setup can limit the range over which outgoing neutron energies can be measured reliably so that only partial spectra are available. Model calculations are required for the extrapolation of the data to the entire energy and reaction phase space needed to produce complete and consistent evaluated data files which are necessary for their use in transport simulations. Several model calculations of the PFNS are described here. When used to produce an evaluation, the model inputs are often tuned to improve the agreement of the calculated results with available experimental data. Reasonable *prior* model input parameters, such as the average total kinetic energy $\langle \mathrm{TKE} \rangle$, are chosen on valid physics grounds, but their final, *posterior*, values should be viewed as biased to fit the PFNS data and not as a precise determination of their values. For instance, the knowledge of $\langle \mathrm{TKE} \rangle$ is NOT improved by a fit to the PFNS data, although its calculated posterior uncertainty will be smaller than its prior value.

A. Empirical Parameterization of Two Watt Spectra

In 1999 Kornilov and coworkers proposed a new empirical formula to describe all available differential PFNS data at the time [136]. The Kornilov parametrization is based on the assumption that neutrons are emitted from heavy and light fragments at different temperatures T_i and kinetic energies E_f^i $(i = L, H)$,

$$\chi_{\scriptscriptstyle K}(E) = \frac{1}{2}[\chi_{\scriptscriptstyle W}(E, T_L, \alpha E_f^L) + \chi_{\scriptscriptstyle W}(E, T_H, \alpha E_f^H)] \; , \tag{19}$$

where $\chi_{\scriptscriptstyle W}(E, T, \alpha E_\nu)$ is the Watt distribution in Eq. (18). The coefficient α accounts for the possibility that some neutrons are emitted before the fragments are fully accelerated, thus $\alpha \leq 1$. The four initial parameters (two for each χ_W) are reduced to two fit parameters, $r = T_L/T_H$ and α, which are assumed to be uncorrelated. The remaining two parameters that define the fitting function are fixed using information from the standard ^{252}Cf(sf) spectrum [136]. The temperatures were scaled to those of ^{252}Cf(sf) by the excitation energies and mass numbers,

$$T_{L,H}^{\mathrm{x}} = T_{L,H}^{\mathrm{Cf}} \sqrt{\frac{U_{\mathrm{x}} A_{\mathrm{Cf}}}{U_{\mathrm{Cf}} A_{\mathrm{x}}}} \; , \tag{20}$$

where $U = \langle E_r \rangle + B_n + E_n - \langle \mathrm{TKE} \rangle$, $\langle E_r \rangle$ is the average energy release, E_n – the incident neutron energy, B_n – the neutron binding energy, and $\langle \mathrm{TKE} \rangle$ the average total kinetic energy of the fragments. The temperature of the heavy fragment, T_H, was fixed to a value for ^{252}Cf(sf) of $T_H = 0.8868$ MeV, with $T_L = rT_H$.

Kornilov obtained the r value for each nucleus by fitting the measured PFNS for E_n from thermal energies up to 5 MeV using Eq. (19). If r is assumed to be independent of both the fissioning nucleus and the incident neutron energy, the r values obtained in the fit can be averaged to determine an average temperature ratio, $\langle r \rangle = T_L/T_H = 1.248 \pm 0.031$. The value of a second model parameter, α, was determined by a least-squares fit to the neutron-induced data for ^{232}Th, ^{233}U, ^{235}U, ^{238}U, ^{237}Np and ^{239}Pu. A total of 26 PFNS were fit in Ref. [136]. The values of α for the individual data sets and the $\langle \alpha \rangle$s (averaged over E_n) for each fissioning nucleus can be found in Ref. [136].

The parameter uncertainties quoted in Ref. [136] are derived from a least-squares fit assuming that the model parameters are independent and that the experimental data for different E_n are uncorrelated. Both assumptions, combined with the two-parameter model, may lead to an underestimation of the PFNS uncertainties, as discussed in Sec. VI.

The Kornilov PFNS for thermal neutron-induced fission of ^{235}U is compared to existing evaluations in Fig. 11. The PFNS in the ENDF/B-VII.1 library [148] is based on the Madland and Nix model [38]. The JENDL evaluation [149] is based on a refined version of Madland and Nix including multiple fission modes [170, 171]. The Kornilov parameterization has a significantly softer spectral shape than the evaluated spectra. The average energy derived by Kornilov from the analysis of thermal neutron-induced fission of ^{235}U is 1.963 ± 0.019 MeV [136]. This difference of the PFNS $\overline{E}$ exists for a rather long time, it was already highlighted at the Working Party Subgroup 9 on International Evaluation Co-operation (WPEC SG-9) [41].

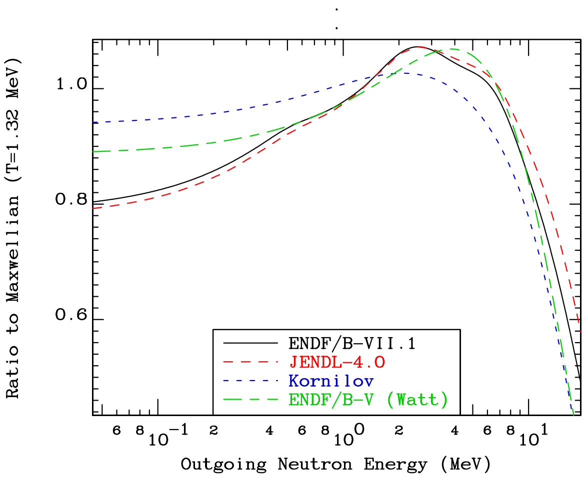

FIG. 11. (Color online) The Kornilov parametrization for thermal-neutron induced fission of ^{235}U [136] compared to the ENDF/B-VII.1 [148], JENDL-4 [149], and ENDF/B-V (Watt formula) PFNS evaluations.

B. The Los Alamos Model

The Los Alamos Model (LAM) [38] has been the workhorse behind most of the modern PFNS data evaluations, thanks in part to a limited number of model input parameters that can be adjusted to reproduce experimental PFNS data and that can be applied to all actinides and incident neutron energies up to 20 MeV (or more). The most important features and assumptions of this model are described here, as well as some of the extensions of the original model that have been implemented.

In the LAM, the prompt fission neutrons are assumed to be emitted from the fully accelerated fission fragments, following a Weisskopf statistical evaporation spectrum [150]. Taking into account the energy dependence of the cross section $\sigma(\epsilon)$ for the inverse process of compound nucleus formation through neutron capture, the center-of-mass neutron energy spectrum reads

$$\phi(\epsilon) = k(T)\,\sigma\,(\epsilon)\,\epsilon\,\exp(-\epsilon/T)\;, \tag{21}$$

where ϵ is the center-of-mass neutron kinetic energy and T is the residual nuclear temperature after neutron emission. The normalization constant $k(T)$ is given by

$$k(T) = \left(\int_0^\infty d\epsilon\,\sigma(\epsilon)\,\epsilon\,\exp(-\epsilon/T)\right)^{-1}\;. \tag{22}$$

Note that the spectrum in Eq. (21) is only valid if the residual nuclear excitation energy is much greater than zero so that the statistical arguments used in its derivation apply.

In order to calculate the average spectrum of all neutrons emitted from all fission fragments, Eq. (21) needs to be folded with a distribution of fission fragment temperatures or excitation energies. The initial total excitation energy, TXE, present in the fission fragments can be obtained from energy conservation

$$\langle \text{TXE} \rangle \;=\; \langle E_r \rangle + B_n + E_n - \langle \text{TKE} \rangle, \tag{23}$$

where $\langle E_r \rangle$ is the average energy release, B_n – the neutron separation energy for the target nucleus, E_n – the incident neutron energy, and $\langle \text{TKE} \rangle$ - the average total kinetic energy of the fragments. In the case of spontaneous fission, $E_n = 0$ and $B_n = 0$. The average energy release is the difference of ground-state nuclear masses between the compound fissioning nucleus (A_0, Z_0) and the two fission fragments:

$$\langle E_r \rangle = \langle M_n(Z_0, A_0) - M_n(Z_L, A_L) - M_n(Z_H, A_H) \rangle\,. \tag{24}$$

The average should be taken over the full mass and charge distribution of the fission fragments. In practice, only a few (at best) most representative fission fragments are considered. In the original work of Madland and Nix [38], the "seven point" approximation, in which seven pairs of fission fragments were used to calculate $\langle E_r \rangle$, was employed. The energy dependence of $\langle \text{TKE} \rangle$ was also neglected below the threshold for second-chance fission. The energy release is averaged over the few fragmentations considered.

Terrell inferred the average initial distribution of fission fragment excitation energies [14] using experimental data on fission fragment kinetic energies and neutron multiplicities. The excitation energies were used to obtain an initial temperature distribution based on the Fermi gas model which was approximated by a triangular distribution

$$P(T) = \begin{cases} 2T/T_m^2, & T \le T_m \\ 0, & T > T_m \end{cases} . \tag{25}$$

The maximum temperature T_m is given by

$$T_m = \sqrt{\frac{\langle \mathrm{TXE} \rangle}{\langle a \rangle}}, \tag{26}$$

where $\langle a \rangle$ is the average level density parameter for the fragments and $\langle \mathrm{TXE} \rangle$ is the average total excitation energy given by Eq. (23). The original LAM [38] assumes that the same temperature distribution $P(T)$ is valid for both light and heavy fragments, and that $T_m^L = T_m^H = T_m$. As a further simplification, Ref. [38] used a linear relation between $\langle a \rangle$ and the mass of the fissioning nucleus, A,

$$\langle a \rangle = \frac{A}{11\,\mathrm{MeV}} . \tag{27}$$

While the relation $\langle a \rangle = A/(8\,\mathrm{MeV})$ would better represent the empirical $\langle a \rangle$ for most nuclei, Eq. (27) is a better choice for nuclei near shell closure where the fission fragment distributions peak. The value of 11 MeV, even though not quite justified by comparison with the empirical values of $\langle a \rangle$ alone, was proposed [38] to improve the PFNS when using an energy-dependent compound nucleus cross section, $\sigma(\epsilon)$, in Eqs. (21) and (22). Note that the `PbP` model, described in Sec. IV C provides values close to 11 MeV as well.

The neutron energy spectrum in the center-of-mass frame can be readily obtained by folding Eq. (21) over the temperature distribution in Eq. (25),

$$\phi(\epsilon) = \frac{2\sigma(\epsilon)\epsilon}{T_m^2} \int_0^{T_m} dT\, k(T)\, T \, \exp(-\epsilon/T) . \tag{28}$$

To obtain the neutron energy spectrum in the laboratory frame, the center-of-mass energy spectrum in Eq. (28) is integrated over ϵ. The limits on the integration take into account the boost due to the kinetic energy per nucleon of the fragment, E_f, so that $\epsilon_\pm = (\sqrt{E} \pm \sqrt{E_f})^2$. If the neutrons are emitted isotropically in the center-of-mass frame of the mother fission fragment, the neutron energy spectrum in the laboratory frame becomes [14]

$$N(E, E_f) = \frac{1}{4\sqrt{E_f}} \int_{\epsilon_-}^{\epsilon_+} d\epsilon \frac{\phi(\epsilon)}{\sqrt{\epsilon}} . \tag{29}$$

For the most probable fragmentation, E_f is readily obtained from momentum conservation,

$$E_f^L = \frac{A_H}{A_L}\frac{\mathrm{TKE}}{A_0} \qquad E_f^H = \frac{A_L}{A_H}\frac{\mathrm{TKE}}{A_0} . \tag{30}$$

The average PFNS in the laboratory frame for neutrons emitted from both fragments is then simply the average of the neutron spectra for the light and heavy fragments,

$$N(E) = \frac{1}{2}\left[N(E, E_f^L) + N(E, E_f^H)\right] . \tag{31}$$

Eqs. (29) and (31) represent the final results of the original LAM. In Ref. [38], the authors studied the influence of the choice of various input parameters on the predicted PFNS. Subsequent papers and studies used this formalism and improved input parameters to produce prompt fission neutron spectra for evaluated libraries, based on available experimental PFNS data.

The average prompt neutron multiplicity in the LAM is calculated by conservation of total excitation energy. One can write

$$\overline{\nu} = \frac{\langle \mathrm{TXE} \rangle - \langle E_\gamma^{\mathrm{tot}} \rangle}{\langle \epsilon_n \rangle + \langle S_n \rangle} , \tag{32}$$

where $\langle E_\gamma^{\rm tot}\rangle$ is the average total energy carried away by prompt photon emission. The average neutron separation energy, $\langle S_n\rangle$, is half the two-neutron separation energy, $\langle S_{2n}\rangle$, averaging over pairing corrections.

Equation (31) implicitly assumes that the same average number of neutrons is emitted from the two fragments. This assumption is consistent with the main feature of the LAM, considering only a single, most probable, fragmentation. The idea of equal neutron multiplicities from both fragments in the most probable fragmentation is supported by the systematic behavior of measured $\overline{\nu}(A)$. All experimental $\overline{\nu}(A)$ data from thermal and low-energy neutron-induced fission of actinides show equal numbers of neutrons emitted by complementary fragments with $A_H \approx 140$, thus the most probable fragmentation is at $A_H \approx 140$. More details about the systematic behavior of the experimental multiplicity ratio $\overline{\nu}_H/(\overline{\nu}_L + \overline{\nu}_H)$ as a function of A_H (initially mentioned by Wahl [151] for ^{233,235}U($n_{\rm th}$,f) and ^{239}Pu($n_{\rm th}$,f)) can be found in Ref. [152].

Over the years, some of the early approximations of the LAM have been removed to better describe the measured average PFNS. The modifications are discussed in turn in the remainder of this section. Each LAM assumption is given at the beginning of each separate discussion, followed by what has been done to make the model less restrictive.

a. Equal fragment temperature. All versions of the LAM use the Weisskopf spectrum as given in Eq. (21). However, the assumption that the temperatures are equal in both fragments at the time of neutron emission has been relaxed. The intrinsic temperatures, or equivalently, level densities in each partner fragment, are not necessarily equal. In fact, near their ground-state configuration, those nuclear level densities could differ significantly, with the light fragment being on average hotter than its heavy counterpart. The extra deformation energy brought in once the neck has snapped, as well as strong shell corrections impacting some of these fragments, may complicate this simple picture. In particular, experimental data on the average prompt neutron multiplicity as a function of the fragment mass, $\overline{\nu}(A)$, can only be reproduced if the assumption of thermal equilibrium between the fragments is lifted (see Secs. IV C and V).

b. Triangular fragment temperature distribution. Terrell [14] adopted a triangular distribution of temperatures, Eq. (25) to best match the experimental data on fission fragment kinetic energies and neutron multiplicity. In fact, the sharp cutoff of the high excitation energy tail imposed by this distribution would tend to soften the high energy tail of the predicted PFNS. This trend is somewhat compensated by the too-hard tail of the PFNS predicted by the Weisskopf spectrum, see Eq. (21). For the highest neutron energies, this equation should fail due to a too small number of final levels available. A somewhat more flexible formula was introduced in Ref. [153] but its impact on the final computed spectrum is small.

c. Equal fragment neutron multiplicities. Eq. (31) implicitly assumes that the average neutron multiplicity is the same for the light and heavy fragments. However, the experimental evidence supports $\overline{\nu}_L \neq \overline{\nu}_H$. A slightly more general formula for the PFNS is

$$N(E) = \frac{\overline{\nu}_L N(E, E_f^L) + \overline{\nu}_H N(E, E_f^H)}{\overline{\nu}_L + \overline{\nu}_H} \ . \tag{33}$$

d. Isotropic neutron emission. The transformation of the neutron energy spectrum from the center-of-mass frame to the laboratory frame, Eq. (29), assumes that all neutrons are emitted isotropically from fully accelerated fragments. Two physics processes, missing from the original LAM, could cause this assumption to fail. If the fragments have a relatively large initial average angular momentum, they would emit neutrons preferentially in a plane perpendicular to the direction of their spin. If neutrons were emitted before the fragments reach their full acceleration, e.g., near the scission point, emission in the center-of-mass frame could be anisotropic. Assuming that the anisotropic component of neutron emission can be described by

$$\phi(\epsilon, \theta) = \phi(\epsilon)(1 + b\cos^2\theta)/(1 + b/3), \tag{34}$$

where ϵ and θ are given in the center-of-mass frame of the fragments and b is a parameter describing the degree of anisotropy, the PFNS in the laboratory frame becomes [14]

$$N(E) = \int_{\epsilon_-}^{\epsilon_+} d\epsilon \frac{\phi(\epsilon)\left[1 + b(E - \epsilon - E_f)^2/(4\epsilon E_f)\right]}{4\left(\epsilon E_f\right)^{1/2}(1 + b/3)} \ . \tag{35}$$

If $b = 0$, Eq. (35) reduces to Eq. (29). For $b > 0$, the calculated laboratory spectrum becomes softer than the isotropic case with $b = 0$.

e. Equilibrium pre-fission neutron emission. At higher incident neutron energies, e.g., $E_n \geq 5 - 6$ MeV, multi-chance fission, in which one or more neutrons are evaporated from the fissioning nucleus prior to scission, may occur. In the original LAM the pre-fission neutron emission spectra ($\phi(\epsilon)$)) were assumed to be equilibrium only. This assumption is valid only below about 10 MeV of neutron incident energy. At higher energies, pre-equilibrium emission, where the incident neutron does not equilibrate with the target nucleus, is also possible. The total fission probability is then a sum over all possible fissions along this chain,

$$\begin{aligned} P_f &= P(n,\mathrm{f}) + P(n,n'\mathrm{f}) + P(n,2n\mathrm{f}) + ... \\ &= P_{f_1} + P_{f_2} + P_{f_3} + ... \,, \end{aligned} \tag{36}$$

where P_{f_i} is the i^{th}-chance fission probability. In the original LAM, this possibility was taken into account without also accounting for any concurrent change in the spectral shapes due to pre-fission neutron emission.

With first chance fission, $i = 1$, the excitation energy, E_{x_i}, is exact,

$$E_{x_1} = E_n + B_n(A_0, Z_0) \; . \tag{37}$$

The average excitation energies of the next nuclei in this chain, $i = 2, 3, .., N$, are:

$$\langle E_{x_i} \rangle = \langle E_{x_{i-1}} \rangle - S_n(A_0 - i + 2, Z_0) - \langle \epsilon_n \rangle_{i-1} \;, \tag{38}$$

where $\langle \epsilon_n \rangle_j$ is the average energy of the j^{th} neutron evaporated prior to fission, with $j = 1, 2, ..., N - 1$.

The total average PFNS is then

$$N(E) = \frac{\sum_{i=1}^{N} P_{f_i} \left[\sum_{j=1}^{i-1} \phi_j(E) + \overline{\nu}_i N_i(E) \right]}{\sum_i P_{f_i} (i - 1 + \overline{\nu}_i)} \; . \tag{39}$$

In Eq. (39), $\phi_j(E)$ is the energy distribution of the neutrons emitted in the j^{th}-chance fission from both evaporation and pre-equilibrium emission. Below E_n~10 MeV, only evaporated neutrons contribute. At higher energies, pre-equilibrium effects, which impact the predicted spectral shape as well as the neutron angular distributions, have to be taken into account. Note also that $\overline{\nu}_i$ is the average multiplicity of prompt neutrons emitted by the fission fragments in i^{th}-chance fission, given by Eq. (32).

Many works have been published by Russian researchers showing the impact of pre-fission neutrons above the emissive fission threshold [96, 105, 154–156], as well as the associated reduction in the PFNS average energy; this reduction was also observed for ^{235,238}U neutron induced fission by Ethvignot et al. [157]. Pre-fission neutrons begin to be apparent in the PFNS above the second-chance threshold (E_n~6–7 MeV for ^{238}U(n,f)). Since the excitation energy of the residual nucleus left after neutron emission is too low to undergo fission, neglecting tunneling through the barrier, the PFNS has an endpoint at $E_n - B_f$, being B_f the corresponding fission barrier. Above this energy, the residual nucleus can decay only through a capture cascade. More recent LAM calculations at 7 MeV, above the $(n, n'\mathrm{f})$ threshold, taking the pre-fission emission into account, are compared with experimental data for ^{238}U(n,f) [50] in Fig. 12. The modified LAM results, in blue, describe the soft neutron peak in the data below 1 MeV reasonably well. These additional low energy neutrons come from the $(n, n'\mathrm{f})$ reaction. Note that the ENDF/B-VII.1 evaluation did not include the endpoint of the integration of the inelastic spectra at $E_n - B_f$ so that there is no observed enhancement at the same energy. This omission has been corrected and will be included in future releases of the ENDF/B library.

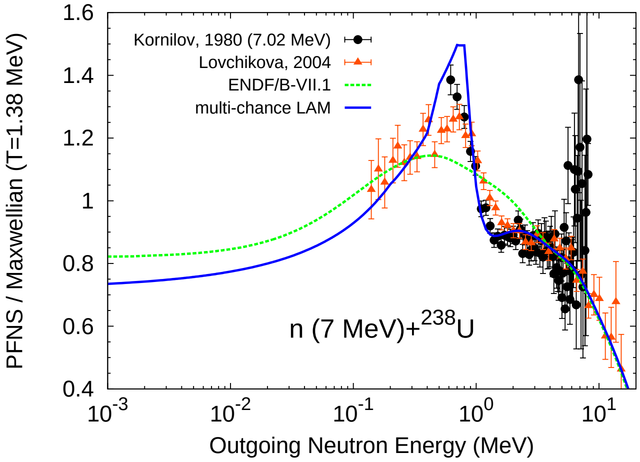

FIG. 12. (Color online) LAM PFNS calculations for ^{238}U(n,f) at $E_n = 7$ MeV (blue) compared with data from EXFOR (symbols) and the ENDF/B-VII.1 evaluation (green).

The pre-equilibrium effects begin to be apparent in the PFNS above incident neutron energies E_n~10 MeV. As the pre-equilibrium neutron spectrum is much harder than the equilibrium one (i.e., more high-energy neutrons are

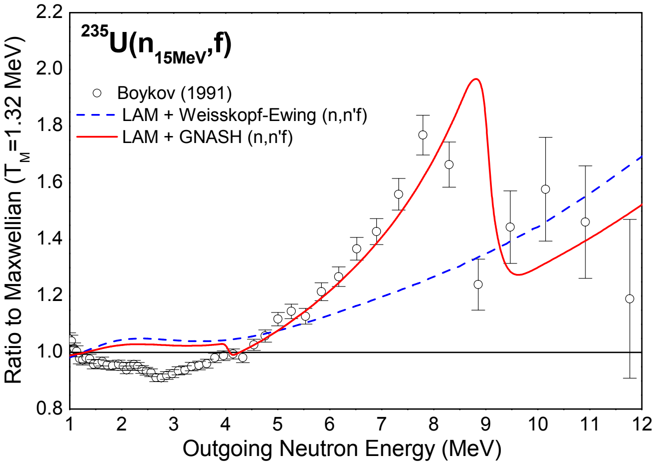

FIG. 13. (Color online) LAM PFNS calculations for $E_n = 15$ MeV ^{235}U(n,f) (red line) compared with data (symbols) and the ENDF/B-VII.1 evaluation (dashed).

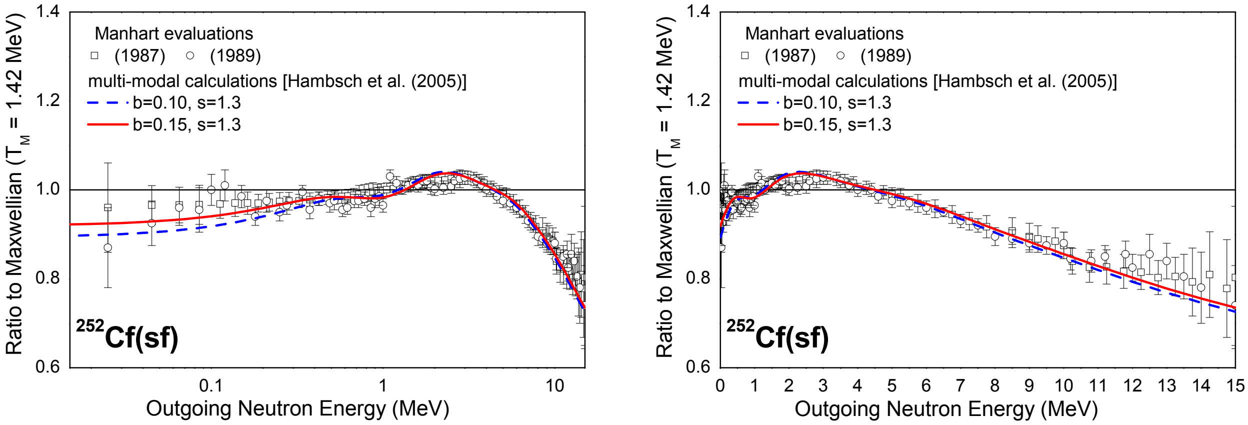

FIG. 14. (Color online) A LAM multi-modal calculation of the ^{252}Cf(sf) PFNS. The results are given as ratios to a Maxwellian and compared to the Mannhart evaluation [36]. The PFNS calculations employed the expression for $P(T)$ in Ref. [153] with $s = 1.3$ with two values of the anisotropy parameter, $b = 0.1$ (dashed blue line) and $b = 0.15$ (solid red line). The left panel is on a log scale to highlight low emission energies while the right panel highlights higher energies with a linear energy scale.

emitted), an enhancement of the PFNS is expected at energies of the $(n, n'\text{f})$ reaction close to $E_n - B_f$. Such effect can be seen for ^{235}U(n,f) PFNS with $E_n = 15$ MeV ($E_n - B_f \approx 9$ MeV), as demonstrated in Fig. 13. The data [78] are compared to the LAM calculations of Ref. [158], shown in red. The increase in neutron yield observed in the PFNS near 8–9 MeV due to the pre-equilibrium effects is nicely reproduced by the calculations that consider a proper pre-equilibrium neutron spectrum (LAM+GNASH code), while those obtained using a Weisskopf-Ewing equilibrium spectrum fail. The undertaken studies indicate that including pre-fission neutron emission with a proper consideration of the pre-equilibrium emission works well up to E_n∼20–25 MeV [159]. At higher energies, fission following charged particle emission becomes important and prompt neutron emission resulting from fission of these nuclei should be considered. The charged particles emitted are dominantly protons for E_n up to 50 MeV since the Coulomb barrier in the outgoing channel hinders emission of heavier particles.

If a chain of pre-fission neutron emission is considered to be the main nucleus chain, as in the original LAM in Eq. (36), secondary nucleus chains associated with charged particle emission followed by neutron emissions, must be included. The extension of the LAM to these higher energies and secondary fission chains was addressed by the University of Bucharest [159]. For $E_n > 50$ MeV, other chains and emission of heavier charged particles such as deuterons and alpha particles become important, see Ref. [159]. A study of fission in n+^{237}Np for E_n up to 40 MeV from the main and first secondary chains can be found in Ref. [160].

f. Single "most probable" fragmentation. In the original LAM, the most probable fragmentation, with A_H∼140, and, consequently equal neutron multiplicities from the complementary fragments, was considered. However, the fissioning nucleus can take several paths, or modes, to reach its final pre-scission configuration of two pre-formed fragments connected by an elongated neck. If the nucleus stretches further beyond its pre-scission shape, the neck will rupture at a random point along its neck. This multi-modal random neck rupture (MM-RNR) model was developed

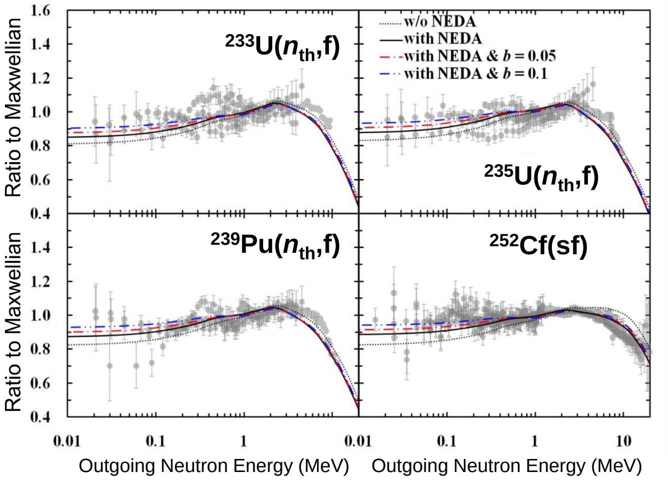

FIG. 15. (Color online) PFNS calculations [174, 175] with and without NEDA, and including different degrees of anisotropy parameter are given as ratios to a Maxwellian $T = 1.32$ MeV for ^{233,235}U($n_{\rm th}$,f), $T = 1.38$ MeV for ^{239}Pu($n_{\rm th}$,f), and $T = 1.42$ MeV for ^{252}Cf(sf). The data, shown in grey, are given in [175].

by Brosa et al. [161] in the eighties.

For most actinides the experimental $Y(A, \mathrm{TKE})$ distributions of fission fragments can be well reproduced by considering three dominant fission modes: the asymmetric standard I (S1) and standard II (S2) modes and the symmetric super-long mode (SL). The asymmetric modes, S1 and S2, are generally thought to be linked with the neutron shells in the fission fragments: the $N = 82$ spherical shell for S1 and the $N = 88$ deformed shell for S2. The three mode formulation gives a good description of the fragment distributions for ^{238}U(n,f) with $0.9 \leq E_n \leq 5.8 MeV$ [162, 163]; ^{237}Np(n,f) with $0.5 \leq E_n \leq 5.5$ MeV [164]; and ^{235}U(n,f) with E_n from thermal to 5.5 MeV [165]. For some spontaneously fissioning systems, such as ^{236,238,240,242,244}Pu(sf) [166–168], the SL mode is negligible. Sometimes more than three fission modes have been required, four for ^{237}Np(n,f) [169] and five for ^{252}Cf(sf) [153].

It should be noted that the same experimental fragment distribution can be described by different sets of multi-modal data, i.e., there is no unique solution. However, each mode corresponds to a distinct class of pre-scission shapes which indirectly convey information about the fission fragment properties: an asymmetric shape gives rise to an asymmetric mass division; a very compact shape (as for S1) leads to a high TKE; and a symmetric mass split with a long neck, as for the SL mode, leads to a low TKE. For most neutron-induced fission below the threshold for second chance fission, the S2 mode is dominant while the SL mode is negligible. The S1 mode branching ratio decreases with E_n while the S2 and SL modes increase relative to S1. Thus, a gradual transition from asymmetric to symmetric fission is typically observed.

The multi-modal fission model can be used to extend the original LAM calculations, by considering a most probable fragmentation for each mode. The total average multiplicity and PFNS are then the superposition of the modal average multiplicities and spectra weighted with the modal branching ratios,

$$\overline{\nu} = \sum_m w_m \overline{\nu}_m \, , \tag{40}$$

$$N(E) = \sum_m w_m N_m(E) \, , \tag{41}$$

where m are the fission modes and w_m are the modal branching ratios which satisfy $\sum_m w_m \equiv 1$. The average prompt neutron multiplicity $\overline{\nu}_m$ and PFNS $N_m(E)$ corresponding to each fission mode are calculated according to the LAM expressions. Equation (33) thus becomes

$$N(E) = \frac{\overline{\nu}_{L,m} N_m(E, E_f^L) + \overline{\nu}_{H,m} N_m(E, E_f^H)}{\overline{\nu}_{L,m} + \overline{\nu}_{H.m}} \, . \tag{42}$$

In addition to the modal branching ratios, modal values of quantities such as the energy release, $\langle E_r \rangle_m$, and the level density parameter, $\langle a \rangle_m$, are required.

Over the last 15 years, this concept has been used extensively for modeling the PFNS, such as the work of Ohsawa et al. [170, 171] in the JENDL libraries (e.g., see JENDL-4 [149]) and the Bucharest and JRC-IRMM team [153, 165, 172, 173].

In Fig. 14, an example of the PFNS obtained with a multi-modal implementation of the LAM for ^{252}Cf(sf) employing a more flexible form of the residual temperature distribution $P(T)$ (with parameter s), and allowing for anisotropic emission (with parameter b from Eq. (35)) is shown. The results, compared to the point-wise Mannhart evaluation [36], describe the data well.

g. Neutron emission from fully accelerated fragments. The multi-modal LAM formulation explained previously was used recently to study possible prompt Neutron Emission During fragment Acceleration (NEDA) [174, 175]. To examine the NEDA effect, it is necessary to analyze the competition between neutron emission from excited fragments and Coulomb acceleration of the fission fragments.

Neutron emission from excited fragments can be described in terms of the average lifetime τ_k of the $k^{\rm th}$ emitted neutron in the Ericson formula [176]. On the other hand, the point-charge model [177] holds between the acceleration time, $t_{\rm acc}$, after scission and the relative acceleration given by the fragment kinetic energy ratio $\chi = {\rm KE}/{\rm KE}_{\rm final}$,

$$t_{\rm acc} = \frac{l}{v_{\rm fin}}\left[\frac{\sqrt{\chi}}{1-\chi} + \frac{1}{2}\ln\frac{1+\sqrt{\chi}}{1-\sqrt{\chi}}\right] \; . \tag{43}$$

Here $v_{\rm fin}$ is the final fragment velocity and l is the charge-center distance at scission, given by $l = Z_L Z_H e^2/{\rm TKE}$, taking fluctuations of TKE into account. The quantity l is sampled randomly based on the TKE distribution. The probability of emitting the first neutron at the time t after scission is $P(t) = 1 - \exp(-t/\tau)$. Using Eq. (43), the probability $P(\chi)$ for neutron emission at the moment of relative acceleration χ is

$$P(\chi) = 1 - \exp\left\{-\frac{l}{\tau v_{\rm fin}}\left[\frac{\sqrt{\chi}}{1-\chi} + \frac{1}{2}\ln\frac{1+\sqrt{\chi}}{1-\sqrt{\chi}}\right]\right\} \; . \tag{44}$$

The PFNS including NEDA is obtained by integrating the total PFNS in the multi-modal LAM over $P(\chi)$,

$$\langle N(E, E_f, T_m)\rangle = \int_0^1 d\chi \, N(E, \chi E_f, T_m)\, P(\chi) \; . \tag{45}$$

In Ref. [175] the multi-modal PFNS in Eq. (45) is calculated taking the neutron-emission anisotropy into account, as discussed in Refs. [153, 178]. Some fraction of the neutrons were seen to be emitted before full acceleration. The probability for NEDA was ∼10% for ^{235}U($n_{\rm th}$,f) and ∼16% for ^{252}Cf(sf). The probability is larger for ^{252}Cf because of its greater fission Q value. Considering NEDA enhanced the low-energy part of the PFNS ($E < 1$ MeV) while reducing the high-energy part ($E > 3$ MeV) because neutrons emitted during the acceleration phase are less boosted in energy due to this effect.

The calculated PFNS relative to a Maxwellian are shown in Fig. 15. Including both NEDA and finite values of the anisotropy parameter b improve the description, especially for low energy neutrons.

1. *Input Model Parameters for Los Alamos Model*

An advantage of using the LAM for calculating the PFNS is that the model contains very few adjustable parameters. The most important are the average total kinetic energy of the fission fragment $\langle TKE\rangle$, the average energy release $\langle E_r\rangle$, and the average level density parameter $\langle a\rangle$. By providing two more parameters, the average neutron separation energy of the fission fragments $\langle S_n\rangle$ and the average total energy carried away through gamma-ray emission $\langle E_\gamma\rangle$, the average prompt fission neutron multiplicity $\langle\overline{\nu}\rangle$ can also be inferred. These parameters have been evaluated systematically by Tudora [179] for the following actinides: $^{226-232}$Th, $^{224-233}$Pa, $^{229-238}$U, $^{231-237}$Np, $^{234-242}$Pu, and $^{240-245}$Am. Some updates to the systematics are provided in this paper in Sec. VII. Interested readers are referred to the original publication.

2. *CEA/DAM Los Alamos Model Calculations of ^{235}U and ^{239}Pu PFNS*

Here a modified LAM calculation [172] of the ^{235}U($n_{\rm th}$,f) PFNS performed at CEA/DAM using the systematics of Ref. [179] is presented. The partial fission cross sections, needed to calculate the (n, xnf) contribution, were taken from reaction model calculations [180] using the TALYS code [181]. The Weisskopf evaporation spectra are replaced by the TALYS spectra used in JEFF-3.2, as originally suggested by Maslov [155, 156].

It was quite challenging to reproduce the data with this version of the LAM [172], as shown in Fig. 16. The calculations are compared to the combined NIIAR data [30–32], given as a ratio to a Maxwellian with $T = 1.32$ MeV. The blue curve has a very different shape from the data. The calculated spectrum is too hard and it agrees with data only between 0.5 and 1.5 MeV. Changing the parameters of the LAM did not soften the spectra. A softer spectrum was produced by using an ad hoc method of assigning different weights to the individual distributions of the light and heavy fragments, also shown in Fig. 16. The red curve in the figure is the result of applying the weights 0.7 and 1.3 to the light and heavy fragment spectra, respectively.

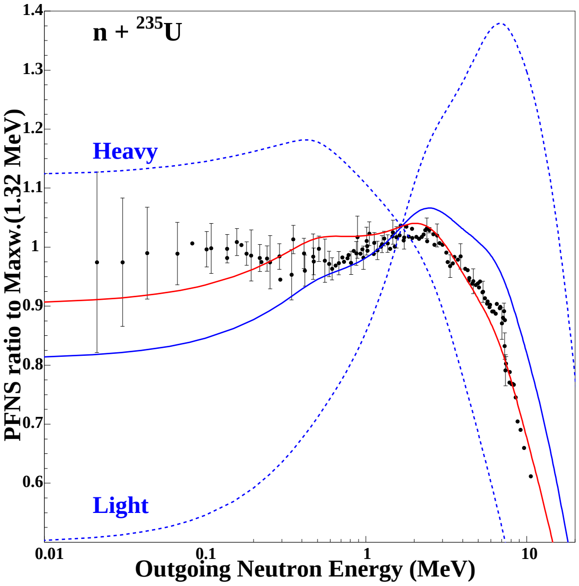

FIG. 16. (Color online) The ratio of the calculated ^{235}U(n_{th},f) PFNS to a Maxwellian. The unweighted spectrum is given by the solid blue curve while the light and heavy fragment contributions are shown in the blue dashed curves. The red curve is produced from the combined light and heavy spectra, weighted by 0.7 and 1.3 respectively. The NIIAR experimental data are shown [30–32].

C. The Point-by-Point Model

The Point-by-Point (`PbP`) model was developed at the University of Bucharest. The primary results of this model are "multi-parametric matrices" of different quantities as a function of fragment mass and charge, A and Z, and as a function of total kinetic energy, TKE, generically labeled $q(A, Z, \text{TKE})$. They are related to both the fission fragments and prompt neutron and photon emission, and they include, e.g., the total excitation energy at full acceleration, $\text{TXE}(A, Z, \text{TKE})$; the fragment level density parameter, $a(A, Z, \text{TKE})$; the average neutron separation energy, $\langle S_n \rangle(A, Z, \text{TKE})$; the prompt neutron multiplicity, $\overline{\nu}(A, Z, \text{TKE})$; the PFNS $N(A, Z, \text{TKE}, E)$; and the prompt photon energy, $E_\gamma(A, Z, \text{TKE})$. They are independent of the fragment yields $Y(A, Z, \text{TKE})$. The matrices $q(A, Z, \text{TKE})$ require input data such as mass excess, deformation parameters, and shell corrections [182] and optical model parameterizations [183]), usually taken from RIPL-3 input parameter library [184].

1. *The Fragmentation Range of the* `PbP` *Treatment*

In the `PbP` treatment, the choice of fission fragments plays a crucial role. The range of fission fragments is constructed following Refs. [187–192].

The A range consists of mass pairs (A_L, A_H), covering a wide range from symmetric fission up to very asymmetric splits. For each A, between two and five integer values of Z are chosen, centered around the most probable charge Z_p, defined as the unchanged charge distribution (UCD) corrected with the charge deviation (polarization) ΔZ,

$$Z_p(A) = Z_{\text{UCD}}(A) + \Delta Z(A) \ . \tag{46}$$

Both the A and Z distributions are taken in integer steps of one unit of mass or charge.

Because the charge distribution is narrow for any fixed A [193], the usual `PbP` treatment considers three values of Z for each A to be sufficient. When available, experimental data are used for ΔZ: ^{233,235}U(n_{th},f); ^{239}Pu(n_{th},f); and ^{252}Cf(sf) [188]. When no ΔZ data are available, Wahl's systematics for Z_p can be used [151] with appropriate parameters, see Ref. [187], and $\Delta Z = \pm 0.5$ (+ for light fragments and − for heavy fragments) is a good approximation.

The TKE values in the "multi-parametric matrices" cover a convenient range (e.g., from 100 MeV to 200 MeV) in steps of 5 MeV.

Prompt emission calculations are made for each value of A, Z and TKE.

2. *Partition of Total Excitation Energy Between Complementary, Fully-accelerated Fragments*

To calculate the matrices for prompt emission, $q(A, Z, \mathrm{TKE})$, the excitation energies of the complementary fully-accelerated fragments, $E^*_{L,H}$, are needed. The partition of the total excitation energy at full acceleration, $\mathrm{TXE} = E^*_L + E^*_H$, is obtained from modeling the system at scission, as described in Ref. [194]. Alternatively, parameterizations based on the systematic behavior of the measured ratio, $\overline{\nu}_H/(\overline{\nu}_L + \overline{\nu}_H)$, as a function of A_H may be employed, as described in Ref. [152].

For each pair of fragments selected as described in the previous section, TXE is defined as $\mathrm{TXE} = E_r + E_n + B_n - \mathrm{TKE}$ where E_r is the energy release, Q-value, calculated using the Audi et al. mass Tables [182], E_n is the incident neutron energy and B_n is the neutron binding energy. For spontaneous fission, $E_n = 0$ and $B_n = 0$.

At scission, for each pair of nascent fragments,

$$E_r + E_n + B_n = E_{\mathrm{pre}} + E_{\mathrm{Coul}} + E^*_{\mathrm{sc}} + E^L_{\mathrm{def}} + E^H_{\mathrm{def}} \ , \tag{47}$$

where E_{pre} and E_{Coul} are the pre-scission kinetic energy and the Coulomb repulsion between the nascent fragments and E^*_{sc} is the available excitation energy at scission. At full acceleration $E_{\mathrm{pre}} + E_{\mathrm{Coul}} = \mathrm{TKE}$ and

$$\mathrm{TXE} = E^*_{\mathrm{sc}} + \Delta E^L_{\mathrm{def}} + \Delta E^H_{\mathrm{def}} \ . \tag{48}$$

Here $\Delta E^{L,H}_{\mathrm{def}}$, "extra-deformation energies", are the difference between the absolute deformation energy of fragments at scission and at full acceleration. They are determined from the liquid drop model including shell corrections [194, 195].

After subtracting the extra-deformation energies from TXE, E^*_{sc} is shared between the complementary fragments, $E^*_{\mathrm{sc}} = E^L_{\mathrm{sc}} + E^H_{\mathrm{sc}}$, assuming statistical equilibrium at scission with a Fermi-gas description of fragment level densities, according to the ratio

$$\frac{E^L_{\mathrm{sc}}}{E^H_{\mathrm{sc}}} = \frac{a^L_{\mathrm{sc}}}{a^H_{\mathrm{sc}}} \equiv \frac{a_{\mathrm{sc}}(A_L, Z_L, \mathrm{TKE})}{a_{\mathrm{sc}}(A_H, Z_H, \mathrm{TKE})} \ , \tag{49}$$

where $a^{L,H}_{\mathrm{sc}}$ are effective level density parameters accounting for collective and intrinsic/single-particle excitation, see Ref. [194]. The values of the excitation energy at scission $E^{L,H}_{\mathrm{sc}}$ and the level density parameters at scission $a^{L,H}_{\mathrm{sc}}$ are obtained simultaneously by an iterative procedure according to Eq. (49).

The level density parameter of each fission fragment at scission with atomic and mass numbers equal to Z_i and A_i, respectively, and excitation energy E_{sc} is given by the generalized super-fluid model [196]

$$a_{\mathrm{sc}} = \begin{cases} \tilde{a}(A_i)(1 + f(A_i, Z_i, U_i)) & E_{\mathrm{sc}} \geq E_{\mathrm{cr}} \\ a_{\mathrm{cr}} & E_{\mathrm{sc}} < E_{\mathrm{cr}} \end{cases} \ , \tag{50}$$

where $i = L, H$, $U = E_{\mathrm{sc}} - E_{\mathrm{cond}}$, $f(A, Z, U) = (\delta W(A, Z)/U)[1 - \exp(-\gamma(A)U]$. The Eq. (50) is also applied at full acceleration to obtain the level density parameter of a fragment with excitation energy E^*, needed in prompt emission calculations. The critical energy E_{cr} is the point where the phase transition between superfluid and normal states occurs. The values of E_{cr} and a_{cr} are calculated iteratively using Eqs. (50) and $E_{\mathrm{cr}} = a_{\mathrm{cr}}\ T^2_{\mathrm{cr}}$. The critical temperature $T_{\mathrm{cr}} = 0.567\Delta$, where $\Delta = 12/\sqrt{A}$ is the pairing correlation function and $n = 0, 1, 2$ for even-even, odd and odd-odd nuclei, respectively. The condensation energy is $E_{\mathrm{cond}} = 3a_{\mathrm{cr}}\ \Delta^2/2\pi^2 - n\Delta$. Finally, δW is the shell correction, $\tilde{a}(A) = 0.073A + 0.115A^{2/3}$ is the asymptotic value of the level density parameter, and $\gamma(A) = 0.4A^{-1/3}$ is related to the damping of shell effects. Different values of $\delta W(A, Z)$ and level density parameters can be found [182]. `PbP` calculations generally employ $\tilde{a}(A)$ [196, 197] with the Möller et al. shell corrections [198]. The excitation energies of complementary fully accelerated fragments are the sum of the extra-deformation and excitation energies at scission,

$$E^*_{L,H} = \Delta E^{L,H}_{\mathrm{def}} + E^{L,H}_{\mathrm{sc}} \ . \tag{51}$$

It is interesting to note that the shape of the ratio E^*_H/TXE as a function of A_H obtained by the energy sharing outlined here is similar to the ratio $\overline{\nu}_H/(\overline{\nu}_L + \overline{\nu}_H)$ from $\overline{\nu}(A)$ data. At low and moderate E_n the ratio is less than 0.5 for $A_H < 140$, with a minimum at $A_H{\sim}130$ due to filled shells at $N = 82$ and/or $Z = 50$. At $A_H{\sim}140$ the ratio is $\sim$0.5 and it increases nearly linearly for $A_H > 140$, see Ref. [152].

3. *Prompt Emission from Individual Fragments*

The `PbP` model of neutron emission generally follows that of the LAM in Sec. IV B. It employs compound nucleus cross sections obtained from optical model calculations using the code SCAT2 [199] with spherical optical model parameterizations [183]. In addition to the triangular $P(T)$ distribution of the original LAM, the form proposed in Ref. [153] with parameter $s \geq 1$ and numerical functions obtained from a rigorous treatment of sequential emission can also be used. Anisotropic neutron emission is taken into account as in Eq. (35). Since the `PbP` model does not assume equal neutron emission from the two fragments, the total PFNS is calculated according to Eq. (33). The average prompt neutron multiplicity is obtained from

$$\mathrm{TXE} = \overline{\nu}(\langle\varepsilon\rangle + \langle S_n\rangle) + \langle E_\gamma\rangle\,, \tag{52}$$

where $\langle\varepsilon\rangle$ is the average neutron kinetic energy in the center of mass, $\langle E_\gamma\rangle$ is the average prompt photon energy and $\langle S_n\rangle$ is the average neutron separation energy of complementary fission fragments.

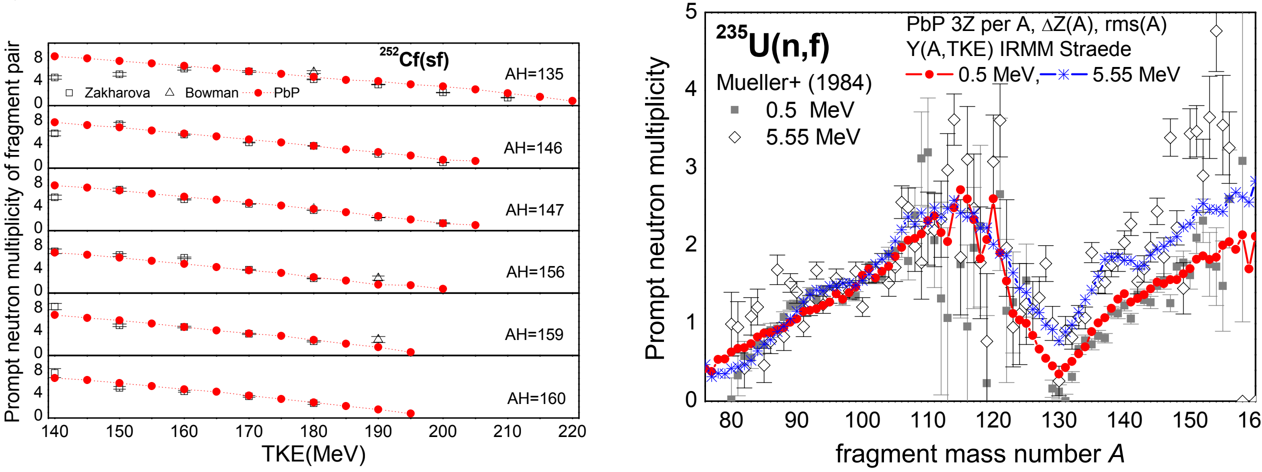

(a) Prompt neutron multiplicity as a function of TKE for given values of A_H, compared to data [204, 205]. The `PbP` points are the solid red circles.

(b) The `PbP` calculation of $\overline{\nu}(A)$ for ^{235}U(n,f) at $E_n = 0.5$ MeV (red circles) and $E_n = 5.55$ MeV (blue stars) compared to data [206].

FIG. 17. (Color online) The data are given by the open symbols for ^{252}Cf(sf) (left) and ^{235}U(n,f) (right).

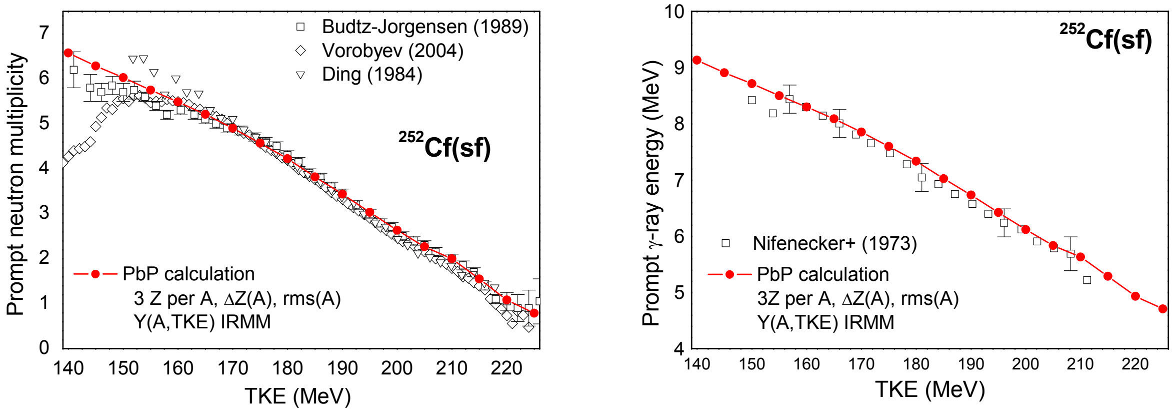

(a) $\overline{\nu}$(TKE) calculated by the `PbP` model compared to experimental data from Refs. [207–209].

(b) E_γ(TKE) calculated by the `PbP` model compared to experimental data [210].

FIG. 18. (Color online) The `PbP` model calculations for ^{252}Cf(sf) PFNS.

The average neutron separation energy of each fragment is calculated by an iterative procedure accounting for sequential emission. If the excitation energy of a fully accelerated fragment exceeds the neutron separation energy $S_n(A, Z)$ of the fragment, a neutron can be evaporated (in competition with photon emission). If the excitation energy of the residual fragment exceeds its separation energy, a second neutron can be evaporated, etc. A total of k neutrons can be emitted when the excitation energy of the $(k-1)^{\mathrm{th}}$ residual nucleus is less than $S_n(A-k, Z)$. The average neutron separation energy is then

$$\langle S_n\rangle(A, Z) = \frac{1}{k}\sum_{i=0}^{k-1} S_n(A-i, Z) = \frac{1}{k} S_{kn}(A, Z)\,. \tag{53}$$

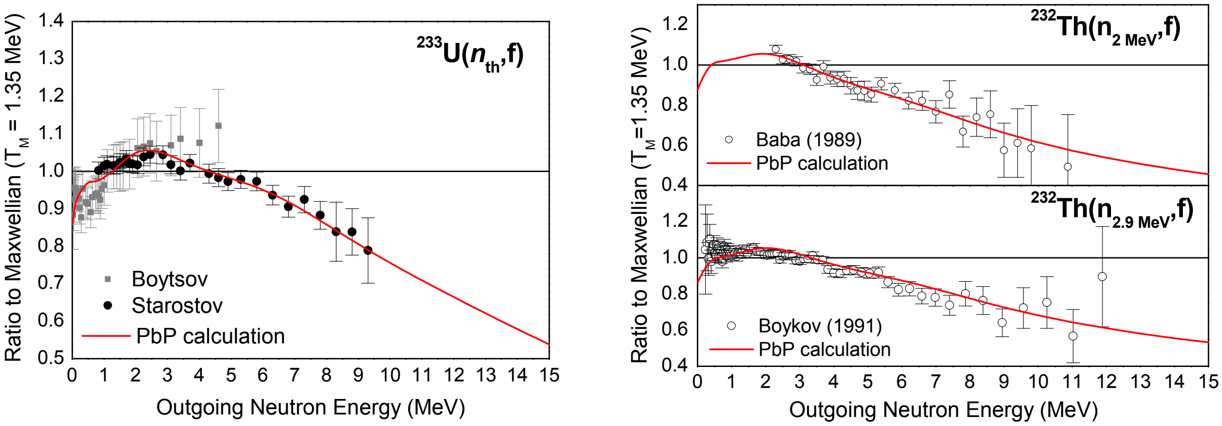

FIG. 19. (Color online) Examples of `PbP` PFNS results (red line) for (left) ^{233}U($n_{\rm th}$,f) and (right) ^{232}Th(n,f) at E_n =2 and 2.9 MeV. The results are given as a ratio to a Maxwellian.

The values of $S_n(A-i,Z)$ are obtained using the mass excesses from nuclear data libraries [182]). In the `PbP` model there is a linear correlation between the average prompt photon energy and prompt neutron multiplicity. The slope of this correlation expresses the competition between the prompt neutron and photon emission for excitation energies above S_n while the intercept is the photon energy for excitation energies below S_n, as described in Ref. [192]. A global parameterization of the slope and intercept [172, 200, 201] was obtained by fitting the (n,n') and (n,γ) competition obtained from nuclear reaction calculations. The direct interaction mechanism was treated with the spherical optical model and compound nucleus mechanism by a statistical Hauser-Feshbach model [202] with fluctuation corrections calculated using the STATIS code. This competition was studied for a limited number of fission fragments in the seven-point approximation for thermal neutron-induced fission of important actinides and spontaneous fission of ^{252}Cf.

4. Fission Fragment Distributions and Average Quantities

To obtain average quantities as a function of A, Z, or TKE, as well as total average quantities (needed in the comparison with data for validation and for evaluation purposes), the matrices $q(A,Z,\mathrm{TKE})$ are averaged over the fragment yields,

$$\overline{q}(A) = \frac{\sum\limits_{Z,\mathrm{TKE}} q(A,Z,\mathrm{TKE})Y(A,Z,\mathrm{TKE})}{\sum\limits_{Z,\mathrm{TKE}} Y(A,Z,\mathrm{TKE})}\,, \tag{54}$$

$$\overline{q}(Z) = \frac{\sum\limits_{A,\mathrm{TKE}} q(A,Z,\mathrm{TKE})Y(A,Z,\mathrm{TKE})}{\sum\limits_{A,\mathrm{TKE}} Y(A,Z,\mathrm{TKE})}\,, \tag{55}$$

$$\overline{q}(\mathrm{TKE}) = \frac{\sum\limits_{Z,A} q(A,Z,\mathrm{TKE})Y(A,Z,\mathrm{TKE})}{\sum\limits_{Z,A} Y(A,Z,\mathrm{TKE})}\,, \tag{56}$$

$$\langle q\rangle = \frac{\sum\limits_{A,Z,\mathrm{TKE}} q(A,Z,\mathrm{TKE})Y(A,Z,\mathrm{TKE})}{\sum\limits_{A,Z,\mathrm{TKE}} Y(A,Z,\mathrm{TKE})}\,. \tag{57}$$

The matrices $q(A,Z,\mathrm{TKE})$, the primary results of the `PbP` model, can be averaged over any experimental or theoretical fragment yields $Y(A,Z,\mathrm{TKE})$. In the usual `PbP` treatment,

$$Y(A,Z,\mathrm{TKE}) = Y_{\rm exp}(A,\mathrm{TKE})p(Z,A)\,, \tag{58}$$

where experimental $Y(A, \mathrm{TKE})$ distributions are preferred. When there are only single distributions for $Y(A)$, $\mathrm{TKE}(A)$ and $\sigma_{\mathrm{TKE}}(A)$ are available, then $Y(A, \mathrm{TKE})$ can be reconstructed as

$$Y_{\mathrm{exp}}(A, \mathrm{TKE}) = \frac{Y(A)}{\sigma_{\mathrm{TKE}}(A)\sqrt{2\pi}} \times \exp[-(\mathrm{TKE} - \mathrm{TKE}(A))^2/2(\sigma_{\mathrm{TKE}}(A)^2)] \; . \tag{59}$$

The charge distribution at each A is Gaussian [187, 188, 191]:

$$p(Z, A) = \frac{1}{\sqrt{\pi c(A)}} \exp[-(Z(A) - Z_p(A))^2/c(A)] \; , \tag{60}$$

where $Z_p(A)$ is defined in Eq. (46) and $c(A) = 2\sigma_z^2(A)$ or $c(A) = 2(\sigma_z^2(A) + 1/12)$[151, 187, 188, 193].

The `PbP` model can also be applied to multiple fission modes. In this case, the primary matrices $q(A, Z, \mathrm{TKE})$ are averaged over the multi-modal distributions $Y_m(A, Z, \mathrm{TKE})$ (m is the fission mode) according to Eqs. (54)-(57). Modal quantities were reported in Refs. [153, 165, 173, 203].

Alternatively, the average fragment quantities $\langle E_r \rangle$, $\langle \mathrm{TKE} \rangle$, $\langle S_n \rangle$ and $\langle a \rangle$ obtained in the `PbP` approach can be used as model inputs, in the original LAM or the extended version [159] including secondary nucleus chains arising from charged particle emission, for calculations with the most probable fragmentation alone. The systematics on the LAM parameters in Ref. [179] are based on the `PbP` treatment.

5. *Examples of* `PbP` *Results*

Some examples of `PbP` results are compared here to available experimental data.

An example of matrix results is shown on the left-hand side of Fig. 17: $\overline{\nu}(A, \mathrm{TKE})$ for the case of ^{252}Cf(sf). The calculated `PbP` $\overline{\nu}(A)$ for ^{235}U(n,f) at $E_n = 0.5$ and 5.5 MeV is shown on the right-hand side of the same figure. The `PbP` calculations [211] describe well the experimental data of ^{252}Cf(sf) [204, 205] (left), as well as the heavy-fragment multiplicity increase with E_n for ^{235}U(n,f) (right), e.g., compare the red circles and blue stars with measured data by Müller et al. [206]. More `PbP` results as a function of A can be found in Refs. [152, 187–191, 194, 212].

The correspondence of the neutron multiplicity and prompt photon energy is demonstrated in their dependence on TKE in Fig. 18 for ^{252}Cf(sf). The data [207–210] are in generally good agreement with the model [211]. Similar results can be found in Refs. [187–189].

Finally, PFNS results are presented in Fig 19 for ^{233}U(n_{th}, f) and ^{232}Th(n,f) at $E_n = 2$ and 2.9 MeV, as a ratio to Maxwellian. See Refs. [190, 191, 213]) for more results.

D. CNDC Semi-empirical Parameterization

In this subsection, a semi-empirical model (SEM) developed by researchers at China Nuclear Data Center (CNDC) was applied to calculate the PFNS for ^{233}U and ^{235}U neutron-induced fission for $E_n < 6$ MeV and ^{252}Cf spontaneous fission. The energy partition is deduced from experimental data on neutron and photon emission at thermal energies and then systematically extrapolated to 6 MeV.

The results show that the total excitation energy is not shared between the fragments in proportion to their masses. The PFNS were calculated using Weisskopf evaporation spectra with temperatures determined from a Fermi gas model.

1. *TXE Partition Method*

In the case of binary fission, the initial excitation energy is carried away by prompt neutron and photon emission. If the excitation energy of each fragment can be obtained, then the energy partition between the two fragments can be deduced from data. For fragment A_i, $i = L, H$, the excitation energy can be expressed solely in terms of experimental quantities,

$$E^*(A_i) = \overline{\nu}_{\mathrm{exp}}(A_i)\langle \eta \rangle(A_i) + E_{\mathrm{exp},\gamma}(A_i) \; . \tag{61}$$

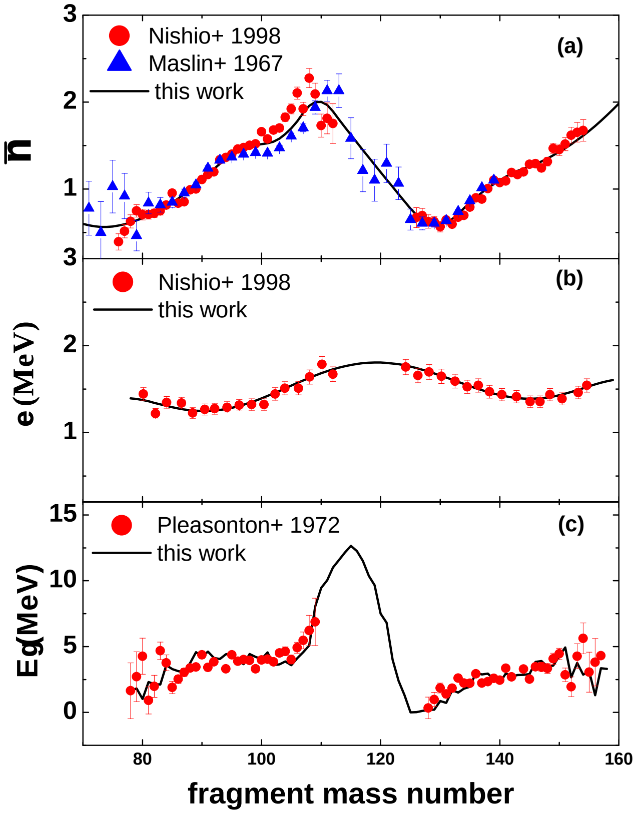

FIG. 20. (Color online) The (a) $\overline{\nu}(A)$, (b) neutron energy $\varepsilon(A)$, and (c) $E_\gamma(A)$ data used in the study of the TXE partition in ^{235}U($n_{\rm th}$,f). The points are the experimental data [214–216] and the lines are the SEM evaluation.

Note that here $\langle\eta\rangle(A_i) = \varepsilon_{\rm exp}(A_i) + S_n(A_i)$, being ε the emitted neutron energy. Using Eq. (61), the ratio, $R(A_{L,H}) = E^*(A_{L,H})/{\rm TXE}$ is

$$R(A_i) = \frac{\overline{\nu}_{\rm exp}(A_i)\langle\eta\rangle(A_i) + E_{{\rm exp},\gamma}(A_i)}{\sum\limits_{i=L,H}[\overline{\nu}_{\rm exp}(A_i)\langle\eta\rangle(A_i) + E_{{\rm exp},\gamma}(A_i)]} . \tag{62}$$

The quantities labeled "exp" in Eq. (62) were taken from Refs. [214–216] for ^{235}U($n_{\rm th}$,f). While data are available, they are lacking in some mass regions. In the work presented here, the "exp" data above were replaced with the evaluated data obtained by fitting the experimental data or by interpolating and extrapolating for mass regions where no experimental data are available.

Fig. 20 shows the SEM evaluated neutron multiplicity, average neutron kinetic energy and average photon energy compared with the experimental data. The SEM evaluations reproduce the experimental data, the neutron multiplicity $\overline{\nu}_{\rm exp}(A)$ and average kinetic energy $\varepsilon_{exp}(A)$, very well. There are, unfortunately, no data on $E_\gamma(A)$ for $110 < A < 130$. Fig. 20(c) displays a prominent spike in this region that arises from interpolating and extrapolating the data in this region. The $\overline{\nu}(A)$ curve in this same region is consistent with the data and deduced from the values of $E_{{\rm eval},\gamma}(A)$, thereby providing indirect evidence for this shape. Since this is important for the present calculations, $E_{{\rm eval},\gamma}(A)$ in Fig. 20(c) was adopted. Based on the CNDC evaluated data, the energy partition between the fragments is calculated according to Eq. (62) and is shown by the solid line in Fig. 21. The dashed line shows the results with the energy partition proportional to the fragment mass A_f/A_C where A_C is the mass of the compound nucleus, $A_C = 236$. The dotted line shows the ratio of the neutron multiplicity for a given fragment relative to the total neutron multiplicity, $\overline{\nu}_f/(\overline{\nu}_L + \overline{\nu}_H)$.

It is clear from a comparison of the solid and dashed lines in Fig. 21 that the energy partition is not proportional to A. The dip at $A{\sim}130$ indicates that the excitation energy of the heavy fragment is minimal as the doubly-closed shell at A_H =132 is approached. Simultaneously, there is a peak near $A_L = 106$ where the excitation energy is a maximum for the light fragment. The hypothesis [217] that the excitation energy is not equilibrated between fragments could be confirmed by this work. The present results also agree with the macroscopic-microscopic model result [218]. The dotted line, the ratio $\overline{\nu}_f/(\overline{\nu}_L + \overline{\nu}_H)$, is similar to the solid curve. The difference can be attributed to neglecting the photon energy.

The data shown here are for thermal neutrons only. Very few data are available at other energies. However, as shown

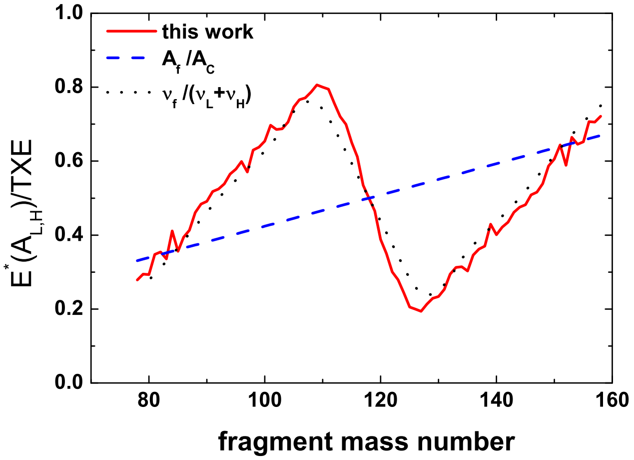

FIG. 21. (Color online) The energy partition between two fragments in the thermal neutron-induced ^{235}U fission reaction.

in the following, based on the energy partition and the systematics of the fragment yields, the excitation energy at higher incident neutron energies can be determined.

According to the temperature-dependent multi-modal model [219], shell effects are responsible for asymmetric fission while the symmetric fission mode can be described by the statistical liquid drop model. The probability of symmetric and asymmetric fission depends on the excitation energy. At very low temperature (excitation energy), asymmetric fission is dominant and the partitioning is based on the solid red curve in Fig. 21, denoted R_0. At sufficiently high energies, shell effects become negligible so that symmetric fission dominates and the partition should follow the ratio $R_L = A_f/A_C$ given by the dashed blue curve. If the excitation energy is above thermal but below the point where shell effects are unimportant, both symmetric and asymmetric modes will contribute and the energy partition will be a linear interpolation of R_0 and R_L, as described below.

For incident neutron energy E_n, the ratio of symmetric to asymmetric fission is required to extrapolate the energy partition. Reference [220] presents systematic research on the energy dependence of the fission fragment mass yields. As shown in Fig. 22, the ratio $R = Y_s/Y_a$ increases with E_n. Thus the energy partition depends on R,

$$R(E_n, A) = (1 - R(E_n))\, R_0(A) + R(E_n)\, R_L(A)\,. \tag{63}$$

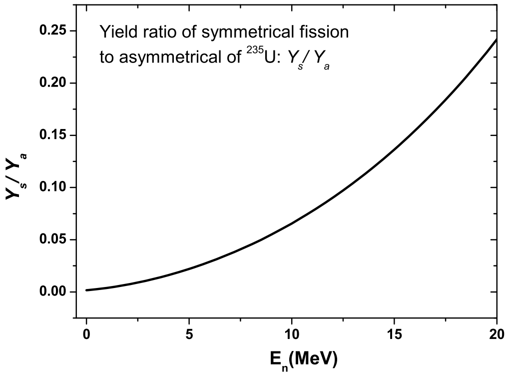

FIG. 22. Yield ratio of symmetric to asymmetric fission as a function of E_n for ^{235}U(n,f).

From Fig. 22, R~0.025 at $E_n = 6$ MeV. Thus the liquid drop contribution at this energy is small. However, Eq. (63) shows that by 20 MeV, the contribution from R_L will be larger.

The total excitation energy for a given value of E_n can be calculated from the energy release, as in the original LAM described in Sec. IV B. The fragment excitation energies are then based on Eq. (63),

$$E^*(E_n, A) = R(E_n, A)\,\mathrm{TXE}\ . \tag{64}$$

The PFNS calculation follows that of the original LAM but it assumes a constant cross section for compound nucleus formation.

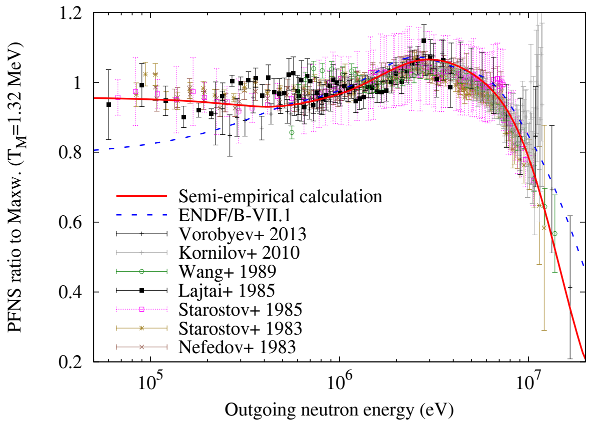

FIG. 23. (Color online) The calculated PFNS (red line) and ENDF/B-VII.1 (blue dashed line) evaluation for ^{235}U($n_{\rm th}$,f), along with experimental data, given as a ratio to a Maxwellian.

2. Results

The above method of excitation energy partition was used to calculate the PFNS for ^{235}U(n,f), ^{233}U(n,f), and ^{252}Cf(sf). The experimental data are retrieved from EXFOR [52] and evaluated as described here. As an example of the results, Fig. 23 shows the results calculated with the given semi-empirical model, labeled as "SEM", for ^{235}U(n,f). The values are presented relative to a Maxwellian. It is compared to thermal neutron data [30, 31, 33, 42, 59, 60, 62] as well as to the ENDF/B-VII.1 evaluation. The calculated PFNS agrees with the data within the uncertainties. However, the tail of spectrum at emitted neutron energies of $6 < E < 20$ MeV is lower than the ENDF/B-VII.1 result, while for $E < 1$ MeV it does not decrease with energy and is higher than that of ENDF/B-VII.1. For other incident energy cases, the calculated PFNS agrees with the measurements.

V. MONTE CARLO MODELS AND CODES

In recent years, several codes have been developed to study the de-excitation of the primary fission fragments on an event-by-event basis. These models are able to calculate relevant fission quantities without an additional averaging procedure implicit in deterministic models discussed in Sec. IV. Each code is discussed separately in the following sections. Before doing so, some common features shared by all these codes are presented first.

Until recently, most of the modeling work on prompt fission neutrons focused almost entirely on calculating the average spectrum and multiplicity of the emitted neutrons. This was done either very heuristically or through significant simplifying assumptions. For instance, the Watt model [12] for the average PFNS is a simple two-parameter formula with parameters adjusted to provide the best agreement with experimental data. While systematics of those model parameters as a function of energy and fissioning isotope can be derived from an analysis of all experimental data, they bear only little resemblance to actual physical parameters and cannot be used to predict more detailed prompt fission neutron data.

More recently, significant efforts have been made to develop models and codes to study the emission of prompt neutrons and photons on an event-by-event basis, through Monte Carlo simulations of the de-excitation of the primary fission fragments.

A particular binary fission event is characterized by the production of a pair of complementary fragments, both characterized by an excitation energy U, a spin J and a parity π. These primary fragments are then treated as compound nuclei and the statistical theory of nuclear reactions can be applied to study their prompt decay via emission of neutrons and photons. (Since the sole interest is in prompt fission data, no β-delayed emission is considered here.) For a given configuration $(A_i, Z_i, U_i, J_i, \pi_i)$ $(i = L, H)$, there is a certain probability of emitting a neutron with energy ϵ_n leading to the residual nucleus $(A_i - 1, Z_i, U_i - \epsilon_n - S_n, J_f, \pi_f)$, with new spin and parity that depend on the angular momentum of the emitted neutron. This neutron emission competes with photon emission that leads to the same fragment but in a less excited state. For each fission fragment configuration, those probability distributions are sampled and a particular "trajectory" in the nuclear phase space is chosen. This process is repeated until the residual nucleus is left in either its ground-state or a long-lived isomeric state.

A typical fission experiment does not produce just one fission event, but instead a large number of them, each characterized by a different initial configuration. A Monte Carlo simulation will mimic such an experiment by first sampling the initial configurations of the fission fragments in mass, charge, kinetic energy, excitation energy, spin and parity. By performing millions of calculations, the full initial fragment yields are reproduced, and the Monte Carlo sampling of the different trajectories lead to the collection of histories of fission fragment decay paths. A straightforward statistical analysis of all these simulated fission events then provides all the observables of interest. In particular, this approach does not only predict average prompt fission data, as in older works, but also a vast amount of data that can be sliced in many sub-spaces, providing distributions and correlations of prompt fission neutrons and photons, e.g., $\overline{\nu}(A, Z, \mathrm{TKE})$ and $P(\nu)$.

While each Monte Carlo code treating this problem share this same basic algorithm, each of them differs in its treatment of various input data. For instance, while recent theoretical efforts have shown some progress in predicting the primary (pre-neutron emission) fission fragment yields in mass, charge and kinetic energy (e.g., see Ref. [221]), most, if not all Monte Carlo codes presented here rely on experimental fission yield data to start their simulation. Those simulations also require the knowledge of nuclear level densities and low-lying nuclear structure for many very neutron-rich isotopes for which experimental knowledge can be scarce. Systematics of nuclear level densities and nuclear reaction model parameters have been developed over the years [184], those were mostly based on experimental data obtained for nuclei near the valley of stability. In addition, the neutron and photon emission probabilities are computed differently in different codes. Even though most employ similar techniques, e.g., Hauser-Feshbach [202], the choice of optical model potential still introduces large uncertainties since no reaction data exist for those particular nuclei.

Not surprisingly, while these new Monte Carlo tools can simulate many more prompt fission observables than earlier models, they also depend on many more input parameters. However, the types of data that can be modeled employing these techniques can be used to constrain some of those parameters, a feat that was impossible with earlier models that could only compute average prompt fission neutron spectra and multiplicities.

A. `CGMF`

The `CGMF` code represents a merger of two codes previously developed at LANL: `FFD` [222], which performed Monte Carlo simulations of fission fragments following the Weisskopf-Ewing statistical theory, and `CGM` [223], a Monte Carlo Hauser-Feshbach code not initially developed for treating fission events. A new version of `CGMF` is being developed, treating both fission and non-fission events naturally. The `CGMF` code is written in C++. A user manual has been written [224] and it will be updated regularly as new versions of the code are developed.

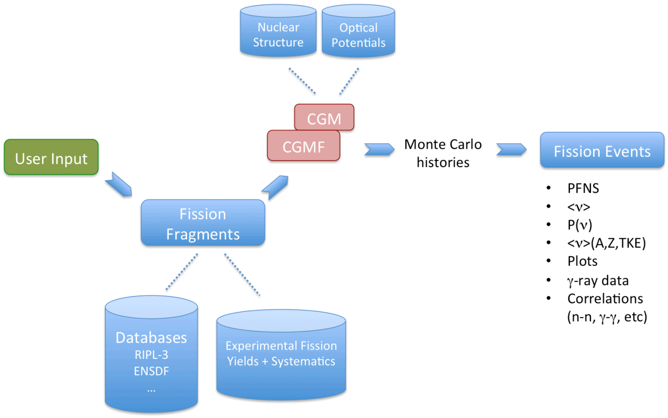

FIG. 24. (Color online) Flowchart describing the input and output of the `CGMF` code.

Initially, primary fission fragment distributions are produced based on available experimental data on partial distributions, e.g., Y(A), $\langle\mathrm{TKE}\rangle(A)$, etc. The full distributions, $Y(A, Z, \mathrm{KE})$, are obtained by combining these measured partial yields. The available experimental data for these yields vary widely, depending on the particular fissioning system and energy. The charge distribution $Y(Z|A)$ is obtained using Wahl's systematics [151]. Fission fragment mass yields have been measured for some systems and energies, mostly in $2E$ experiments, in which the kinetic energy of each fragment is recorded. Given some assumptions about the average neutron multiplicity as a function of the fragment mass, the pre-neutron emission fission fragment yields can be obtained with a typical 3-5 units mass resolution. This approach is reasonable, albeit imprecise, for thermal neutron-induced reactions for which experimental data on $\overline{\nu}(A)$ are available. It becomes problematic at higher excitation energies for which mass-dependent neutron multiplicity data have not been measured. Recent efforts to measure the fission fragment yields in $2E-2v$ experiments, in which the velocities of both fragments are also recorded, should cast new light on this old problem. The evolution of the total kinetic energy as a function of excitation energy is also being the focus of renewed experimental efforts [225].

So far, `CGMF` is applicable to very few isotopes and incident neutron energies. Work is in progress to extend its scope to incident neutron energies up to 20 MeV and to many isotopes by developing a simplified model for the yields $Y(A,Z,\mathrm{TKE})$. Theoretical developments [226–229] are also very encouraging and they should provide useful data in the near future. It is interesting to note that the accuracy to which those quantities need to be known strongly depends on the fission observable(s) one is interested in. For instance, the average $\langle\mathrm{TKE}\rangle$ has a strong influence on the calculated average prompt neutron multiplicity, but the details of $Y(\mathrm{TKE})$ are only important for the calculation of more detailed neutron data such as the neutron multiplicity distribution $P(\nu)$.

Once the fragment yields are known, they are randomly sampled to provide a pair of light and heavy fragments characterized by $(A,Z,\mathrm{KE})_{L,H}$. The sum of the light and heavy masses (charges) is equal to the compound fissioning mass (charge), and the kinetic energies of the fragments are easily obtained by momentum conservation. For a specific fragmentation, the total excitation energy available for the emission of neutrons and photons is computed as the difference between the Q_f value of the fission reaction and the total kinetic energy TKE. The quantity Q_f is relatively well-known with accurate nuclear mass measurements and model predictions. The total excitation energy TXE available is therefore known. This energy can be written as the sum of the individual intrinsic and collective energies in the fragments. The question of how much energy is bound in the deformation degrees of freedom before and after scission remains unclear and several simple phenomenological models have been used to estimate those energies in each fragment. It is understood that the deformation of the nascent fragments plays a key role in calculating the pre-scission kinetic energy that finds its way into the final total kinetic energy of the fragments. After scission, the energy stored in the deformation degrees of freedom of the fragments gets quickly converted into extra intrinsic excitation energy, which is then expended by the evaporation of neutrons and photons. Figure 25 shows the initial excitation energy distributions in the light and heavy fragments for ^{252}Cf (sf) as calculated in `CGMF`.

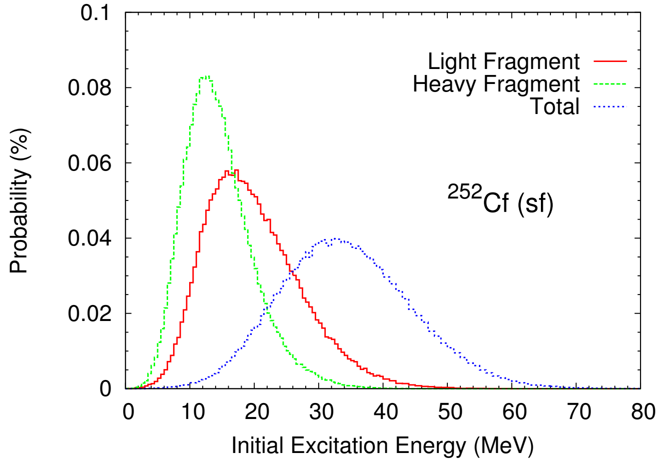

FIG. 25. (Color online) Excitation energy distributions in the light and heavy fragments as calculated by `CGMF` in ^{252}Cf(sf).

In the present version of the `CGMF` code, several options can be explored to determine the energy sorting between the complementary fragments. The default calculations use a simple parameter to share TXE so as to reproduce the measured average prompt fission neutron multiplicity as a function of the fragment mass, $\overline{\nu}(A)$.

The initial angular momentum distribution in each fragment is given by

$$P(J) \propto (2J+1)\exp\left(-\frac{J(J+1)}{2B^2}\right) , \tag{65}$$

where the spin cut-off parameter B is a function of the ground-state moment of inertia $\mathcal{I}_0(A,Z)$ and the nuclear temperature T

$$B^2 = \alpha\frac{\mathcal{I}_0(A,Z)T}{\hbar^2} . \tag{66}$$

The quantity α is a global adjustable parameter that is used to correctly reproduce the observed prompt neutron and photon multiplicities. A higher initial spin distribution leads to a higher number of photons emitted at the expense of neutron evaporation. Isomeric ratio data were used to infer some optimal values for α [230]. It was found that different α values would be needed to reproduce both neutron and photon multiplicities simultaneously. In addition, isomeric ratio calculations were found to be strongly sensitive to the exact low-lying structure in those nuclei, for which only limited structure information is available. Even for thermal neutron-induced reactions for which much more reliable data are available, the results were rather inconclusive. A global value for α, the same value for all fission fragments, was used in Ref. [231]. The observed prompt fission photon spectra could be reproduced rather well, although higher α values were typically needed to reproduce the neutron multiplicity consistently. The parity distribution is simply taken as 1/2 in the continuum. Note that the current version of `CGMF` does not include any correlation between the two complementary fragment spin distributions.

The initial distributions are sampled by Monte Carlo to obtain a unique initial starting point characterized by $(A, Z, \mathrm{KE}, U, J, \pi)_0$ for both the light and heavy fragments. In this state, the fragments can be considered as compound nuclei, whose decay can be simulated using the Hauser-Feshbach formalism [202]. This formalism has been used successfully over the years to study nuclear reactions in the statistical regime for light particle-induced reactions on medium to heavy nuclei. A schematic view of the decay process is shown in Fig. 26.

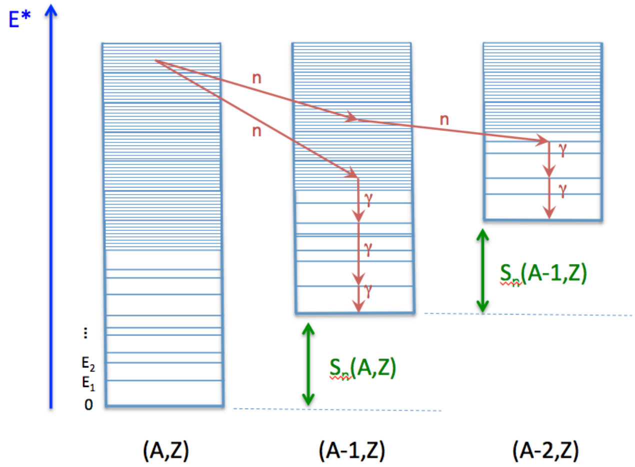

FIG. 26. (Color online) Schematic view of the de-excitation process starting in an excited state in the (A, Z) compound nucleus. Only neutron and photon emission are considered here.

The probabilities of emitting neutrons and photons are calculated using transmission coefficients calculated using the optical model and photon strength functions, respectively. An optical model calculation is used to compute the neutron transmission coefficients. The default optical model potential used in `CGMF` is the global spherical Koning-Delaroche potential [232]. The neutron emission probability distribution is

$$P(\epsilon_n)dU \propto T_n(\epsilon_n)\rho(A-1, Z, U-\epsilon_n-S_n)dU, \tag{67}$$

where S_n is the neutron separation energy for this particular nucleus and ρ represents the level density in the nucleus $(A-1, Z)$ at the residual excitation energy $U-\epsilon_n-S_n$.

Similarly, the probability for emitting a prompt fission photon at energy ϵ_γ is given by

$$P(\epsilon_\gamma)dU \propto T_\gamma(\epsilon_\gamma)\rho(A, Z, U-\epsilon_\gamma)dU\ . \tag{68}$$

The photon transmission coefficient is obtained using the photon strength functions

$$T^{Xl}(\epsilon_\gamma) = 2\pi f_{Xl}(\epsilon_\gamma)\epsilon_\gamma^{2l+1}\ , \tag{69}$$

where Xl is the multipolarity of the photon and $f_{Xl}(\epsilon_\gamma)$ is the energy-dependent photon strength function.

For $E1$ transitions, the generalized Lorentzian strength function of Kopecky-Uhl [233],

$$\begin{aligned} f_{E1}(\epsilon_\gamma, T) = {} & K_{E1}\left[\frac{\epsilon_\gamma\Gamma_{E1}(\epsilon_\gamma)}{(\epsilon_\gamma^2-E_{E1}^2)^2+\epsilon_\gamma^2\Gamma_{E1}(\epsilon_\gamma)^2}\right. \\ & + \left.\frac{0.7\Gamma_{E1}4\pi^2T^2}{E_{E1}^5}\right]\sigma_{E1}\Gamma_{E1}\ , \end{aligned} \tag{70}$$

is used where σ_{E1}, Γ_{E1}, and E_{E1} are the standard giant dipole resonance (GDR) parameters. $\Gamma_{E1}(\epsilon_\gamma)$ is an energy-dependent damping width,

$$\Gamma_{E1}(\epsilon_\gamma) = \Gamma.\frac{\epsilon_\gamma^2+4\pi^2T^2}{E_{E1}^2}\ , \tag{71}$$

and T is the nuclear temperature,

$$T = \sqrt{\frac{E^* - \epsilon_\gamma}{a(S_n)}} \; . \tag{72}$$

Here E^* is the nuclear excitation energy and $a(S_n)$ is the level density parameter at the neutron separation energy. The quantity K_{E1} is a normalization factor.

For $E2$ and $M1$ transitions, the Brink-Axel standard Lorentzian [234, 235] is used instead,

$$f_{Xl}(\epsilon_\gamma) = K_{Xl} \frac{\sigma_{Xl}\epsilon_\gamma\Gamma^2_{Xl}}{(\epsilon^2_\gamma - E^2_{Xl})^2 + \epsilon^2_\gamma\Gamma^2_{Xl}} \; . \tag{73}$$

In version 1.0.5 of `CGMF`, only $E1$, $M1$ and $E2$ transitions are considered. Higher multipolarity transitions are neglected.

The nuclear structure is represented by a set of well-identified discrete levels at low excitation energy and by a continuum of states at higher energies. The known nuclear structure is taken from the RIPL-3 library [184], closely matching the ENSDF structure database. The representation of the continuum follows the Gilbert-Cameron formalism [236] using a constant temperature $\rho(E) \propto \exp(E/T)$ at the lower excitation energies, followed by a Fermi-gas representation $\rho(E) \propto \exp(2\sqrt{aU})$ above a certain matching energy. The Ignatyuk model [196] describing the washing-out of shell effects with increasing energy is also included in the energy dependence of the level density parameter $a(A, Z, U)$.

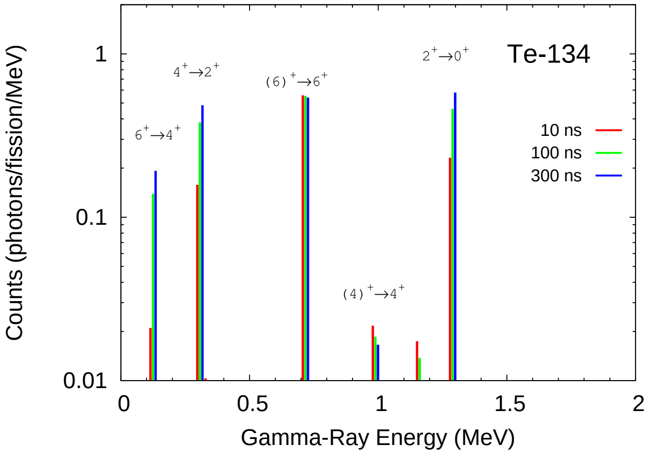

FIG. 27. (Color online) The strengths of specific γ lines can be significantly impacted by the time-coincidence window that is used to define prompt fission events. Shown on this figure are predictions for low-lying γ lines in ^{134}Te, using the `CGMF` code.

A time coincidence window can be set up in the `CGMF` input file to reproduce the experimental conditions of prompt fission photon measurements. This is important as many isomeric states in the fission fragments can lead to late gammas that would not necessarily be observed in a given experimental time coincidence window, often of the order of a few to a few hundred ns. The calculated photon multiplicity and energy spectrum can change appreciably for different time windows, as illustrated in Fig. 27 for ^{134}Te.

At each stage of the decay, emission probability distributions are calculated and then sampled using the Monte Carlo technique. The result is a (usually long) series of Monte Carlo histories that describe a particular fission event and decay path. Once calculated, fission event history files can be read back in `CGMF` and/or processed separately. Straightforward statistical analyses of those events are then used to obtain average quantities, distributions and correlations among the emitted particles and the characteristics of the initial fission fragments. An example of such data is shown in Fig. 28 for the calculated and measured prompt neutron multiplicity distribution of ^{252}Cf(sf). In the calculation, the neutrons emitted from the light and heavy fragments can be separated easily . Other examples of `CGMF` results are given in the code comparison section V F and will therefore be omitted here.

Because `CGMF` follows the decay of every fragment exactly, including the decay from the discrete states identified in the ENSDF nuclear structure database, details such as the fluctuations observed in the prompt fission photon spectra can be reproduced rather accurately. However, for this reason, `CGMF` calculations can be computationally intensive and often requires the use of a small cluster to provide adequate statistics for accurate reproduction of the tails of distributions and spectra which receive contributions from a small number of Monte Carlo histories. Efforts are being made to improve the situation.

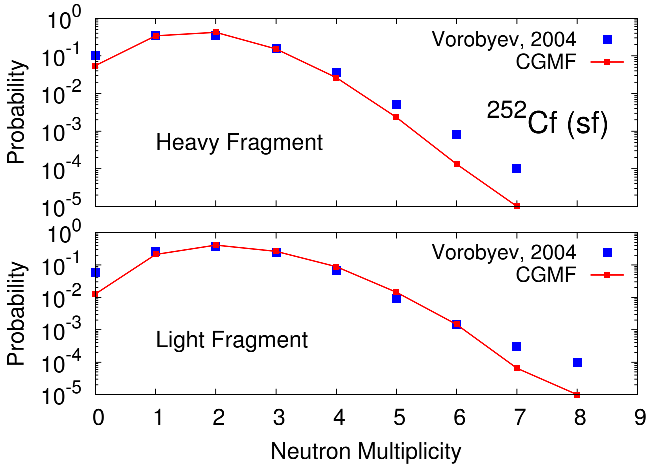

FIG. 28. (Color online) Prompt fission neutron multiplicity distributions for the light and heavy fragments in the spontaneous fission of ^{252}Cf, calculated by `CGMF`, and compared to Vorobyev et al. data [209].

B. `FIFRELIN`

The `FIFRELIN` code has been developed at CEA-Cadarache (France) with the aim of calculating the main fission observables, and in particular the energy spectra and multiplicities of the emitted prompt particles. In the first version of the code [237], prompt neutron emission was simulated using a Weisskopf spectrum [150]. In a more recent version [238] and [239], the de-excitation of the fission fragments is treated by using the Hauser-Feshbach formalism [202]. This last version has been used in the present work to investigate thermal neutron-induced fission of ^{239}Pu and ^{235}U as well as the spontaneous fission of ^{252}Cf.

1. *Calculational Procedure*

The `FIFRELIN` approach follows three successive stages which are briefly described here. More details can be found in [237–240].

First, the mass, charge and kinetic energy of the light fragment are sampled. The mass is sampled from the fission fragment distributions shown in the upper part of Fig. 29. The light fragment charge, Z_L, is calculated from Wahl's systematics [241]. The mass and charge of the heavy fragment can be deduced from mass and charge conservation.

The fragment kinetic energies can be constructed from the average energies and distribution widths shown in the middle and lower parts of Fig. 29, assuming a Gaussian distribution of the kinetic energies. The total kinetic energy is then TKE= KE$_L$ + KE$_H$. In `FIFRELIN`, J is sampled from the empirical distribution,

$$P_{L,H}(J) = \frac{2J+1}{2\sigma_{L,H}^2} \exp\left(-\frac{(J+0.5)^2}{\sigma_{L,H}^2}\right) , \tag{74}$$

where $\sigma_{L,H}$ is the spin cutoff for the light and heavy fragments. A constant value, σ_L (σ_H), is assumed for all light (heavy) fragments. The spin cutoffs, σ_L and σ_H are free parameters. The probability for positive or negative parity is taken as 0.5. Next, the excitation energies of the light and heavy fragments are determined. This step is very important because it governs prompt neutron and photon emission. Scission neutrons are neglected, as is neutron emission during the acceleration of the fission fragments. Thus the only source of prompt neutrons is the evaporation of the fission fragments. Also during the acceleration phase, the deformation energy of the fission fragments at scission is assumed

TABLE 20. The values of the adjustable parameters obtained in the fit by `FIFRELIN` used in the present work.

	^{235}U$(n_{\rm th},f)$	^{239}Pu$(n_{\rm th},f)$	^{252}Cf(sf)
$R_T^{\rm min}$	0.85	0.64	0.25
$R_T^{\rm max}$	1.23	1.30	1.50
σ_L	10	8.7	10.5
σ_H	10.5	9.2	11.0
$k_{\rm rigid}$	1	1	0.8

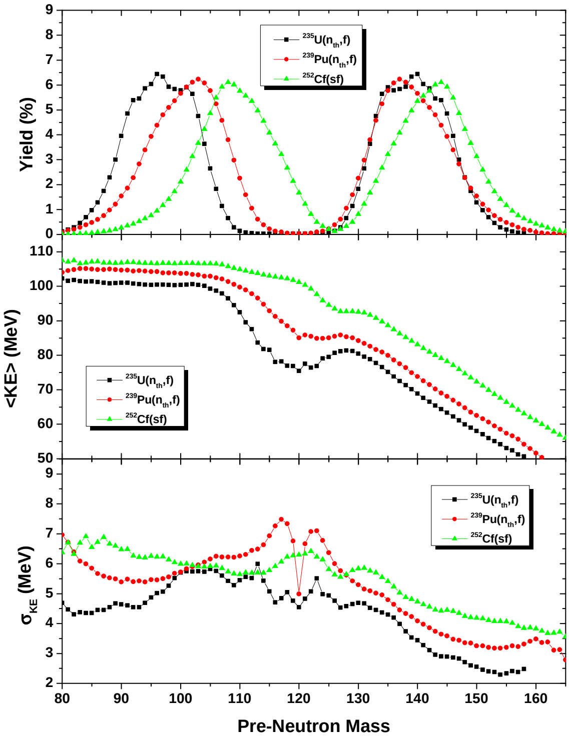

FIG. 29. (Color online) Initial pre-neutron data used for `FIFRELIN` Monte Carlo calculations: mass yield (top), average kinetic energy (middle) and width of the kinetic energy (bottom). Data sources are: ^{239}Pu$((n_{\rm th}, f)$ [167, 168, 242]; ^{235}U$(n_{\rm th}, f)$ [243]; and ^{252}Cf(sf) [244].

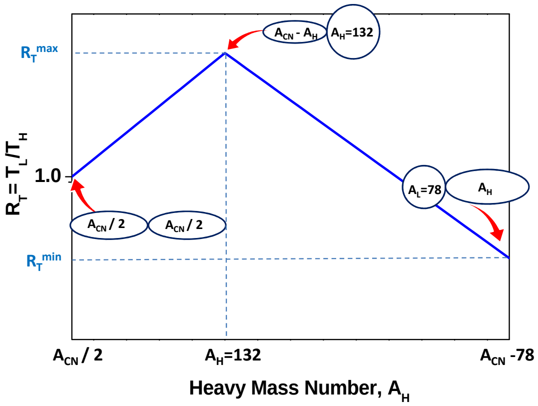

FIG. 30. (Color online) The ratio between the light and heavy fragment temperatures as a function of the heavy fragment mass.

to be converted into intrinsic excitation energy, see Ref. [245]. Consequently, after this relaxation phase, the fission fragments are considered to be rotating Fermi gas nuclei with their ground state deformations.

The total excitation energy, TXE, available at scission is then $\mathrm{TXE} = Q + E_n + B_n - \mathrm{TKE}$, where E_n is the incident neutron energy and B_n is the neutron binding energy. Since the fission fragments are assumed to be rotating Fermi gas nuclei, TXE can also be written as

$$\mathrm{TXE} = a_L T_L^2 + a_H T_H^2 + E_L^{\rm rot} + E_H^{\rm rot} \tag{75}$$

where $a_i T_i^2$ is the intrinsic fragment excitation energy and $E_i^{\rm rot}$ is the rotational energy. The level density a_i is calculated employing the Ignatyuk prescription [196]. The intrinsic excitation energy is partitioned between the fragments following an empirical mass-dependent temperature ratio: $R_T = T_L/T_H \equiv R_T(A)$. This ratio is constructed from physical constraints based on the expected fragment deformation at scission for three different mass splits, as schematically illustrated in Fig. 30. A near-spherical shape is assumed for $A_H = 132$ at scission ($Z_H = 50$ is a closed proton shell and $N_H = 82$ is a closed neutron shell). The complementary light fragment, $A_L = A - 132$, is expected to be significantly more deformed than its heavy partner. Since the deformation energy is transformed into intrinsic

TABLE 21. (Color online) Comparison of the calculated and measured average prompt neutron multiplicities. The data are from [214] (^{235}U(n_{th},f)) and [209] (^{252}Cf(sf). The evaluated value from the JEFF-3.2 library [180] is given for ^{239}Pu(n_{th},f).

		^{235}U(n_{th},f)	^{239}Pu(n_{th},f)	^{252}Cf(sf)
	$\overline{\nu}$	2.42	2.86	3.76
`FIFRELIN`	$\overline{\nu}_L$	1.41	1.66	2.06
	$\overline{\nu}_H$	1.01	1.20	1.70
	$\overline{\nu}$	2.43	2.87	3.75
Data	$\overline{\nu}_L$	1.42		2.05
	$\overline{\nu}_H$	1.01		1.70

excitation energy after the fragment acceleration, the light fragment will be characterised by a higher temperature compared to its doubly-magic partner. Therefore R_T will be at its maximum: $R_T(A_H = 132) = R_T^{\max} > 1$. The same reasoning is applied for the light fragment mass $A_L = 78$ ($Z = 28$ is closed proton shell and $N = 50$ is a closed neutron shell). Here the heavy fragment is more deformed at scission than its light partner. Consequently, $R_T(A_H = A - 78) = R_T^{\min} < 1$. At symmetry, the deformation of the two fragments is assumed to be identical, $R_T(A_H = A/2) = 1$. A linear interpolation/extrapolation based on these three mass split configurations, as shown in Fig. 30, is performed to fix the temperature ratio for all masses. In `FIFRELIN`, $R_T^{\min}$ and $R_T^{\max}$ are free parameters.

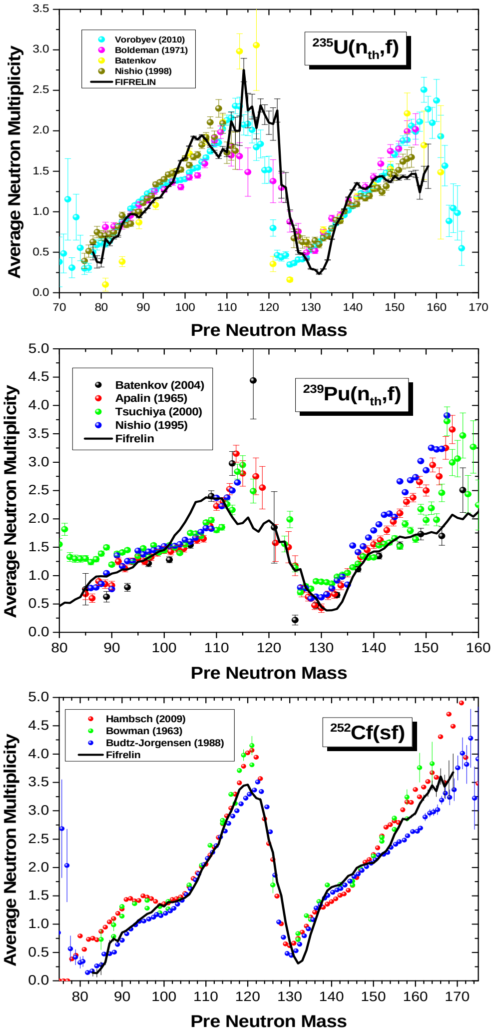

FIG. 31. (Color online) The average prompt neutron multiplicity as a function of fragment mass. `FIFRELIN` calculations (black curves) are compared to EXFOR data for ^{235}U(n_{th},f) (top), ^{239}Pu(n_{th},f) (middle) and ^{252}Cf(sf) (bottom).

The rotational energy E^{rot} is estimated from the rotating liquid drop model: $E^{\mathrm{rot}} = \hbar J(J+1)/2\Im$. The moment of inertia $\Im$ is assumed to be a fraction of the rigid body moment of inertia, $\Im = k_{\mathrm{rigid}}\Im_{\mathrm{rigid}}$ where k_{rigid} is a free parameter.

Each fission fragment is thus characterized by the quantities A_i, Z_i, J_i^{π}, E_i^* and E_i^{rot}. The fission fragment de-excitation is simulated using the Hauser-Feshbach model [202] which accounts for conservation of energy, spin and parity in the initial and final states. An improved numerical method has been recently developed to compute neutron and photon de-excitation, see Ref. [240]. The prompt neutron and gamma emission probabilities are

$$\begin{aligned} P(\varepsilon_n)d\varepsilon_n &\propto T_n(\varepsilon_n)\rho(Z,A-1,U-\varepsilon_n-S_n) \ , \\ P(\varepsilon_\gamma)d\varepsilon_\gamma &\propto T_\gamma(\varepsilon_\gamma)\rho(Z,A,U-\varepsilon_\gamma) \ , \end{aligned} \tag{76}$$

where T_n and T_γ are the neutron and gamma transmission coefficients while ρ is the level density. The neutron coefficient T_n is calculated employing TALYS-1.4 [181] with the Koning-Delaroche potential [232] and stored for use in the main program. The composite Gilbert Cameron Model (CGCM) [184] is employed for the level densities. Finally, T_γ is deduced from the strength functions in the enhanced generalized Lorentzian (EGLO) model [184].

2. *Results*

`FIFRELIN` has five free parameters: σ_L, σ_H, $R_T^{\rm min}$, $R_T^{\rm max}$ and $k_{\rm rigid}$. For each fissioning system investigated, these parameters are adjusted to obtain good agreement with the measured average light, $\overline{\nu}_L$; heavy, $\overline{\nu}_H$; and total, $\overline{\nu}$, prompt neutron multiplicities. If $\overline{\nu}_L$ and $\overline{\nu}_H$ are not measured, only $\overline{\nu}$ is used. The parameter values are given in Table 20. The results for the average prompt neutron multiplicities are given in Table 21.

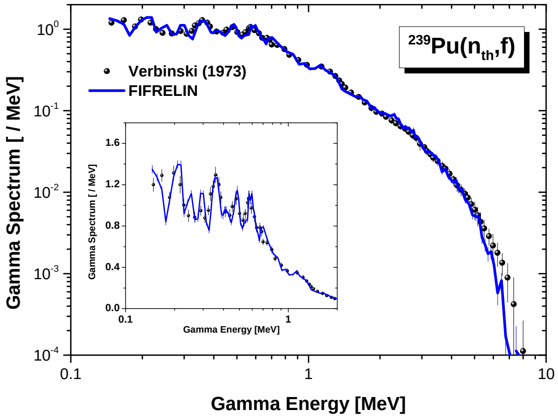

FIG. 32. (Color online) The calculated prompt fission gamma spectrum compared with the Verbinski data [246] for ^{239}Pu($n_{\rm th}$,f). The insert shows the low energy part of the photon spectrum.

Once the five free parameters are determined, 500000 fission events were simulated for each of the three systems discussed. `FIFRELIN` results for several observables are presented here. Others are shown in the code comparison section.

The calculated average prompt neutron multiplicity as a function of the fragment mass is compared to data in Fig. 31. Good agreement with the data is seen, despite its dispersion, in particular for ^{235}U($n_{\rm th}$,f) and ^{239}Pu($n_{\rm th}$,f).

The calculated prompt photon spectrum is shown in Fig. 32. There is good agreement with the Verbinski data [246]. The figure insert shows the low energy part of the photon spectrum. The fine structure seen by Verbinski can be reproduced nicely with `FIFRELIN`. Similar satisfactory results were obtained for other nuclei [247]. Other results can be found in the code comparison section.

C. `FREYA`

The event-by-event Monte Carlo fission model `FREYA` (Fission Reaction Event Yield Algorithm) has been developed through a collaboration between LLNL and LBNL. `FREYA1.0`, focused on neutron emission with a still primitive photon emission package, has been released [248]. `FREYA` incorporates the relevant physics with a few key parameters determined by comparison to data [249–255]. It simulates the entire fission process and produces complete fission events with full kinematic information on the emerging fission products and the emitted neutrons and photons, incorporating sequential neutron and photon evaporation from the fission fragments. `FREYA` is available for downloading at Ref. [256] and details of the inputs and how to use `FREYA` can be found in Ref. [248].

`FREYA` relies on data-related inputs of the fission yields, $Y(A)$, as a function of energy (for neutron-induced fission) and total fragment kinetic energy, TKE. Additionally, the Gaussian widths of the fragment charge distributions are based on previous measurements [251]. There are some universal inputs including ground-state masses, taken from data [185] and supplemented by theory [198] when required; fission barrier heights; and pairing energies and shell corrections. `FREYA` also has several input parameters that can depend on the identity of the fissile nucleus. These include:

dTKE,: the shift of the measured TKE required to match the average neutron multiplicity;

e_0,: the asymptotic level density parameter;

x,: the advantage in excitation energy given to the light fragment;

c,: the relative thermal fluctuations in the fragment temperature distribution;

$Q_{\rm min}$,: the energy above the neutron separation energy where photon emission begins to dominate over neutron emission; and

c_S,: the ratio of the "spin temperature" to the scission temperature.

In the remainder of this section, the functionality of `FREYA` is described more fully. First pre-fission neutron emission, necessary for a description of fission for incident neutron energies above the neutron separation energy for the fissile target, is described. Both multi-chance fission and pre-equilibrium neutron emission are included in `FREYA`. The mass and charge partition, in particular, the energy dependence of the fragment yields, is then discussed. The partition of the excitation energy between the two fragments, including the rotational energy, follows. Finally, fragment de-excitation by neutron and photon emission is described.

1. *Pre-fission Neutron Emission*

At low incident neutron energies, below a few MeV, the neutron is absorbed into the target nucleus resulting in an equilibrated compound nucleus which may have a variety of fates. Most frequently it will fission directly. But, since the compound nucleus was formed by neutron absorption, it is energetically possible for it to re-emit a neutron. In that circumstance, the daughter nucleus cannot fission and will de-excite by sequential photon emission. `FREYA` generally discards such events because it is designed to provide fission events (but their frequency is noted). Neutron evaporation from a fissionable compound nucleus is treated in the same manner as neutron evaporation from fission fragments, as described later. The possibility of pre-fission photon emission is ignored.

2. *Multichance Fission*

As the energy of the incident neutron is raised, neutron evaporation from the compound nucleus competes increasingly favorably with direct (first-chance) fission. The associated probability is given by the ratio of the fission and evaporation widths $\Gamma_{\rm f}(E^*)$ and $\Gamma_n(E^*)$ according to the transition-state estimate [257],

$$\frac{\Gamma_n(E^*)}{\Gamma_{\rm f}(E^*)} = \frac{2g_n\mu_n\sigma}{\pi\hbar^2}\frac{\int_0^{X_n}(X_n-x)\rho_n(x)dx}{\int_0^{X_{\rm f}}\rho_{\rm f}(x)dx} , \tag{77}$$

where $g_s = 2$ is the spin degeneracy of the neutron, μ_n is its reduced mass, and $\sigma = \pi R^2 = \pi r_0^2 A^{2/3}$. Furthermore, $\rho_n(x)$ is the level density in the evaporation daughter nucleus at the excitation energy x, whose maximum value is given by $X_n = Q_n = E^* - S_n$, where Q_n is the Q value for neutron emission and S_n is the neutron separation energy. Similarly, $\rho_{\rm f}(x)$ is the level density of the transition configuration for the fissioning nucleus, i.e., when its shape is that associated with the top of the fission barrier; the excitation x is measured relative to that barrier top, so its maximum value is $X_{\rm f} = E^* - B_{\rm f}$, where $B_{\rm f}$ is the height of the fission barrier (the corresponding quantity for neutron emission is the neutron separation energy S_n).

Neutron evaporation is possible whenever the excitation energy of the compound nucleus exceeds the neutron separation energy, $E^* > S_n$. The excitation energy of the evaporation daughter nucleus is $E^*_d = E^* - S_n - E$ where E is the kinetic energy of the relative motion between the emitted neutron and the daughter nucleus. Using the Hill-Wheeler expression for the transmission probability, it is determined whether subsequent fission is possible. The same procedure is then applied to the daughter nucleus, thus making further pre-fission neutron emission possible.

3. *Pre-equilibrium Neutron Emission*

At higher incident neutron energies, there is a growing chance that complete equilibrium is not established before the first neutron is emitted. Under such circumstances the calculation of statistical neutron evaporation must be replaced by a suitable non-equilibrium treatment. The two-component exciton model [258] is employed. (See also Ref. [259].)

A given many-exciton state consists of $p_{\nu(\pi)}$ neutron (proton) particle excitons and $h_{\nu(\pi)}$ neutron (proton) hole excitons. The total number of neutron (proton) excitons in the state is $n_{\nu(\pi)} = p_{\nu(\pi)} + h_{\nu(\pi)}$. The incident neutron provides the initial state consisting of a single exciton, namely a neutron particle excitation: $p_\nu = 1$ and $p_\pi = h_\nu = h_\pi = 0$.

The temporal development of the associated probability distribution $P(p_\nu, h_\nu, p_\pi, h_\pi)$ is described by a master equation that accounts for the transitions between different exciton states. The pre-equilibrium neutron emission spectrum is then given by

$$\begin{aligned}\frac{d\sigma_n}{dE} &= \sigma_{\rm CN} \sum_{p_\pi=0}^{p_\pi^{\max}} \sum_{p_\nu=1}^{p_\nu^{\max}} W(p_\pi, h_\pi, p_\nu, h_\nu, E) \\ &\quad \times \tau(p_\pi, h_\pi, p_\nu, h_\nu)\, P(p_\pi, h_\pi, p_\nu, h_\nu) \qquad (78)\end{aligned}$$

where $\sigma_{\rm CN}$ is the compound nuclear cross section, W is the rate for emitting a neutron with energy E from the exciton state $(p_\pi, h_\pi, p_\nu, h_\nu)$, τ is the lifetime of this state, and $P(p_\pi, h_\pi, p_\nu, h_\nu)$ is the (time-averaged) probability for the system to survive the previous stages and arrive at the specified exciton state. In the two-component model, contributions to the survival probability from both particle creation and charge exchange need to be accounted for. The survival probability for the exciton state $(p_\pi, h_\pi, p_\nu, h_\nu)$ can be obtained from a recursion relation starting from the initial condition $P(p_\nu = 1, h_\nu = 0, p_\pi = 0, h_\pi = 0) = 1$ and setting $P = 0$ for terms with negative exciton number. Particle emission is assumed to occur only from states with at least three excitons, $n_p + n_\nu \geq 3$ [259]. Excitons up to $p_\nu^{\max} = p_\pi^{\max} = 6$ are considered.

The emission rate, $W(p_\pi, h_\pi, p_\nu, h_\nu, E_k)$, is largely governed by the particle-hole state density, $\omega(p_\pi, h_\pi, p_\nu, h_\nu, E^*)$. The rate for a neutron ejectile of energy E is given by Ref. [260]

$$\begin{aligned}W(p_\pi, h_\pi, p_\nu, h_\nu, E_k) &= \frac{g_n}{\pi^2 \hbar^3} \mu_n E\, \sigma_{n,\rm inv} \\ \times \frac{\omega(p_\pi, h_\pi, p_\nu - 1, h_\nu, E^* - E - S_n)}{\omega(p_\pi, h_\pi, p_\nu, h_\nu, E^*)} & \qquad (79)\end{aligned}$$

where $\sigma_{k,\rm inv}$ is the inverse reaction cross section and E^* is the total excitation energy of the system. Although effectively negligible below a few MeV, the probability for pre-equilibrium emission grows approximately linearly to about 24% at 20 MeV.

The reaction cross sections used in Eqs. (78) and (79) define the overall magnitude of the cross sections for the pre-equilibrium processes. Since `FREYA` principally deals with probabilities, high accuracy is not required for the magnitude of the reaction cross sections. Therefore, the compound-nucleus cross sections and inverse cross sections were computed using the optical-model program `ECIS06` and the global optical model potential of Koning and Delaroche [232].

For each event generated, `FREYA` first considers the possibility of pre-equilibrium neutron emission and, if it occurs, a neutron is emitted with an energy selected from the calculated pre-equilibrium spectrum. Subsequently, the possibility of equilibrium neutron evaporation is considered, starting either from the originally agitated compound nucleus, e.g., ^{240}Pu*, or the less excited nucleus, ^{239}Pu*, remaining after pre-equilibrium neutron emission has occurred. Neutron evaporation is iterated until the excitation energy of a daughter nucleus is either below the fission barrier (in which case the event is abandoned) or the nucleus succeeds in fissioning.

4. *Mass and Charge Partition*

After any possible pre-fission processes, the compound nucleus, $^{A_0}Z_0$, is fission-ready, having an excitation energy E_0^*. The first task is to divide it into a heavy fragment $^{A_H}Z_H$ and a complementary light fragment $^{A_L}Z_L$. Since no quantitatively useful model is yet available for the calculation of the fission fragment mass yields, experimental data are invoked.

The mass yields $Y(A_f)$ of the fission fragments are assumed to exhibit three distinct modes, each one being of Gaussian form [261],

$$Y(A_f) = S_1(A_f) + S_2(A_f) + S_L(A_f)\ . \qquad (80)$$

The first two terms represent asymmetric fission modes associated with the spherical shell closure at $N = 82$ and the deformed shell closure at $N = 88$, respectively, while the last term represents a broad symmetric mode, referred to as super-long [161, 262]. Although the symmetric mode is relatively insignificant at low excitations, its importance increases with the excitation energy and ultimately dominates the mass distribution.

The asymmetric modes have a two-Gaussian form,

$$\begin{aligned} S_i &= \frac{N_i}{\sqrt{2\pi}\sigma_i} \left[\exp[-(A_f - \bar{A} - D_i)^2/2\sigma_i^2]\right. \\ &\quad \left. + \exp[-(A_f - \bar{A} + D_i)^2/2\sigma_i^2]\right], \end{aligned} \tag{81}$$

while the symmetric mode is given by a single Gaussian

$$S_L = \frac{N_L}{\sqrt{2\pi}\sigma_L} \exp[-(A_f - \bar{A})^2/2\sigma_L^2], \tag{82}$$

with $\bar{A} = \frac{1}{2}A_0$. Since each event leads to two fragments, the yields are normalized so that $\sum_A Y(A) = 2$. Thus,

$$2N_1 + 2N_2 + N_L = 2 \ , \tag{83}$$

apart from a negligible correction because A_f is discrete and bounded from both below and above.

Most measurements are of fission *product* yields [263], the yields after prompt neutron emission is complete. However, `FREYA` requires fission *fragment* yields, i.e., the probability of a given mass partition before neutron evaporation has begun. In the absence of such data for Pu, more detailed data for $^{235}\mathrm{U}(n,\mathrm{f})$ as functions of both mass and total kinetic energy, $Y(A_f, \mathrm{TKE})$ for $E_n \leq 6$ MeV [243] are employed. Guided by the energy dependence of these data, together with other available data on the product yields from $^{235}\mathrm{U}(n,\mathrm{f})$ [264] and $^{239}\mathrm{Pu}(n,\mathrm{f})$ [265] an approximate energy dependence of the fragment yields up to $E_n = 20$ MeV is derived.

The displacements, D_i, away from symmetric fission in Eq. (81) are anchored above the symmetry point by the spherical and deformed shell closures. Because these occur at specific neutron numbers, the values of D_i are assumed to be energy independent. The values obtained from the fit of the displacements for $^{235}\mathrm{U}(n,f)$ are $D_1 = 23.05$ and $D_2 = 16.54$. The values of D_i should be smaller for ^{239}Pu than for ^{235}U, $D_i^{\mathrm{U}} - D_i^{\mathrm{Pu}} \approx 2$, because the larger Pu mass is closer to the shell closure locations. The values of D_i for first chance fission of $A_0 = 240$ are $D_1 = 20.05$ and $D_2 = 14.54$ [251]. These values are increased by $\frac{1}{2}$ for each pre-fission neutron emitted.

The widths of the asymmetric modes, σ_i, are expanded to second order in energy: $\sigma_i = \sigma_{i0} + \sigma_{i1}E_n + \sigma_{i2}E_n^2$. The energy dependence of σ_i is fixed from the $^{235}\mathrm{U}(n,f)$ fragment yields as a function of mass and total kinetic energy of Ref. [243]. The general energy dependence of the parameters is assumed to be the same even though the values at $E_n = 0$ are different. When the fissioning nucleus is the original system, then E_n is the value of the actual incident neutron energy. But when the fissioning nucleus is lighter, i.e., when ν_0 pre-fission neutrons have been emitted, then E_n is the equivalent incident neutron energy, i.e., the incident energy that would generate the given excitation energy E_0^* when absorbed by the nucleus ${}^{A_0-\nu_0}Z_0$. The width of the super-long component, σ_L, is assumed to be constant, independent of both the incident energy and the fissioning isotope, $\sigma_L = 12$.

The normalizations N_i change only slowly with incident energy until symmetric fission becomes more probable, after which they decrease rapidly. The energy dependence of N_i is modeled by a Fermi distribution,

$$N_i = N_i^0 \left(1 + \exp[(E_n - E_1)/E_2]\right)^{-1} \ . \tag{84}$$

The midpoint and the width are assumed to be the same for both modes so that the relative normalizations for the asymmetric modes have the same energy dependence. The values of E_1 and E_2 are identical for all Z because the transition from asymmetric to more symmetric fission can depend on Z and A [264, 265]. With N_1 and N_2 given by Eq. (84), N_L is determined from Eq. (83). For the values currently used in `FREYA`, see Ref. [248].

The overall broadening of the yields at higher energies is due in part to the larger widths of the S_1 and S_2 modes at higher energies and in part to the increased contribution of the S_L component. While σ_L does not change, the larger N_L enhances the importance of this component.

Once the Gaussian fit has been performed, it is straightforward to make a statistical selection of a fragment mass number A_f. The mass number of the partner fragment is then readily determined since $A_L + A_H = A_0 - \nu_0$.

The fragment charge, Z_f, is selected subsequently. A Gaussian form is employed, following Ref. [266],

$$P_{A_f}(Z_f) \ \propto \ \exp[-(Z_f - \bar{Z}_f(A_f))^2/2\sigma_Z^2] \,, \tag{85}$$

with the condition that $|Z_f - \bar{Z}_f(A_f)| \leq 5\sigma_Z$. The centroid is determined by requiring that the fragments have, on average, the same charge-to-mass ratio as the fissioning nucleus, $\bar{Z}_f(A_f) = A_f Z_0/A_0$. The dispersion is the measured value, $\sigma_Z = 0.5$ [266]. The charge of the complementary fragment then follows using $Z_L + Z_H = Z_0$.

Energy partition Once the partition of the total mass and charge among the two fragments has been selected, the Q value associated with that particular fission channel is

$$Q_{LH} \;=\; M(^{240-\nu_0}\mathrm{Pu}^*) - M_L - M_H \;. \tag{86}$$

`FREYA` takes the required nuclear ground-state masses from the compilation by Audi et al. [185], supplemented by the calculated masses of Möller et al. [198] when no data are available. The Q_{LH} value for the selected fission channel is then divided up between the total kinetic energy (TKE) and the total excitation energy (TXE) of the two fragments.

Near symmetry, the fission fragments are mid-shell nuclei subject to strong deformations. Thus the scission configuration will contain significant deformation energy and a correspondingly low TKE. At $A_H = 132$, the heavy fragment is close to the doubly-magic closed shell having $Z_H = 50$ and $N_H = 82$ and is therefore resistant to distortions away from sphericity. The scission configuration is fairly compact here so that TKE is a maximum even though the complementary light fragment is far from a closed shell and thus significantly deformed.

The TKE values employed were generally obtained in experiments using thermal neutrons and they are not typically available at higher incident energy. The energy-dependent average TKE as a function of the heavy fragment mass is assumed to take the form

$$\overline{\mathrm{TKE}}(A_H, E_n) \;=\; \overline{\mathrm{TKE}}_{\mathrm{data}}(A_H) + d\mathrm{TKE}(E_n) \;. \tag{87}$$

The first term is extracted from the data while the second term is a parameter adjusted to ensure reproduction of the measured energy-dependent average neutron multiplicity, $\overline{\nu}(E_n)$. In a particular event, the actual TKE is obtained by adding a thermal fluctuation to the above average, as explained later.

Once the average total fragment kinetic energy has been obtained, the average combined excitation energy in the two fragments follows by energy conservation,

$$\overline{\mathrm{TXE}} \;=\; \overline{E}^*_L + \overline{E}^*_H \;\doteq\; Q_{LH} - \overline{\mathrm{TKE}} \;-E^{\mathrm{rot}}_L - E^{\mathrm{rot}}_H . \tag{88}$$

The first relation indicates that the total excitation energy is partitioned between the two fragments. The rotational energy of the two fragments is neglected in the version of `FREYA` employed in the creation of these evaluations. As is common, the fragment level densities are assumed to be of the form $\rho_i(E^*_i) \sim \exp(2\sqrt{a_i U_i})$, where U_i is the effective statistical energy in the fragment.

The level density parameter is computed based on the back-shifted Fermi gas (BSFG) model [196, 267],

$$\tilde{a}_i(E^*_i) = \frac{A_i}{e_0}\left[1 + \frac{\delta W_i}{U_i}\left[1 - \exp(-\gamma U_i)\right]\right] \tag{89}$$

where $U_i = E^*_i - \Delta_i$ and $\gamma = 0.05$ [268]. The pairing energy of the fragment, Δ_i, and its shell correction, δW_i, are tabulated in Ref. [267] based on the mass formula of Koura et al. [269] where e_0 is a model parameter. If the shell corrections are negligible, $\delta W \approx 0$, or the available energy, U, is large, then this renormalization is immaterial and the BSFG level-density parameter is proportional to the mass, $\tilde{a}_i \sim A_i/e_0$. In Ref. [251], $e_0{\sim}10$ MeV.

If the two fragments are in mutual thermal equilibrium, $T_L = T_H$, the total excitation energy will, on average, be partitioned in proportion to the respective heat capacities which in turn are proportional to the level density parameters, i.e., $\overline{E}^*_i \sim \tilde{a}_i$. `FREYA` therefore first assigns average excitation energies based on such an equipartition,

$$\acute{E}^*_i \;=\; \frac{\tilde{a}_i(\tilde{E}^*_i)}{\tilde{a}_L(\tilde{E}^*_L) + \tilde{a}_H(\tilde{E}^*_H)}\,\overline{\mathrm{TXE}} \;, \tag{90}$$

where $\tilde{E}^*_i = (A_i/A_0)\overline{\mathrm{TXE}}$. Subsequently, because the observed neutron multiplicities suggest that the light fragments tends to be disproportionately excited, the average values are adjusted in favor of the light fragment

$$\overline{E}^*_L = x\acute{E}^*_L \;,\; \overline{E}^*_H = \overline{\mathrm{TKE}} - \overline{E}^*_L \;, \tag{91}$$

where x is an adjustable model parameter expected to be larger than unity.

After the mean excitation energies have been assigned, `FREYA` considers the effect of thermal fluctuations. In Weisskopf's statistical model of the nucleus, which considers the excited nucleus as a degenerate Fermi gas, the mean excitation of a fragment is related to its temperature T_i by $\overline{E}^*_i = \tilde{a}_i T_i^2$ [150] and the associated variance in the excitation is $\sigma^2_{E_i} = -\partial^2 \ln \rho_i(E_i)/\partial E_i^2 = 2\overline{E}^*_i T_i$. Therefore, for each of the two fragments, a thermal energy fluctuation δE^*_i is sampled from a Gaussian distribution of variance $2c\overline{E}^*_i T_i$ and modify the fragment excitations accordingly, arriving at

$$E^*_i \;=\; \overline{E}^*_i + \delta E^*_i \;,\; i = L, H. \tag{92}$$

Due to energy conservation, there is a compensating opposite fluctuation in the total kinetic energy, so that

$$\mathrm{TKE} \; = \; \overline{\mathrm{TKE}} - \delta E_L^* - \delta E_H^* \; . \tag{93}$$

The factor c multiplying the variance can, in principle, be tuned to the neutron multiplicity distribution $P(\nu)$. As a default value, `FREYA` takes $c = 1.0$.

It is assumed that neutron emission continues until no further neutron emission is energetically possible, i.e., when $E_d^* < S_n + Q_{\min}$, where S_n is the neutron separation energy in the prospective daughter nucleus, $S_n = M({}^{A_d}Z_d) - M({}^{A_d-1}Z_d) - m_n$. The value $Q_{\min} = 0.01$ MeV is chosen as a default so that neutrons can be emitted even if the energy is very close to the neutron separation energy.

In Ref. [254], the fissile nucleus is allowed to have some initial angular momentum. In addition to the rigid rotation of the dinuclear configuration prior to scission, assumed to be inherited by the fragments, the fragments also acquire fluctuations around the rigid rotation axis. Of these fluctuations, the wriggling and bending modes, with rotating in the same or opposite sense around an axis perpendicular to the dinuclear axis. These fluctuations are assumed to be statistically excited during scission. Thus, in each event, the values of $\boldsymbol{s}_\pm$, the spin of the normal modes (the plus refers to wriggling modes (with parallel rotations) while the minus refers to bending modes (with opposite rotations)) are being sampled from distributions of the form

$$\begin{aligned} &P_\pm(\boldsymbol{s}_\pm = (s_\pm^x, s_\pm^y, 0))\, ds_\pm^x ds_\pm^y \sim \\ &\quad \exp(-s_\pm^2/2\mathcal{I}_\pm T_S)\, ds_\pm^x ds_\pm^y \; , \end{aligned} \tag{94}$$

where the "spin temperature" T_S is regarded as a global but somewhat adjustable parameter, $T_S = c_S T_{\rm sc}$ where $T_{\rm sc}$ is the scission temperature. As the default, $c_S = 1$, corresponding to the assumption that the spin degrees of freedom are fully equilibrated at scission. This value of c_S yields $\overline{S}_L{\sim}6.2\hbar$, $\overline{S}_H{\sim}7.6\hbar$ in rather good agreement with the average energy of photons emitted in fission.

The moments of inertia, $\mathcal{I}_\pm$, depend on the moments of inertia of the light and heavy fragments, $\mathcal{I}_L$ and $\mathcal{I}_H$, as well as the moment of inertia of the relative fragment motion, $\mathcal{I}_R$. The rigid rotator moment of inertia, $\mathcal{I} = (c_I/5)MR^2$ where M and R are the mass and radius of the fragment, $R = r_0 A^{1/3}$, is employed with the commonly accepted value $c_I = 0.5$ [253, 254].

5. *Neutron Evaporation*

Neutron emission is treated by iterating a simple neutron evaporation procedure for each of the two fragments separately.

At each step in the evaporation chain, the excited mother nucleus ${}^{A_i}Z_i$ has a total mass equal to its ground-state mass plus its excitation energy, $M_i^* = M_i^{\rm gs} + E_i^*$. The Q-value for neutron emission from the fragment is then $Q_n = M_i^* - M_f - m_n$, where M_f is the ground-state mass of the daughter nucleus and m_n is the mass of the neutron. (For neutron emission, $A_f = A_i - 1$ and $Z_f = Z_i$.) The Q-value is equal to the maximum possible excitation energy of the daughter nucleus, achieved if the final relative kinetic energy vanishes. The temperature in the daughter fragment is then maximized at $T_f^{\rm max}$. Thus, once Q_n is known, the kinetic energy of the evaporated neutron may be sampled. `FREYA` assumes that the angular distribution is isotropic in the rest frame of the mother nucleus and uses a standard spectral shape [150],

$$f_n(E) \; \equiv \; \frac{1}{N_n}\frac{dN_n}{dE} \; \sim \; E\, \exp(-E/T_f^{\rm max}) \; , \tag{95}$$

which can be sampled efficiently [250].

Although relativistic effects are very small for neutron evaporation, they are taken into account to ensure exact conservation of energy and momentum, which is convenient for code verification purposes. The sampled energy E represents the *total* kinetic energy in the rest frame of the mother nucleus, i.e., it is the kinetic energy of the emitted neutron *plus* the recoil energy of the excited residual daughter nucleus. The daughter excitation is then given by

$$E_d^* \; = \; Q_n - E \; . \tag{96}$$

and its total mass is thus $M_d^* = M_d^{\rm gs} + E_d^*$. The magnitude of the momenta of the excited daughter and the emitted neutron can then be determined [250]. Sampling the direction of their relative motion isotropically, the two final momenta are obtained. These are subsequently boosted into the overall reference frame by the appropriate Lorentz transformation.

This procedure is repeated until no further neutron emission is energetically possible, i.e., when $E_d^* < S_n$.

6. *Photon Radiation*

After the neutron evaporation has ceased, the excited product nucleus may de-excite by sequential photon emission. `FREYA` treats this process in a manner analogous to neutron evaporation, i.e., as the statistical emission of massless particles. This treatment is currently being refined to include more realistic strength functions, as well as transitions between discrete levels.

There are two important technical differences relative to the treatment of neutron emission. There is no separation energy for photons and, since they are massless, there is no natural end to the photon emission chain. An infrared cutoff of 200 keV is therefore introduced. Whereas the neutrons may be treated by nonrelativistic kinematics, the photons are ultrarelativistic. As a consequence, their phase space has an extra energy factor,

$$f_\gamma(E) \equiv \frac{1}{N_\gamma}\frac{dN_\gamma}{dE} \sim E^2 \exp(-E/T_f^{\max}) \ . \tag{97}$$

The photons are assumed to be emitted isotropically with energies sampled from Eq. (97) [250]. The procedure is repeated until the available energy is below the specified cutoff, yielding a number of kinematically fully-characterized photons for each of the product nuclei.

The above procedure is repeated until the available statistical excitation energy has been exhausted. The angular momentum is then disposed of by simulating a stretched E2 cascade. Thus, as long as $S > 2$, the angular momentum will be reduced by two units and a photon is emitted with energy $E = \frac{1}{2}[S^2 - (S-2)^2]\hbar^2/\mathcal{I} = 2(S-1)\hbar^2/\mathcal{I}$. At the end of the cascade, when $S < 2$, the remaining excitation energy is carried away by a single final photon. This approximate procedure is currently being refined.

D. `FINE`

The (FIssion Neutron Emission) `FINE` code was developed by N. Kornilov and is described in detail in Ref. [270]. Only a minimal description is given here.

`FINE` constructs a two-dimensional fission fragment yield, $Y(A, \mathrm{TKE})$ from one-dimensional data on $Y(A)$ and $\mathrm{TKE}(A)$. The multimodal model of fragment yields in Ref. [161] is employed. The unchanged charge distribution is used to obtain the fragment charges. The system is assumed to be in thermal equilibrium when the excitation energy is split between the light and heavy fragments. For each mass split, the energy release and binding energy is estimated for up to 10 neutrons in the de-excitation cascade. Neutron emission by evaporation is assumed to proceed only after the fragments are fully accelerated. The results, given in the lab frame, were validated by comparison to data.

E. `GEF`

The `GEF` model (GEneral description of Fission observables) is a semi-empirical model that combines new experimental information [271–274], with several model parameterizations that make it amenable to generalization [217, 275–279]. It has been developed by Schmidt and Jurado and is documented in the report of Ref. [280].

`GEF`, like the other codes described here, is a Monte Carlo code that provides all correlations between the different fission observables. Due to its generality, `GEF` can be applied to nuclei between polonium and $Z = 110$ and beyond, including systems for which no experimental information exists. Since it employs simple parameterizations that can be applied to a wide range of nuclei, `GEF` is a very fast code. For more detail, see Ref. [280] and the accompanying paper in this volume [221].

While `GEF` is a Monte Carlo (MC) model, it employs a different methodology from all other MC approaches. The main differences are in the semi-empirical parameterizations of the fragment distributions and excitation energies. Because once the fragments are chosen, their excitation energies are calculated employing model parameterizations dependent on A and Z, `GEF` does not have to rely on models or data on the fragment TKE to obtain the total excitation energy or to partition the TXE between fragments. Instead the TKE is calculated and is, in fact, an output of `GEF` while it is a required input for the other codes discussed here.

The remainder of this section describes the model of fragment distributions briefly; the calculation of the fragment excitation energy at scission; and a few general statements about neutron and photon emission in `GEF`.

`GEF` is able to calculate fission fragments yields over a range of incident neutron energies due to its parameterization of fission barriers, $B_f \approx B_f^{\rm mac} - E_{\rm gs}^{\rm exp} + E_{\rm gs}^{\rm mac} + 14n/\sqrt{A}$ where $n = 0, 1,$ or 2 for even-even, odd-even (even-odd), or odd-odd nuclei, respectively. The Thomas-Fermi model is employed to calculate $B_f^{\rm mac}$ [281] and $E_{\rm gs}^{\rm mac}$ [276] while $E_{\rm gs}^{\rm exp}$ is taken from the 2012 Atomic Mass Evaluation. If $E_{\rm gs}^{\rm exp}$ is unavailable, $E_{\rm gs}^{\rm exp} - E_{\rm gs}^{\rm mac}$ is replaced by the microscopic contribution,

$E^{\rm mic}_{\rm gs}$, calculated in Ref. [198]. Additional contributions to the barrier height include Z-dependent parameterizations of an empirical correction, ΔB_f, and the difference in energy between the outer and inner barriers.

The fission barrier heights play an important role in `GEF` in the determination of the fragment yields. The potential energy landscape between the outer fission barrier and the scission point is characterized by valleys with constant mass-asymmetric deformations associated with the shell structure of the fissioning system. The `GEF` model assumes that the shells on the fission path are determined by the fragment shells, and the shell effects forming the fission valleys are generalized as a function of the fragment charge and neutron number. `GEF` attributes the empirical fission yields as well as their mass asymmetry and charge polarization to statistical equilibrium at different characteristic times with specific potential energy properties and characteristic temperatures. It is the dependence on temperature that governs the energy dependence of the fragment yields. For more information, see Ref. [221].

In `GEF`, the level densities are calculated with a modified composite formula with a constant temperature below and a shifted Fermi gas description above a critical pairing energy. The critical energy is that value where the level densities and their slopes are equal in the two descriptions. For more detail, see Ref. [278].

The excitation energies of the light and heavy fragments in `GEF` include components from the intrinsic energy at scission, $E^{\rm int}_{L,H}$, shared between the two fragments according to their level densities; the collective energy, $E^{\rm coll}$, shared equally between the two fragments; the deformation energy at scission relative to a spherical shape, $E^{\rm def}_{L,H}(\beta_{L,H})$; and the rotational energy, $E^{\rm rot}_{L,H}$,

$$E^*_{L,H} = E^{\rm int}_{L,H} + 0.5E^{\rm coll} + E^{\rm def}_{L,H}(\beta_{L,H}) + E^{\rm rot}_{L,H}\,. \tag{98}$$

The total intrinsic energy, $E^{\rm int}$, depends on the incident neutron energy and neutron binding energy (for neutron-induced fission), the barrier height, and the dissipation energy. As previously mentioned, it is partitioned between the two fragments based on their level densities. The deformation parameter, $\beta_{L,H}$, is parameterized as a function of fragment charge. The rotational energy is calculated similar to `CGMF` and `FIFRELIN`. The total excitation energy is thus TXE= $E^*_L + E^*_H$. Therefore TKE is the difference between the energy release (fission Q value, fixed by the fragment Z and A) and TXE. The energetics of fission and the `GEF` energy sorting mechanism are more completely described in Refs. [217, 282].

The de-excitation of the fission fragments, after scission, by neutron and photon emission, including the acceleration phase, is calculated within a statistical model. The de-excitation of each individual fragment is followed, with the emitted neutron energy and momentum sampled by Monte Carlo. Changes in the angular momentum of the fragments during neutron and statistical photon emission is assumed to be negligible [283] and is neglected. `GEF` considers neutron-photon competition for energies higher than the neutron separation energy. The photon strength functions are calculated according to Ref. [284] assuming axially-symmetric shapes. When the yrast line is reached, the angular momentum is carried away by a cascade of E2 gammas. See also Ref. [221].

GEF have been used by Schmidt and Jurado to calculate the emission of prompt neutrons and gammas for neutron-induced reactions and spontaneous fission of selected nuclei [221, 280].

F. Monte Carlo Code Comparisons

As an exercise, comparisons between several of the codes discussed in this section, as well as the `PbP` model described earlier are made here for several prompt fission neutron observables in the thermal-neutron induced fission of ^{235}U. All codes used a common set of fission fragment yield as a function of mass, charge, and kinetic energy, thereby removing one important source of discrepancy between the numerical results. The goal of this exercise is not to assess or even discuss which code gives the best representation of the data since all codes have additional parameters and approaches to better match data. This exercise is only intended to provide a sense of the range of results to be expected using similar codes to treat the problem of prompt fission neutron emissions.

All numerical results shown below were obtained by considering ^{235}U($n_{\rm th}$,f) with the fission fragment yields, $Y(A,{\rm TKE})$ obtained from IRMM [285, 286]. They were complemented by Wahl's systematics to obtain the charge distribution for each mass chain.

Figures 33–37 illustrate the results obtained with `FIFRELIN`, `FREYA`, `PbP` and `CGMF`, for the average prompt fission neutron spectrum (Fig. 33), the prompt neutron multiplicity distribution $P(\nu)$ (Fig. 34), the average neutron multiplicity as a function of fragment mass (Fig. 35), the average neutron kinetic energy in CMS as a function of fragment mass (Fig. 36), and the average neutron multiplicity as a function of the total kinetic energy (Fig. 37).

The calculated average prompt fission neutron spectra are rather similar in the outgoing neutron energy range of $1-5$ MeV, but important differences appear in both the high and low energy tails. As expected, the `FREYA` code, based on Weisskopf evaporation, gives a harder high energy tail than the Hauser-Feshbach codes `FIFRELIN` and `CGMF`. The softest spectrum is obtained with `CGMF`, while `PbP` results are comparable to `FIFRELIN`. At the lowest energies however,

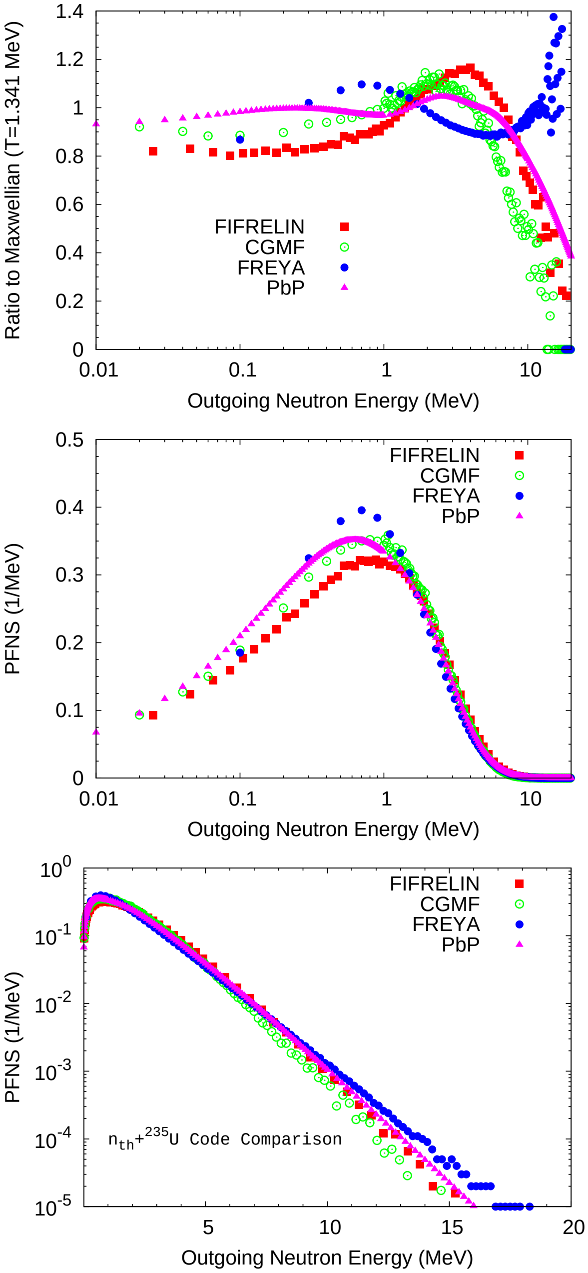

FIG. 33. (Color online) Average prompt fission neutron spectra.

TABLE 22. Calculated prompt fission neutron multiplicity distributions for ^{235}U($n_{\rm th}$,f).

	`FIFRELIN`	`CGMF`	`FREYA`	`PbP`
P(0)	0.072	0.070	0.016	0.026
P(1)	0.159	0.140	0.132	0.187
P(2)	0.312	0.291	0.375	0.323
P(3)	0.249	0.273	0.341	0.283
P(4)	0.154	0.167	0.122	0.131
P(5)	0.045	0.051	0.013	0.045
P(6)	0.008	0.009	6.2e-4	5.1e-3
P(7)	7.3e-4	6.3e-4	5.0e-5	0.0
P(8)	3.3e-5	4.7e-5	1.0e-5	0.0
$\langle\overline{\nu}\rangle$	2.426	2.517	2.464	2.458
$\langle\overline{\nu}(\overline{\nu}-1)\rangle$	5.147	5.521	4.547	4.956

below 1 MeV, `FIFRELIN` is lower than the rest of the calculations and `CGMF` and `PbP` are rather similar. The maximum

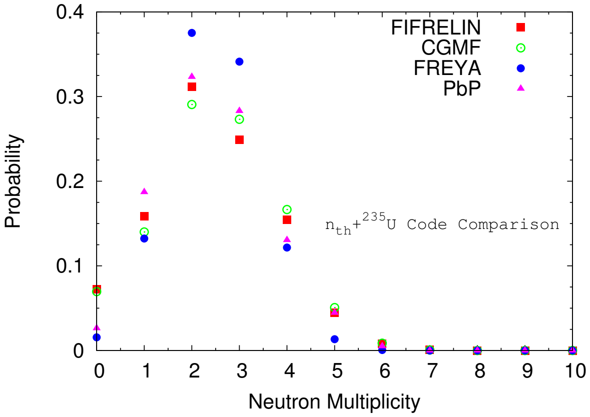

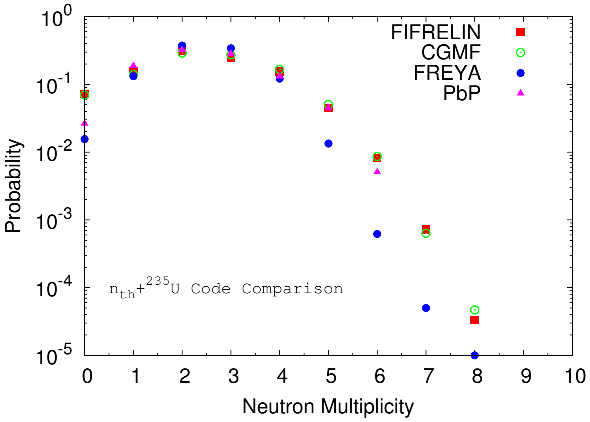

FIG. 34. (Color online) Prompt fission neutron multiplicity distributions on a linear scale (top) and log scale (bottom) to better show the high multiplicity tail of the distributions.

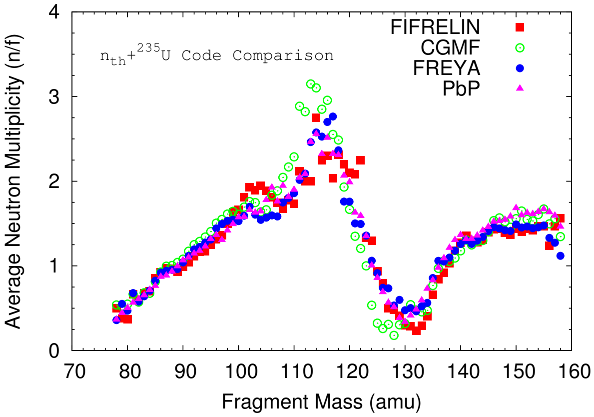

FIG. 35. (Color online) Average prompt fission neutron multiplicity as a function of the fragment mass.

differences observed between the codes are ∼20% near 1 MeV and up to a factor of 2 at 10 MeV. Note that the shape of the `FREYA` code is significantly different than others, with a maximum around 800 keV, while the `CGMF` and `PbP` maximum is ∼1–2 MeV while `FIFRELIN` reaches the maximum at 4 MeV.

Variations in the calculated neutron multiplicity distribution $P(\nu)$ can be seen in Fig. 34, as well as in Table 22 summarizing the average, variance and standard deviations of the calculated neutron multiplicity distributions. The calculated average neutron multiplicities differ by a maximum of ∼3.6%. The average value of the initial TKE distribution used in this code comparison exercise is $\langle \mathrm{TKE} \rangle = 169.4$ MeV, about 1 MeV lower than the "recommended" value of 170.5 ± 0.5 MeV [287]. Therefore, one would expect the predicted $\overline{\nu}$ to be larger than the evaluated value of about 2.42 for $^{235}\mathrm{U}(n_{\mathrm{th}},\mathrm{f})$, except for `FIFRELIN` since its five free parameters were tuned to reproduce $\overline{\nu}$.

All codes produce similar trends for the mass-dependent average neutron multiplicity $\overline{\nu}(A)$ (see Fig. 35) although a

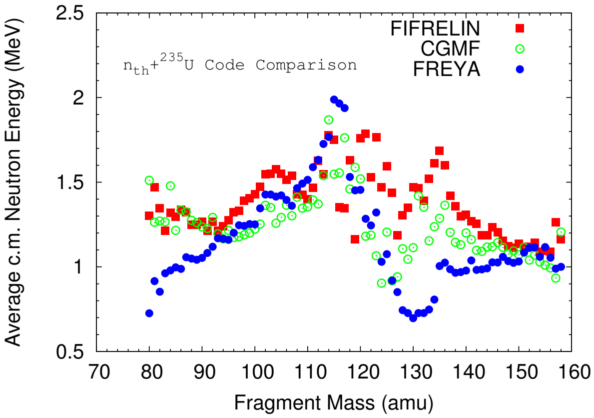

FIG. 36. (Color online) Average prompt fission neutron kinetic energy (CMS) as a function of the fragment mass.

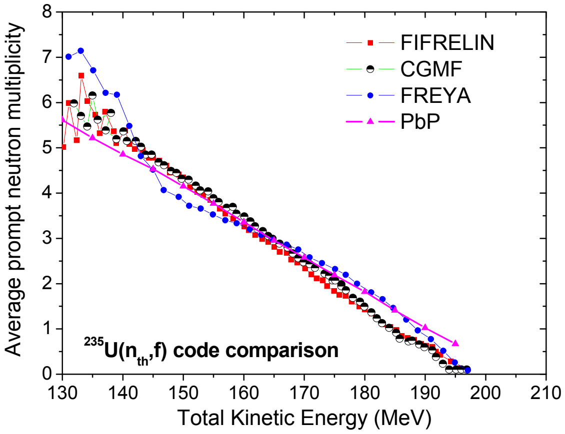

FIG. 37. (Color online) Average prompt fission neutron multiplicity as a function of the fragment total kinetic energy.

few important differences are noticeable. The calculated location of the minimum near $A\sim130$ is lower for `CGMF`, higher for `FIFRELIN`, and somewhat in the middle for both `FREYA` and `PbP`. Also, a higher neutron multiplicity is calculated near the maximum at $A\sim115$ by `CGMF` than the other codes. Because $\overline{\nu}(A)$ is often used to constrain the excitation energy sharing between the light and heavy fragments, and is therefore somewhat fitted, this quantity might not be of as much interest for this particular comparison. Of greater interest is the mass-dependent neutron kinetic energy, $\langle\epsilon_{\rm cm}\rangle(A)$, shown in Fig. 36. Large discrepancies appear between the different code predictions, reflecting differences among the level density prescriptions for the fission fragments used in the various codes. Note that the differences are largest near the double shell closure $A\sim132$.

Finally, the code predictions for the average neutron multiplicity as a function of TKE are shown in Fig. 37. All results describe the expected trend of decreasing $\overline{\nu}$ with increasing TKE, or equivalently decreasing total excitation energy. Near TKE = 200 MeV, the calculated neutron multiplicity goes to zero, as one reaches the maximum Q-value of the fission reaction. `CGMF` and `FIFRELIN` follow a very similar trend, while both `PbP` and `FREYA` have a slightly softer slope. Rather large discrepancies appear below $A\sim140$, but the Monte Carlo statistics become rather poor in this mass region.

VI. EVALUATION METHODOLOGIES

This section examines various technical issues associated with the evaluation of PFNS shape data, with a focus on discussions held and lessons learned during the course of the present CRP. Particularly valuable insights gained during the course of this CRP are separated from the rest of the text as italicized bullets through Sect. VI.F. Here we stress one valuable lesson learned from this endeavor:

- *While the evaluation of PFNS data resembles cross-section data evaluation in several respects, and many of the same computational tools are employed, there are some important distinctions that cannot be ignored in the quest to obtain "reasonable" evaluated PFNS evaluations.*

Since the prompt fission neutron spectrum (PFNS) is a probability distribution function, i.e., a shape, by definition its integral over the entire possible outgoing neutron energy range should equal unity. In other words, a PFNS is a normalized distribution function.

A. PFNS Scaling Procedures

In a comparison of different experimental PFNS data sets from various detectors, the normalizations of these data may be quite different, even if neutron emission from neutron-induced fission for a particular isotope is measured relative to the PFNS of ^{252}Cf(sf) in the same experimental setup to avoid calibrating the detector efficiency. There are many possible reasons for this difference, including sample mass differences, corrections for neutron scattering unique to a particular experiment, detector geometry, etc. If the intent of this CRP was to evaluate absolute neutron yields, i.e., $\overline{\nu}$, then all these effects would need to be understood and taken into account by the evaluators, based on the experimental documentation. However, as pointed out in the Introduction, the focus here is on the **shape** of the PFNS, not on the absolute yields. While this emphasis results in considerable simplification of the evaluation effort, it also involves certain technical considerations that are not encountered in cross-section data evaluation. In particular, the data sets need to be **scaled** in such a way that they become comparable for a PFNS evaluation. The main technical aspects involved in scaling PFNS data are discussed briefly in general terms here since, for the most part, they are documented in considerable detail in recent publications [141, 147, 288].

Model calculations of the PFNS differ in several respects from experimental PFNS data. In the present context, the most important difference is that [38]:

- *Model representations of the PFNS are generally inherently normalized so that integration over the entire spectral energy range with respect to the outgoing neutron energy, E, yields unity regardless of the model parameters.*

The above constraint also imposes certain restrictions on modeled PFNS covariances which are derived from consideration of uncertainties in the model parameters. There are also important implications for PFNS data evaluation methodologies. These points are discussed in more detail in a later section of this paper.

A fundamental principle of data evaluation is that the inputs to an evaluation should be comparable; otherwise one is dealing with a proverbial “apples” and “oranges” situation which, in an evaluation context, clearly leads to meaningless results. Consequently:

- *PFNS data sets that will be included in an evaluation need to prepared so that they are mathematically “comparable”* .

For example, if an evaluation is to be performed using a defined energy-group structure, then all the data sets should be numerically adjusted to conform to this group structure as much as possible without distorting the inherent spectrum information provided by each set. The same concept applies if an energy-point approach is employed where the data are adjusted to a common selected energy node structure. In some evaluation codes these tasks may be accomplished internally without direct intervention by the evaluator, e.g., Refs. [289–291]. The purpose for doing this is to prepare the diverse data sets so that they can be treated as comparable. These techniques apply to cross section data evaluation as well as to PFNS data evaluation, as discussed in , e.g., Refs. [141, 147, 292]. However, scaling is an additional step in preparing PFNS data evaluations that is usually not needed for cross section evaluations since cross section data sets are assumed to be properly normalized.

- *There is no unique way to scale diverse PFNS data sets prior to their evaluation.*

Several approaches to scaling PFNS data have been suggested, as described in the literature, e.g., Refs. [55, 56, 141, 288]. The scaling approach described here is based on Ref. [141] since it appears to be conceptually intuitive as well as flexible. In this approach, the operations of scaling PFNS and evaluating them are treated separately. In Ref. [55] these two procedures are integrated owing to the nature of the software used by the authors in their analyses [289–291]. The reader can refer to the mentioned references to gain an understanding of the various alternative approaches to the scaling issue.

Conceptually, scaling according to Ref. [141] involves multiplying each original PFNS data set by a constant factor specific to that set so that the adjusted PFNS can be treated as comparable. The corresponding covariance matrix for the original data set is then scaled by multiplying it by the square of that same constant. In principle, scaling should be applied to both experimental and modeled PFNS data before performing an evaluation. Of course, since modeled PFNS are usually unit normalized, as mentioned above, this fact may need to be taken into consideration, especially when considering the covariances of modeled PFNS. For example, if the modeled PFNS is treated as the "anchor shape", then, for the purposes of the evaluation, the scale factor for this spectrum will be exactly unity. The important point to grasp in the context of evaluating shape data is:

- *The absolute magnitudes of the scale values are generally unimportant when scaling data sets; only the* ***relative*** *magnitudes of the constant scale factors for the data sets included in the evaluation are of consequence.*

Several closely-related techniques for deriving constant scale factors are described in Ref. [141]. They are illustrated in that report by several numerical examples involving hypothetical PFNS data.

The choice of a particular technique to derive the scale factors employed within the framework described in Ref. [141] is often driven by the characteristics of the collection of PFNS data available for an evaluation. Generally speaking, modeled PFNS sets include numerical values for each spectral energy group (or energy node) whereas experimental PFNS sets tend to be more restrictive owing to experimental limitations such as poor statistics for high-energy neutrons, detector response energy-range limitations, etc. All of these techniques involve specifying an anchor shape to which all PFNS are scaled. This may be a modeled PFNS that spans the entire energy range, or one generated by comparing values of a selected ensemble of modeled and/or experimental PFNS data sets over a limited energy range where all energy groups (or nodes) are represented by all the spectra. It might even be simply an ad hoc but plausible guide to the shape of the data based on general physical considerations, e.g., [55, 56]. The techniques used to determine the scale factors range from calculations of simple ratios of sums of PFNS values (with or without weighting based on uncertainties) to more complex techniques involving computation of least-square fits. (See Ref. [141] for the formulas used in these procedures.) Regardless of the way these scale factors are derived, they are applied over the entire energy range covered by each individual PFNS data set to produce the collection of scaled PFNS data sets and covariance matrices required for a proper evaluation.

While the evaluator's choice of the employed scaling technique is not unique, an important criteria for judging the adequacy of the scaling method applied for a particular PFNS evaluation is [141]:

- *An optimal scaling procedure in a specific application is the one that leads to the smallest possible* χ^2 *allowed by the scatter of the shape data available for use in the evaluation.*

This criteria is qualitatively reasonable since failure to remove scale biases in one or more PFNS data sets introduced as a consequence of inadequate scaling will inevitably lead to larger χ^2 and, very possibly, to biases in the actual non-normalized evaluated results, e.g., as a consequence of Peelle's Pertinent Puzzle (PPP) [292]. By the same token, it is also important that all the PFNS input data to be used in an evaluation be simultaneously included in the scaling process, i.e., all PFNS are scaled to the same single anchor, not to several distinct ones. Once again, it is obvious that a multiplicity of distinct anchors will lead to increased χ^2 for an evaluation owing to the residual biases. When these criteria are satisfied, as concluded from the numerical exercises performed in Ref. [141], the quality of the scaled result is rather insensitive to the specific scaling technique used. It is therefore reasonable that an evaluator should probably choose the simplest possible scaling approach that yields reasonable χ^2 values for a particular evaluation. To be conservative, an evaluator should probably investigate more than one approach to a particular situation and compare the χ^2 obtained for each technique. We note that if the generalized least-squares (GLS) technique is employed in an evaluation, the value of χ^2 can be obtained prior to making the evaluation [289, 291–293]. This is a feature of the GLS that is very convenient when dealing with the large numbers of data values encountered in realistic PFNS evaluations.

B. Least-squares Evaluation Procedures

The least-squares approach is indisputably the most widely used approach in contemporary nuclear cross section evaluations as well as for PFNS evaluations. In addition to providing spectral results, it concurrently generates covariance data that are consistent with the evaluated spectrum itself. It has been applied exclusively in the PFNS evaluation work performed in the present CRP. This approach is described in great detail in many references, see e.g., [141, 289, 291–293] for applicable formulas and relevant computational details. As noted earlier, least-squares methods can be employed to determine PFNS data scale factors as well as for PFNS evaluations. The following important caveat [293] should be noted:

- *Most least-squares computational procedures that are widely used in nuclear data evaluations are inherently linear in nature and assume that the data are distributed according to a normal distribution. If the data are significantly non-normal, or if the data uncertainties are very large, this may affect the outcome of evaluations produced using these procedures in ways that are difficult to trace.*

PFNS experimental data are often measured as ratio data to ^{252}Cf(sf), which makes them inherently non-normal and non-linear; additional studies are planned on new evaluation methods (e.g., the Unified Monte Carlo method [294–296]) to deal with this problem. Fortunately, in most realistic nuclear data evaluations, including of the PFNS, the conditions are such that the assumptions inherent to least-squares procedures are satisfied to a sufficient extent that they will yield satisfactory results as long as the input data are properly prepared (e.g., all ratios are converted to the PFNS space by multiplying them by a reference ^{252}Cf(sf) PFNS).

There are two broad variants of the least squares approach, the simple least squares (SLS) method and the generalized least squares (GLS) method. For the benefit of the reader, it is useful to explain the distinction between the SLS and GLS evaluation methods in the context of the present PFNS evaluations. In several ways they are similar but, depending on the circumstances, it can be useful to exploit distinctions between these two methods.

The SLS method can be described in the most general terms as a multi-parameter weighted averaging approach in which input covariance data (either correlated or uncorrelated) are used for weighting purposes, e.g., Ref. [293]. Each data set is handled in the same manner. In this method, the total number of data points must exceed the number of parameters being evaluated. It is not possible in this method to determine the chi-square value that will ultimately be generated by the procedure prior to performing the evaluation which, of course, is a drawback. This method can be applied if there are several non-normalized, scaled PFNS data sets, each of which spans the entire energy range of the evaluation. In practice, there are relatively few instances in PFNS evaluations where this situation arises, but this approach was utilized in a few hypothetical numerical examples treated in Ref. [141].

The GLS method is based on the concept of Bayesian updating, as described in Ref. [292]. It is more versatile than the SLS method for PFNS data evaluations since it can accommodate data sets having as few as a single data point, as long as at least one of the input PFNS data sets provides numerical values for every single energy group (or energy node) of the spectrum. One of these comprehensive sets serves as the prior knowledge while the remaining data sets (in most cases with fewer points than the prior set) serve to update knowledge of the PFNS, i.e., to generate the evaluation. In practice, although not always, the prior is a model-based PFNS.

- *Considerable flexibility is afforded by the GLS method in that the least-square updating analysis can be executed mathematically in the space of PFNS model parameters, in actual PFNS space, or in a space defined by the ratios of actual PFNS values to a fixed shape, such as a nominal Maxwell-Boltzmann (Maxwellian) energy distribution.*

Employing a ratio to a Maxwellian for PFNS evaluations has been widely exploited in the present CRP since it reduces the dynamic ranges of numerical values that need to be manipulated (e.g., in matrix inversion operations) when performing an evaluation. Incidentally, if a non-informative prior (one where very large uncertainties with no correlations are assumed) is utilized in a GLS analysis, it becomes essentially mathematically comparable to an SLS procedure. This approach was employed in Refs. [55, 56].

Implementation of the GLS approach has varied in the procedural and computational details for the evaluations performed in the present CRP, mainly as a consequence of distinct features of the various codes employed for these evaluations [289, 291, 297], but the underlying concept is identical for all of them.

C. Issues Related to the Use of Model-generated PFNS

As mentioned earlier in Sec. IV, models play an important role in PFNS evaluations because, for most applications, a quantitative characterization of the spectral shape is required both over the entire energy range of emitted neutrons and for all incident neutron energies. This is reflected in the stated requirement that evaluated PFNS in application libraries should be provided for $0 < E < 20$ MeV [44] for each incident neutron energy, E_n, tabulated in the library. Only in rare cases (one of them is discussed in Sec. VII of this paper) can this be achieved using predominantly experimental data, and then, only with the aid of simple ad hoc extrapolations to lower and higher energies which amount to less than 2% of the total fission neutron yield [55]. PFNS models are appealing because they can provide numerical values for any desired value of E and also for a wide range of incident neutron energies [38]. The current status regarding the quality and reliability of PFNS results produced by these models is discussed in Sec. IV. Here, a different issue is addressed: What is the effect on the PFNS evaluation process (by GLS or SLS) of certain features of model PFNS data and covariances that tend to be quite different from experimental PFNS data? There are three characteristic features of model PFNS that strongly influence the role they play in evaluations:

- *Model PFNS uncertainties derived from propagation of model parameter uncertainties tend to be smaller at some outgoing energies E than those typically encountered for experimental PFNS.*
- *Model PFNS covariance matrices usually exhibit quite strong correlations as well as correlation patterns that are quite different from those of experimental PFNS data covariances.*
- *Model PFNS are generally normalized to unity after integration over all E.*

The influence of each of these features on PFNS data evaluation is discussed in the following three paragraphs.

Small uncertainties are often encountered in modeled data, for cross sections as well as the PFNS, even when the estimated uncertainties on the model parameters propagated through to the observable quantities seem reasonable. This is a long standing issue that has been discussed many times, most recently in Refs. [297, 298]. The most likely explanation is that all contemporary models of nuclear processes are approximations that attempt to describe the main features of the physical processes but can never adequately describe all the details because of the complexity of nuclear systems. Additional uncertainties attributable to model shortcomings, labeled as "model-defect uncertainties", are usually not estimated and not included in the evaluation process [299, 300]. An exception was the recent evaluation of the ^{239}Pu PFNS for $E_n = 500$ keV where an attempt was made to include model defects, see Ref. [297] for details. A significant impact of underestimated model uncertainties on the PFNS evaluation is that the model spectra, which in most cases serve as the prior in GLS procedures, often dominates the evaluation process and effectively excludes or strongly suppresses the experimental contributions. If the shape of the model PFNS is at odds with the experimental data in energy regions where the neutron yield is significant, it can be detrimental to the evaluation outcome.

- *Attempts have been made in specific evaluation work for this CRP to generate reasonable model PFNS covariance data and to prevent the model data from overwhelming the evaluation process (see Sec. VII).*

The effects of small model-PFNS uncertainties tend to be amplified by the strong correlations often encountered in modeled PFNS covariance matrices. The presence of these correlations in the model prior inhibits the ability of the experimental data to influence the shape of the evaluated PFNS. Consequently, if the model PFNS shape is defective, which is often the case, as mentioned above, the evaluation suffers. Strong correlations in model-PFNS covariances are a consequence of the fact that the models used, such as the Madland-Nix model [38], tend to have very few parameters. However, it should be noted that model predictive capabilities are also linked to a reduced number of model parameters.

- *Under the auspices of this CRP, efforts have been devoted to developing new PFNS models, or variants of existing models, that exhibit larger uncertainties and weaker correlations, see Secs. IV, V, and VII.*

Normalization to unity is not necessarily an inescapable feature of model PFNS, e.g., both non-normalized and unit-normalized expressions can be provided for the Maxwellian distribution which is arguably the simplest and best known formula used to represent PFNS shapes [141]. However, traditionally, the mathematical formulations of models commonly used in PFNS evaluations, such as Ref. [38], have been structured so that energy-integrated spectra yield unity, regardless of the model parameters. The issue of PFNS normalization, and its impact on the evaluation process, is discussed in detail in the following section.

D. PFNS Normalization Procedures and Consequences

The significant differences between the properties of a scaled PFNS and a unit-normalized PFNS are important to understand since the implications are considerable for both generating and using these evaluations.

- *Considerable effort was devoted to understanding the distinction between scaling and normalizing PFNS and to exploring the ramifications on PFNS data evaluations in this CRP.*

Scaling a PFNS and the consequences on both the spectrum and its covariance matrix, are discussed in Sec. VI A, and, in greater detail in Refs. [141, 147, 297]. The consequence, for both the spectrum and its covariance matrix, of scaling a spectral representation $\mathbf{\Phi}$ by a constant c is that a new representation $\mathbf{\Psi} = c\mathbf{\Phi}$, of the same dimension, is produced. The discrete elements that represent the spectrum are related by $\Psi_\mathrm{i} = c\Phi_\mathrm{i}$. The relationship between the covariance matrices is given by $\mathrm{Cov}(\mathbf{\Psi}) = c^2\mathrm{Cov}(\mathbf{\Phi})$. Note that the correlation patterns of the covariance matrices $\mathrm{Cov}(\mathbf{\Phi})$ and $\mathrm{Cov}(\mathbf{\Psi})$ are identical in this transformation.

The concept of normalizing a PFNS resembles that of scaling a PFNS in that each element of the original spectral representation $\mathbf{\Phi}$ is divided by a constant G to produce a new spectrum $\mathbf{\Omega}$. However, in this case G is determined from the requirement at the integral of the new spectrum from 0 to ∞ is always exactly unity [141, 147]. If two PFNS are each characterized by finite collections of m contiguous energy-group values, then $\Omega_i = \Phi_i/G$ where $G = \sum_i \Phi_i$. The transformation from the non-normalized PFNS $\mathbf{\Phi}$ to the corresponding unit-normalized representation $\mathbf{\Omega}$ is clearly nonlinear. Consequently, the transformation of $\mathrm{Cov}(\mathbf{\Phi})$ to $\mathrm{Cov}(\mathbf{\Omega})$ is more complicated than for simple scaling [141, 147]. This transformation can be accomplished using the linear uncertainty propagation formula $\mathrm{Cov}(\mathbf{\Omega}) = \mathbf{T}\mathrm{Cov}(\mathbf{\Phi})\mathbf{T}^+$, where $\mathbf{T}^+$ is the transpose of the transformation matrix $\mathbf{T}$ whose elements are $T_{ik} = (G\delta_{ik} - \Phi_i)/G^2$, where δ_{ik} is the Kronecker Delta function [143].

A normalized covariance matrix such as $\mathrm{Cov}(\mathbf{\Omega})$ possesses the special property that the sums of the elements of all rows and columns should be exactly equal to zero. This is a consequence of imposing the sum-to-unity constraint on those variables whose uncertainties are represented by this matrix, thus inducing correlations characteristic of such a constraint. The same result is obtained for a covariance matrix generated using a PFNS model which results in a unit-normalized spectrum. In practice, the widely-used ENDF nuclear data formats require that these sums must never exceed 10^{-5} [44]. Correspondingly, normalized covariance matrices include both correlations and anti-correlations, reflecting the fact that changes in one section of the PFNS must be compensated by corresponding opposing changes elsewhere to preserve the integral of the spectrum. In fact there is a particular energy, known as the pivot point, above and below which correlations of opposite sign are observed in the opposing quadrants of the matrix [141, 147]. This is a feature not observed in covariance matrices of experimental PFNS, nor is the sum-to-zero feature of the rows and columns imposed on these matrices.

One of the issues that has been explored in the present CRP is whether it is reasonable to mix a normalized PFNS, such as one corresponding to a nuclear model used as a prior, with PFNS that have only been scaled, such as those from experiments, in performing a least-squares evaluation. While some evaluators might prefer not to mix normalized and non-normalized data in evaluations, based on philosophical arguments, results from investigations carried out in the present CRP [55, 56, 141] suggest that:

- *In practice PFNS evaluations can be performed with mixtures of normalized and non-normalized input PFNS as long as these data are appropriately scaled so that they can be treated as comparable.*

The key requirements for achieving a reliable PFNS evaluation are: (i) the assumption of linearity needed to validate use of SLS or GLS evaluation procedures must be adequately satisfied for the PFNS data being treated; (ii) the scaled PFNS data should be described by a normal distribution to a good approximation, and therefore not be seriously discrepant from normal; and (iii) the results generated by the least-squares analysis process ultimately must be normalized to satisfy the sum-to-unity constraint for the final PFNS, as well as the row and column sum-to-zero condition for the derived covariance data, as the final step in the evaluation process.

E. PFNS Average Energy

The average energy of the PFNS can be straightforwardly calculated once the evaluation is complete. The average energy is defined as $\overline{E} = \int dE\, E\, \Omega(E)$, provided that $\int dE\, \Omega(E) = 1$. For a non-normalized PFNS, Φ(E), the corresponding expression is $\overline{E} = \int dE\, E\, \Phi(E) / \int dE\, \Phi(E)$. In practice, the PFNS will be represented in discrete terms, $\mathbf{\Omega}$ or $\mathbf{\Phi}$, with corresponding covariance matrices $\mathrm{Cov}(\mathbf{\Omega})$ or $\mathrm{Cov}(\mathbf{\Phi})$, respectively. The average energies are then calculated using discrete sums and their uncertainties are derived by error propagation as described in Refs. [141, 143]. To achieve adequate computational precision to permit meaningful comparison among various evaluated PFNS on the basis of their predicted average energies, the energy grid (or energy point) structure must be sufficiently fine, not only for the energies around the maximal neutron yield, but also at higher energies. In practice, this corresponds to a computational precision that can distinguish differences in $\overline{E}$ as small as 10 keV ($\approx 0.5\%$). Furthermore, the evaluated PFNS must extend over a sufficiently wide energy range, especially at the high-energy end, so that no significant contribution to $\overline{E}$ is lost. The requirement of complete energy coverage is even more stringent for the PFNS covariance matrix if one is to obtain a reliable estimate of the uncertainty on $\overline{E}$.

Some criticality benchmarks are particularly sensitive to the average energy of the fission neutrons. To ascertain which energy regions of the PFNS contribute most significantly to the average energy, we define $\epsilon(E) = \int_0^E dE'\, E'\, \Omega(E')$.

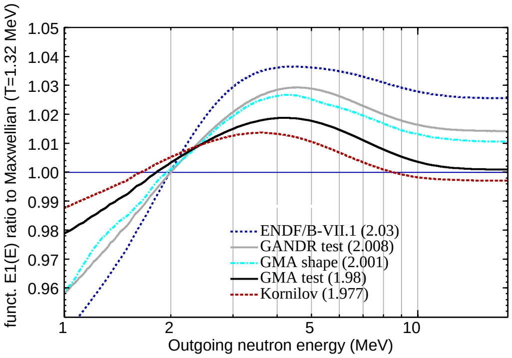

FIG. 38. (Color online) Ratios of the first moments of the fitted spectra (function E1). The calculated average energy for each curve is given in parentheses in the legend.

As $E \to \infty$, $\epsilon \to \overline{E}$. The values of ϵ were calculated for several evaluated representations of the ^{235}U(n_{th}, f) PFNS [55] (see also Sec. VII). The ratios of ϵ for these evaluated spectra to those of a Maxwellian are shown in Fig. 38.

Figure 38 shows how the contributions to $\overline{E}$ change as a function of E relative to the Maxwellian. Around 2 MeV, also the location of the PFNS pivot point (where model uncertainties reach the minimum), the contributions of all evaluated spectra are about equal to that of the Maxwellian. Therefore the differences in PFNS shape below 2 MeV only affect the average energy through the normalization. Above this energy, the contributions to ϵ increase compared to the Maxwellian albeit at different rates. The differences in ϵ for the evaluations shown in Fig. 38 relative to the Maxwellian continue to increase up to $E{\sim}5$ MeV where they no longer change since higher energies make an small contribution to ϵ. However, the ratios relative to a Maxwellian decrease until ~10 MeV because the evaluated spectra fall off more rapidly with E than a Maxwellian. Note that the asymptotic value of the ratio is always larger than unity. Finally note that differences in ϵ accumulated between 2 and 5 MeV contribute to $\overline{E}$.

- *Differences in the PFNS spectral representations in the relatively narrow energy range from 2 to 5 MeV mainly determine differences in the predicted average energy. This is a very important conclusion since it means that the PFNS shape in this energy region practically determines the PFNS. Fortuitously, this is also the energy range that is the most favorable for measuring PFNS.*

Two additional investigations that represent alternatives approaches to that of Ref. [55] are discussed here, so that they can be compared in the context of their predicted PFNS average energies and uncertainties.

The PFNS investigation by Smith et al. [34, 35] for ^{233}U, ^{235}U, and ^{239}Pu at $E_n{\sim}0.525$ MeV and for ^{240}Pu at $E_n{\sim}0.850$ MeV, relative to ^{252}Cf(sf), incorporated a relatively simple analytic approach to determining average energies based largely on experimental data. Ten individual, well-shielded organic liquid scintillators simultaneously measured ten comparable fission-neutron spectra, using time-of-flight techniques, for neutrons in the energy $0.5 < E < 10$ MeV. (The usable range for analysis purposes was $1 < E < 8$ MeV.) These measurements were performed in a very clean geometry in which neutron scattering perturbations of the measured neutron spectra were very modest. Timing signals for the ^{252}Cf(sf) measurements were derived from a fission chamber containing the ^{252}Cf(sf) source. Pulsed beams of neutrons provided a timing capability for the PFNS measurements that also utilized small cylindrical samples of the specified actinide materials.

Analysis of the PFNS data measured in this work, following corrections for multiple scattering and spectrum background effects, assumed that all the PFNS, including ^{252}Cf(sf), could be modeled by Maxwellians. This simplifying assumption enabled differences in $\overline{E}$ from $\overline{E}_{\mathrm{Cf}}$ to be easily extracted by fitting linear functions to the natural logarithms of measured ratios of PFNS values to those of ^{252}Cf over the usable energy range. The PFNS average energies were calculated based on assuming $\overline{E}_{\mathrm{Cf}}$=2.130 MeV, the best available value at the time, and close to the currently accepted value of 2.121 MeV [36]. Unfortunately, the original data from this experiment are not available in EXFOR [52] and are presumably lost.

Plots of selected data from this experiment were published in Refs. [34, 35]. An attempt was made to digitize them in the CRP. However, it is not clear from the references whether these plots are based on raw data or whether they already include multiple scattering corrections. The authors tabulate the differences in average energies, before and after applying multiple-scattering correction and found them to be significant, ~15–25 keV. The average energies extracted from the corrected spectra are systematically larger than for the uncorrected spectra. This implies that neutron-scattering effects shifted neutrons to the lower portions of the measured raw PFNS. The fission neutron spectra for all actinides were measured several times in all ten detectors, yielded multiple values of $\overline{E}$. Conservative values of the uncertainties were estimated from statistical analyses of these redundant determinations of the uncertainty $\Delta\overline{E}$ of 24–30 keV. In particular, this work yielded $\overline{E}$=1.973±0.024 keV for the ^{235}U(n_{th}, f) PFNS. In spite of the simplifying assumption that all PFNS have a Maxwellian shape, an assumption which, more than three decades later, has been examined and brought into question by the work of the present CRP (see Sec. VII), the results of this work [34, 35] are generally within uncertainties of recent results for $\overline{E}$.

Kornilov [288] has developed the "Scale Method", a semi-empirical technique for evaluating PFNS. This approach is based on the assumption that the shapes of all PFNS are essentially the same as for ^{252}Cf(sf), adjusted for energy scale. In particular, if $\Phi(E)$ is the fitted representation for an arbitrary PFNS and $\Psi(E)$ is the representation for ^{252}Cf(sf), then $\Phi(E) = (b/a)\Psi(E_{\rm Cf})\overline{E}_{\rm Cf}$ defines the relationship between these two spectra, with $E_{\rm Cf} = (E/a)\overline{E}_{\rm Cf}$ and $\overline{E}_{\rm Cf}$ is the average energy of the ^{252}Cf(sf) PFNS. The parameter b depends on the fitted experimental data set while a is the constant scale factor, proportional to the PFNS $\overline{E}$. A nonlinear fitting procedure was used to extract the values of a and b for a particular experimental data set.

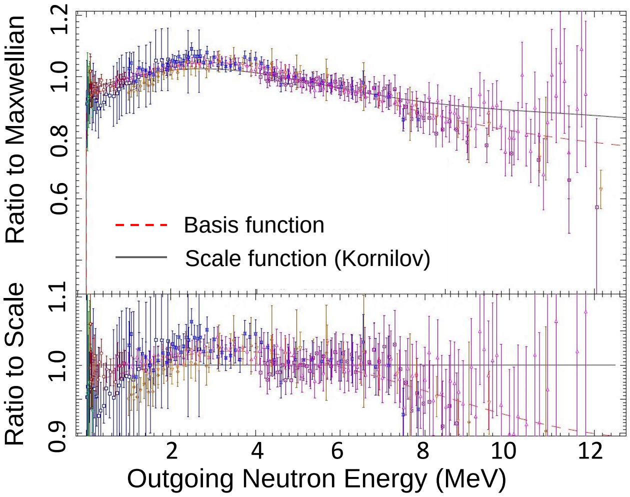

FIG. 39. (Color online) Fit of scaled ^{235}U($n_{\rm th}$,f) PFNS experimental data using a Watt-Maxwellian (WM) basis function [55, 56] (dashed) and SCALE basis function [288] (solid) plotted as a ratio to Maxwellian with $T = 1.32$ MeV. The ratio of experimental data and WM basis function to the SCALE basis function is shown in the bottom panel.

The SCALE method was applied by Kornilov [288] in the PFNS evaluation of ^{235}U($n_{\rm th}$, f). It was noted that, while different values of b were obtained for different experimental data sets, as would be expected based on their different normalizations, the fits all led to similar values of a. Kornilov contends that this result supports the notion that a can be viewed as a characteristic parameter of a particular PFNS within the context of the broader assumption that the PFNS shapes should be essentially the same as the ^{252}Cf(sf) spectral shape. Several data sets were also treated simultaneously, allowing for several different values of b along with a in the fits. The result obtained for a is about the same as that obtained when all the PFNS data sets are considered separately. It was claimed that this method yields results with a 1–2% accuracy for the ^{235}U PFNS shape representation in the range $0.1 < E < 10$ MeV. It is noted that correlations between experimental PFNS datasets were not considered [288]. The obtained average energy is $\overline{E}$=1.974±0.002 MeV, with a considerably smaller uncertainty than suggested by Refs. [34, 35]. Similarly, the average energy derived by Kornilov in 2010 [60] was $\overline{E}$=1.985±0.003 MeV. In comparison, Trkov et al. found $\overline{E}$=2.000±0.009 MeV, and the reference ^{252}Cf(sf) spectrum corresponds to the value $\overline{E}_{\rm Cf}$=2.122±0.008 MeV.

We emphasize that, unlike Smith et al. [34, 35], Kornilov [288] does not assume that the ^{252}Cf(sf) spectral shape is Maxwellian. In fact, it employs the same spectral representation as in standards applications [36], a Maxwellian multiplied by an eight-parameter polynomial function of E. While Kornilov's methodology is quite interesting, and gives reasonable results to a certain level of accuracy, other work in the present CRP (see Secs. VII B,VII C and Ref. [55]) suggests that this approach, which involving only a single parameter, may not be adequate to provide sufficiently accurate PFNS representations to satisfy user needs in spite of the small uncertainties on $\overline{E}$ predicted by the method.

In Fig. 39, rescaled ^{235}U($n_{\rm th}$,f) PFNS data are compared to the basis functions derived by Trkov et al. [55] (labeled WM and described in Eq. (102)) and Kornilov [288] (labeled SCALE method)[8]. The SCALE function shape effectively depends on only one parameter, a (proportional to the PFNS $\overline{E}$), while the WM basis is a combination of Watt and Maxwellian functions that depends on four parameters. Obviously, the WM basis function is more flexible. Thus the data are better fit by the WM than by the SCALE method. This is especially true in the $2 < E < 5$ MeV energy

---

[8] A similar plot, Fig. 6 presented in Ref. [288], shows experimental data rescaled relative to the SCALE function on a much larger scale of the Y-axis (0.5-1.5) compared to the scale used in Fig. 39.

region critical for the determination of $\overline{E}$. The bottom part of Fig. 39 clearly shows a systematic bias of about 2% for $2.5 < E < 4$ MeV, with the SCALE basis function being lower than the data. An underestimate in this E region directly leads to an underestimate of $\overline{E}$ by ∼20 keV (1.974 ± 0.002 MeV in Ref. [288] compared to 2.000 ± 0.009 MeV in Ref. [55, 56][9].

Holden's review [39] of $\overline{E}$ for the PFNS of ^{252}Cf(sf) and neutron-induced fission of ^{233,235}U and ^{239,241}Pu (referred to as mean energies in Ref. [39]) was mentioned briefly in Sec. II. This important work merits further attention here for the thoroughness with which it compiled and analyzed the experimental information available up to the time it was prepared (1985), as well as for the other additional useful information included in the paper, including numerous references. The review includes tabulated average energies and ratios of average energies as follows: the ratio ^{233}U to ^{235}U , 13 values; the ratio ^{239}Pu to ^{235}U ratio, 20 values; the ratio ^{241}Pu to ^{235}U ratio, 1 value; the ratio ^{252}Cf to ^{235}U ratio, 10 values; ^{233}U, 10 values; ^{235}U, 34 values; ^{239}Pu, 23 values; ^{241}Pu, 1 value; and ^{252}Cf, 35 values. Estimated uncertainties are also provided for many of these data. In addition to the average energies, these tables also include: principal author; year of publication; spectral energy range; detector type and experimental method; and value of E_n.

As indicated in Sec. II, Holden offered recommended values for $\overline{E}$ and its uncertainties for ^{252}Cf(sf), ^{233,235}U, and ^{239,241}Pu based on an analysis of the data compiled in the review. Reference [39] does not make clear how Holden arrived at these recommendations since no statistical procedure is specified. However, the paper does state that the uncertainty estimates are based on consideration of both systematic uncertainties and experimental precision. Holden suggests that the spread of $\overline{E}$ resulting from using a variety of experimental techniques to obtain the data allows reasonable estimates of the systematic errors. Although this paper is relatively short, it also provides a number of additional useful comments relevant to this topic. For example, Holden notes the importance of considering neutron scattering corrections and observed that, in the absence of such corrections, it was more likely for lower values of $\overline{E}$ to be reported than for experiments where such corrections were made, echoing comments made in Refs. [34, 35]. A trend toward larger $\overline{E}$ for PFNS with increasing E_n was also observed. However, Holden stated that it was not clear whether this was a consequence of larger high energy neutron yields at larger E_n or a consequence of experimental effects. The scatter in the reported results was too large to attribute a clear cause. This observation is in good agreement with results from the present CRP, within the quoted uncertainties.

F. A Pragmatic Approach to PFNS Data Evaluation

This subsection outlines a generic approach to evaluating PFNS data that reflects practical experience acquired during the course of the present CRP. Several aspects of this approach are incorporated in the evaluations performed during this CRP, as described in Sec. VII, although the details of these evaluations do not necessarily reflect the "template" presented here. The present approach takes into consideration characteristic features of both modeled and experimental PFNS data, as well as of PFNS evaluation procedures, as discussed earlier. It strives to take advantage of these features while, at the same time, avoiding or compensating for certain computational "traps" that can lead to unreasonable outcomes. The following description of this approach, for convenience, is based on an energy-group formulation. However, a similar approach could be developed that is based on an energy-point formulation. Note that the procedure described below can be performed for the direct spectra or for spectra expressed as ratios to a Maxwellian since the latter offers certain practical technical advantages, as mentioned earlier.

Step 1: Assemble all available experimental data sets, including covariances, and adjust the given values to conform to a common energy-grid structure. Note that, in general, these data will be non-normalized and will eventually need to be scaled.

Step 2: Identify those energy groups where experimental values are missing and insert ad hoc auxiliary numerical values into them that are reasonably statistically consistent in magnitude with measured PFNS data in neighboring or nearby energy groups. As long as these values are plausible, albeit fictitious, they will have negligible quantitative influence on the ensuing analysis since 100% uncertainties should be assigned to each of them. This step ensures that each experimental PFNS, once augmented by these auxiliary values, gives complete coverage over the entire range of E. The corresponding augmented covariance matrices should also be constructed. These matrices will reflect the true uncertainties on and correlations of the actual experimental data, but 100% uncertainties on the auxiliary values and no correlation between these values with any others in the augmented PFNS. The reason for generating these augmented PFNS with their associated covariance matrices will become clear in further steps.

---

[9] Kornilov explained the difference in the obtained PFNS $\overline{E}$ based on different arguments [270].

Step 3: Choose a model and use it to calculate model PFNS values for each energy group of the spectrum. Furthermore, generate a corresponding covariance matrix, Cov(M), for this modeled PFNS by propagating best-estimates of the uncertainties on the parameters. In most realistic evaluations, this model will be based on physical considerations, but this is not a necessary condition for applying the present approach. It does not matter whether or not these model results are normalized even though they usually are.

Step 4: Scale all the augmented experimental PFNS, as well as their corresponding covariance matrices, to the chosen modeled PFNS using one of the methods described in Ref. [141]. Thus, the modeled PFNS is designated as the anchor spectral shape. The purpose of this is to scale the augmented experimental PFNS. Note also that these augmented PFNS and their covariance matrices, while scaled, will remain non-normalized!

Step 5: Perform a SLS evaluation of all scaled, augmented experimental PFNS, excluding the modeled PFNS from this procedure. The necessity of introducing the auxiliary values, with large uncertainties, into the experimental PFNS should now be evident: it allows these spectra to be evaluated by the SLS method independent of the modeled PFNS since each augmented spectrum spans the entire PFNS energy range. Furthermore, the auxiliary values are essentially "dummy" values, since they are assigned large uncertainties and, consequently, they do not alter the essential characteristics of the spectrum for the purposes discussed in the following two steps of the present approach.

Alternatively, Steps 2, 4 and 5 could be replaced by a procedure in which the model PFNS uncertainties are arbitrarily set to 100%, the model correlations are set to zero, and no auxiliary data are introduced into the experimental PFNS. All the input data are scaled and a GLS procedure is instead employed in the calculations. The same results would be obtained.

Step 6: Normalize the PFNS obtained from Step 5, as well as its covariance matrix, using the procedure described in Sec. VI D.

Step 7: Examine the magnitudes of the uncertainties obtained in Step 6 for the energy groups in the region of the spectrum best represented by good quality experimental data. This region will most likely include the pivot point (defined above) where the uncertainty is most likely the smallest over the entire range of E. These are the evaluated PFNS uncertainties that would be obtained by only considering experimental data sets. As part of this assessment, the evaluator should be aware that specific uncertainty values in any energy groups where ad hoc auxiliary data were introduced should generally be ignored. Since the uncertainties on auxiliary data introduced for the purpose of this analysis should undoubtedly be much larger than those of real data, and are not correlated with any other data points, they will not influence the outcome for energy groups represented solely by real data.

Step 8: Examine the magnitudes of the uncertainties predicted for the model PFNS. They will be reflected in the covariance matrix Cov(M). These model uncertainties should then be compared with corresponding experimental results from Step 7. The model uncertainties are likely to be significantly smaller than the experimental values, especially at or close to the pivot point, if the model is based on nuclear theory (as discussed above). Due to these small model uncertainties, if the model PFNS were included in an evaluation with experimental data without some additional modification, the model result would likely dominate the evaluation in the energy region where the PFNS should be predominantly determined by the experimental results. While work undertaken in this CRP (see Sec. VI) has in part succeeded in increasing the model uncertainties near the pivot point, the existence of artificially small model uncertainties remains an issue.

Step 9: This potentially controversial step has been suggested as a pragmatic attempt to deal with a technical problem associated with PFNS evaluations incorporating both experimental data and modeled spectra. This approach can be justified only if following it generates evaluated results that are reasonable and trustworthy, and that reflect the evaluator's best-judged assessment of the current understanding of a particular PFNS based on all available information. In this step a model-defects covariance matrix, Cov(MD), is constructed with the objective of weakening the influence of the model PFNS in regions of the spectrum that should be most strongly influenced by experimental data. It also avoids unnecessarily discarding important benefits accrued by employing a model spectrum. Cov(MD) is added to the covariance matrix of the model parameters, Cov(M), to produce an extended model PFNS covariance matrix, Cov(ME) = Cov(M) + Cov(MD), that is used to make a PFNS evaluation incorporating only real experimental data (no auxiliary values) along with modeled spectra. Note that there is no change in the central values of the modeled PFNS, only its covariance matrix. Also, note that even if Cov(M) is normalized and satisfies the criterion that the rows and columns of the matrix sum to zero, this will not be the case for Cov(ME). Further discussion of possible ways to construct Cov(MD) to achieve the desired results appears later in this section.

Step 10: The original non-normalized experimental PFNS, minus the auxiliary values introduced in Step 2, are scaled, along with their covariance matrices, to the anchor spectral shape, assumed to be the model PFNS with its extended covariance matrix Cov(ME).

Step 11: A GLS evaluation procedure is performed using the input assembled in Step 10.

Step 12: The normalization transformation described in Sec. VI D is applied to the results from Step 11 to generate the final normalized, evaluated PFNS and its corresponding normalized covariance matrix.

The addition of a model-defects component, Cov(MD), to the assumed covariance matrix for the model PFNS provides the evaluator with a tool for addressing some of the problems associated with using both experimental and model data in PFNS evaluations. It is a very flexible and powerful tool that can be misused as well as used beneficially.

Some thoughts on how it might be used beneficially, based on experience gained during the CRP, are offered here. It must be kept in mind that the goal of an evaluator is to utilize the information available, both theoretical and experimental, in as objective a way as possible without being undermined by the evaluation process. As discussed in Sec. VI, nuclear models of the PFNS have many limitations. The fission process is a complex, many-body phenomenon and the physics of the process is not completely understood. Contemporary PFNS models, such as Ref. [38] which do embody physical features, are largely phenomenological. Comparisons with experiment, as discussed in this paper, exhibit clear deficiencies at a certain level of accuracy even though they do a reasonable qualitative job of describing the PFNS. At energies where reliable experimental results are available, these should define the PFNS shape and not the model. However, where data are sparse or unreliable (largely at the highest and lowest E for major actinides) the model can play a significant role for interpolation and extrapolation in the absence of experimental results. These considerations suggest that Cov(MD) should be constructed to distribute the experimental and modeled PFNS data so that the appropriate type of data contributes to the evaluation in the region where it is best suited.

The simplest construction of Cov(MD) would be a diagonal matrix with a constant percentage statistical uncertainty in all energy groups. The magnitude of this uncertainty might be selected so that the total model uncertainty for E near the pivot point is ≈ 3 times larger than the experimental values obtained in Step 6. This would reduce the model influence to $\sim$10% of the collected experimental results without completely discarding the model. Of course, this would also impact the predicted uncertainties for E values where there is minimal impact from experiments and the model spectrum dominates. Whether this is acceptable or not in a particular situation is left to the evaluator's judgment. Of course, a somewhat more complicated version of Cov(MD) could be constructed where different statistical uncertainties are assumed for different regions of the PFNS. It would also be possible to introduce partially (or fully) correlated components to Cov(MD) in situations where the model uncertainty should be enhanced, such as at higher E without sacrificing the "stiffness" of the evaluated shape at those energies.

Clearly, the power and flexibility offered to evaluators by the introduction of a model-defect uncertainty in the evaluation process must be exploited cautiously. Evaluation is part art and part science. The important point is that if an evaluator chooses to use such a tool, it must be done transparently so that evaluated data reviewers and users of evaluated data will understand exactly what assumptions have been made and what procedures have been applied in generating a particular PFNS evaluation.

G. Non-model PFNS Evaluation

If sufficient good quality experimental PFNS data are available for an evaluation to be performed without making extensive use of a model, then the issues associated with theoretical models, including a possible need to introduce model-defect uncertainties, as discussed in the preceding section, can be avoided. However, most of the other aspects of PFNS data evaluation do need to be addressed. While the circumstances under which model-independent evaluations can be performed are fairly rare, an evaluation of the ^{235}U(n_{th}, f) PFNS by Capote, Trkov and Pronyaev [55] has recently been performed[10]. See Sec. VII for details of this work and the results. The present section describes the general features of such an evaluation in the context of Ref. [55].

---

[10] ^{252}Cf(sf) PFNS evaluation by Mannhart (1987) [36] was exclusively based on experimental time-of-flight measurements. GMA evaluations described in Sec. VII C are also non-model dependent.

In order to perform such an evaluation, it is necessary to use an anchor spectral shape to which all experimental PFNS can be scaled. In Ref. [55], this is referred to as a basis function. The basis function was generated as an ad hoc linear combination of Watt and Maxwell-Boltzmann distributions. A particular combination of the relative weights of these two components, as well as reasonable values of the parameters employed in the Watt and Maxwell-Boltzmann functions, were found by fitting the parameters of the basis function to the PFNS data as well as to selected high-threshold integral dosimetry reaction data for ^{252}Cf(sf) and ^{235}U($n_{\rm th}$, f). The dosimetry data provided a basis function representation for $E > 8$ MeV consistent with well-known integral (SACS) data sensitive to the PFNS in this region. The resulting basis function shape was a good representation of the data over the range of energies corresponding to 99% of the fission neutron yield. Nevertheless, large, uncorrelated uncertainties (100%) were assigned to the basis function values since they were intended to be used in this evaluation only for scaling the experimental data and for extrapolation to the very highest energies, $E > 8$ MeV, and very lowest energies, $E < 20$ keV.

The PFNS data, including uncertainties, were assembled and some data were accepted and others rejected, based on their perceived reliability. In general, the largest discrepancies between the data and the anticipated PFNS shape were observed for $E > 8$ MeV. The experimental points retained were scaled using the basis function and a scaling method resembling those described in Ref. [141]. A GLS evaluation procedure was then performed using the GANDR code [291]. The non-normalized evaluation, and its covariance matrix, were subsequently normalized using the method described in Sec. VI D.

VII. EVALUATIONS

The evaluation of prompt fission neutron spectra for inclusion in evaluated nuclear data libraries follows the same basic process as for the evaluation of reaction cross sections, but there are some important differences as discussed in previous section. We summarize in this Section evaluations undertaken within this project.

A. General Remarks

A modern evaluated nuclear data file reflects our current knowledge of particular reactions and products of reactions on a given isotope. It is almost always the result of a combination of experimental data and model calculations. A notable exception is the evaluation of so-called "standard" cross sections [46, 47] for which only accurate experimental data are used in a statistical analysis. The evaluation of the ^{252}Cf(sf) PFNS by Mannhart [36, 37] is also considered a "standard" and it has been evaluated via a least-square fit of time-of-flight data only.

Experimental data provide important guides to constrain model predictions, which can be very uncertain if model input parameters are free to vary even within reasonable limits. However, experimental data alone are often limited to specific reactions and incident energies, as well as outgoing energies of the spectrum of produced secondaries, for instance. Model calculations allow extrapolation of the experimental data to the entire energy and reaction phase space to produce complete and consistent evaluated data files, necessary for their later use in applications.

The evaluation of the PFNS follows a similar procedure as cross sections, but differs in at least a couple of important aspects:

1. A PFNS is a probability density function. By definition, the integral of the PFNS over all E is equal to unity. In other words, a PFNS is a *normalized* distribution function.
2. In the ENDF-6 format, the covariance matrix elements refer to the absolute covariances of the spectrum bin integrals. As a corollary to item 1, a PFNS covariance matrix must obey the zero-sum rule, which states that the sums of the elements in any row or column of the covariance matrix must be zero to ensure that a PFNS perturbed from the evaluated value sampled from this matrix remains normalized. In practice, the ENDF-6 manual requires that these sums be less than 10^{-5} [44].

Experimental PFNS data sets never span the entire E range where the spectrum is non-negligible. (Only about 99% of the integral over E is covered.) Limitations on detector sensitivity thresholds, as well as multiple scattering corrections, tend to prevent accurate measurements of very low E. At the other end of the spectrum, above ~10–12 MeV, spectral values are orders of magnitude lower than those of the spectrum at its peak and statistical uncertainties dominate the measured signal. Because of these limitations, a measured PFNS can at best be considered as a *shape* measurement, mostly relative to the reference ^{252}Cf(sf) PFNS [36, 37]. However, the scale factor is determined by the normalization condition

$$\int_0^\infty \chi(E_n)dE_n = \overline{\nu}, \text{ or, } \int_0^\infty \tilde{\chi}(E_n)dE_n = 1, \tag{99}$$

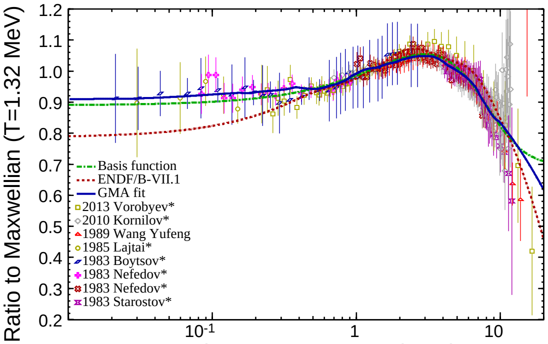

FIG. 40. (Color online) The fitted spectrum using the least-squares GMA code (solid), prior basis function (dot-dashed), and the ENDF-B/VII.1 evaluation (dotted) in comparison with rescaled "shape" differential data (symbols).

where χ is normalized to the average prompt neutron multiplicity, $\overline{\nu}$, and $\tilde{\chi}$, the quantity present in evaluated data libraries, is normalized to unity. The average multiplicity, $\overline{\nu}$, is measured in completely different fission experiments that can make a very precise determination of how many neutrons are emitted per fission event but provides a very poor determination of their energy spectrum. PFNS measurements are focused instead on an accurate spectral shape and not on the total number of neutrons emitted.

Comparing experimental PFNS data with model calculations requires both PFNS shapes to be normalized to the same quantity. As discussed in Appendix B of Ref. [38], a simple procedure can be followed to perform meaningful comparisons. If an experimental PFNS, $\chi^{(i)}_{\mathrm{exp}}$, is measured for $E_{\mathrm{min}} < E < E_{\mathrm{max}}$ and the sum of its bin values is given by

$$\sum_i \chi^{(i)}_{\mathrm{exp}}(E_i)\Delta E_i = N_{\mathrm{exp}} \ , \tag{100}$$

while the integral of the calculated PFNS, $\chi_{\mathrm{th}}(E_n)$, over the same energy range is

$$\int_{E_{\mathrm{min}}}^{E_{\mathrm{max}}} \chi_{th}(E_n) dE_n = N_{\mathrm{th}} \ , \tag{101}$$

then the experimental PFNS data can be normalized by multiplying the data by the factor $(N_{\mathrm{th}}/N_{\mathrm{exp}})$.

B. Non-model GANDR Evaluation of ^{235}U PFNS for Thermal and Fast Neutron-Induced Fission

1. *Basis Function for Scaling and Extrapolation*

Following the evaluation methodology discussed in Sec. VI, all data sets were converted to "shape" ratios to a Maxwellian spectrum with $T = 1.32$ MeV, scaled to match a chosen basis function by minimizing the squared differences between the measurement and the basis function. The basis function, $f_{WM}(E)$, is the Watt-Maxwellian function mentioned earlier: a linear combination of a Maxwellian, f_M, and a Watt, f_W, which represents the data reasonably well [55]

$$\begin{aligned} f_{WM}(E) &= w_M f_M(E, E_M) + (1 - w_M) f_W(E, a_W, b_W) \\ f_M(E, E_M) &= K_M \sqrt{E} e^{-E/E_M} \\ f_W(E, a_W, b_W) &= K_W e^{-E/a_W} \sinh \sqrt{b_W E}, \end{aligned} \tag{102}$$

where w_M is the weight of the Maxwellian; $E_M = T$ is its temperature; a_W and b_W are the parameters of the Watt function; and K_M, K_W are normalization constants, expressible analytically.

Equation (102) is only used for scaling the experimental data and for extrapolating data beyond the range where experimental data are available and statistically consistent, i.e., $0.020 < E < 10$ MeV. Therefore, the basis function serves only as an auxiliary tool with negligible effect on the fitted spectral shape. The parameters of the WM function derived in Ref. [55] are: $w_M = 0.7424$, $E_M = 1.316$ MeV, $a_W = 0.6859$ MeV, and $b_W = 9.366$ MeV^{-1}. While these parameters are not unique, the proposed function can be used for the scaling of experimental data.

After rescaling, the combined experimental data sets cover more than 99 % of the spectral integral. Since the scaling is done relative to the arbitrary WM reference function, the spectral integral after the fit procedure is not necessarily exactly unity, even if the chosen basis function is normalized, as in this case. A subsequent renormalization produces an additional scale factor of 1.0125 in this case.

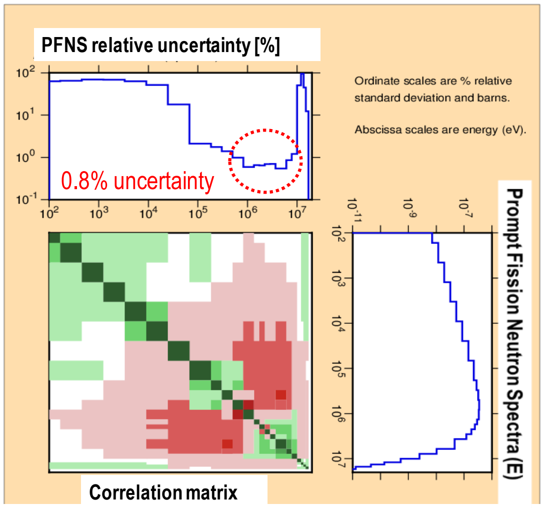

FIG. 41. (Color online) Uncertainty and correlation matrix of the normalized GANDR fitted PFNS for the thermal neutron-induced fission of ^{235}U.

2. *Generalized Least Squares Fit*

The fit to the experimental data was performed with the GANDR code [291]. GANDR uses the generalized least-squares, GLS, technique. It calculates the parameters of a piecewise-linear correction function defined on a fixed energy grid and applied to an input prior. The chosen prior was "non-informative", with the shape of the previously-defined basis function given by Eq. (102), but an assigned 100% uncorrelated uncertainty. Thus the prior has practically no influence on the final solution in the energy region where measured data are available.

The advantage of GANDR is that the fit function is defined at every point and does not require either pre-processing or transformation of experimental data to a fixed energy grid. It produces a smoother output function but it cannot track any real structure in the data between grid points that are not included in the prior. The prior covariance matrix was generated by sampling the parameters of Eq. (102). To soften the stiffness of the modeled covariance matrix, the diagonal elements of the relative covariance matrix were increased by different amounts, ranging from 0.0009 to 0.04, equivalent to adding some 3–20% statistical uncertainty. The prior uncertainties are increased in a narrow range around $\overline{E}$. This additional uncertainty can be interpreted as a model "shape" uncertainty [297]. The prior covariance matrix is a typical model covariance matrix with positive correlations over the whole energy range. Those correlations are slightly weakened by the assumed model "shape" uncertainty.

3. *PFNS for Thermal Neutron-Induced Fission*

The scale factors for each data set are listed in Table 23. These are values by which the EXFOR entries have to be divided to match the final fit result. For the ratio measurements the factors include the assumed average neutron multiplicity ratios, $\overline{\nu}_{\mathrm{Cf}}/\overline{\nu}_{^{235}\mathrm{U}_{n_{\mathrm{th}}}} = 3.759/2.421 = 1.55266$. The precise value of this ratio is irrelevant, since only the product, which is obtained from matching the data, is needed.

TABLE 23. Measured differential PFNS data sets for thermal induced fission of ^{235}U used in the GANDR evaluation with derived scale factors. A typical uncertainty of the quoted scale factors is 5%.

First Author & Year	Accepted	Scale factor
Vorobyev (2013) [59]	Yes	1.5250
Kornilov 2011 [61]	Yes	1.5720
Wang (1989) [42]	Above 1.3 MeV	6.4433
Lajtai (1985) [62]	Below 0.2 MeV	1.0125
Nefedov (1983) [30]	Yes	1.6128
Nefedov (1983) [30]	Yes	1.6571
Starostov (1983) [31]	Yes	1.6436
Boytsov (1983) [32, 33]	Below 2.7 MeV	1.0039

The ratios of the evaluated PFNS for ^{235}U($n_{\rm th}$,f) to a Maxwellian with T =1.32 MeV are compared in Fig. 40. The results are shown on logarithmic energy scale. The basis function is also depicted. For $E < 20$ keV and $E > 10$ MeV, the evaluation agrees with the prior basis function, as expected.

The normalization of the spectrum is trivial: by definition the integral must be equal to unity. Normalization of the covariance matrix, however, is less straightforward. The covariance matrix is evaluated in terms of absolute uncertainties over specified energy intervals. In a normalized covariance matrix, the sum of elements of any row or column equals zero. Since a residual normalisation uncertainty is present in the covariance matrix obtained directly from the fitting procedure, the zero-sum property is not respected *a priori*. The covariance matrix was normalized according to Eq. (35.2) in the ENDF-6 manual [44].

The uncertainty of the non-normalized PFNS around the spectral peak is ∼3.5%. The evaluated shape uncertainty after normalization and the corresponding correlation matrix are shown in Fig. 41. The minimum uncertainty near the peak of the normalized spectrum is ∼0.8%, which corresponds, by definition, to the estimated "shape" uncertainty. The average energy is $\overline{E}$=2.000±0.009 MeV.

4. *PFNS for Fast Neutron-Induced Fission*

The same evaluation procedure was applied to derive the shape of the fast neutron-induced PFNS. The selected data sets and the corresponding scale factors for each data set are listed in Table 24. The scale factors are defined the same way as for the thermal neutron-induced PFNS in Table 23. It is important to note that the data sets listed correspond to a range of incident energies, $0.5 < E_n < 1.5$ MeV. A proper evaluation of such data requires a model that depends on E_n. Therefore, results of the non-model fit for fast neutron-induced fission should be treated with care.

TABLE 24. Measured differential PFNS data sets for fast neutron-induced fission of ^{235}U used in the GANDR evaluation with derived scale factors. A typical uncertainty of the quoted scale factors is 5%.

First Author & Year	Accepted	Scale factors
Sugimoto-Lestone (2015) [71, 72]	No*	1.0298
Lestone (2014) [66]	Below 8 MeV	1.0229
Staples (1995) [74]	0.95–4 MeV	1.0063
Smith (1980) [35]	Yes	8.8443
Abramson (1977) [80]	0.95–8 MeV	17587.
Johansson (1977) [82]	0.95–7.9 MeV	5.2167
Adams (1975) [84]	0.95–8 MeV	3255.5
Islam (1973) [85]	Below 4.8 MeV	55.819

* Not available at the time of evaluation.

The previous data by Cranberg from 1957 were excluded because of the large scatter in the data and their large uncertainties [13]. In addition, the data by Noda [73] and by Trufanov [77] were excluded because of their large uncertainties and non-physical trends at high E. Several other data sets that were included deviated from the bulk at the extremes of the measured region. Therefore the data used in the fit were somewhat subjectively truncated to the accepted range, as given in Table 24. Further study revealed that the Adams data [84] are likely the preliminary results of the Johansson data [82] and should also be excluded from the fit.

The Sugimoto-Lestone data [71, 72] were given in Table 3, this set was not included in the fit because it was not available in time.

The overall conclusion is that the current fit is in good agreement with the available data. However, for $E > 5$ MeV, the fit was strongly influenced by the earlier Adams and Lestone data. A new fit, which is likely to raise the spectrum for $E > 5$ MeV and thus somewhat increase $\overline{E}$, will be made. This new fit is not expected to increase $\overline{E}$ to the current value of the ENDF/B-VII.1 evaluation for ^{235}U PFNS.

The GANDR fast-neutron fit has been performed without a rigorous uncertainty analysis. It should thus be viewed as a preliminary study before a more thorough generalized least-squared analysis is performed.

C. Non-model GMA Evaluation of ^{233}U($n_{\rm th}$,f), ^{235}U($n_{\rm th}$,f) and ^{239}Pu($n_{\rm th}$,f) PFNS

The IAEA/NDS held a Consultants Meeting [301] on "International Neutron Cross Section-Standards: Measurements and Evaluation Techniques" in October 2008 to consider the possibility of extending the energy ranges and including new reactions that could be considered for adoption as reference cross sections. The meeting participants made the explicit recommendation to "obtain a new evaluation of the ^{252}Cf(sf) and ^{235}U($n_{\rm th}$,f) PFNS based exclusively on experimental data", due to the importance of ^{235}U for applications. This recommendation led to the first attempt by Pronyaev to use the GMA code for PFNS evaluation. That PFNS evaluation was based on a GMA combined fit of PFNS experimental data on thermal neutron-induced fission with ^{233}U, ^{235}U and ^{239}Pu as well as the ^{252}Cf(sf) PFNS. The Mannhart pointwise (unsmoothed) ^{252}Cf(sf) evaluation [36], with its corresponding covariance matrix, was used as pseudo-experimental ^{252}Cf(sf) data in the fit. The combined fit included mostly PFNS ratio measurements relative to the ^{252}Cf(sf) reference spectrum (see Table 25). A few data sets, not measured as ratios (e.g., the Wang ^{235}U data [42]), were used in the fit as "shape" data. To reduce the possible biases due to unknown normalization errors (PPP) and minimize numerical instabilities, all spectra were divided by a Maxwellian with $T = 1.32$ MeV and the evaluation was performed in this transformed PFNS space. Thus this first GMA fit produced a PFNS evaluation for three major fissile actinides, as well as ^{252}Cf(sf). The evaluated covariance matrices included cross-nuclide correlations. However, the derived uncertainty of the ^{235}U(n_{th},f) evaluation was unrealistically small.

Further discussion of the evaluation methodology and results took place in the next two Consultant Meetings of the Neutron Standards Project held in 2012 [302] and 2014 [303]. At the last meeting, the suggestion was made to test the evaluation methodology by comparing Generalized Least Squares fits for ^{252}Cf(sf) and ^{235}U(n_{th},f) PFNS obtained by different codes using as close as possible input data including uncertainties and correlations [303]. Shortly after the meeting, evaluations undertaken by Mannhart (using his own code) and Pronyaev (using the GMA code), based primarily on absolute ratio data, were compared. The evaluated spectra and their uncertainties were found to be in excellent agreement with minimal discrepancies due to small differences in the methodology of preparing the experimental covariance matrices [303].

A similar comparison was done between the GANDR fit, discussed in Sec. VII B, and the GMA fit. In this case, all data were treated as "shape data" (as discussed in Sec. VI). Although there were larger differences in the experimental covariance matrices used in the GANDR and GMA fits, no substantial differences were found in the evaluated spectra or the normalized covariances. The evaluated average PFNS energies also agreed well within the quoted uncertainties. These extensive inter-comparisons validated the GMA fit. Therefore, the GMA fit is considered to be the "reference method" for evaluation of the PFNS in thermal neutron-induced fission of ^{233}U,^{235}U and ^{239}Pu due to proper consideration of experimental uncertainties and correlations in the data [55]. Such an evaluation is purely based on experimental PFNS data. Therefore, it is considered to be a non-model evaluation. It is worth noting that the evaluation methodology based on "shape" data (see Sec. VI) has an advantage in estimating experimental uncertainties and correlations since several complex contributions to the uncertainty, which should be accounted for in fits to absolute spectra, are not needed.

The GMA code allows the experimental data to be input as "shape" data. Thus the scale factor for the data is an additional fit parameter. Therefore, it is not necessary to scale the data prior to the evaluation, in contrast to the GANDR least-square fit in Sec. VII B. All experimental spectra used in the GMA evaluation (except Wang et al. [42] and Boytsov et al. [32, 33]) were taken to be primary measured shape ratios. The Wang and Boytsov data were used as shape data redefined as ratios to a Maxwellian with $T = 1.32$ MeV. While the specific temperature chosen is not important, working with ratios to a Maxwellian reduces the dynamical range of the fit values, increasing the accuracy of the interpolation in the fits.

A least-square GMA fit was employed to produce simultaneous PFNS evaluations of thermal neutron-induced fission of ^{233}U, ^{235}U, and ^{239}Pu. Both absolute spectral data and data presented as measured relative to the ^{252}Cf(sf) reference spectrum were considered. The pointwise ^{252}Cf(sf) reference spectrum, with covariances evaluated by Mannhart [36, 37], was used as a pseudo-experimental data. The experimental data used as input for the evaluation are listed in Table 25. The Lajtai et al. [62] data were excluded from the evaluation because of strong non-physical fluctuations observed, and very large corrections to the original data applied by authors [63]. A GMA combined fit is possible because all three isotopes are related to the common ^{252}Cf(sf) reference by cross-nuclide correlations. Employing ratio data substantially reduces the uncertainties of the experimental data because common uncertainties such as the neutron detector efficiency and fragment mass determination cancel in the ratio. Only the statistical and part of the systematic uncertainty, not directly related to the spectra normalization, remain in the uncertainty budget (see Sec. III M 1 for more details). The combined set of all experimental data covers the energy range over which ∼98–99% of all neutrons are emitted.

The GMA combined fit results in evaluated PFNS mean values and covariances for all three fissile targets as well as for ^{252}Cf(sf). The evaluated ^{252}Cf(sf) PFNS agrees with the Mannhart evaluation [36, 37] within uncertainties, providing a self-consistent check of the GMA results. (Note that no new ^{252}Cf(sf) data were employed in the GMA evaluation). The next step in the evaluation process was smoothing the evaluated spectra using a third-order polynomial fit. PFNS ratios to a Maxwellian spectrum have a weaker energy dependence than absolutely normalized spectra and can thus be fit reasonably well by a third-order polynomial. Results of the non-model GMA fit of the ^{233}U(n_{th},f), ^{235}U(n_{th},f), and ^{239}Pu(n_{th},f) PFNS (short blue dashed lines) are compared to the corresponding polynomial-smoothed curves (short dashed red lines) in Fig. 42. Fluctuations of a few percent observed in evaluated spectra reflect structures present in the experimental data. However, polynomial smoothing was found to change the calculated average energy of the PFNS by up to 6 keV, which is unacceptable because the calculated uncertainty of the average energy in the GMA fit was ∼10 keV. To circumvent this unacceptably large bias, a generalized Savitzky-Golay (SG) smoothing method that explicitly treats the nonuniformity of the energy mesh was introduced. The SG-smoothed data for all three fissile

TABLE 25. Measured differential PFNS data sets for thermal induced fission of ^{233}U, ^{235}U, and ^{239}Pu used in the GMA evaluation and the fitted scale factors. All data were considered as shape data. Uncertainty was increased for (*) below 1.3 MeV, and for (**) above 2.7 MeV. Vorobyev et al. ^{239}Pu(n_{th},f) data were not available for the fit. A typical uncertainty of the quoted scale factors is 5%.

First Author & Year	E(MeV)	Scale factor
	^{233}U(n_{th},f)	
Vorobyev (2013) [59]	0.21–8.8	1.0304
Nefedov (1983) [30]	0.085–4.7	0.9843
Starostov (1983) [31]	4.8–9.3	1.0273
Boytsov (1983) [32, 33]	0.025–4.5	1.0312
	^{235}U(n_{th},f)	
Vorobyev (2013) [59]	0.221–16.65	0.9884
Kornilov 2011 [61]	0.7–11.8	1.0074
Wang (1989) [42]	0.56–15.*	0.9627
Nefedov (1983) [30]	0.084–0.91	0.9847
Nefedov (1983) [30]	1.0–7.8	1.0445
Starostov (1983) [31]	4.11–12.0	1.0481
Boytsov (1983) [32, 33]	0.021–5.5**	1.0246
	^{239}Pu(n_{th},f)	
Vorobyev et al., see Sec. III I	0.241–10.286	–
Nefedov (1983) [30]	0.084–1.8	1.005
Nefedov (1983) [30]	1.2–9.1	0.998
Starostov (1983) [31]	3.1–11.0	0.9963
Boytsov (1983) [32, 33]	0.021–4.5	0.9756

targets are shown as the bold black line in Fig. 42. Employing this method reduced the bias due to the smoothing to about 1 keV. This additional uncertainty should be added to the final estimated uncertainty of the average energy of the PFNS.

The resulting average energies of the PFNS evaluations for thermal neutron-induced fission was determined over $0.025 < E < 10$ MeV, a range containing $98 - 99\%$ of the spectra. The averages were, for all practical purposes, independent of the extrapolation scheme used below 0.025 and above 10 MeV. The final average energies derived from the GMA fit are: 2.000 ± 0.01 MeV for ^{235}U, 2.030 ± 0.013 MeV for ^{233}U, and 2.073 ± 0.01 MeV for ^{239}Pu thermal neutron-induced PFNS.

D. ^{233}U(n_{th},f), ^{235}U(n_{th},f) and ^{239}Pu(n_{th},f) PFNS Extrapolation for Outgoing Neutron Energies Above 10 MeV using Spectrum Averaged Cross Sections

The last step of the evaluation requires extrapolation of the evaluated spectra from 0.025 MeV down to 10^{-5} eV, and from the highest energy in the evaluated spectrum up to 30 MeV and adjusting the subsequent PFNS normalization to comply with the specifications of the ENDF-6 format [44]. A maximum energy of 30 MeV was ad hoc considered to be the endpoint of the PFNS. A third-order polynomial fit of the ratio to a Maxwellian provides a reasonable extrapolation of the spectra for $E < 25$ keV. Indeed, the energy dependence of the ratio is very weak in this region so that the PFNS can be well represented by a Maxwellian at low E.

The experimental PFNS data for $E > 10$ MeV are either discrepant or nonexistent. Fortunately, the neutron flux for these energies is very low in reactors (less than 1–2%) and thus this region is not relevant for many applications. The exceptions are high energy neutron dosimetry applications and estimation of neutron radiation damage.

To address this region, two different extrapolation schemes have been employed. In the first, the extrapolation is based on measurements in the range $6 < E < 10$ MeV. To a good first approximation, the PFNS in this region can be described by an exponential function for all three fissile nuclei. This exponential fit can then be used to extrapolate the PFNS up to 30 MeV. However, this approach is based on data at lower E and lacks experimental support.

A second, more realistic, approach employs selected spectrum-averaged cross section (SACS) measurements of high-threshold (n,2n) dosimetry reactions combined with the use of the Maxwellian function (high-energy PFNS) to fit the selected "integral" data. The SACS is defined as $\mathrm{SACS}(E_{\mathrm{thr}}) \equiv \int_{E_{\mathrm{thr}}}^{\infty} dE\, \sigma(E)\, \Omega(E)$, provided that $\int dE\, \Omega(E) \equiv 1$. $\Omega(E)$ denotes the PFNS, and $\sigma(E)$ is the evaluated differential cross section of the dosimetry reaction (usually taken from IRDFF [3]) with threshold E_{thr}.

The requirement of continuity of the PFNS at the chosen matching energy point fixes the normalization of the Maxwellian. Therefore, only one parameter, the Maxwellian temperature, T, needs to be fitted to reproduce the selected dosimetry reaction rates. The impact of this modification to the overall normalization at lower neutron

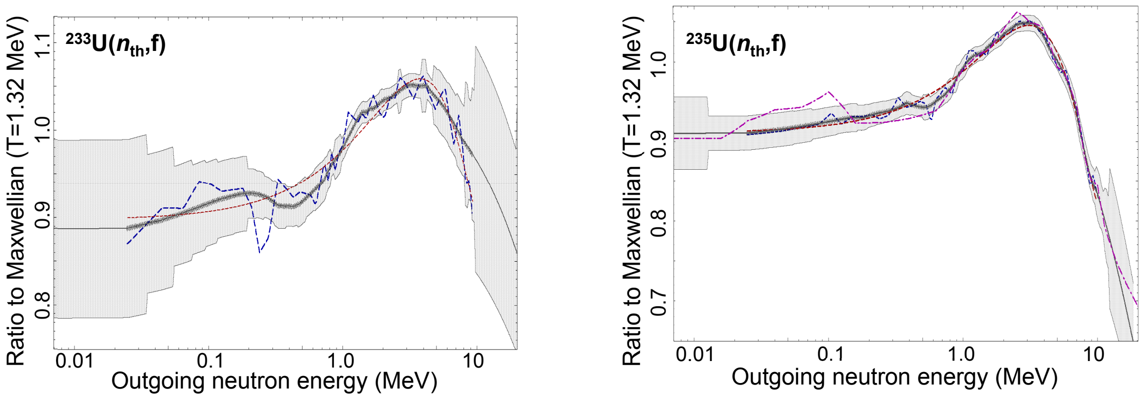

(a) Fitted and interpolated/extrapolated PFNS of ^{233}U($n_{\rm th}$,f) (b) Fitted and interpolated/extrapolated PFNS of ^{235}U($n_{\rm th}$,f)

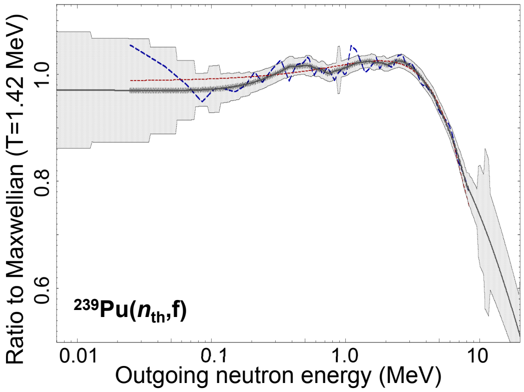

(c) Fitted and interpolated/extrapolated PFNS of ^{239}Pu($n_{\rm th}$,f)

FIG. 42. (Color online) GMA combined PFNS evaluation (dashed blue line) for thermal neutron-induced fission of ^{233}U, ^{235}U, and ^{239}Pu respectively. GMA fit results are compared to the third order polynomial smoothed data (short dashed red line), and to the Savitsky-Golay smoothing (grey solid line) with uncertainty bands (greyed area). Extrapolations to the low and high-energy regions are also shown (grey solid lines) in the region where no experimental data are plotted.

emission energies was found to be negligible [55].

Ideally, the SACS of a high-threshold (n,2n) reaction with a well known excitation function should be measured in the studied neutron field as well as in the ^{252}Cf(sf) reference neutron field. The SACS ratio makes it possible to minimize the impact of decay data uncertainties and reduce the necessary corrections to the measured spectrum-averaged cross sections. An ideal candidate is the ^{27}Al(n,2n) reaction with threshold $E_{\rm thr} = E_n = 13.55$ MeV. The excitation function of this reaction had been measured to high accuracy by Wallner et al. [304] using accelerator mass spectrometry (AMS). Evaluation of the excitation function based on existing differential measurements is ongoing with support of the IAEA. Unfortunately, no SACS data are available for this reaction. Such measurements are strongly encouraged.

Many other $(n, 2n)$ SACS reaction data have been measured and evaluated based on averages over the ^{252}Cf(sf) and ^{235}U($n_{\rm th}$,f) PFNS fields. However, there are no available SACS data from the ^{239}Pu($n_{\rm th}$,f) PFNS field and only one SACS experiment published by Kobayashi et al. [308] in the ^{233}U($n_{\rm th}$,f) PFNS field. From the list of measured SACS by Kobayashi et al. [308–311] and evaluated data by Kobayashi et al. [312] and Mannhart [142], two high-threshold reactions (with the energy at which the reaction rate decreases to half its maximum value, $E50\%$, given in parentheses) have been selected: ^{27}Al(n,α) ($E50\% = 10$ MeV) and ^{90}Zr(n,2n) ($E50\% = 14.56$ MeV). These are dosimetry reactions [3] with evaluated excitation functions known to high accuracy up to at least 20 MeV and have SACS measurements for the ^{233}U($n_{\rm th}$,f), ^{235}U($n_{\rm th}$,f), and ^{252}Cf(sf) PFNS fields.

If a parabolic dependence of measured SACS on the PFNS average energy, $\overline{E}$, is assumed, then the expected SACS values for the ^{239}Pu($n_{\rm th}$,f) PFNS field ($\overline{E}$=2.073 MeV) can be predicted by interpolation using the measured SACS in the ^{235}U($n_{\rm th}$,f) ($\overline{E}$=2.00 MeV), ^{233}U($n_{\rm th}$,f) ($\overline{E}$=2.03 MeV) and ^{252}Cf(sf) ($\overline{E}$=2.13 MeV) PFNS fields. The measured SACS values for ^{235}U($n_{\rm th}$,f), ^{233}U($n_{\rm th}$,f) and ^{252}Cf(sf) fields, and the interpolated (*in italics*) SACS for ^{239}Pu($n_{\rm th}$,f)

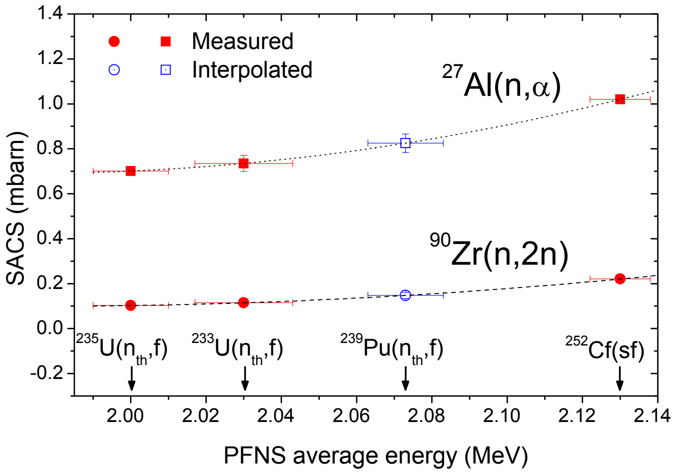

FIG. 43. (Color online) SACS dependence on PFNS average energies for high-threshold dosimetry reactions: ^{27}Al(n,α) (squares), and ^{90}Zr(n,2n) (circles). The measured SACS values (red symbols) are shown for ^{235}U($n_{\rm th}$,f), ^{233}U($n_{\rm th}$,f) and ^{252}Cf(sf), and the interpolated ones (blue symbols) for ^{239}Pu($n_{\rm th}$,f). Fitted polynomials are shown with dotted and dashed lines for ^{27}Al(n,α) and ^{90}Zr(n,2n) reactions, respectively. The polynomial parameters are listed in Table 26.

TABLE 26. Measured (upright) and interpolated (*italics*) ^{27}Al(n,α) and ^{90}Zr(n,2n) SACS in studied PFN fields. SACS measurements by Kobayashi et al. [308] were renormalized to the predicted value of the ^{58}Ni(n,p) SACS equal to 107.9 mb (factor= 1.068). A parabolic dependence of the SACS on the evaluated PFNS $\overline{E}$ (in parentheses, left column) is assumed for the interpolation. The uncertainty in parentheses of interpolated values (center and right columns) does not consider the $\overline{E}$ uncertainty.

PFN field ($\overline{E}$ [MeV]), ref.	^{27}Al(n,α) [mb]	^{90}Zr(n,2n) [mb]
^{235}U($n_{\rm th}$,f) (2.000±0.010) [305, 306]	0.701(9)	0.103(3)
^{233}U($n_{\rm th}$,f) (2.030±0.013) [308]	0.735(36)	0.115(6)
^{239}Pu($n_{\rm th}$,f) (2.073±0.010)*	*0.825(41)*	*0.148(7)*
^{252}Cf(sf) (2.13±0.008) [307]	1.020(10)	0.221(6)

(*) The parabolic interpolation used was:

$$^{27}\mathrm{Al}(n,\alpha) \quad \mathrm{SACS}(\overline{E}) = 52.047 - 52.083\overline{E} + 13.205\overline{E}^2 \ \mathrm{mb}$$
$$^{90}\mathrm{Zr}(n,2n) \quad \mathrm{SACS}(\overline{E}) = 19.915 - 20.06\overline{E} + 5.0769\overline{E}^2 \ \mathrm{mb}$$

field are listed in Table 26. The listed SACS of the ^{90}Zr(n,2n) reaction for the ^{233}U($n_{\rm th}$,f) PFNS field (0.115 mb) was estimated from the Kobayashi et al. “measured” value (0.086 mb) after applying two correction factors (1.068 and 1.091). The measured (and interpolated for ^{239}Pu) SACS values for the ^{90}Zr(n,2n) reaction have been used to define the high-energy tails of the evaluated ^{235}U($n_{\rm th}$,f), ^{233}U($n_{\rm th}$,f), and ^{239}Pu($n_{\rm th}$,f) PFNS. The chosen high-energy PFNS extrapolations (grey lines at highest outgoing neutron energies for all fissile targets) can be seen in Fig. 42.

Figure 44 shows the calculated to measured, C/E, SACS ratios for measurements by Kobayashi et al. [308] for ^{233}U($n_{\rm th}$,f) PFN field as a function of the E50% energy. The agreement with Kobayashi data [308] (renormalized to the predicted value of the ^{58}Ni(n,p) SACS equal to 107.9 mb (factor= 1.068)) is very good except for the ^{115}In(n,n') reaction, and the uncorrected (as explained in the legend) ^{90}Zr(n,2n) reaction. As discussed below, the SACS for reactions with E50% close to $\overline{E}$ are expected to have a very weak dependence on the neutron field, as is the case for ^{115}In(n,n'). However, the measured in the ^{233}U neutron field is about 10% higher than those obtained in ^{235}U and ^{252}Cf fields. This is an evidence for potential problems in the Kobayashi et al. measurement, which is, unfortunately, the only one in the ^{233}U($n_{\rm th}$,f) neutron field.

We have found the remarkable feature that the ratio of SACS in two different PFN fields is equal to unity within uncertainties for dosimetry reactions with 1.5 < E50% < 2 MeV, as shown in Fig. 45. This is equivalent to stating that the linear dependence of SACS on the E50% becomes constant if the E50% condition stated above is met. The dosimetry reactions that fulfill this condition are ^{235}U(n,f), ^{239}Pu(n,f), ^{237}Np(n,f), and ^{10}B(n,α). This explains why the measured SACS ratios for these reactions are practically independent of the PFNS detailed shape from different fissile nuclides, since all have a broad plateau in this energy region. It is also the reason that both ^{235}U(n,f) and ^{239}Pu(n,f) reactions have been often used as monitor or transfer reactions in relative measurements. Therefore, we predict that the expected values of the SACS for these reactions in the ^{239}Pu($n_{\rm th}$,f) and ^{233}U($n_{\rm th}$,f) neutron fields to be equal to measured values in ^{235}U($n_{\rm th}$,f) and ^{252}Cf(sf) within the given experimental uncertainties.

The calculated SACS ratios for the ^{235}U(n,f), ^{239}Pu(n,f), and ^{237}Np(n,f) dosimetry cross sections [3] in ^{252}Cf(sf) and ^{235}U($n_{\rm th}$,f) PFN fields are in excellent agreement with measured data, as shown in Fig. 45. In particular, the measured SACS value of the ^{237}Np(n,f) reaction is equal to 1361 ± 22 mb and 1350 ± 24 mb in the ^{252}Cf(sf) and

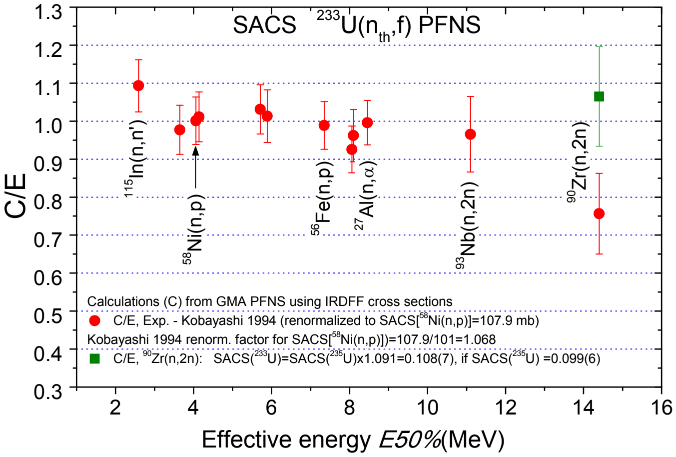

FIG. 44. (Color online) Calculated to measured C/E (red circles) SACS ratio in ^{233}U($n_{\rm th}$,f) PFN field as a function of the reaction $E50\%$ energy. The following dosimetry reactions are plotted in order of increasing $E50\%$: ^{115}In(n,n'), ^{47}Ti(n,p), ^{58}Ni(n,p), ^{54}Fe(n,p), ^{27}Al(n,p), ^{46}Ti(n,p), ^{56}Fe(n,p), ^{48}Ti(n,p), ^{24}Mg(n,p), ^{27}Al(n,α), ^{93}Nb(n,2n), and ^{90}Zr(n,2n). SACS measurements by Kobayashi et al. [308] were renormalized to the value of the ^{58}Ni(n,p) SACS equal to 107.9 mb (factor= 1.068). An additional correction (green square) to the measured ^{90}Zr(n,2n) SACS was considered from the measured ratio 1.091% of SACS in the ^{233}U($n_{\rm th}$,f) and ^{235}U($n_{\rm th}$,f) fields [308].

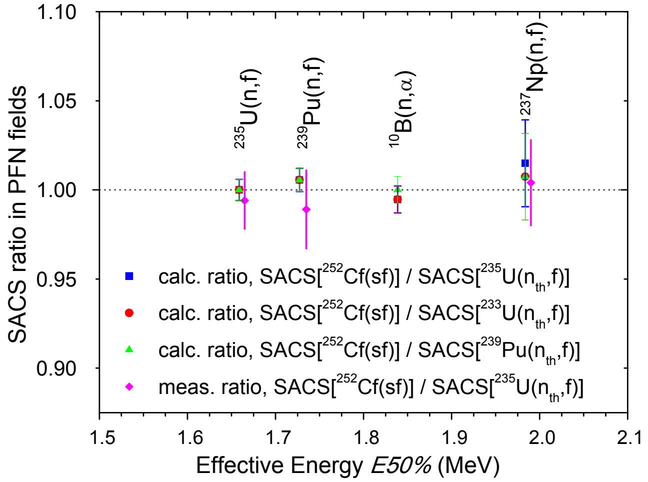

FIG. 45. (Color online) Ratio of SACS in ^{252}Cf(sf) PFNS to the SACS in thermal neutron-induced PFNS of fissile nuclei as a function of the $E50\%$ energy for the ^{235}U(n,f), ^{239}Pu(n,f), ^{237}Np(n,f), and ^{10}B(n,α) dosimetry reactions from IRDFF [3].

^{235}U($n_{\rm th}$,f) PFN fields, respectively, confirming that the SACS ratio is independent of the PFN field for this reaction. The SACS value obtained with the GMA evaluation of ^{235}U($n_{\rm th}$,f) PFNS (Sec. VII C) using ^{237}Np(n,f) IRDFF cross sections [3] is equal to 1342 ± 22 mb in excellent agreement with the measured value. The calculated SACS ratios for the same reactions in the ^{252}Cf(sf) and ^{233}U($n_{\rm th}$,f) PFN fields, as well as in the ^{252}Cf(sf) and ^{239}Pu($n_{\rm th}$,f) PFN fields are all equal to one within uncertainties, as shown in Fig. 45. This result represents a tight integral constraint for the evaluation of energy-dependent cross sections for reactions with $1.5 < E50\% < 2$ MeV, based on differential measurements.

E. Bayesian Evaluation of the ^{239}Pu(n,f) PFNS

A new evaluation of the ^{239}Pu PFNS was performed including recent experimental data [66, 67, 92] and improved modeling compared to ENDF/B-VII.1 [148].

The evaluation was carried out in two steps: (1) An evaluation of the ^{239}Pu PFNS induced by incoming neutrons of 500 keV and associated covariances [297, 313] was undertaken with special emphasis on extending the model and a thorough uncertainty quantification of both model predictions and experimental data. This specific E_n was chosen to compare to a previous evaluation [314] for ENDF/B-VII.1 and thus study the impact of model extensions and

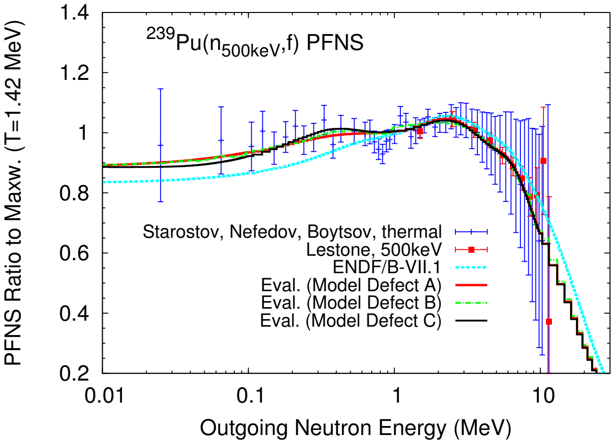

FIG. 46. (Color online) Evaluated ^{239}Pu PFNS at E_n =500 keV are displayed as ratio to a Maxwellian for three different model defect formulations in comparison to experimental data of Refs. [30–33, 66, 67] and ENDF/B-VII.1 [148]. The experimental data are those with the smallest uncertainties in the present evaluation and they were scaled with respect to the new evaluation (Model Defect A).

improved uncertainty quantification. The new evaluation at E_n = 500 keV was used as a basis for (2) an evaluation of the ^{239}Pu PFNS induced by thermal to 30 MeV neutrons and associated covariances [313]. Below, we summarize briefly the differences of the evaluations compared to those of ENDF/B-VII.1 and show selected results.

1. *Evaluation of the ^{239}Pu PFNS at 500 keV Incident Neutron Energy*

The evaluated data and covariances of this evaluation were obtained by the GLS algorithm described in Ref. [141]. Model predicted PFNS and covariances computed by an extended Los Alamos model (see Refs. [38, 297, 313] and Sec. IV B) were used as prior information. Experimental data of Refs. [30–33, 62, 66, 67, 94] and the data of Ref. [74] at E_n = 500 keV and their associated covariances were also considered. The following extensions and changes were made compared to information underlying ENDF/B-VII.1:

- It is considered that the neutrons can be emitted anisotropically in the center-of-mass frame following [14] and Eq. (35). The anisotropy was already implemented in this manner in an evaluation of the ^{239}Pu PFNS by [298].
- The inverse compound nucleus formation cross section $\sigma(\epsilon)$ is calculated from an optical model potential fitted to strength functions S_0 and S_1 of Sr and Zr isotopes and based on Ref. [232].
- The average light and heavy fission fragment PFNS in Eq. (33) are weighted by their respective neutron multiplicities, $\overline{\nu}_L$ and $\overline{\nu}_H$.
- The maximum temperatures of the average light and heavy fission fragments, T_{mL} and T_{mH}, can assume different values following Ref. [171].
- The more realistic temperature distribution of the fission fragments proposed in Ref. [153] was used.
- Uncertainties were considered for the optical model potential parameters, the anisotropy parameter, the temperature distribution parameter, $\overline{\nu}_R = \overline{\nu}_L/\overline{\nu}_H$, the average total γ-ray energy and the neutron separation energy in addition to those considered in Ref. [314].
- The data of Refs. [30, 31, 66, 67] and those measured with a stilbene neutron detector of Ref. [33] were included in addition to those used in Ref. [314].
- A detailed uncertainty quantification was performed for each experimental data set [89] following the procedure described in Sec. III M 2 and information from Ref. [315].
- Three different formulations of model defect uncertainties were added to the prior covariances in order to obtain reasonable evaluated uncertainties given the experimental data used in the evaluation procedure.

The above-mentioned changes led to differences of the evaluated PFNS compared to ENDF/B-VII.1 as shown in Fig. 46 for all three formulations of model defects.

2. *Incident Energy Dependent Evaluation of the ^{239}Pu PFNS*

The evaluated data and covariances for incident neutron energies ranging from thermal to 30 MeV were also obtained by a GLS algorithm. Experimental data of Refs. [30–33, 62, 66, 67, 94] are used, as well as the data of Ref. [92] for $E_n \leq 15$ MeV that were corrected as proposed in Ref. [93]. The data of Staples et al. [74] were not included in this evaluation, as known but uncorrected issues of the data (multiple scattering, detector efficiency [75, 315]) would lead to questionably soft evaluated PFNS. The same experimental covariances for the data of Refs. [30–33, 62, 67, 94] were used as for the evaluation at $E_n = 500$ keV, and they were extended to include data sets measured at higher E_n. The incident energy dependence of the experimental data was taken into account in the evaluation procedure. The same formulation of the LAM was used to predict model PFNS and associated covariances as for $E_n = 500$ keV, but further extensions were needed to describe physics processes at higher incident energies. The following changes were made in the model description compared to the evaluation for ENDF/B-VII.1 [148] and in addition to these for the evaluation at $E_n = 500$ keV:

- Only fission neutrons are considered in the PFNS, i.e., only those neutrons where the associated residual nucleus actually fissions.
- The pre-fission neutrons emitted in a pre-equilibrium process are considered using the exciton model.
- An incident-energy dependence of the average total kinetic energy and energy release of the fission fragments is taken into account, following parameterizations and predictions of Refs. [316, 317].

Evaluated covariances are provided not only for $E_n = 500$ keV – as is the case for ENDF/B-VII.1 – but also for all incident neutron energies and cross-correlations. A recent benchmark study by Rising et al. [318] shows that including the cross-correlations between different incident neutron energies in k_{eff} calculations significantly increases k_{eff} uncertainties of, e.g., the Jezebel critical assembly.

In Fig. 47, the results at $E_n = 500$ keV are in reasonable agreement with the evaluation solely at this incident neutron energy, showing the consistency of the incident energy dependent evaluation. The difference from the ENDF/B-VII.1 evaluation at $E_n = 6$ MeV, namely the bump around $E = 300$ keV, in Fig. 47 stems from the $(n,n'\mathrm{f})$ pre-fission neutrons (see IV B 0 e). This effect is most prominent at $E_n = 6$ MeV, because the soft neutrons associated to the second chance fission process can only be emitted if $E_n > B_f$, and the associated fission barrier is $B_f \approx 6$ MeV. The evaluated PFNS at $E_n = 14$ MeV is shown in Fig. 47 in comparison to ENDF/B-VII.1 to highlight the difference caused by the pre-fission pre-equilibrium component (structure below $E = 10$ MeV as $E \approx E_n - B_f$), which is not properly considered in ENDF/B-VII.1. Benchmarking and adjustment of the data are currently ongoing.

F. Los Alamos Model PFNS Evaluation for Neutron-Induced Fission of Uranium and Plutonium isotopes

PFNS evaluations for a suite of uranium and plutonium isotopes for incident neutron energies from thermal up to 5 MeV have been performed [298]. An extension to higher incident energies is in progress. The main approach and results obtained in this work are outlined here.

The PFNS evaluations were obtained using the Kalman filter [319], in conjunction with the Los Alamos model predictions as the prior information and experimental data sets to update this knowledge and thereby generate the posterior evaluated results. The Los Alamos model, as presented in Sec. IV B, was used for this purpose. The only modification from the original LAM [38] included here was the use of non-isotropic emission of the neutrons in the center-of-mass of the fission fragments. Systematics for the LAM parameters for the suite of isotopes considered were taken from Tudora [179] to infer prior model input parameters. In total, 7 parameters α_i were considered. The average total kinetic energy $\langle \mathrm{TKE} \rangle$ and average energy release $\langle E_r \rangle$ at thermal energy are

$$\langle \mathrm{TKE} \rangle_{\mathrm{th}} = \alpha_1 + \alpha_2 \frac{Z^2}{A^{1/3}} \ , \tag{103}$$

$$\langle E_r \rangle_{\mathrm{th}} = \alpha_3 + \alpha_4 x + \alpha_5 x^2 \ , \tag{104}$$

where x is the fissility parameter given by

$$x = \frac{(Z^2/A)}{(50.883[1 - 1.7826((N-Z)/A)^2])} \ . \tag{105}$$

The average level density parameter is

$$\langle a \rangle = A/\alpha_6 \ , \tag{106}$$

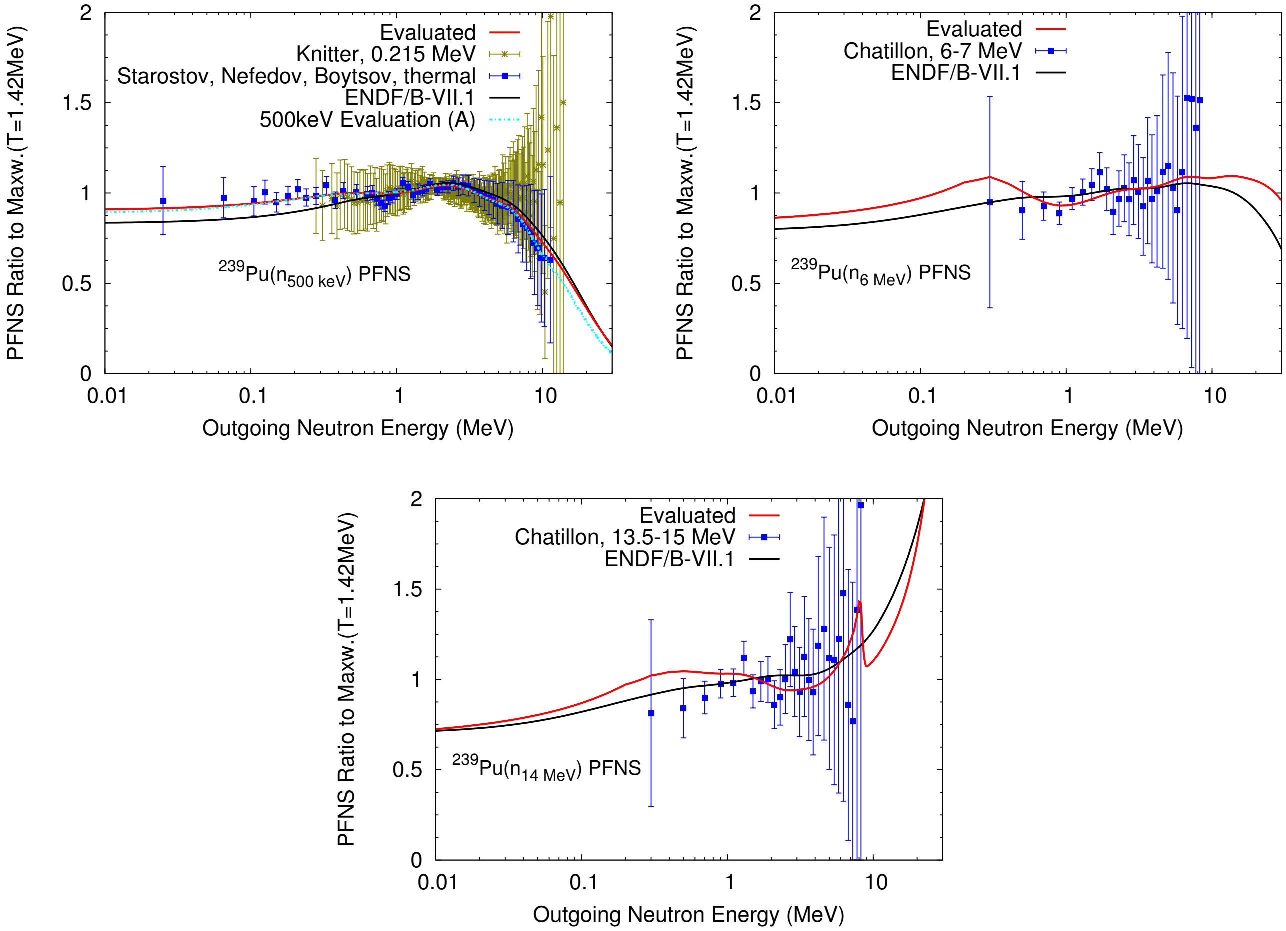

FIG. 47. (Color online) Evaluated ^{239}Pu PFNS at $E_n = \{500\text{ keV}, 6\text{ MeV}, 14\text{ MeV}\}$ are displayed as a ratio to a Maxwellian in comparison to experimental data of Refs. [30–33, 92, 94] and ENDF/B-VII.1 [148]. The experimental data were scaled with respect to the new evaluation.

and the anisotropy coefficient is simply

$$b = \alpha_7\ . \tag{107}$$

No energy dependence of the parameters was taken into account since only incident neutron energies up to 5 MeV were considered.

In the case of uranium isotopes, all available experimental data sets for incident energies from thermal up to 5.0 MeV for the isotopes ^{233}U, ^{235}U, and ^{238}U were collected and analyzed. Only a rough estimate of their uncertainties and correlations was performed. Different correlations were considered: short energy range (statistical and energy resolution), medium energy range, and long energy range (such as normalization). Some experimental analysis work was already performed at the IAEA [49]. This work was extended to analyze other experimental data not considered in this initial study. Note that no cross-experiment correlations are taken into account. In the case of Pu isotopes, only experimental data on ^{239}Pu could be used.

The Bayesian statistical technique was used to combine model predictions and experimental data, following an approach similar to Refs. [320, 321]. Instead of applying the Kalman filter directly to the LAM input parameters, the optimization was performed on the α_i parameters. In this way, cross-isotope correlations were generated through the model parameter systematics. In other words, experimental data on the ^{233}U PFNS, for instance, have an impact on the PFNS for the other uranium isotopes.

Figure 48 shows the prior and posterior values and their one-sigma bands obtained for $\langle \text{TKE} \rangle$ as a function of $Z^2/A^{1/3}$. While the posterior values obtained are not necessarily in agreement with the ones reported in Ref. [316], what is important for the PFNS calculation is the difference between the average energy release and the average total kinetic energy, as this difference determines how much average total excitation energy is available for neutron emission from the fission fragments.

An interesting example illustrating the importance of cross-isotope correlations is depicted in Fig. 49. The cross-isotope correlations imposed by the LAM parameter systematics prevents the calculated ratio from remaining flat, as is to some extent indicated by the experimental data. The ^{238}U PFNS is expected to be softer than for ^{235}U at the

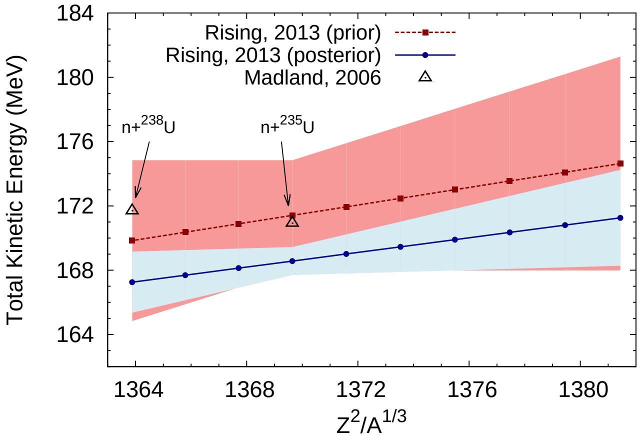

FIG. 48. (Color online) Prior and posterior values for the average total kinetic energy $\langle\text{TKE}\rangle$ of the fission fragments used in calculation of the PFNS for neutron-induced fission reactions on $^{229-238}$U.

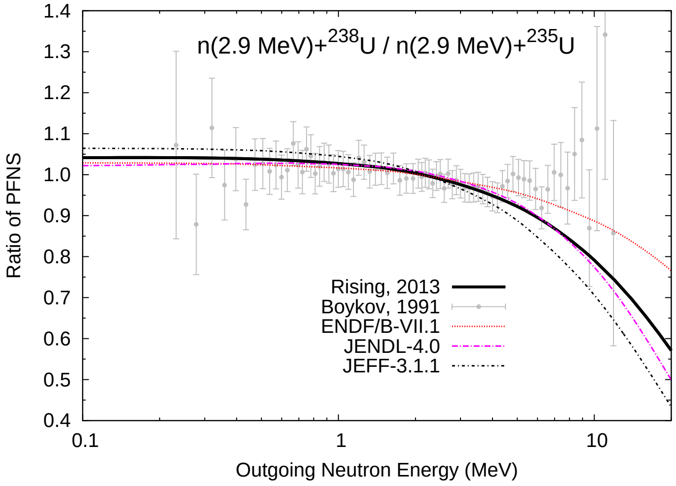

FIG. 49. (Color online) The calculated [298] ratio of the PFNS for ^{238}U and ^{235}U for $E_n = 2.9$ MeV is compared to experimental data by Boykov et al. [78] and evaluated libraries.

same energy. The ENDF/B-VII.1 evaluation tried to match those data somewhat artificially by softening the ^{238}U PFNS near 3 MeV compared to 2 MeV.

All the uranium and plutonium evaluations were performed up to $E_n = 5$ MeV and associated covariance matrices were produced. The evaluated uncertainties were later used in Ref. [322] and propagated using optimized sampling techniques in the fast critical assemblies Jezebel and Godiva. Uncertainties in the multiplication factor k_{eff}, total leakage, and spectral indices were estimated for both assemblies. The uncertainties Δk_{eff} were calculated as 0.16% and 0.23% for Jezebel and Godiva, respectively. Uncertainties in the total leakage were about 0.2%, while uncertainties in spectral indices ranged from 0.16% up to 1.70%.

G. `PbP` Evaluation of ^{232}Th(n,f), ^{233,234}U(n,f) and ^{237}Np(n,f) PFNS

The PFNS evaluation for neutron-induced fission of ^{232}Th, ^{233,234}U and ^{237}Np with incident neutron energies from thermal to 20 MeV in the `PbP` approach is exclusively model based. At energies below the threshold for second-chance and higher fission, the calculation follows the description in Sec. IV C directly, and quantities such as the PFNS, $N(A, Z, \text{TKE}, E)$, are straightforward to obtain in the model. When multi-chance fission is possible, the spectra for higher fission chances can be calculated at the average value of the (continuum) excitation energies of secondary compound nuclei (i.e, residual nuclei after particle emission) . However, the associated fission fragment yields are essentially unknown. Therefore, only the most probable fragmentation is considered for the secondary compound nuclei, as in the original Los Alamos Model, see Sec. IV B.

In the `PbP` approach, as in that of the Los Alamos Model itself, every effort was made to achieve the best possible

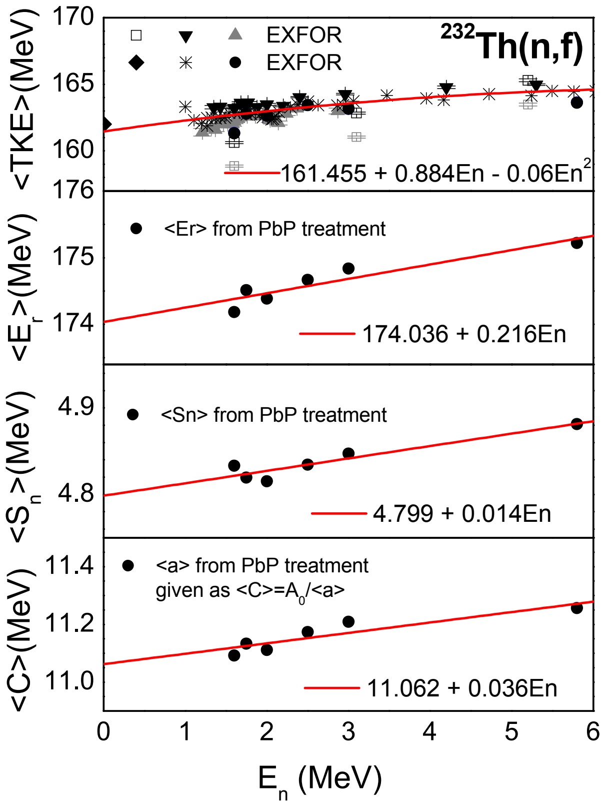

FIG. 50. (Color online) From top to bottom are shown the energy dependence of $\langle \mathrm{TKE} \rangle$, $\langle E_r \rangle$, $\langle S_n \rangle$ and $\langle C \rangle = A_0/\langle a \rangle$ obtained in the `PbP` model for ^{232}Th(n,f), along with a fit to the model points. The EXFOR data for $\langle \mathrm{TKE} \rangle$ as a function of E_n are also shown. Note the suppressed zeroes on the y-axes.

agreement with existing data not only for the PFNS but also other prompt fission observables such as the prompt neutron multiplicity and prompt photon energy as a function of fragment mass and TKE. The input data are either taken directly from experiment or, if measurements are not available, inputs from models or systematics are used.

in the `PbP` treatment the mass number A goes from symmetric fragmentation to very asymmetric mass splits. For each A, three integer values of Z, the nearest integers above and below the most probable charge, are included. The charge polarizations, ΔZ, for ^{233,234}U(n,f) were obtained as described in Refs. [188, 191, 323]. For ^{237}Np(n,f) and ^{232}Th(n,f), $\Delta Z = \pm 0.5$ is taken for all fragments (the $+$ is for light fragments while the $-$ is for heavy fragments), as supported in the sensitivity studies of Ref. [324]. For each value of A and Z, the `PbP` calculations are done in the range $100 < \mathrm{TKE} < 200$ MeV in steps of 5 MeV.

1. *Experimental Inputs*

Experimental yields, $Y(A, \mathrm{TKE})$, are required to obtain the matrix inputs to the `PbP` model, such as $\langle E_r \rangle$ and $\langle a \rangle$. The data are typically available in a rather limited energy range, usually restricted to be below the threshold for second chance fission.

Data from IRMM for fourteen energies in the range $0.2 < E_n < 5$ MeV are available for ^{234}U(n,f) [286, 325] and for ^{237}Np(n,f) with $0.3 < E_n < 5.5$ MeV [164]. EXFOR data were employed for ^{233}U(n,f) [326] and ^{232}Th(n,f) [327].

In most cases the experimental distributions are only functions of a single quantity, such as $Y(A)$ and TKE(A). The three-dimensional yields $Y(A, Z, \mathrm{TKE})$ are constructed following Eqs. (58–60) given in Sec. IV C (`PbP` model). The root-mean-square of the Z distribution is taken as a function of A for ^{233,234}U and a constant value of 0.6 was assumed for ^{237}Np and ^{232}Th. Data on the variation of $\langle \mathrm{TKE} \rangle$ with E_n, needed for multi-chance fission were taken from the EXFOR library. See Refs. [190, 191] for more details.

Experimental data of $\langle \mathrm{TKE} \rangle$ for ^{232}Th(n,f) are shown in the top panel of Fig. 50 for $E_n \leq 6$ MeV. Those data were used to establish the $\langle \mathrm{TKE} \rangle$ variation with E_n shown by a solid line in the top panel. The `PbP` treatment for ^{232}Th(n,f) reaction produced the total average quantities $\langle E_r \rangle$, $\langle S_n \rangle$, and $\langle C \rangle = A_0/\langle a \rangle$ shown in the three lower panels of Fig. 50 (filled black circles), being $\langle a \rangle$ the effective level density parameter. The solid (red) lines are a fit to the energy dependence of those results. The bottom panel also shows that the effective level density is indeed $\langle a \rangle \approx A/(11\,\mathrm{MeV})$ in the `PbP` treatment, as discussed in Secs. IV B and IV C.

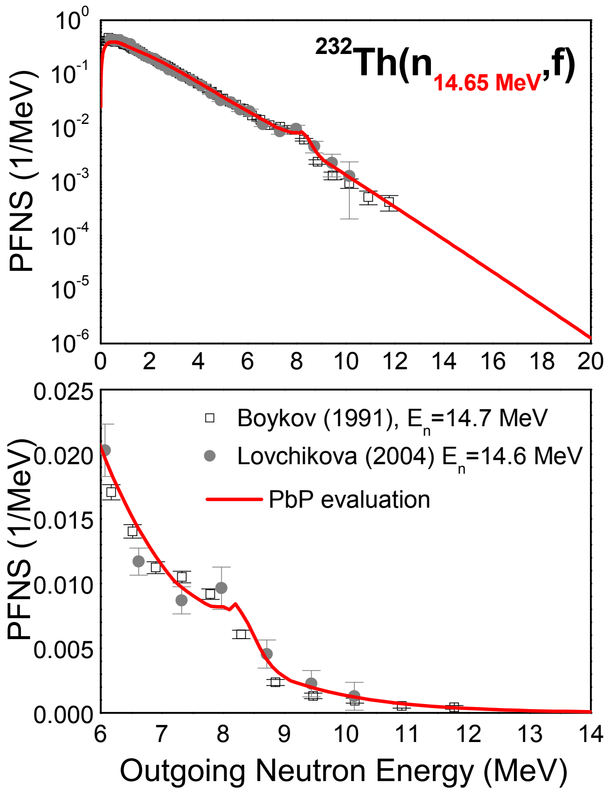

FIG. 51. (Color online) The `PbP` PFNS for ^{232}Th at $E_n = 14.65$ MeV is compared to data. The distribution shown with a log scale in the upper part of the figure is presented for a smaller range of outgoing energies and a linear scale to show the agreement with the data at the endpoint for pre-equilibrium emission.

2. Model Inputs

These inputs refer to nuclear structure-related quantities such as mass excess, shell corrections and fission cross sections that are not related to prompt neutron emission. Most of these inputs are taken from RIPL-3 [184], as described in Sec. IV C 3.

The compound nucleus cross section $\sigma(\epsilon)$ (corresponding to the neutron incident on a fission fragment, see Eq. (21)) is obtained from optical model calculations using the SCAT2 code [199]. Different optical model parameterizations were tested including Becchetti-Greenlees [328], Koning-Delaroche [232], and Wilmore-Hodgson [329] potentials (taken from RIPL-3 [183]), and the formula proposed by Iwamoto [330]. In most cases, the Becchetti-Greenlees [328] optical model parameterization gave the best description of the PFNS shapes. For more details, see Ref. [191].

A modified version of the GNASH code was used to calculate the relative contributions from multi-chance fission to complete the evaluations up to 20 MeV. The sum of the (n, xnf) contributions were shown to agree with the total fission cross section [160]

To compare the calculated spectral shapes with those of the experimental data, each data set was rescaled to the calculated spectrum by the integral of the spectrum, as suggested by Madland and Nix [38]. Systematics [179] are used at higher energies when multi-chance fission from (n, xnf) is considered, see also Refs. [190, 191].

An example of the PFNS from the `PbP` ^{232}Th evaluation is shown in Fig. 51 for $E_n = 14.65$ MeV, between the energies measured by Boykov (14.7 MeV) [78] and Lovchikova (14.6 MeV) [96]. This energy was chosen to show that the `PbP` method can reproduce the PFNS when the pre-fission neutron emission and the pre-equilibrium emission are considered. The enhancement in the PFNS at ~8 MeV$\simeq E_n - B_f$, visible in the log scale in the upper panel of the figure, is reproduced by the calculation, as emphasized in the lower panel with the linear scale. B_f is the estimated fission barrier for the ^{232}Th(n,f) reaction that defines the highest energy at which the $(n, n'\text{f})$ reaction occurs with emission of pre-equilibrium neutrons.

H. FREYA Evaluation of ^{235}U(n,f) and ^{239}Pu(n,f) PFNS

1. *Computational Approach for* FREYA *Evaluations*

Here the statistical method used for determining model parameters and reaction observables in FREYA is described. The analysis uses the Monte Carlo approach to Bayesian inference, see e.g., Ref. [331].

In the FREYA evaluations, only e_0, x and dTKE are adjusted, see Sec. V C for the definition of all variables. The parameters c and $Q_{\min}$ were held fixed. The evaluations were done with an earlier version of FREYA that did not include the parameter c_S. The parameters e_0, x, and dTKE could, in principle, be adjusted for each incident neutron energy E_n. However, because independent fits to the experimental data tend to yield values of e_0 and x that are nearly independent of E_n [249], these two parameters are assumed to be energy independent. This simplification facilitates the optimization procedure. Thus a given model realization is characterized by the two values e_0 and x together with the function $d\mathrm{TKE}(E_n)$ which, for practical purposes, will be defined by its values at certain selected energies, $\{d\mathrm{TKE}_\ell\}$. For formal convenience, the set of model parameter values is denoted as $\boldsymbol{m} = \{m_k\}$.

When FREYA is used with any particular value set $\boldsymbol{m}$, it yields a sample of fission events from which observables, $\boldsymbol{d}(\boldsymbol{m})$, are extracted that can be compared directly to the corresponding experimental values, $\boldsymbol{d}_{\rm exp}$. For example, the energy-dependent mean neutron multiplicity, $\overline{\nu}(E_n)$, may be compared with the values given in the ENDF/B-VII.0 evaluation [332].

It is assumed that the experiment provides not just the values but also the entire associated covariance matrix $\boldsymbol{\Sigma}_{\rm exp}$. (The square roots of the diagonal elements of $\boldsymbol{\Sigma}_{\rm exp}$ are the uncertainties on the individual observables.) The degree to which the particular model realization defined by the parameter values $\boldsymbol{m}$ describes the measured data $\boldsymbol{d}_{\rm exp}$ is then expressed by

$$P(\boldsymbol{d}_{\rm exp}|\boldsymbol{m}) \sim \exp\left(-\tfrac{1}{2}\chi^2(\boldsymbol{m})\right) . \tag{108}$$

where $\chi^2(\boldsymbol{m})$ is the generalized least-squares deviation between the model $\boldsymbol{m}$ and experiment,

$$\chi^2 = (\boldsymbol{d}_{\rm exp} - \boldsymbol{d}(\boldsymbol{m})) \cdot (\boldsymbol{\Sigma}_{\rm exp})^{-1} \cdot (\boldsymbol{d}_{\rm exp} - \boldsymbol{d}(\boldsymbol{m}))^T . \tag{109}$$

Employing merely the diagonal part of $\boldsymbol{\Sigma}_{\rm exp}$, i.e., the variances alone, ensures that well-measured observables carry more weight than poorly measured ones. This approach was used in the previous PFNS evaluation [249], which was restricted to lower energy ($E_n < 5.5$ MeV). Here the full covariance matrix is employed, thereby ensuring that correlations between measured observables are also taken into account. These correlations do impact the results.

Using the above framework, the weighted averages of arbitrary observables $\boldsymbol{O} = \{\mathcal{O}_i\}$ are computed. Physically reasonable values of the model parameters $\boldsymbol{m}$ are assumed to be uniformly distributed within a hypercube in parameter space. This defines the a-priori model probability distribution $P(\boldsymbol{m})$. The *best estimate* of the observable $\mathcal{O}_i$ is then given by

$$\prec \mathcal{O}_i \succ = \int d\boldsymbol{m}\, P(\boldsymbol{m})\, P(\boldsymbol{d}_{\rm exp}|\boldsymbol{m})\, \mathcal{O}_i(\boldsymbol{m}) . \tag{110}$$

being $\prec \mathcal{O}_i \succ$ – the expectation value of the stochastic quantity $\mathcal{O}_i$. The best estimate for the covariance between two such observables can be obtained similarly,

$$\begin{aligned} O_{ij} &\equiv \prec \mathcal{O}_i\mathcal{O}_j \succ - \prec \mathcal{O}_i \succ \prec \mathcal{O}_j \succ \\ &= \prec (\mathcal{O}_i - \prec \mathcal{O}_i \succ)(\mathcal{O}_j - \prec \mathcal{O}_j \succ) \succ . \end{aligned} \tag{111}$$

In particular, the best estimate of $\overline{\nu}$,

$$\prec \overline{\nu} \succ = \int d\boldsymbol{m}\, P(\boldsymbol{m})\, P(\boldsymbol{d}_{\rm exp}|\boldsymbol{m})\, \overline{\nu}(\boldsymbol{m}) , \tag{112}$$

and the prompt neutron spectrum, as well as the covariances between those quantities, is computed.

In practice, parameter space is averaged over employing a Monte Carlo approach, thereby reducing the integral over all possible parameter values $\boldsymbol{m}$ to a sum over N sampled model realizations, $\{\boldsymbol{m}^{(n)}\}$,

$$\prec \mathcal{O}_i \succ \approx \frac{1}{N}\sum_{n=1}^{N} P(\boldsymbol{m}^{(n)})\, P(\boldsymbol{d}_{\rm exp}|\boldsymbol{m}^{(n)})\, \mathcal{O}_i(\boldsymbol{m}^{(n)}) . \tag{113}$$

The joint probability $w_n \equiv P(\boldsymbol{m}^{(n)})P(\boldsymbol{d}_{\rm exp}|\boldsymbol{m}^{(n)})$ may be viewed as the likelihood that the particular model realization $\boldsymbol{m}^{(n)}$ is “correct” . Since it depends exponentially on χ^2_n, the likelihood tends to be strongly peaked around

TABLE 27. The values obtained for the two energy-independent parameters of `FREYA` included in the present fits.

Fissioning system	e_0 (MeV)	x
^{239}Pu(n,f) $\overline{\nu}$ only	10.007 ± 0.568	1.154 ± 0.085
^{239}Pu(n,f) $\overline{\nu}$ + spectra	9.801 ± 0.538	1.113 ± 0.077
^{235}U(n,f) $\overline{\nu}$ only	10.014 ± 0.530	1.150 ± 0.087
^{235}U(n,f) $\overline{\nu}$ + spectra	9.978 ± 0.563	1.133 ± 0.081

the favored set. It is important that the parameter sample be sufficiently dense in the peak region to ensure that many sets have non-negligible weights. Latin Hypercube sampling (LHS) [333, 334] is used which samples a function of K variables with the range of each variable divided into M equally-spaced intervals. Each combination of M and K is sampled at most once, with a maximum number of combinations being $(M!)^{K-1}$. The LHS method generates samples that better reflect the distribution than a purely random sampling would. Consequently, relative to a simple Monte Carlo sampling, the employed sampling method requires fewer realizations to determine the optimal parameter set. The optimal parameter values are obtained from 5000 realizations of the parameter space.

Two fits were made for both ^{235}U(n,f) and ^{239}Pu(n,f), one including the spectral shapes and one without. These fits to the ^{239}Pu(n,f) spectral shapes were made prior to the release of the Chatillon et al. [92] data and should be updated. The small uncertainties on the evaluated $\overline{\nu}$ drive the results. When only the evaluated $\overline{\nu}$ is used to constrain the PFNS evaluation, as in Ref. [249], the spectrum is an outcome rather than a comparative observable. The evaluated $\overline{\nu}$ in ENDF/B-VII.0 [332], with the covariance resulting from the least-squares fit to the available data described in Ref. [335], is employed. The energy-dependent neutron multiplicity, $\overline{\nu}(E_n)$ is represented as a locally linear fit to the experimental data. Since the nodes in this fit do not align with fitted data, the fit introduces energy correlations that are encoded into the covariance matrix.

Because the spectral data are often given with an arbitrary normalization, they are normalized to unity while preserving their spectral shapes, following the prescription of Ref. [249]. This procedure could introduce some bias into the result because a particular functional form has been assumed to obtain the integral normalization.

For each model realization, `FREYA` is used to generate a large sample of fission events (typically one million events for each parameter set) for each of the selected incident neutron energies, and the resulting average multiplicity $\overline{\nu}(E_n)$ is extracted from the generated event sample.

2. *Results*

Here the `FREYA` fits are discussed and some selected results are shown. The value of e_0 is varied between 8 and 12 MeV while $1 \leq x \leq 1.4$ is assumed. These two parameters are taken to be independent of the incident neutron energy. Because dTKE represents the shift in the total fragment kinetic energy from the value obtained for incident thermal neutron energies, dTKE should depend on the incident neutron energy. The parameter dTKE is fit at six values of incident neutron energy, $E_n = 10^{-11}$, 0.25, 1, 5, 14 and 20 MeV, to keep the parameter space manageable. These points are chosen to reflect the physics of the fission process: the region between 0.25 and 1 MeV is where $\overline{\nu}(E_n)$ changes slope while the second-chance fission threshold is just above 5 MeV. The full 20-point grid of the `FREYA` evaluation is then covered by means of a linear interpolation between these node points.

The values of e_0 and x obtained for each fit are given in Table 27. The results for both parameters are consistent with each other within the uncertainties for both isotopes. In further work, $e_0 \sim 10$ MeV for all systems. This value is consistent with those found when no collective effects are included. Based on the RIPL-3 systematics [184], a larger value, e.g., $e_0 \sim 13$ MeV, is expected.

The fitted values of dTKE are shown in Fig. 52. The error bars on dTKE at the node points are the standard deviations obtained from the averaging over the range of parameter values while the error bars on dTKE between two node points are the interpolated dispersions between those two points. The values of dTKE are practically energy independent for ^{239}Pu(n,f) while they increase almost linearly up to $E_n \sim 14$ MeV for ^{235}U(n,f). Above 14 MeV, the ENDF/B-VII.0 $\overline{\nu}$ evaluation is not based on data but on a linear extrapolation of measurements taken for higher incident energies. Thus, $\overline{\nu}$ is not well constrained near the high end of the energy range. The values of dTKE are positive, indicating that using the thermal average value of TKE leads to too many neutrons. The positive dTKE is then required to reduce the excitation energy sufficiently to give a good fit to $\overline{\nu}$.

The sensitivity of $\overline{\nu}$ to changes in the parameter values can be checked by changing one parameter while keeping the other two fixed. For example, reducing dTKE by 10% increases $\overline{\nu}$ by 0.55% while decreasing x by 10% decreases $\overline{\nu}$ by 0.1%. The largest change in $\overline{\nu}$ arises when e_0 drops by 10%. In this case, $\overline{\nu}$ is 0.86% larger.

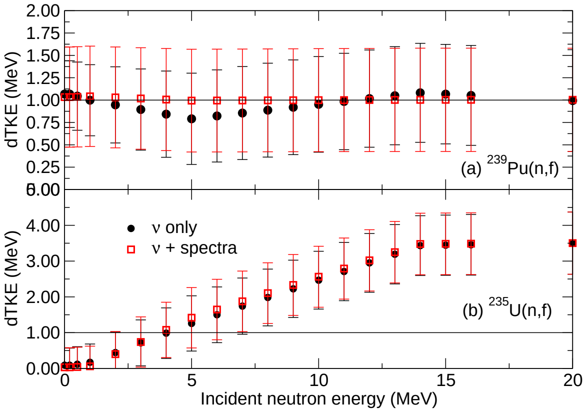

FIG. 52. (Color online) The fitted values of dTKE for (a) ^{239}Pu(n,f) and (b) ^{235}U(n,f). Results from fitting to ν only are given by the black filled circles while those including the spectral shapes are given by the open red squares.

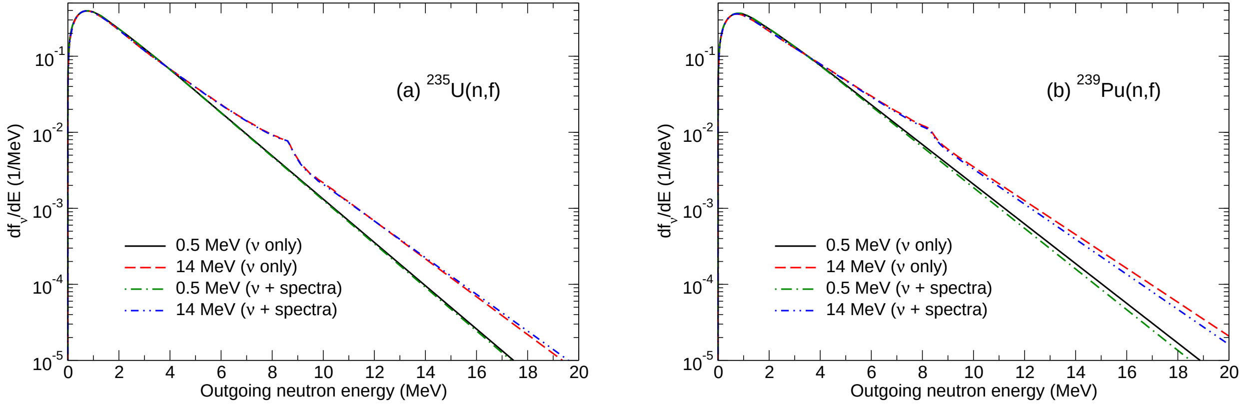

FIG. 53. (Color online) Comparison of spectral shapes obtained for the two fits for (a) ^{235}U(n,f) and (b) ^{239}Pu(n,f).

Examples of the resulting prompt fission neutron spectral shapes,

$$f_n^\nu(E) \;\equiv\; \frac{1}{\nu}\frac{d\nu}{dE}\ , \tag{114}$$

normalized to unity, are shown in Fig. 53. Results are presented for two representative energies: $E_n = 0.5$ and 14 MeV. The convergence of the two fits (with and without including the spectral shapes) appears to be better for ^{235}U(n,f) since the two results are equivalent on the log scale of the plots while there is some clear difference between the fits for ^{239}Pu(n,f). An inspection of the spectra obtained for 14 MeV reveals abrupt drops in value at the energies corresponding to the effective threshold for pre-equilibrium neutron emission and subsequent fission. The kink in the spectrum at $\hat{E}_2 \approx E_n - B_f(^{239}\mathrm{Pu}) = 8.4$ MeV is the endpoint of pre-equilibrium neutron emission for $E_n = 14$ MeV, being B_f – the corresponding fission barrier. Going from the fits to a full spectral evaluation is not straightforward due to the Monte Carlo nature of `FREYA`. It is impossible to generate smooth spectra over the entire range of outgoing neutron energies required without introducing (sometimes significant) massaging. The procedure with `FREYA` is briefly described here.

First, the values of e_0, x, and dTKE determined from the fits are used to generate output spectra for each incident neutron energy in the grid. Two runs are made. One takes a smaller energy bin size to partially populate the low energy end of the spectrum, $E < 2$ MeV. A larger bin size is used to obtain a smoother spectrum at $E > 5$ MeV. Both of these outputs are produced with 5 million events, an approximate one minute run for each realization. Since these outputs are still not smooth and the small bin size for the lower energies are still inadequate to the task of populating statistics down to 10^{-5} MeV, the output spectra are fit to either a Watt spectrum (see Sec. IV) or an exponential. A Watt spectrum works well for $E < 2$ MeV while either functional form can work for the high energy tail but this has to be checked on a case by case basis.

Special care has to be taken once above the threshold for pre-fission neutron emission since it is not possible to simply fit regions with significant changes in slope as illustrated in Fig. 53. This task does not immediately lend itself to automation because the fit results need to be checked to see if they make sense. The `ROOT` package [336] is employed for these fits. Finally, smooth spectra are produced at the required grid points by using the fit coefficients obtained

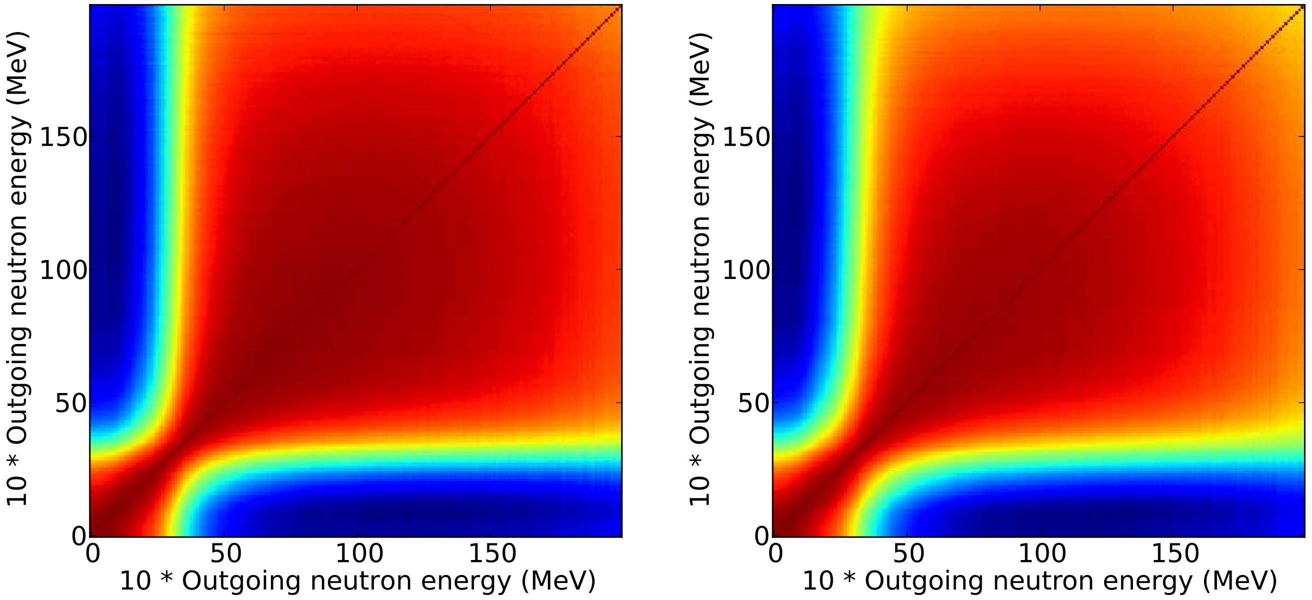

(a)^{239}Pu(n,f) PFNS when fitting to $\overline{\nu}$ only.

(b)^{239}Pu(n,f) PFNS when fitting to $\overline{\nu}$ and the spectral shape.

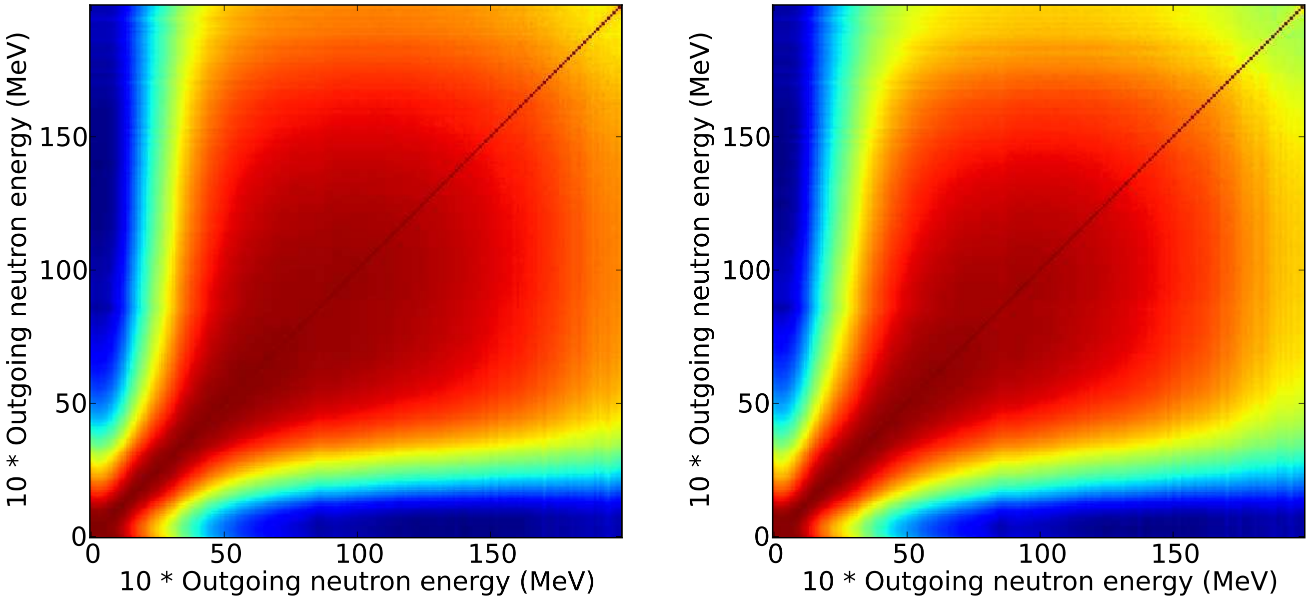

(c)^{235}U(n,f) PFNS when fitting to $\overline{\nu}$ only.

(d)^{235}U(n,f) PFNS when fitting to $\overline{\nu}$ and the spectral shape.

FIG. 54. (Color online) Contour plot of the correlation coefficient for ^{239}Pu(n,f) (top panels) and for ^{235}U(n,f) (bottom panels), see Eq. (111), between the spectral strengths at two different energies, C_{E_1,E_2}, as obtained for $E_n = 14$ MeV when fitting as indicated for the corresponding target. The correlation changes from values near $+1$ in the reddish regions (lower-left and central regions) to values near -1 in the bluish regions (near the two axes).

by the above procedure at low and high energies. In the intermediate energy range, typically around the peak but extending over the discontinuities caused by pre-fission emission at higher E_n, smoothed interpolated `FREYA` spectra are used directly. Finally, the quality of the interpolation procedure is checked at each energy. Clearly some streamlining would be required to make this practical on a large scale.

3. Covariances

Covariances and correlation coefficients can be calculated between the optimal model parameter values as well as between the various output quantities using Eq. (111). The covariance between two parameters m_k and $m_{k'}$ is

$$\Sigma_{kk'} \equiv \prec (m_k - \prec m_k \succ)(m_{k'} - \prec m_{k'} \succ) \succ \quad . \tag{115}$$

The diagonal elements, Σ_{kk} are the variances $(\Delta m_k)^2$, representing the squares of the uncertainty on the optimal value of the individual model parameter m_k, while the off-diagonal elements give the covariances between two different model parameters. It is often more instructive to employ the associated *correlation coefficients*, $C_{kk'} \equiv \Sigma_{kk'}/[\Sigma_{m_k}\Sigma_{m_{k'}}]$, which is plus (minus) one for fully (anti)correlated variables and vanishes for entirely independent (uncorrelated) variables.

The covariance between the spectral strengths at different outgoing energies E may also be computed using Eq. (111). The resulting correlation coefficients C_{E_1,E_2} are shown in Fig. 54 for $E_n = 14$ MeV. In both top and bottom rows of the figure, the left-hand side shows the result from fitting to $\overline{\nu}$ alone while the right-hand side shows the result including the spectra. Note that $C_{E_1,E_2} \approx 1$ (dark red areas) when the two specified energies lie on the same side of the crossover region, ∼3.5 MeV for ^{239}Pu(n,f), while $C_{E_1,E_2} \approx -1$ (dark blue areas) when they lie on opposite sides. The crossover region around 3.5 MeV for this value of E_n indicates that the spectrum tends to pivot around this point when the parameter space is explored, similar to Ref. [249].

The results illustrated in Fig. 54 are representative of the results at all energies. The correlations between the outgoing energies are stronger when fitting to $\overline{\nu}$ only, as can be seen from the broader dark red regions of the left-hand plots. The overall correlation is weaker and "noisier" for ^{235}U(n,f) (bottom panels) relative to ^{239}Pu(n,f) (top panels), particularly at higher outgoing energies where an anticorrelation is seen for ^{235}U(n,f) with the spectral shapes included. Some of this noise is due to poorer spectral statistics for high neutron energies since the ^{235}U(n,f) spectral shape is softer than that of ^{239}Pu(n,f). These correlation matrices are based on the raw fit results, not on the subsequently smoothed spectra included in the evaluation which would, presumably, produce sharper correlation matrices over all energies.

VIII. DATA TESTING

A. Processing of the Data

Evaluated PFNS of selected nuclei provided by the authors were given in different forms. To be able to use them in data verification and testing, consistent ENDF files were produced using the assigned MAT, MF=5, and MT=18 designations in ENDF terminology [44]. In this form the data could be inserted into an existing evaluation. Any evaluated library could be used for this purpose, but in this paper the ENDF/B-VII.1 file [148]) was adopted. Processing with the NJOY2012.50 code system [337] was done to prepare the corresponding ACE libraries for use with the MCNP Monte Carlo transport code [119].

The evaluated PFNS were converted also into equivalent ENDF-6 representation using MF=3, MT=261 and MF=33 for covariances (when available) with different MAT numbers to distinguish different data sets. This form is used in dosimetry applications [3] for calculating reaction rates with the dosimetry cross section library, and it is convenient for plotting and intercomparison. Local codes (`MF35TO33` and `MF33TO35`, available on request from A. Trkov) were used for the conversion. In this form the uncertainties in the spectrum averaged cross sections and the average energies could be calculated with the `RR_UNC` code [338] (using an artificial "cross section" equal to the incident energy for the latter).

The evaluated (transport) data files created in this way should by no means be considered "a complete evaluation" and are not expected to perform better than the original files. They are intended to demonstrate the effect of the PFNS alone. A true new evaluation should reevaluate all other reaction channels and neutron multiplicities, which may compensate the effects of the PFNS on the neutron flux, and therefore on the calculated criticality.

B. Benchmarking of the ^{235}U PFNS

The PFNS files for ^{235}U in ENDF-6 format contributed to the CRP by N. Kornilov (SCALE) [288], V. Maslov (cf Minsk Actinide Library) B. Morillon (cf Sec. IV B 2), P. Talou (cf Sec. VII F), Shu N.-C. (cf Sec. IV D), Vogt (cf Sec. VII H) and A. Trkov (GANDR fit, cf Sec. VII B) were considered in the analysis and processed as described above. The PFNS provided by the authors included incident energy dependence, except for Kornilov and Pronyaev (only thermal), and Trkov, which was evaluated at the thermal energy and in the interval between 0.5 MeV and 2 MeV. The thermal point was added, interpolated linearly to 0.5 MeV, with invariant spectrum up to 2 MeV and adopting the original ENDF/B-VII.1 spectrum above. No working library was produced for the Pronyaev (GMA) PFNS as it was considered that GANDR benchmark results are representative of the GMA results.

The evaluated spectra differ significantly both in shape (see Fig. 55 for the PFNS comparison for thermal neutrons) and average neutron energy $\overline{E}$ (see Table 28). Vogt et al. (`FREYA`) and Shu et al. evaluations are the outliers both in shape and average energy. The `FREYA` evaluation for thermal neutrons gives the lowest $\overline{E}$ at 1.91 MeV, while the Shu et al. evaluation corresponds to the highest $\overline{E}$ at 2.082 MeV.

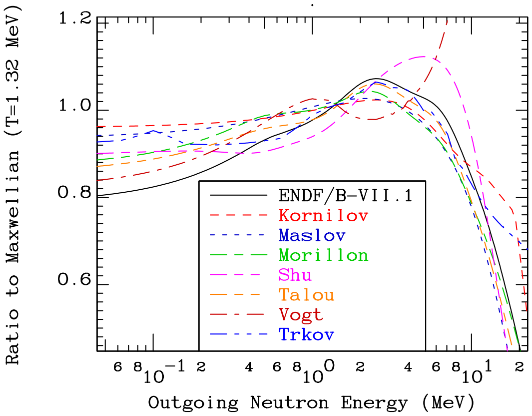

FIG. 55. (Color online) Comparison of PFNS of ^{235}U($n_{\rm th}$,f) from different CRP calculations and evaluations shown as ratios to a Maxwellian.

TABLE 28. Comparison of the PFNS average energies (in MeV) of ^{235}U(n,f) for the calculations and evaluations discussed within the IAEA CRP. The column header is the incident neutron incident energy, E_n, in MeV. The estimated uncertainty on the average energy due to the PFNS uncertainty is 10 keV. The * indicates an average over incident neutron energies, $0.3 \leq E_n \leq 2$ MeV.

PFNS source	Thermal	0.5 MeV	2 MeV	5 MeV
ENDF/B-VII.1 [148]	2.031	2.045	2.057	2.110
Maslov [156]	1.960	1.981	2.029	2.120
Kornilov (SCALE) [288]	1.970	–	–	–
Morillon (Sec. IV B 2)	1.970	1.978	2.002	2.050
Shu (Sec. IV D)	2.082	2.082	2.114	2.234
Vogt (Sec. VII H)	1.911	1.933	1.980	2.057
Talou (Sec. VII F)	2.001	2.014	2.054	2.129
GANDR fit (Sec. VII B)	2.001	2.017*	–	–
GMA fit (Sec. VII C)	2.000	–	–	–

The shape of the PFNS and in particular the average energy strongly affect the criticality of reactor systems. The reactivity of thermal systems increases with decreasing $\overline{E}$ because less moderation is required to thermalize the neutrons. The high-leakage systems are affected most strongly because a lower average energy reduces the fraction of very fast neutrons that have the highest probability of escaping from the system. High-leakage thermal solution benchmarks from Oak Ridge National Laboratory and Idaho National Laboratory (Rocky Flats) collected in the ICSBEP compilation [339] were analyzed. Selected fast assemblies that were found sensitive to the PFNS were also included in the analysis, although they were only calculated for the Trkov evaluation as a representative case of new evaluations. Indeed, the GANDR, the GMA and Talou evaluations feature almost exactly the same PFNS $\overline{E}$ as seen in Table 28.

The list of thermal benchmarks is shown in Table 29. The differences $\Delta k_{\rm eff}$ from the reference benchmark values of the multiplication factors $k_{\rm eff}$ in units of *pcm* (parts per 100 000) are shown in Fig. 56 for selected thermal benchmarks.

TABLE 29. List of highly-enriched (HEU) ^{235}U thermal-solution benchmarks selected for the analysis.

ICSBEP full name	Short name	Common name
HEU-SOL-THERM-009	hst009-1	ORNL_S1
HEU-SOL-THERM-009	hst009-2	ORNL_S2
HEU-SOL-THERM-009	hst009-3	ORNL_S3
HEU-SOL-THERM-009	hst009-4	ORNL_S4
HEU-SOL-THERM-013	hst013-1	ORNL_T1
HEU-SOL-THERM-013	hst013-2	ORNL_T2
HEU-SOL-THERM-013	hst013-3	ORNL_T3
HEU-SOL-THERM-013	hst013-4	ORNL_T4
HEU-SOL-THERM-001	hst001-01	Rocky Flats-01
HEU-SOL-THERM-001	hst001-02	Rocky Flats-02
HEU-SOL-THERM-001	hst001-08	Rocky Flats-08
HEU-SOL-THERM-001	hst001-09	Rocky Flats-09
HEU-SOL-THERM-001	hst001-10	Rocky Flats-10
HEU-SOL-THERM-042	hst042-1	ORNL_C1
HEU-SOL-THERM-042	hst042-2	ORNL_C2
HEU-SOL-THERM-042	hst042-3	ORNL_C3
HEU-SOL-THERM-042	hst042-4	ORNL_C4
HEU-SOL-THERM-042	hst042-5	ORNL_C5
HEU-COMP-THERM-015	hct015-11	LWTR SB-1
HEU-COMP-THERM-015	hct015-15	LWTR SB-5

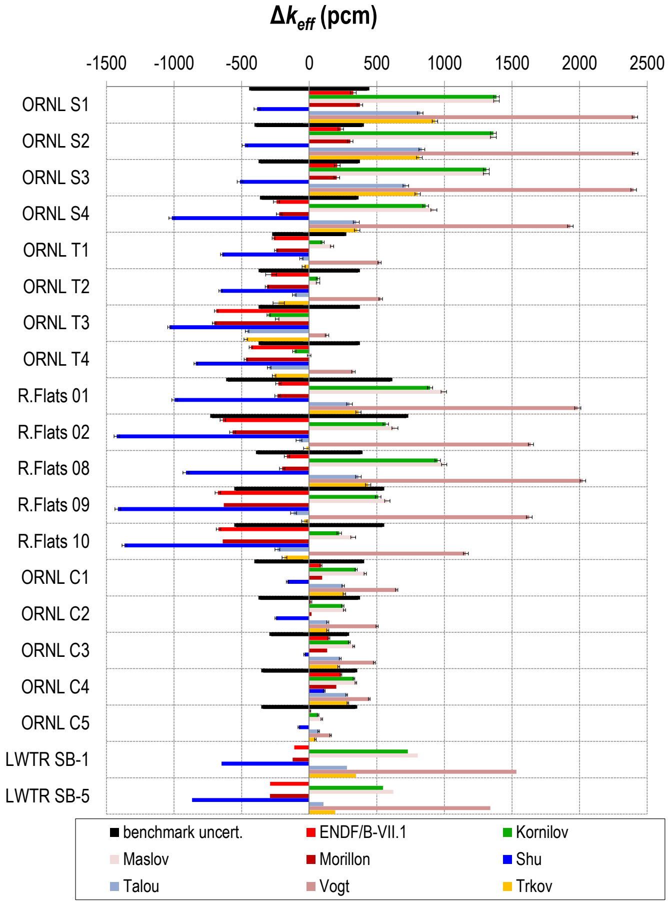

FIG. 56. (Color online) Differences from the reference benchmark values of the multiplication factors k_{eff} for highly-enriched ^{235}U thermal-solution benchmarks. The black uncertainty bars correspond to the evaluated benchmark uncertainty.

No benchmark calculations were done with the GMA spectrum since it is only available for incident thermal neutrons and its average energy is practically coincident with the spectrum from the GANDR fit. The results with the ENDF/B-

VII.1 library are in reasonable agreement with the measured values within the quoted uncertainties. A general trend is observed that the PFNS with higher average neutron energies (see Table 28) result in lower reactivities compared to ENDF/B-VII.1 results and vice versa.

From the figure it is evident that for both the ORNL S_n and the Rocky Flat series of thermal solution benchmarks the sensitivity of the core reactivity to the average energy of the PFNS is extremely high, which implies that realistically there is limited flexibility in the values that the average energy of the neutrons can take; large changes in other cross sections, resonance parameters, or neutron multiplicities needed to compensate the reactivity swing could be un-physical and would severely affect other benchmarks. The two largest deviations are seen for high-leakage thermal solution benchmarks. The measured criticality for ORNL hst009-1 and Rocky Flats hst001-01 benchmarks is over-predicted by 2400 *pcm* and 2000 *pcm* with FREYA evaluation that features the lowest PFNS average energy (1.911 MeV $= -9\sigma$ away from the non-model GMA evaluation). On the other side, the measured criticality for Rocky Flats hst001-02 and hst001-09 benchmarks is under-predicted by 1400 *pcm* with the Shu et al. evaluation that features the highest PFNS average energy (2.082 MeV $= +8.2\sigma$ away from the non-model GMA evaluation). Non-model evaluations (GANDR and GMA) have $\overline{E}$ lower by 30 keV than the ENDF-B/VII.1, therefore increasing the criticality in thermal-solution benchmarks with high leakage. Such increase will need to be compensated by changes in other physical parameters.

TABLE 30. List of fast-neutron benchmarks selected for the ^{235}U(n,f) analysis. Both highly-enriched and intermediately-enriched ^{235}U assemblies were considered. All assemblies but Godiva contain a significant amount of ^{238}U.

ICSBEP full name	Short name	Common name
HEU-MET-FAST-001	hmf001	Godiva
HEU-MET-FAST-028	hmf028	Flattop-25
IEU-MET-FAST-007	imf007	Big Ten
HEU-MET-FAST-002	hmf002-1	Topsy-1
HEU-MET-FAST-002	hmf002-2	Topsy-2
HEU-MET-FAST-002	hmf002-3	Topsy-3
HEU-MET-FAST-002	hmf002-4	Topsy-4
HEU-MET-FAST-002	hmf002-5	Topsy-5
HEU-MET-FAST-002	hmf002-6	Topsy-6
IEU-MET-FAST-001	imf001-1	Jemima-1
IEU-MET-FAST-001	imf001-2	Jemima-2
IEU-MET-FAST-001	imf001-3	Jemima-3
IEU-MET-FAST-001	imf001-4	Jemima-4

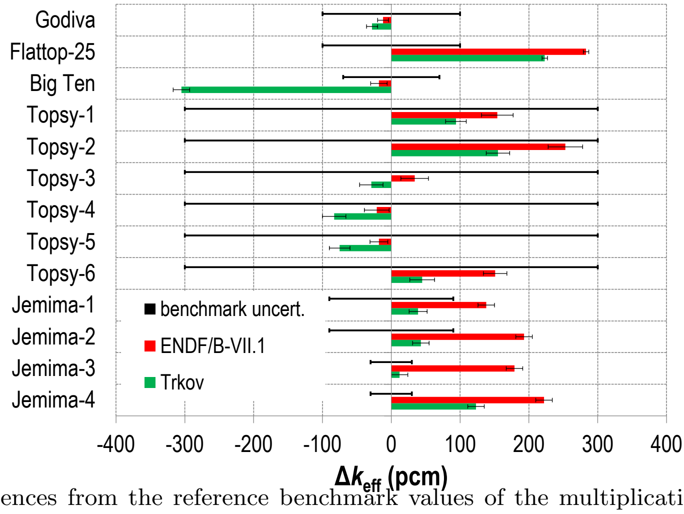

FIG. 57. (Color online) Differences from the reference benchmark values of the multiplication factors k_{eff} for selected ^{235}U fast-neutron assemblies. The black uncertainty bars correspond to the evaluated benchmark uncertainty.

The list of fast neutron benchmarks is shown in Table 30. The differences in the multiplication factors k_{eff} from the fast-assembly reference benchmark values in units of *pcm* are shown in Fig. 57. It illustrates that lowering $\overline{E}$, e.g., from 2.03 MeV for the ENDF/B-VII.1 evaluation to 2.000 MeV in the GANDR evaluation [55, 56], decreases the reactivity in fast assemblies because neutrons are more effectively slowed down into the resonance region where they undergo capture. The decrease for the Trkov et al. (GANDR) evaluation was as high as 300 *pcm* for the Big Ten benchmark.

TABLE 31. Comparison of the PFNS average energies (in MeV) of ^{239}Pu(n,f) for calculations and evaluations discussed within the IAEA CRP. The column header is the neutron incident energy E_n. The estimated uncertainty of the average energy due to the PFNS uncertainty is 10 keV.

PFNS source	Thermal	1 MeV	2 MeV	5 MeV
JEFF-3.1.1 [340]	2.112	2.140	2.168	2.226
ENDF/B-VII.1 [148]	2.112	2.138	2.163	2.236
JENDL-4.0 [149]	2.116	2.140	2.165	2.236
Maslov [341]	2.092	2.122	2.152	2.242
Morillon (Sec. IV B 2)	2.085	2.099	2.114	2.145
Talou (Sec. VII F)	2.083	2.111	2.138	2.215
Neudecker (Sec. VII E)	2.074	2.103	2.131	2.211
GMA fit (Sec. VII C)	2.074	–	–	–

C. Benchmarking of the ^{239}Pu PFNS

The ^{239}Pu PFNS considered in this analysis are mainly those evaluated by Morillon (Sec. IV B 2), Talou (Sec. VII F) and by Neudecker (Sec. VII E). The latter evaluation follows the methodology reported in Ref. [297], but includes spectra for all incident neutron energies as described in Sec. VII E. There is new evaluation work by Pronyaev et al. for thermal neutrons for the Standards project (denoted GMA fit, Sec. VII C). The average energies from these evaluations and those from major evaluated nuclear data files are compared in Table 31. The spectra are compared in Fig. 58. All the new spectra are softer than ENDF/B-VII.1. There is good agreement between the Talou, Neudecker, Morillon and GMA evaluations at the thermal point. The average energies derived from the new evaluations are about 30 keV lower for thermal neutrons than those of the existing libraries. This reduction is similar to that observed for the ^{235}U(n_{th},f) PFNS. The evaluated PFNS were inserted into the ENDF/B-VII.1 ^{239}Pu evaluation and processed the same way as for ^{235}U to obtain ACE libraries for MCNP. High-leakage thermal solution benchmarks from the Batelle Pacific Nortwest Laboratory (PNL), Hanford and Valduc facilities in the ICSBEP compilation [339] were analyzed. The list of benchmarks is shown in Table 32. The differences of the multiplication factors from the reference benchmark values in units of *pcm* are shown in Fig. 59. As in the case of the ^{235}U PFNS, the high-leakage assemblies show very large sensitivity to $\overline{E}$. The reason behind this high sensitivity was investigated by Peneliau et al. [2] and was attributed to greatly reduced neutron leakage with energies above 1 MeV when the PFNS is softened.

Fast neutron benchmarks are also included in Table 32. The results are given in Fig. 60. The effect of reducing $\overline{E}$ on fast systems reduces the reactivity by ∼250 *pcm*, similar to ^{235}U. Neudecker evaluation was especially tested in Jezebel benchmark [297], it was shown that the C/E values for spectral indexes in the central region of the Jezebel critical assembly are improved for the high-energy threshold $(n, 2n)$ reaction of ^{238}U, ^{169}Tm and ^{191}Ir(n,2n) compared to ENDF/B-VII.1 and perform similarly well for (n, γ) reactions of, e.g., ^{238}U and fission reactions of, e.g., ^{239}Pu and ^{238}U, while the criticality of Jezebel and Flattop departs farther from unity than is the case when the ENDF/B-VII.1 PFNS is used. The benchmark results are rather insensitive to the choice of model defects discussed in Section VII E.

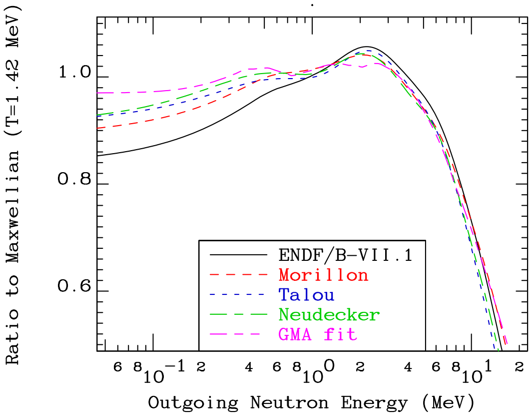

FIG. 58. (Color online) Comparison of PFNS of ^{239}Pu(n_{th},f) from different sources. The results are given as ratios to a Maxwellian.

The general trends are similar to those observed for ^{235}U(n,f): a decrease of the average neutron energy in thermal PFNS increases reactivity, while a decrease of the average energy in fast PFNS reduces the reactivity in the calculations of the benchmark assemblies.

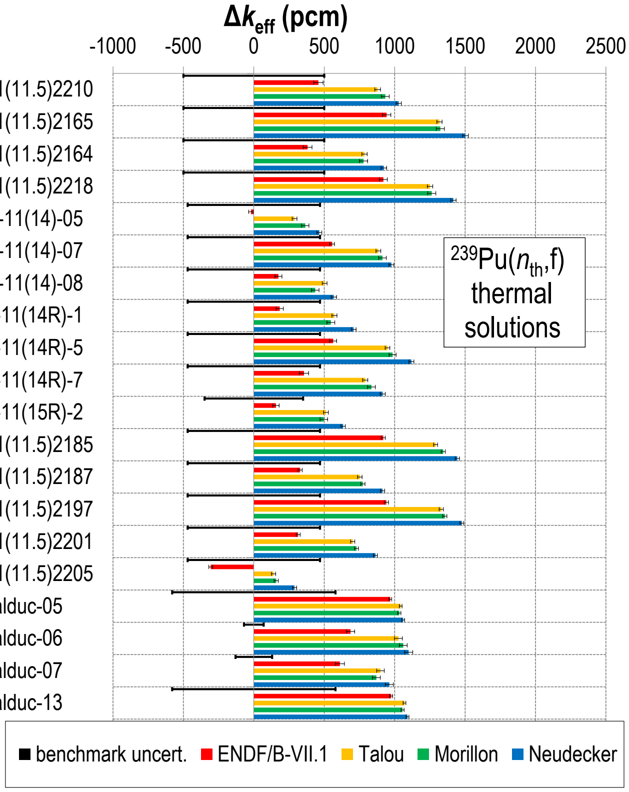

FIG. 59. (Color online) Differences in the multiplication factors $k_{\rm eff}$ from the reference benchmark values for highly-enriched ^{239}Pu thermal solutions. The black uncertainty bars correspond to the evaluated benchmark uncertainty.

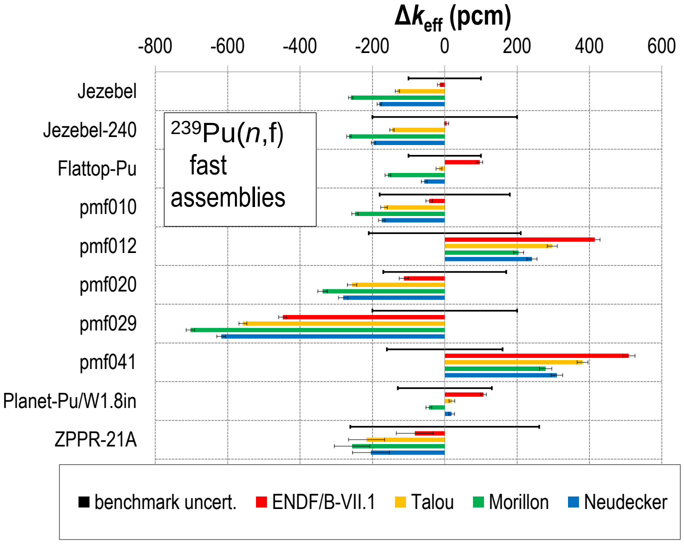

FIG. 60. (Color online) Differences in the multiplication factors $k_{\rm eff}$ from the reference benchmark values for highly-enriched ^{239}Pu fast assemblies. The black uncertainty bars correspond to the evaluated benchmark uncertainty.

D. Benchmarking of the ^{233}U PFNS

The $^{233}U(n_{\rm th}$,f) PFNS provided by Talou, Tudora and the GMA fit are compared to the spectrum from the ENDF/B-VII.1 evaluation in Fig. 61. The structure in the GMA fit is likely to be unphysical, but reflects the scattering in the experimental data, which are less abundant for this nuclide. The average energies of thermal neutron-induced PFNS are given in Table 33. The spectrum in the ENDF/B-VII.1 library is constant up to 1.5 MeV. The list of benchmarks included in the study of the impact of the PFNS is given in Table 34.

TABLE 32. List of fast and high-leakage thermal-solution ^{239}Pu benchmarks selected for the analysis.

ICSBEP full name	Short name	Common name
PU-MET-FAST-001	pmf001	Jezebel
PU-MET-FAST-002	pmf002	Jezebel-240
PU-MET-FAST-006	pmf006	Flattop-Pu
PU-MET-FAST-010	pmf010	
PU-MET-FAST-012	pmf012	
PU-MET-FAST-020	pmf020	
PU-MET-FAST-029	pmf029	
PU-MET-FAST-041	pmf041	
PU-MET-FAST-005	pmf005	Planet-Pu/W1.8in
PU-MET-FAST-033	pmf033	ZPPR-21A
PU-SOL-THERM-001	pst001-1	PNL-1(11.5)2210
PU-SOL-THERM-001	pst001-3	PNL-1(11.5)2165
PU-SOL-THERM-001	pst001-4	PNL-1(11.5)2164
PU-SOL-THERM-001	pst001-6	PNL-1(11.5)2218
PU-SOL-THERM-004	pst004-05	PNL-11(14)-05
PU-SOL-THERM-004	pst004-07	PNL-11(14)-07
PU-SOL-THERM-004	pst004-08	PNL-11(14)-08
PU-SOL-THERM-005	pst005-1	PNL-11(14R)-1
PU-SOL-THERM-005	pst005-5	PNL-11(14R)-5
PU-SOL-THERM-005	pst005-7	PNL-11(14R)-7
PU-SOL-THERM-006	pst006-2	PNL-11(15R)-2
PU-SOL-THERM-007	pst007-02	PNL-1(11.5)2185
PU-SOL-THERM-007	pst007-03	PNL-1(11.5)2187
PU-SOL-THERM-007	pst007-05	PNL-1(11.5)2197
PU-SOL-THERM-007	pst007-06	PNL-1(11.5)2201
PU-SOL-THERM-007	pst007-09	PNL-1(11.5)2205
PU-SOL-THERM-012	pst012-05	Valduc-05
PU-SOL-THERM-012	pst012-06	Valduc-06
PU-SOL-THERM-012	pst012-07	Valduc-07
PU-SOL-THERM-012	pst012-13	Valduc-13

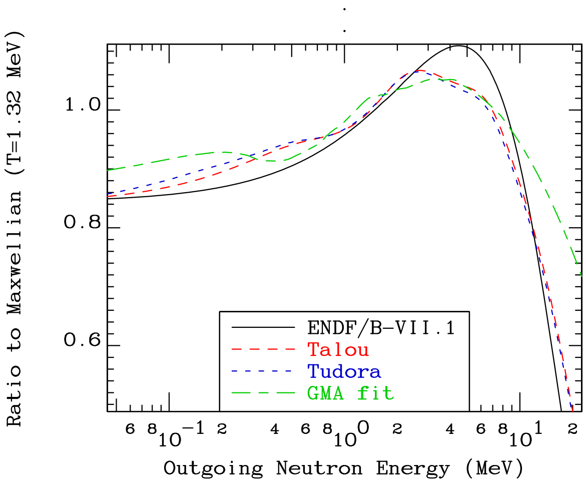

FIG. 61. (Color online) Comparison of the ^{233}U(n_{th},f) PFNS from different sources, given as ratios to a Maxwellian.

Fast assemblies with a ^{233}U core are affected to a lesser extent by the reduction in the PFNS $\overline{E}$ (Jezebel-23, Flattop-23 and the Planet assemblies in Fig. 62). There is some improvement in the tungsten-reflected Planet assemblies, but insufficient to remove the discrepancy for the Planet assembly with a thicker reflector. A considerable increase in reactivity is observed in several thermal solution benchmarks (U3ORNL cases). Larger than expected increase of reactivity is noted in some thermal lattices fuelled by ^{233}U (SB- series). The overall performance of the ENDF/B-VII.1 evaluation appears remarkably better, but one should consider carefully other cross section data of ^{233}U, particularly

TABLE 33. Comparison of the PFNS average energies (in MeV) of ^{233}U(n,f) for the evaluations discussed within the IAEA CRP. The column header is the incident neutron incident energy, E_n, in MeV. The estimated uncertainty of the average energy due to the PFNS uncertainty is 13 keV

PFNS source	Thermal	0.5 MeV	2 MeV	5 MeV
ENDF/B-VII.1 [148]	2.074	2.074	2.078	2.131
Talou (Sec. VII F)	2.032	2.045	2.084	2.159
Tudora (Sec. VII G)	2.024	2.040	2.085	2.172
GMA fit (Sec. VII C)	2.030	–	–	–

TABLE 34. List of benchmarks for testing the sensitivity to the PFNS of ^{233}U, including fast assemblies, thermal solutions, thermal lattices and tungsten-reflected fast assemblies.

ICSBEP full name	Short name	Common name
U233-MET-FAST-001	umf001	Jezebel-U233
U233-MET-FAST-006	umf006	Flattop-23
U233-SOL-THERM-001	ust001-1	U3ORNL-S1
U233-SOL-THERM-001	ust001-2	U3ORNL-S2
U233-SOL-THERM-001	ust001-3	U3ORNL-S3
U233-SOL-THERM-001	ust001-4	U3ORNL-S4
U233-SOL-THERM-001	ust001-5	U3ORNL-S5
U233-SOL-THERM-008	ust008	U3ORNL-11
U233-COMP-THERM-001	uct001-20	SB-2
U233-COMP-THERM-001	uct001-25	SB-2h
U233-COMP-THERM-001	uct001-30	SB-3
U233-COMP-THERM-001	uct001-40	SB-4
U233-COMP-THERM-001	uct001-70	SB-7
U233-MET-FAST-004	umf004-1	Planet-U3/W_1in
U233-MET-FAST-004	umf004-2	Planet-U3/W_2in

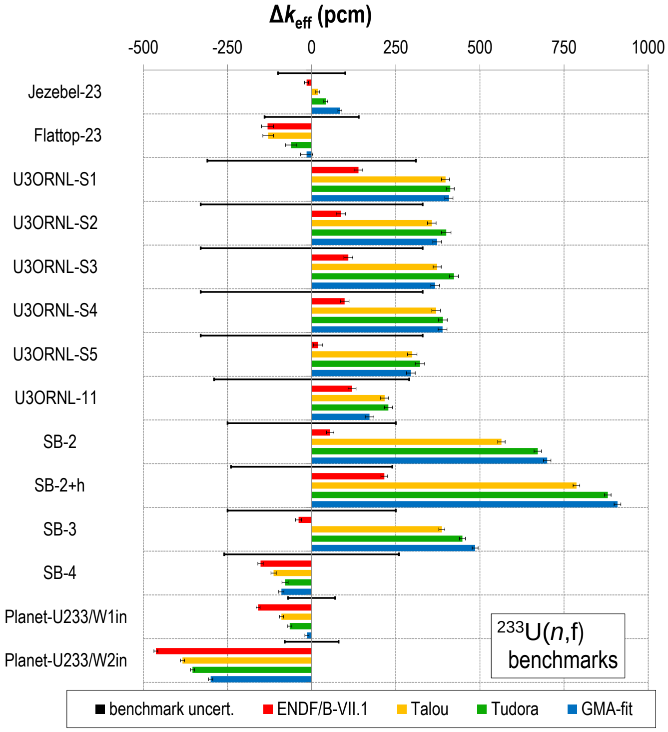

FIG. 62. (Color online) Differences of the multiplication factors $k_{\rm eff}$ from the reference benchmark values for selected ^{233}U benchmarks. The black uncertainty bars correspond to the evaluated benchmark uncertainty.

the inelastic cross sections, which are known to compensate the similar deviations in data for ^{235}U and ^{239}Pu.

E. Compensating Effects in Benchmark Calculations

Previous subsections have shown the large (sometimes huge) impact that new PFNS evaluations with lower average neutron energy, $\overline{E}$, have on criticality calculations. Does that mean that new PFNS evaluations are wrong as we are not able to accurately reproduce the criticality of extremely well-studied benchmarks? In this section we show that very modest tuning of existing libraries combined with updated nuclear reaction modeling can restore the desired benchmark performance, a clear evidence of the strong compensating effects involved as suggested by CEA colleagues in Ref. [342].

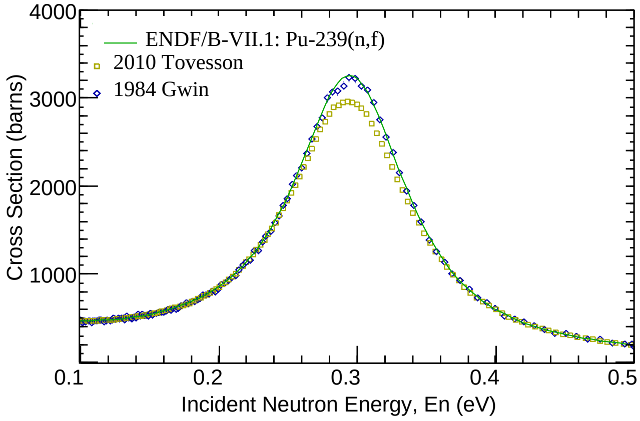

+

FIG. 63. (Color online) Comparison of the fission cross section of ^{239}Pu in the first resonance.

There is little flexibility in the adjustment of the thermal $\overline{\nu}$, and thermal capture and fission cross sections, which were pre-evaluated by Axton [48] including differential and integral measurements made in thermal Maxwellian spectra[11]. The Axton evaluation is in good agreement with results from the IAEA Standards project [46, 47], and with ENDF-B/VII.1 library [148].

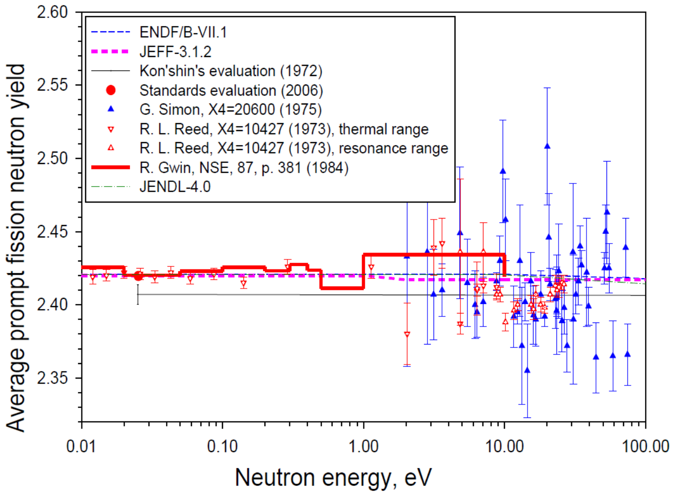

FIG. 64. (Color online) Comparison of the $\overline{\nu}$ values of ^{235}U in the thermal and epithermal energy regions.

Re-evaluation of the capture and fission cross sections around the first resonances in ^{235}U (0.7 eV) and in ^{239}Pu (0.3 eV) may increase the capture-to-fission ratios in these resonances, which will consequently decrease the multiplication factor k_{eff} in critical assemblies. New measurements of the fission cross section of ^{239}Pu from LANL [343] support such a

---

[11] Differences for derived ^{235}U thermal constants in Neutron Standard fits depending on the inclusion of integral data remain unexplained.

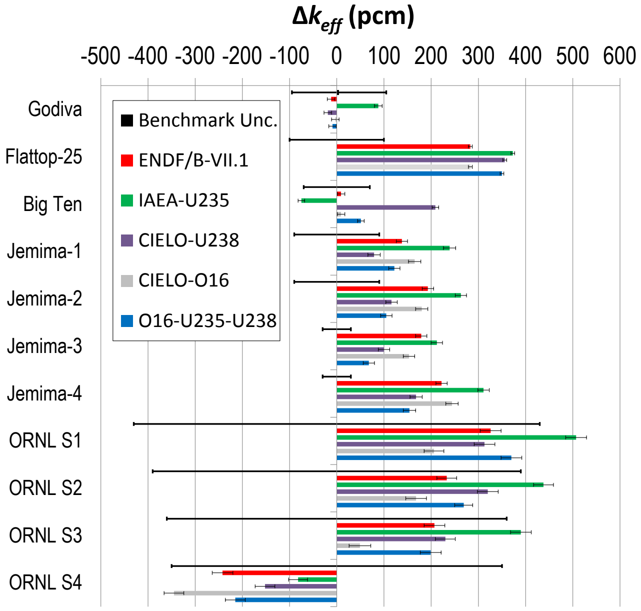

FIG. 65. (Color online) Results for a selected number of benchmarks, demonstrating the compensating effects of different evaluations due to cross-reaction and cross-material correlations. The black uncertainty bars correspond to the evaluated benchmark uncertainty.

change, as shown in Fig. 63. The capture cross section data in the first resonance region of these nuclides are even less reliable. Furthermore, additional uncertainties should be considered in the 0.4 eV resonance of ^{241}Pu, present in the plutonium fuel in many benchmarks.

The average number of prompt neutrons per fission ($\overline{\nu}$) in the resonances can be also different from the thermal multiplicity. Several $\overline{\nu}$ data sets exist for ^{239}Pu, which decrease by about 0.5% in the first resonance and exhibit 1–1.5% fluctuations in the range $8 < E_n < 30$ eV. An attempt to consider such structure based on $(n, \gamma\mathrm{f})$ reactions has been undertaken by WPEC SG-34 [1] for ^{239}Pu. Additional measurements are desirable. The $\overline{\nu}$ energy dependence should be carefully studied for major actinides and the evaluated files revised accordingly. The available experimental data for ^{235}U, shown in Fig. 64, could support a slight decrease of $\overline{\nu}$ in the 0.7 eV resonance of ^{235}U.

The inelastic scattering cross sections are badly known for all fissile nuclei. There are significant discrepancies among different evaluations for major actinides [345]. Decreasing the inelastic scattering cross sections in the region $0.5 < E_n < 4$ MeV, where most neutrons are emitted, will increase the criticality of fast assemblies due to the lower leakage of source neutrons. Such an increase partially compensates the effect of decreasing $\overline{E}$ for fast and thermal systems, as suggested in this work. Preliminary calculations of $n+^{235}$U reaction undertaken at the IAEA support this effect (see IAEA-U235 file below). Further research is ongoing within the CIELO Collaboration [64, 65, 346].

To demonstrate these compensating effects, we focus on the new ^{235}U(n_{th},f) PFNS evaluation based on the GMA fit. A trial evaluation was assembled (IAEA-U235 file) in which the thermal $\overline{\nu}$ was reduced by 0.38% relative to the ENDF/B-VII.1 evaluation to cancel the tuning done in the ENDF/B-VII.1 (and the ENDF-B/VI) libraries for better agreement with criticality benchmarks. The rest of the fission data was taken from the ENDF/B-VII.1 evaluation because these fission cross sections are consistent with the IAEA Standards [46, 47]. Resonance parameters were taken from the new ORNL evaluation submitted to the CIELO project [64]. The capture cross sections above the resonance range were taken from JENDL-4 [149], but scaled to be 2% lower than ENDF/B-VII.1 around 25 keV and 4% lower around 426 keV. The decrease in capture is indicated by the Wallner measurement [347] based on the accelerator mass spectrometry technique. All other cross sections were taken from EMPIRE calculations using a dispersive optical model potential, RIPL 2408 [183], that couples 8 levels of the ground state rotational band. The fission model parameters were adjusted to reproduce the Standards evaluation of the ^{238}U(n,f) cross section [46, 47].

Due to the importance of ^{238}U for many benchmarks, the latest ^{238}U transport file (u238ib44) [348] developed within the NEA/WPEC CIELO project [65, 346] and available from the IAEA/NDS web site [64] is included in the analysis (CIELO-U238). This file combines the IAEA/NDS evaluation [64, 348] in the fast neutron range with new evaluations undertaken for the thermal and unresolved-resonance ranges by ORNL/IRMM collaborations within the CIELO project [65]. The new evaluation of ^{16}O by Hale contributed to the NEA/WPEC CIELO project [65] is adopted for the present analysis (CIELO-O16).

A selected number of benchmarks were run with the above combination of data, with labels IAEA-U235, CIELO-U238 and CIELO-O16 for the ^{235}U, ^{238}U and ^{16}O cases, respectively. The data set including all three nuclides simultaneously is denoted O16-U235-U238. The results are shown in Fig. 65. With relatively small changes of the physical observables (e.g., inelastic cross sections, thermal $\overline{\nu}$), and and updated evaluation of the ^{238}U file, it is possible to compensate the large impact of the new PFNS evaluations for fast as well as thermal assemblies, and obtain results comparable or better than those achieved with a reference library. However, the adjustments are not unique. A larger set of benchmarks should be investigated to find an optimal solution that will work in all cases.

F. Spectrum Averaged Cross Sections in Thermal Neutron-Induced PFN Fields

Integral data, such as spectrum-averaged cross sections (SACS), are a useful tool to check the validity of evaluated differential cross sections $\sigma(E)$ [305]. As pointed out by Mannhart *"an essential prerequisite to this procedure are well established spectrum-averaged data and an adequate description of the spectral distribution* $N(E)$ *of the corresponding neutron field"*. However, if it is assumed that a selected set of evaluated differential cross sections is known to high accuracy (e.g., selected dosimetry reactions from the IRDFF library [3]), then the neutron spectral distribution could be validated as done in Ref. [4]). A similar approach is followed here for PFNS validation and testing. However, it is important to remark that such validation of the neutron field is relevant and feasible only for $0.020 < E < 10$ MeV, where consistent experimental differential PFNS data exist. Moreover, the analysis in this Section does not consider derived spectral uncertainties which are large at higher emission energies. Therefore, mentioned agreement or discrepancies should be taken with care as quoted uncertainties are a lower bound to the real uncertainties especially above 5–6 MeV.

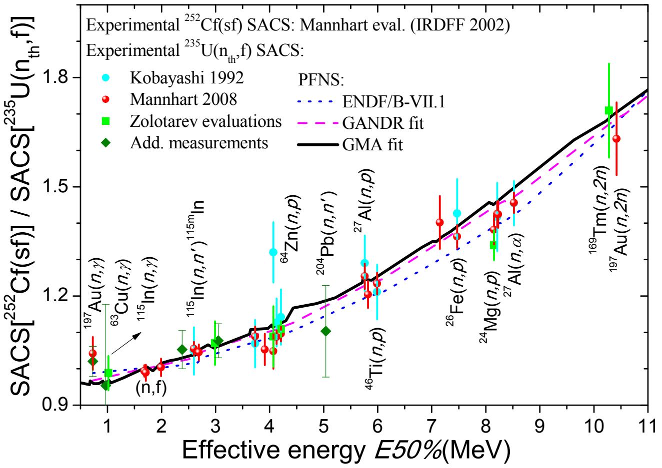

FIG. 66. (Color online) The SACS ratio of results in the ^{252}Cf(sf) neutron field relative to that of the ^{235}U($n_{\rm th}$,f) neutron fields as a function of the $E50\%$ energy for $0.5 < E50\% < 10.5$ MeV.

Accurate integral SACS data for selected dosimetry reactions have been measured in ^{252}Cf(sf) and ^{235}U($n_{\rm th}$,f) neutron fields and evaluated by Mannhart [305, 306], Kobayashi et al. [312], and Zolotarev [349–354]. Evaluated PFNS are validated by comparing measured reaction rates in the corresponding PFN fields to the corresponding calculated values using dosimetry cross sections from the IRDFF library [3]. To minimise the effects of the systematic uncertainties due to uncertainties in the decay and reaction data of the monitor cross sections, cf. Refs. [305, 309], the reaction rates were not compared directly. Instead, the SACS ratio in the ^{252}Cf(sf) and ^{235}U($n_{\rm th}$,f) neutron fields was used.

Values of $E50\%$ are taken as averages between $E50\%$ calculated in the ^{252}Cf(sf) and ^{235}U($n_{\rm th}$,f) PFN fields, correspondingly. The uncertainty in the energy is equal to half of the difference between $E50\%$ for the ^{252}Cf(sf) and ^{235}U($n_{\rm th}$,f) values. Kobayashi et al. [308, 309, 311] and coworkers have measured large SACS sets both in ^{252}Cf(sf) reference field as well in the very clean ^{235}U and ^{233}U fission-plate experiments undertaken at the Research Reactor Institute of Kyoto University (KURRI). In those SACS measurements, the KURRI reactor neutron beam was thermalized by passing through 136 cm of heavy water, and it was later filtered by graphite (48 cm) and bismuth (15 cm) layers, respectively. Such a beam is considered to be free of high energy fission neutrons that often contaminate in-reactor SACS measurements. Therefore, the Kobayashi et al. SACS measurements at KURRI are the favored choice for PFNS validation, as well as for testing the extrapolated PFNS at energies above 10 MeV. The SACS ^{252}Cf(sf) evaluations by Mannhart [307] are combined with KURRI fission-plate data.

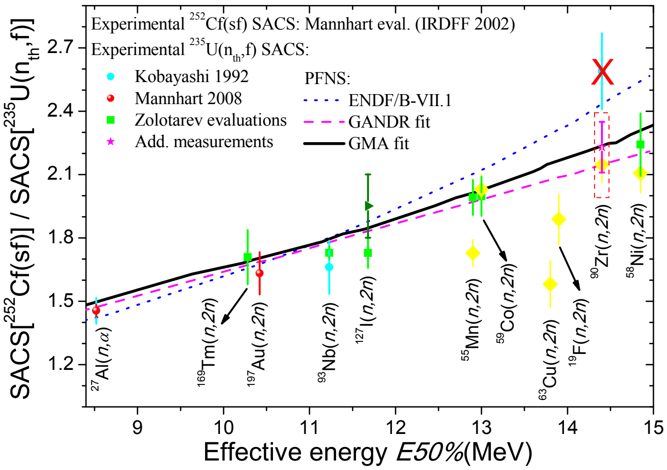

FIG. 67. (Color online) The SACS ratio in the ^{252}Cf(sf) to the ^{235}U($n_{\rm th}$,f) PFNS fields (lines) as a function of the $E50\%$ energy is compared with evaluated experimental data by Mannhart for ^{252}Cf(sf) [307] and ^{235}U($n_{\rm th}$,f) [306], Kobayashi et al. [312], and Zolotarev [349–354], and with fission plate measurements by Kobayashi et al. [311] for mean energy of the reaction rate response $E50\% > 8.4$ MeV.

Figure 66 shows that for $E50\%$ between 1.5 and 10 MeV the ratio of experimental SACS data by Kobayashi for the ^{235}U($n_{\rm th}$,f) PFNS [311] to the evaluated SACS by Mannhart [305–307] for ^{252}Cf(sf) (cyan solid circles) is rather consistent with the calculated values from all evaluations except for ^{64}Zn(n,p) with $E50\% = 4.095$ MeV. The value for this reaction obtained by Kobayashi, 31.7 ± 1.8 mb [311], is lower than that evaluated by Mannhart, 35.4 ± 1.1 mb [305, 306], and much lower than that evaluated by Zolotarev [351], 38.9 ± 2.8 mb, based on additional measurements. For the same reaction, the SACS value in the ^{252}Cf(sf) neutron field evaluated by Mannhart of 40.6 ± 0.7 mb [305, 306] is also lower than the value evaluated by Zolotarev [351] of 42.3 ± 0.9 mb. The corresponding SACS ratio for Zolotarev's evaluation of ^{64}Zn(n,p) is 1.09 ± 0.03, in excellent agreement with the calculated SACS ratio at the same energy. Otherwise, Fig. 66 shows that there is excellent agreement between the GANDR evaluation [55, 56] (dashed line) and the GMA evaluation (solid line, this work) with SACS experimental data. Therefore the proposed non-model evaluations are validated by the SACS integral data. The ENDF/B-VII.1 PFNS of ^{235}U($n_{\rm th}$,f) is slightly hotter (so the ratio is lower) for $2 < E < 10$ MeV than the non-model evaluations. However, the differences could be considered within the quoted experimental uncertainty of the integral data, in agreement with previous conclusions [4].

a. Testing of the PFNS high energy extrapolation. At $E > 10$ MeV there are either no consistent differential PFNS data measured, cf ^{235}U($n_{\rm th}$,f), or there are no measurements at all. Therefore, a non-model PFNS evaluation is not possible. An extrapolation of non-model PFNS evaluations was suggested in Sec. VII D based on measured SACS data for the ^{90}Zr(n,2n) dosimetry reaction and on the linear dependence of the SACS on $\overline{E}$. We could use the available SACS ratio measured in the reference ^{252}Cf(sf) neutron field relative to the one measured in the investigated PFNS field to test the suggested extrapolation to higher E, as shown in Fig. 67 for $E50\% > 8.4$ MeV.

The ratio of the evaluated SACS ^{252}Cf(sf) data by Mannhart [305–307] to the experimental SACS data by Kobayashi for the ^{235}U($n_{\rm th}$,f) PFNS [311] are rather consistent for all reactions except ^{90}Zr$(n,2n)$ at $E50\% = 14.565$ MeV. The cross section measured by Kobayashi [311] of 0.0860 ± 0.0065 mb (red crossed) has been increased in a subsequent evaluation by the same author [312] to 0.099 ± 0.005 mb in very good agreement with Mannhart's evaluation value of 0.103 ± 0.003 mb (see the dashed square corresponding to the corrected ^{90}Zr$(n,2n)$ data). The new evaluated value by Kobayashi [312] decreases the corresponding SACS ratio in Fig. 67 to 2.23, in excellent agreement both with the Mannhart evaluation and with the calculated PFNS ratio. A similar consistency between two of the evaluations can be seen for other reactions shown in the figure, including the high-threshold reactions ^{59}Co$(n,2n)$ and ^{58}Ni$(n,2n)$.

The evaluated SACS experimental data for these reactions is also in excellent agreement with extrapolated PFNS values calculated from the GMA (solid line) and GANDR (dashed line) fits. The ENDF-B/VII.1 PFNS (dotted line) results in calculated SACS ratios higher than the measured data for $E50\% > 11.5$ MeV as discussed in Ref. [4]. The observed systematic overestimation of the SACS ratio is related to the high-energy tail of the ^{235}U($n_{\rm th}$,f) PFNS being lower than required by the measured/evaluated SACS data. It should be noted that there are discrepant evaluations of the measured SACS ratio, as shown in Fig. 67 for ^{55}Mn$(n,2n)$, ^{63}Co$(n,2n)$ and ^{19}F$(n,2n)$. However, all the discrepant experimental SACS ratios are well below the SACS calculated from PFNS evaluations, below the ENDF/B-VII.1 PFNS curve. The observed discrepancies in the evaluated SACS are probably related to deficiencies in the dosimetry reaction evaluations in the IRDFF library [3], except for the ^{55}Mn$(n,2n)$ reaction where the Zolotarev evaluated SACS ratio of 1.99 ± 0.07 [352] is discrepant with the Mannhart evaluated value of 1.72 ± 0.07 [306]. The Zolotarev evaluation is in excellent agreement with the calculated SACS ratios using the extrapolated GMA and GANDR fits. Additional differential and integral measurements for those reactions are needed to resolve noted discrepancies.

It may be concluded, that there is good consistency between the SACS ratios in the ^{252}Cf(sf) PFNS to the ^{235}U($n_{\rm th}$,f) PFNS derived from the Kobayashi data [311, 312] and those evaluated by Mannhart [305–307] and Zolotarev [349–354], as well as the ratios calculated from the ^{252}Cf(sf) reference PFNS and the ^{235}U($n_{\rm th}$,f) PFNS evaluated in the current work (GANDR and GMA fits). The GMA evaluation has been extrapolated above 10 MeV using the measured SACS of the ^{90}Zr($n,2n$) reaction in the ^{235}U($n_{\rm th}$,f) neutron field as evaluated by Mannhart [306]. A similar extrapolation using the same reaction (with values predicted from systematics) was undertaken for the GMA evaluation of the ^{233}U($n_{\rm th}$,f) and ^{239}Pu($n_{\rm th}$,f) neutron fields.

IX. SUMMARY AND CONCLUSIONS

The IAEA Coordinated Research Project on “Prompt Fission Neutron Spectra of Actinides” galvanized research activities during the last five years on the topic of emission of prompt neutrons and gammas from nuclear fission. It also provided a forum for comprehensive technical discussions on experimental and theoretical challenges in studies of prompt fission phenomena.

As is evident from the Table of Contents, and as reflected in the material contained in the distinct sections of this paper, these investigations could be categorized as follows: experiments and uncertainty quantification, deterministic and Monte Carlo modeling, evaluation methods, explicit evaluations, and integral testing of these evaluations. While it would be impractical to specifically list the various individual investigations and their achievements that were encompassed by the present CRP in this summary, in general terms the efforts in these areas can be described very briefly as follows:

In the experimental category, new experimental data have been measured within the CRP framework and older data have been compiled and reassessed, leading to updated or new data sets that have been incorporated in new PFNS evaluations. Re-examination of existing experimental information has involved more careful assessments of background neutron sources and multiple scattered neutrons that negatively impacted the quality of these earlier data for $E < 2$ MeV. This was accomplished using modern Monte Carlo models and computational procedures that were not feasible previously. Newer experimental investigations that are not yet complete offer promise for improved data in the difficult regions below 2 MeV, where large corrections are inevitably needed, and above 10 MeV, where data are limited and statistical uncertainties tend to be large. Considerable effort was devoted in the CRP to estimating uncertainties and covariances for available experimental data so they could be employed in evaluations that use modern evaluation procedures.

New time-of-flight experiments are welcome that expands the available experimental database for major actinides at E_n from thermal up to 5 MeV for outgoing neutron energies $E < 2$ MeV. It should be stressed that PFNS ratio measurements (e.g. of ^{239}Pu/^{235}U, ^{239}Pu/^{238}U, ^{235}U/^{233}U, ^{239}Pu/^{252}Cf(sf), etc), allow minimizing the needed experimental corrections (in particular, the multiple scattering corrections in the detection system), and are very much encouraged. Reaction rate measurements of high-threshold (n,2n) and (n,3n) reactions in clean ^{239}Pu, ^{235}U and ^{233}U PFN fields for different neutron incident energies are recommended to improve our knowledge of the high-energy PFNS tail. The use of clean PFN fields (e.g., measuring outside the reactors), and a detailed Monte Carlo simulation of the experimental set-up including the surrounding structures, are critical to achieve target accuracies of 5–10% in measured reaction rates.

Some modest improvements have been made in the development of advanced deterministic models, in attempts to include more realistic physics, to better fit experimental data, and to generate uncertainty information more consistent with intuitive expectations. Nevertheless, even these more sophisticated models continue to be largely phenomenological in nature and their predictive power is largely based on empirical systematics.

Monte Carlo models have explored fission at a microscopic level, leading to interesting qualitative insights that, in the longer term, should lead to better representations of the physical phenomena than possible with deterministic models. These models also provide additional physical information such as $\overline{\nu}(A)$, neutron-photon and neutron-neutron correlations, etc. Efforts haven been made towards a global and consistent semi-empirical description of essentially all fission quantities, including the properties of the prompt fission neutrons. However, the ability of these stochastic models to quantitatively represent measured PFNS data to an adequate degree remains elusive.

Investigations of evaluation methodology in this CRP, for the most part, remained firmly rooted within the realm of traditional least-squares techniques for merging experimental and model data. However, considerable insight was achieved, within the framework of these evaluation procedures, of how to handle with the problem of too small uncertainties in the vicinity of $E{\sim}2$ MeV encountered due to the limitations in deterministic model PFNS data. Additionally, the importance of recognizing, for evaluation purposes, that all PFNS data are “shape” data was realized.

This CRP generated new PFNS evaluations, including covariance data, for several important isotopes at energies relevant to applications, which include the non-model GMA evaluations of the thermal neutron fission of ^{233}U, ^{235}U, and ^{239}Pu exclusively based on experimental information for $0.020 < E < 10$ MeV (about 99% of the PFNS flux). These evaluations are intended to constrain the PFNS models and model parameters with the best PFNS data available, namely those measured at the thermal point. New Los Alamos Model PFNS evaluations of neutron-induced fission of ^{233}U, ^{235}U, and ^{239}Pu for E_n from thermal up to 20 MeV may serve as examples of evaluations over the whole energy range that are consistent with the non-model results at the thermal point within quoted uncertainties. Improved calculations were also generated for several other isotopes relevant to applications, such as the `PbP` calculations of ^{232}Th, ^{234}U and ^{237}Np. These calculations reproduce the scarce experimental data available for these targets and may be considered evaluations mostly based on model results.

It has been shown from many integral studies that certain integral parameters like $k_{\rm eff}$ are very sensitive to the PFNS average energy. Consequently, it is both significant and fortuitous that work carried out in this CRP has demonstrated that determinations of $\overline{E}$ are dominated by data in the range $2 < E < 5$ MeV, also the energy region most accessible to experimental studies. This finding enabled a non-model evaluation of the thermal PFNS for ^{235}U to be performed to sufficient accuracy to be considered as a reference PFNS standard. This also resulted in new non-model PFNS evaluations of thermal neutron-induced fission of ^{233}U, ^{235}U, and ^{239}Pu, finding the average energy to be ~30 keV lower than in existing evaluations.

The PFNS evaluation of thermal neutron-induced fission of ^{235}U has been subjected to integral data testing by comparisons with experimental data from dosimetry benchmarks. The proposed non-model evaluation of thermal neutron fission of ^{235}U has been shown to be consistent with current dosimetry data, in the energy range from 0.5 to 10 MeV where differential experimental data are statistically consistent. However, both differential and spectrum-averaged dosimetry data (SACS) are discrepant above 10 MeV. Further integral measurements are needed (implicitly acknowledging that new differential measurements at those energies are extremely challenging). Spectrum-averaged cross section (SACS) measurements of $(n,2n)$ reactions are strongly encouraged in the ^{235}U($n_{\rm th}$,f) and ^{252}Cf(sf) neutron fields. SACS measurements of dosimetry reactions are also needed in the ^{233}U($n_{\rm th}$,f) and ^{239}Pu($n_{\rm th}$,f) neutron fields to validate the new PFNS evaluations.

The PFNS evaluations of neutron-induced fission of ^{233}U, ^{235}U, and ^{239}Pu have also been subjected to integral data testing, in both thermal and fast spectrum systems, by comparisons with high-accuracy experimental data from neutronic benchmarks. It is well known that neutronics benchmarks are very complex systems. The criticality $k_{\rm eff}$ is very sensitive to the PFNS, but it is also sensitive to resonance parameters, angular distributions, capture, fission, elastic and inelastic cross sections, as well as $\overline{\nu}$. Despite the observed ~30 keV reduction of $\overline{E}$, the outcomes suggested that new evaluations can, in most instances, achieve the same (or better) integral performance with respect to earlier evaluations. However, further work is required to understand the strong compensating effects observed in multi-element benchmarks (such as the Big Ten and Flaptop assemblies) due to changes in the neutron flux resulting from changes in underlying physical data for ^{235}U or ^{239}Pu and ^{238}U at the same time. Additional attention should be paid to describing measured reaction rates in fast assemblies which are sensitive to the PFNS in a broader incident neutron energy range. Such descriptions unavoidably require the use of PFNS models to produce evaluations valid for many incident neutron energies.

Finally, in the domain of fundamental physics, there is evidence from the work of this CRP albeit depending on model assumptions, that a very small percentage of neutrons emitted in fission are actually scission neutrons. Nevertheless, the overwhelming source of PFNS neutrons appear to originate from accelerated fission fragments associated with binary fission. A recent theoretical investigation [355] demonstrated that due to a very fast “rupture of the neck”, neutrons are emitted together with fission fragments at the time of scission, and have very strong angular distribution relative to fragments. New experiments to study the mechanism of neutron emission without references to the angular distribution should be developed (e.g., see Ref. [161]). Further experimental and theoretical research in this area would be important.

Perhaps the most important contribution of the present CRP has been to generate a snapshot of the present status of understanding the PFNS, to provide significantly improved PFNS evaluations and evaluation methodology, and to provide a timely road map for future work in this field. In this respect, the CRP activity has served as a worthy, and in most respects more comprehensive, successor to the valuable status review by Holden [39] some 30 years ago.

ACKNOWLEDGMENTS

Our sincere thanks to all colleagues who have contributed to and worked on this project during the last five years. The preparation of this paper would not have been possible without the support, hard work and endless efforts of a large number of individuals and institutions.

First of all, the IAEA is grateful to all participant laboratories for their assistance in the work and for support of the CRP meetings and activities. The work described in this paper would not have been possible without IAEA Member States contributions.

We are in debt to W. Mannhart and D. G. Madland for their precedent work and scientific legacy. Mannhart, who evaluated the standard ^{252}Cf(sf) neutron spectrum more than 25 years ago, is still actively collaborating with the IAEA; his advise and comments at the IAEA Neutron Standards Project meetings are acknowledged as a source of knowledge and inspiration. Madland, who together with J. R. Nix, wrote the paper that established "Los Alamos Model" in 1982, has also been a key project advisor.

Special thanks to V. M. Maslov who was involved in the IAEA Consultants' Meeting leading to the start of the project, and who for many years had pointed out deficiencies in existing PFNS evaluations.

We would like to thank M. B. Chadwick and E. Bauge who were also involved in the IAEA Consultants' Meeting leading to the start of the project, for their continuous support, permanent enthusiasm, and advices.

We would like to thank our OECD NEA Data Bank colleagues F. Michel-Sendis, O. Cabellos, J. Gulliford, I. Hill, and E. Dupont for the organization of CIELO meetings, and for their valuable technical support.

We very much appreciate valuable contributions made by I. Kodeli, G. Manturov, S. Ganesan, T. Granier, and K.-H. Schmidt during the project meetings. We would like to thank close collaborators T. Kawano, M. E. Rising, I. Stetcu, A. C. Kahler, and J. Randrup, who contributed to the overall success of the project.

We would like to thank M. C. White, T. N. Tadeucci, R. C. Haight, T. Burr, and the Chi-Nu team from LANL, for their help in discussing and assessing the uncertainty quantification of past PFNS experiments. The authors acknowledge contribution to the clarification and planning of integral experiments provided by S. Simakov, A. J. Plompen, and A. Wallner.

We would like to thank anonymous referees for the extensive and detailed revision of the paper and valuable comments and suggestions which improved the original manuscript.

Last but not least, the lead author would like to thank D. L. Smith and R. Vogt for their extensive and invaluable help in editing the assembled manuscript.

[1] C. De Saint Jean (Coord.), R. D. McKnight (Monitor), "Co-ordinated Evaluation of Plutonium-239 in the Resonance Region", Report **NEA/NSC/WPEC/DOC(2014)447**, Nuclear Energy Agency, OECD, Paris, France (2014).
[2] Y. Peneliau, O. Litaize, P. Archier, C. De Saint Jean, "^{239}Pu Prompt Fission Neutron Spectra Impact on a Set of Criticality and Experimental Reactor Benchmarks", NUCL. DATA SHEETS **118**, 459–462 (2014).
[3] R. Capote, K. I. Zolotarev, V. G. Pronyaev, A. Trkov, "Updating and Extending the IRDF-2002 Dosimetry Library", J. ASTM INTERNAT. **9**, JAI104119 (2012). Data available online at https://www-nds.iaea.org/IRDFF/.
[4] R. Capote, K. I. Zolotarev, V. G. Pronyaev, A. Trkov, "Validating the ENDF-B/VII ^{235}U(n$_{\rm th}$,f) prompt fission neutron spectrum using updated dosimetry cross sections (IRDFF)", in PHYSOR 2012 CONFERENCE, Knoxville, Tennessee, USA, April 15–20, 2012, paper 243 on CD-ROM (American Nuclear Society, LaGrange Park, IL, 2012).
[5] N. Feather, "The Time Involved in the Process of Nuclear Fission", NATURE **143**, 597–598 (1939).
[6] O. Hahn, F. Strassmann, "Über den Nachweis und das Verhalten der bei der Bestrahlung des Urans mittels Neutronen entstehenden Erdalkalimetalle", NATURWISS. **27**, 11–15 (1939).
[7] L. Meitner, O. R. Frisch, "Disintegration of uranium by neutrons: a new type of nuclear reaction", NATURE **143**, 239–240 (1939).
[8] N. Feather, U.S. ATOMIC ENERGY COMMISSION DOCUMENT **BR 335A**, 1942 (unpublished); as quoted by Terrell in Ref. [14].
[9] T. W. Bonner, M. A. Ferrell, R. C. Rinehart, "A study of the spectrum of the neutrons of low energy from the fission of U-235", PHYS. REV. **87**, 1032–1034 (1952).
[10] N. Nereson, "Fission neutron spectrum of U-235", PHYS. REV. **85**, 600–602 (1952).
[11] D. L. Hill, "The neutron energy spectrum from U-235 thermal fission", PHYS. REV. **87**, 1034–1037 (1952).
[12] B. E. Watt, "Energy spectrum of neutrons from thermal fission of ^{235}U", PHYS. REV. **87**, 1037–1041 (1952).
[13] L. Cranberg, G. Frie, N. Nereson, L. Rosen, "Fission Neutron Spectrum of U-235", PHYS. REV. **103**, 662–670 (1956).
[14] J. Terrell, "Fission Neutron Spectra and Nuclear Temperature", PHYS. REV. **113**, 527–541 (1959).
[15] N. Bohr, J. A. Wheeler, PHYS. REV. **56**, 426–450 (1939).
[16] L. A. Turner, "Nuclear Fission", REV. MOD. PHYS. **12**, 1–29 (1940).
[17] R. Peierls, "Energy distribution of fission neutrons", DTA REPORT **MS-65**, 1942 (PRO no. AB4/902).
[18] F. Bloch, H. Staub, U.S. ATOMIC ENERGY COMMISSION DOCUMENT **AECD-3158**, 1943 (unpublished); as quoted by Terrell in Ref. [14].
[19] First IAEA Symp. on "Physics and Chemistry of Fission", Salzburg, 22–26 March 1965, Report **STI-PUB-101, Vol.2**, IAEA, Vienna, Austria (1965).
[20] J. Terrell, "Prompt neutrons from fission", pp.3–23 in Ref. [19].
[21] H. Condé, G. During, "Fission-neutron spectra of ^{235}U, ^{239}Pu and ^{252}Cf", pp.93–102 in Ref. [19].
[22] Second IAEA Symp. on "Physics and Chemistry of Fission", Vienna, 28 July–21 August 1969, Report **STI-PUB-234**, IAEA, Vienna, Austria (1969).
[23] S. Weinstein, R. Reed, R.C. Bloch, "Neutron multiplicity measurements for ^{233}U, ^{235}U and ^{239}Pu resonance fission",

pp.477–485 in Ref. [22].

[24] IAEA Consult. Meet. on "Prompt Fission Neutron Spectra", Report **STI/PUB/329**, IAEA, Vienna, Austria (1972).

[25] Third IAEA Symp. on "Physics and Chemistry of Fission", Rochester, New York, 13–17 August 1973, Report **STI-PUB-347, Vol. II**, IAEA, Vienna, Austria (1974).

[26] IAEA Consult. Meet. on "Neutron Cross Sections for Reactor Dosimetry", Vienna, 15–19 November 1976, Report **IAEA-208, Vols. I,II**, IAEA, Vienna, Austria (1978).

[27] IAEA Symp. on "Physics and Chemistry of Fission", Julich, 14–18 May 1979, Report **STI-PUB-256, Vols.I, II**, IAEA, Vienna, Austria (1980).

[28] IAEA Consult. Meet. on "Physics of Neutron Emission in Fission", Mito, Japan, 24–27 May 1988, Report **INDC(NDS)-220**, IAEA, Vienna, Austria (1989).

[29] IAEA Consult. Meeting on "Nuclear Data for Neutron Emission in the Fission Process", Vienna, 22–24 October 1990, Report **INDC(NDS)-251**, IAEA, Vienna, Austria (1991).

[30] V. N. Nefedov, B. I. Starostov, A. A. Boytsov, "Precision Measurements of ^{252}Cf, ^{233}U, ^{235}U and ^{239}Pu Prompt Fission Neutron Spectra (PFNS) in the Energy Range 0.04 - 5 MeV", PROC. 6-TH ALL-UNION CONF. ON NEUTRON PHYSICS, KIEV, 2-6 OCT. 1983, **Vol. 2**, 285–289 (1983) [report **INDC(CCP)-0457**, IAEA, Vienna, Austria (2014)], EXFOR 40871011, 40871012.

[31] B. I. Starostov, V. N. Nefedov, A. A. Boytsov, "Precision Measurements of ^{252}Cf, ^{233}U+n$_{\text{th}}$, ^{235}U+n$_{\text{th}}$ and ^{239}Pu+n$_{\text{th}}$ Prompt Fission Neutron Spectra (PFNS) in the Energy Range 2 - 11 MeV", PROC. 6-TH ALL-UNION CONF. ON NEUTRON PHYSICS, KIEV, 2–6 OCT. 1983, **Vol. 2**, 290–293 (1983) [report **INDC(CCP)-0458** IAEA, Vienna, Austria (2014)], EXFOR 40872007.

[32] A. A. Boytsov, A. F. Semenov, B. I. Starostov, "Relative Measurements of ^{233}U+n$_{\text{th}}$, ^{235}U+n$_{\text{th}}$ and ^{239}Pu+n$_{\text{th}}$ Prompt Fission Neutron Spectra (PFNS) in the Energy Range 0.04 – 5 MeV", PROC. 6-TH ALL-UNION CONF. ON NEUTRON PHYSICS, KIEV, 2–6 OCT. 1983, **Vol. 2**, 294–297 (1983) [report **INDC(CCP)-0459** IAEA, Vienna, Austria (2014)], EXFOR 40873004.

[33] B. I. Starostov, V. N. Nefedov, A. A. Boytsov, "Prompt Neutron Spectra from Fission of ^{233}U, ^{235}U and ^{239}Pu by Thermal Neutrons and from Spontaneous Fission of ^{252}Cf in the 0.01-12 MeV Energy Range", VOPR. AT. NAUK. TECH., SER. YAD. KONST., **Issue.3**, p.16 (1985) [report **INDC(CCP)-293/L**, p.19 IAEA, Vienna, Austria (1989)], EXFOR 40930.

[34] A. Smith, P. Guenther, G. Winkler, R. McKnight, "Prompt-fission-neutron Spectra of ^{233}U, ^{235}U, ^{239}Pu and ^{240}Pu Relative to that of ^{252}Cf", Report **ANL/NDM-50**, Argonne National Laboratory, Argonne, USA (1979), EXFOR 10911.

[35] A. Smith, P. Guenther, G. Winkler, R. McKnight, "Note on the Prompt-fission-neutron Spectra of Uranium-233 and -235 and Plutonium-239 and -240 Relative to That of Californium-252", NUCL. SC. ENG. **76**, 357-361 (1980).

[36] W. Mannhart, "Evaluation of the Cf-252 Fission Neutron Spectrum between 0 MeV and 20 MeV", in *Properties of Neutron Sources*, Report **IAEA-TECDOC-410**, pp.158–171 IAEA, Vienna, Austria (1987).

[37] W. Mannhart, "Status of the Cf-252 Fission Neutron Spectrum Evaluation with Regard to Recent Experiments", pp.305–336 in Ref. [28].

[38] D. G. Madland, J. R. Nix, "New calculation of prompt fission neutron spectra and average prompt neutron multiplicities", NUCL. SCI. ENG. **81**, 213–271 (1982).

[39] N. E. Holden, "Prompt Neutron Fission Spectrum Mean Energies for the Fissile Nuclides and ^{252}Cf, in *Int. Comm. for Radionuclide Metrology, June 3-7, 1985, Grenoble, France.* Report **BNL-NCS-36552**, Brookhaven National Laboratory, New York, USA (1985).

[40] N. V. Kornilov, A. B. Kagalenko, K. I. Zolotarev, "On the contradiction between microscopic and macroscopic data for 235U fission neutron spectrum at thermal energy", pp.242–251, in *Proc. VI Int. Seminar on Interaction of Neutrons with Nuclei (ISINN-6), Dubna, May 13–16, 1998*, JINR report **E3-98-202**, Dubna, Russia (1998).

[41] D. G. Madland (Coord.), A. V. Ignatyuk (Monitor), "Fission Neutron Spectra of Uranium-235", report **NEA/WPEC-9**, (Nuclear Energy Agency, OECD, Paris, 2003).

[42] Wang Yufeng, Bai Xixiang, Li Anli, Wang Xiazhong, Li Jingwen, Meng Jiangchen, Bao Zhongyu, "Experimental study of the prompt neutron spectrum of U-235 fission induced by thermal neutrons", CHIN. J. NUCL. PHYS. (BEIJING), **11**, No.4, 47 (1989), EXFOR 32587002.

[43] R. Capote Noy, V. M. Maslov, E. Bauge, T. Ohsawa, A. Vorobyev, M. B. Chadwick, S. Oberstedt, "Consultants' Meeting on Prompt Fission Neutron Spectra of Major Actinides", Report **INDC(NDS)-0541** IAEA, Vienna, Austria (2009).

[44] A. Trkov, M. W. Herman, D. A. Brown (Eds.), "ENDF-6 Formats Manual, Data Formats and Procedures for the Evaluated Nuclear Data Files ENDF/B-VI and ENDF/B-VII", CSEWG DOCUMENT ENDF-102, REPORT BNL-90365-2009 REV.2, National Nuclear Data Center, Brookhaven National Laboratory, Upton, NY.

[45] R. Gwin et al., "Measurements of the Energy Dependence of Prompt Neutron Emission from ^{233}U, ^{235}U, ^{239}Pu, and ^{241}Pu for E(n) = 0.005 to 10 eV Relative to Emission from Spontaneous Fission of ^{252}Cf", NUCL. SCI. ENG. **87**, 381 (1984), EXFOR 12833.

[46] S. Badikov et al., INTERNATIONAL EVALUATION OF NEUTRON CROSS-SECTION STANDARDS, Report **STI/PUB/1291** IAEA, Vienna, Austria (2008).

[47] A. D. Carlson, V. G. Pronyaev, D. L. Smith et al., "International Evaluation of Neutron Cross Section Standards", NUCL. DATA SHEETS **110**, 3215 (2009).

[48] E. J. Axton, "Evaluation of Thermal Constants of ^{233}U, ^{235}U, ^{239}Pu and ^{241}Pu and the Fission Neutron Yield of ^{252}Cf", Report **GE/PH/01/86**, Commission of the European Communities, Joint Research Centre, Geel, 1986. Available online at *www-nds.iaea.org/standards/Reports/Axton-GE-PH-01-86.pdf* .

[49] R. Capote Noy (Ed), "First Research Coordination Meeting on Prompt Fission Neutron Spectra of Major Actinides", IAEA Headquarters, 6-9 April 2010, Summary Report **INDC(NDS)-0571** IAEA, Vienna, Austria (2010).

[50] R. Capote Noy (Ed), "Second Research Coordination Meeting on Prompt Fission Neutron Spectra of Major Actinides", IAEA Headquarters, 13–16 December 2011 Summary Report **INDC(NDS)-0608** IAEA, Vienna, Austria (2013).

[51] P. Talou, R. Capote Noy, S. Simakov (Eds), "Third Research Coordination Meeting on Prompt Fission Neutron Spectra of Major Actinides", IAEA Headquarters, 21–24 October 2013 Summary Report **INDC(NDS)-0655** IAEA, Vienna, Austria (2014).

[52] N. Otuka, E. Dupont, V. Semkova, B. Pritychenko, et al., "Towards a More Complete and Accurate Experimental Nuclear Reaction Data Library (EXFOR): International Collaboration Between Nuclear Reaction Data Centres (NRDC)", NUCL. DATA SHEETS , **120**, 272–276 (2014). Data available online (e.g., at *www-nds.iaea.org/exfor/*).

[53] IAEA Coordinated Research Project on "Prompt Fission Neutron Spectra of actinides", ; data available online (see *www-nds.iaea.org/pfns/expdata/*).

[54] N. V. Kornilov, "Verification of the ^{252}Cf standard in the energy range 2-20 MeV", Report **INDC(USA)-108**, IAEA, Vienna, 2015].

[55] A. Trkov, R. Capote, V.G. Pronyaev, "Current Issues in Nuclear Data Evaluation Methodology: ^{235}U Prompt Fission Neutron Spectra and Multiplicity for Thermal Neutrons", NUCL. DATA SHEETS **123**, 8–15 (2015).

[56] A. Trkov, R. Capote, "Evaluation of the prompt fission neutron spectrum of thermal neutron-induced fission of ^{235}U", PHYS. PROCEDIA **64**, 48–54 (2015).

[57] H. Werle, H. Bluhm, "Fission-neutron Spectra Measurements of ^{235}U, ^{239}Pu and ^{252}Cf", J. NUCL. ENERGY **26**, 165–176 (1972), EXFOR 20616.

[58] O. A. Batenkov et al., "Prompt Neutron Emission in the Neutron Induced Fission of ^{239}Pu and ^{235}U", NDST 2004, Santa Fe, NM, USA, AIP CONF. PROC. **769**, 1003–1006 (2004), EXFOR 41502.

[59] A. S. Vorobyev, O. A. Shcherbakov, "Total prompt fission neutron spectrum from thermal-neutron-induced fission of 235U", VOPR. AT. NAUK. TECH., SER. YAD. KONST., ISSUE 1-2, 37–54 (2013) [report **INDC(CCP)-0455**, IAEA, Vienna, 2014], EXFOR 41597002.

[60] N. V. Kornilov, F.-J. Hambsch, I. Fabry, S. Oberstedt, T.Belgya, Z.Kis, L.Szentmiklosi, S.Simakov, "The ^{235}U(n,f) Prompt Fission Neutron Spectrum at 100 K Input Neutron Energy ", NUCL. SCI. ENG. **165**, 117–127 (2010).

[61] N. V. Kornilov, F.-J. Hambsch, "Absolute Ratio ^{252}Cf to ^{235}U Prompt Fission Neutron Spectra ", NUCL. SCI. ENG. **168**, 73–74 (2011), EXFOR 31692006.

[62] A. Lajtai, J. Kecskemeti, J. Safar, P. P. Dyachenko, and V. M. Piksaikin, "Energy Spectrum Measurements of Neutrons for Energies 30 keV–4 MeV from Thermal Fission of Main Fuel Elements", NDST 2004, Santa Fe, NM, USA, AIP CONF. PROC. **769**, 613–616 (1985), EXFOR 30704003.

[63] A. Lajtai, P.P. Dyachenko, V.N. Kononov, E.A. Seregina, "Low-Energy Neutron Spectrometer and Its Application for ^{252}Cf Neutron Spectrum Measurements", NUCL. INST. METH. PHYS. RES. **A293**, 555–561 (1990), EXFOR 41158.

[64] "IAEA CIELO Data Development Project" within the International Pilot Project of the OECD/NEA [65], 2014. (see *www-nds.iaea.org/CIELO/*).

[65] OECD, Nuclear Energy Agency, "Collaborative International Evaluated Library Organisation (CIELO) Pilot Project", WPEC Subgroup 40 (SG40) (see *www.oecd-nea.org/science/wpec/sg40-cielo/*).

[66] J. P. Lestone, E. F. Shores, "Uranium and Plutonium Average Prompt-fission Neutron Energy Spectra (PFNS) from the Analysis of NTS NUEX Data", NUCL. DATA SHEETS **119**, 213–216 (2014).

[67] J. P. Lestone, E. F. Shores, "Uranium and Plutonium Prompt-fission-neutron Spectra (PFNS) of NTS NUEX Data and the Corresponding Uncertainty Budget", LANL report **LA-UR-14-24087**, Los Alamos, USA (2014).

[68] A. Enqvist, B. M. Wieger, Lu Huang, M. Flaska, S. A. Pozzi, R. C. Haight, H.-Y. Lee, E. Kwan, C.-Y. Wu, "Neutron-induced ^{235}U fission spectrum measurements using liquid organic scintillation detectors", PHYS. REV. **C86**, 064605 (2012).

[69] N. V. Kornilov, F.-J. Hambsch, I. Fabry, S. Oberstedt, S. P. Simakov, A. S. Vorobyev, "New experimental and theoretical results for the ^{235}U fission neutron spectrum", CONF. ON NUCL. DATA FOR SCI. AND TECH., NICE 2007 **Vol.1**, 387–390 (CEA, EDP Sciences, France, 2008). DOI:10.1051/ndata:07735

[70] M. Sugimoto, A. B. Smith, P. Guenther, "Ratio of the Prompt Fission Neutron Spectra of Pu-239 to that of ^{235}U", Report **ANL/NDM-96**, Argonne National Laboratory, Argonne, USA (1976), EXFOR 14418.

[71] M. Sugimoto, A. B. Smith, P. Guenther, "Ratio of the Prompt Fission Neutron Spectra of Pu-239 to that of ^{235}U", NUCL. SC. ENG. **97**, 235–238 (1987).

[72] J. P. Lestone, private communication by M. Chadwick, "^{235}U Prompt-fission-neutron Spectra derived from Sugimoto et al. [70, 71] ^{239}Pu/^{235}U ratio data using ^{239}Pu NUEX PFNS from Refs. [66, 67].

[73] S. Noda, R. C. Haight, R. O. Nelson et al., "Prompt Fission Neutron Spectra from Fission Induced by 1 to 8 MeV Neutrons on ^{235}U and ^{239}Pu using the Double Time-of-flight Technique", PHYS. REV. **C83**, 034604 (2011), EXFOR 14290.

[74] P. Staples, J. J. Egan, G. H. R. Kegel, A. Mittler, M. L. Woodring, "Prompt Fission Neutron Energy Spectra Induced by Fast Neutrons", NUCL. PHYS. **A591**, 41–60 (1995), EXFOR 13982.

[75] J. P. Lestone, "Summary of Lestone's reanalysis of Staples et al. ^{239}Pu(n,f) PFNS", LANL report **LA-UR-15-23283**, Los Alamos, USA (2015).

[76] J. K. Dickens, "SCINFUL: A Monte Carlo Based Computer Program to Determine a Scintillator Full Energy Response to Neutron Detection for E_n between 0.1 and 80 MeV: User's Manual and FORTRAN Program Listing", Report **ORNL-6462** (ORNL, TN, USA, 1988). Available online at *web.ornl.gov/info/reports/1988/3445605995426.pdf*. RSIC package number **PSR-267A**, last updated in 1989.

[77] A. M. Trufanov, G. N. Lovchikova, G. N. Smirenkin, A. V. Polyakov, V. A. Vinogradov, "Measurements and estimates of the average energy of neutrons from the U-235(N,F) reaction ", YAD. FIZ. , **57**, 606 (1994) [PHYS. AT. NUCL. **57**, 572 (1994)], EXFOR 41162003.

[78] G. S. Boykov, V. D. Dmitriev, G. A. Kudyaev, Yu. B. Ostapenko, M. I. Svirin, G. N. Smirenkin, "Spectrum of Neutrons Accompanying Fission of ^{232}Th,^{235}U, and ^{238}U by 2.9-MeV and 14.7-MeV Neutrons (Below and Above the Threshold of Emission Fission)", YAD. FIZ. **53**, 628–648 (1991) [SOV. J. NUCL. PHYS. **53**, 392–406 (1991)], EXFOR 41110.

[79] G. S. Boykov, V. D. Dmitriev, G. A. Kudyaev et al., "Neutron spectrum in the fission of Th-232, U-235, and U-238 by neutrons with energies 2.9 and 14.7 MeV", PHYS. ATOMIC NUCL. **57**, 572 (1994).

[80] D. Abramson, C. Lavelaine, "Fission Neutron Spectra of ^{235}U and 239Pu", pp.40–48, Ref. [81]. EXFOR 20997. See corrections in Appendix A, AERE-R-8636 (1977) [81].

[81] B. H. Armitage and M. G. Sowerby (Eds), PROC. EURATOM SPECIALIST MEETING ON INELASTIC SCATTERING AND FISSION NEUTRON SPECTRA, AERE, HARWELL, 14-16 APRIL 1975, Report **AERE-R-8636**, AERE, Harwell, UK (1977). See Appendix A with detailed corrections and numerical data for ^{235}U earlier measurements [80, 82, 84, 85].

[82] P. I. Johansson, B. Holmqvist, "An Experimental Study of the Prompt Fission Neutron Spectrum Induced by 0.5-MeV Neutrons Incident on ^{235}U", NUCL. SCI. ENG. **62**, 695–708 (1977), EXFOR 20175003. See corrections in Appendix A, AERE-R-8636 (1977) [81].

[83] Z. A. Aleksandrova, V. I. Bol'shov, V. F. Kuznetsov et al., "Spectra of secondary neutrons at fission of U-235 and Pu-239 by neutrons with energy 0.1 MeV", SOV. ATOMIC ENERGY **38**, 140–141 (1975).

[84] P. I. Johansson, J. M. Adams, "Fast neutron fission spectrum measurement of U-235 at 0.52 MeV incident neutron energy", CONF. ON NUCL. CROSS-SECT. AND TECH., WASHINGTON 1975, **Vol.2**, 631–634 (1975), EXFOR 20996002. See corrections in Appendix A, AERE-R-8636 (1977) [81].

[85] M. M. Islam, H.-H. Knitter, "The Energy Spectrum of Prompt Neutrons from the Fission of Uranium-235 By 0.40-MeV Neutrons", NUCL. SCI. ENG. **50**, 108–114 (1973), EXFOR 20385003. See corrections in Appendix A, AERE-R-8636 (1977) [81].

[86] H.-H. Knitter, M. M. Islam, M. Coppola, "Investigation of Fast Neutron Interaction with U-235 ", Z. PHYS. **257**, 108–123 (1972), EXFOR 20394008. See corrections in Appendix A, AERE-R-8636 (1977) [81].

[87] H. Condé, G. During, J. Hansén, "Fission Neutron Spectra, Part I, A Neutron Detector for Fast Neutron Time-of-flight Spectroscopy", ARKIV FÜR FYSIK **29**, 307–312 (1965), EXFOR 20575.

[88] H. Condé, G. During, "Fission Neutron Spectra, Part II, Fission Neutron Spectra of U^{235}, Pu^{239} and Cf^{252}", ARKIV FÜR FYSIK **29**, 313–319 (1965), EXFOR 20575.

[89] D. Neudecker, T.N. Taddeucci, R.C. Haight, H.Y. Lee, M.C. White, "The need for new and precise experimental data on Prompt Fission Neutron Spectra from neutron-induced fissions of ^{239}Pu", LANL report **LA-UR-15-20824**, Los Alamos, USA (2015); submitted to Nucl. Data Sheets.

[90] P. I. Johansson, B. Holmqvist, T. Wiedling, and L. Jéki, "Precision Measurement of Prompt Fission Neutron Spectra of ^{235}U, ^{238}U, and ^{239}Pu", CONF. ON NUCL. CROSS-SECT. AND TECH., WASHINGTON 1975, **Vol.2**, 572–575 (1975) (data are not compiled in EXFOR yet). See corrections in Appendix A, AERE-R-8636 (1977) [81].

[91] L. M. Belov, M. V. Blinov, N. M. Kazarinov, A. S. Krivokhatsky, A. N. Protopopov, "The Energy Spectra of Prompt Neutrons in the Fission of ^{244}Cm, ^{242}Pu and ^{239}Pu", Report **INDC-260E**, pp. 94–95 IAEA, Vienna, Austria (1969) [SOV. J. NUCL. PHYS. **9**, 421–423 (1969)], EXFOR 40137.

[92] A. Chatillon, G. Baglier, T. Granier, B. Laurent, B. Morillon, J. Taieb, R. C. Haight, M. Devlin, R. O. Nelson, S. Noda, J. M. O'Donnell, "Measurement of prompt neutron spectra from the ^{239}Pu(n,f) fission reaction for incident neutron energies from 1 to 200 MeV", PHYS. REV. **C89**, 014611 (2014), EXFOR 14379.

[93] Th. Granier, "Reanalysis of ^{239} Pu Prompt Fission Neutron Spectra", PHYS. PROCEDIA **64**, 183–189 (2015).

[94] H.-H. Knitter, "Measurement of the Energy Spectrum of Prompt Neutrons from the Fission of Pu 239 by 0.215 MeV Neutrons", ATOMKERNENERGIE **26**, 76–79 (1975), EXFOR 20576. See corrections in Appendix A, AERE-R-8636 (1977) [81].

[95] T. Miura, M. Baba, Than-Win, M. Ibaraki, Y. Hirasawa, T. Hiriishi, T. Aoki, ".Measurements of the fast neutron-induced prompt neutron fission spectra of ^{233}U, ^{238}U, ^{232}Th ", J. OF NUCL. SCI. TECH. SUPPL., **Issue.1**, 409 (2002), EXFOR 22688.

[96] G. N. Lovchikova, A. M. Trufanov, M. I. Svirin, V. A. Vinogradov, A. V. Polyakov , "Spectra and Mean Energies of Prompt Neutrons from ^{238}U Fission Induced by Primary Neutrons of Energy in the Region $E_n < 20$ MeV", YAD. FIZ. **67**, 1270–1287 (2004) [PHYS. AT. NUCLEI **67**, 1246–1263 (2004)], EXFOR 41447.

[97] A. M. Trufanov, G. N. Lovchikova, M. I. Svirin, A. V. Polyakov, V. A. Vinogradov, V. D. Dmitriev, G. S. Boykov, "Investigation of the Spectra of Neutrons Originating from ^{238}U Fission Induced by 5.0- and 13.2-MeV Neutrons", YAD. FIZ. **64**, 3–10 (2001) [PHYS. AT. NUCLEI **64**, 1–8 (2001)], EXFOR 41450.

[98] G. N. Smirenkin, G. N. Lovchikova, A. M. Trufanov, M. I. Svirin, A. V. Polyakov, V. A. Vinogradov, V. D. Dmitriev, G. S. Boykov, "Measurement of Energy Spectrum of Neutrons Accompanying Emission Fission of U-238 nuclei", YAD. FIZ. **59**, 1934–1939 (1996) [PHYS. AT. NUCLEI **59**, 1865–1870 (1996)], EXFOR 41461.

[99] B. V. Zhuravlev, L. E. Kazakov, V. J. Kononov, N. V. Kornilov, B. D. Kuz'minov, V. V. Malinovskij, E. D. Poletaev, O. D. Sal'nikov, N. N. Semenova, "Investigations of the Interactions of Neutrons with ^{238}U Nuclei", Report **INDC(CCP)-154/L**, IAEA, Vienna, Austria (1980).

[100] V. Ya. Baryba, N. V. Kornilov, O. A. Sal'nikov, Report **947** IPPE, Obninsk, Russia (1979) (in Russian), available in INIS, EXFOR 40740.

[101] N. V. Kornilov, V. Ja. Baryba, O. A. Sal'nikov, All Union Conf. on Neutron Phys., Kiev, 15–19 Sep 1980 **Vol.3**, 104 (1980) (in Russian), EXFOR 40631.

[102] M. Baba, H. Wakabayashi, M. Ishikawa, N. Nakashima, N. Ito, N. Hirakawa, "Fission Spectrum Measurement of ^{232}Th and ^{238}U for 2 MeV Neutrons", pp.149–159 in Ref. [28], EXFOR 22112.

[103] G. S. Boykov et al., "New Data on Prefission Neutrons", Z. Phys. **A340**, 79–84 (1991).

[104] V. V. Desai, B. K. Nayak, A. Saxena, S. V. Suryanarayana, R. Capote, "Prompt fission neutron spectra in fast neutron induced fission of ^{238}U", Phys. Rev. **C92** 014609 (2015).

[105] G. N. Lovchikova, A. M. Trufanov, M. I. Svirin, V. A. Vinogradov, "Neutron Emission from the Reaction ^{232}Th$(n, xn'f)$", Yad. Fiz. **67**, 914–924 (2004) [Phys. At. Nuclei **67**, 890–900 (2004)], EXFOR 41446.

[106] T. Win, M. Baba, M. Ibaraki, T. Miura, T. Sanami, T. Iwasaki, N. Hirakawa, "Measurement of Prompt Fission Neutron Spectrum of Neptunium-237 for 0.62 MeV Incident Neutrons", J. Nucl. Sc. Tech. (Japan), **36**, 486–492 (1999), DOI:10.3327/jnst.36.486.

[107] A. M. Trufanov, G. N. Lovchikova, S. E. Sukhikh, A. V. Polyakov, V. G. Demenkov, V. A. Vinogradov, H. Marten, A. Ruben, I. During, "Energy Distributions of ^{237}Np Fission Neutrons", Yad.Fiz. **55**, 298 (1992) [Sov. J. Nucl. Phys. **55**, 162 (1992)].

[108] A. M. Trufanov, G. N. Lovchikova, B. V. Zhuravlev, S. E. Sukhikh, A. V. Polyakov, V. A. Vinogradov, A. Ruben, I. During, "The fission neutron spectrum of ^{237}Np", pp.105–108 in Ref. [29].

[109] N. V. Kornilov, A. B. Kagalenko, V. Ya. Baryba, V. G. Demenkov, C. V. Pupko, P. A. Androsenko, "Inelastic neutron scattering and prompt fission neutron spectra for ^{237}Np", Ann. Nucl. Energy**27**, 1643–1667 (2000).

[110] Z. A. Aleksandrova et al., "Spectra of the Prompt Neutrons Arising from the Spontaneous Fission of ^{252}Cf, ^{244}Cm, and ^{240}Pu", Sov. Atomic Energy **36**, 355–358 (1974). DOI: 10.1007/BF03327617

[111] B. Gerasimenko, L. Drapchinsky, O. Kostochkin, T. Kuzmina, N. Skovorodkin, V. Trenkin, "Precision measurements of prompt neutron spectra in ^{240}Pu and ^{242}Pu spontaneous fission", Conf. on Nucl.Data for Sci. and Tech., Tsukuba 2011, Japan, J. Nucl. Sci. Tech. (Japan) **Suppl. Vol.2**, 362, 2002. Data tabulated in Report Int. Science and Tech. Center **ISTC-183B-96**, Russia, 1999 (unpublished).

[112] N. I. Kroshkin, Ju. S. Zamyatnin, "Measurement of energy spectrum and average number of prompt fission neutrons", At. Energ. **29**, 95–98 (1970) [Sov. At. Energy **29**, 790–793 (1970)]. DOI=10.1007/BF01159590

[113] L. V. Drapchinsky et al., "Measurements of the prompt neutron spectra of minor actinides – Fast neutron induced fission of ^{241}Am and ^{243}Am, thermal neutron induced fission of ^{243}Cm", Report Int. Science and Tech. Center **ISTC-1828-01**, Russia, 2004 (unpublished).

[114] G. S. Boykov, B. F. Gerasimenko, V. D. Dmitriev, L. V. Drapchinsky, O. I. Kostochkin, K. A. Petrzhak, B. M. Shiryaev, V. A. Trenkin, "Precision prompt neutron spectrum measurements of minor actinides for transmutation problem", Conf. on Nucl.Data for Sci. and Tech., Trieste 1997, Italy, **Vol.2**, p.1310 (1997).

[115] O. I. Batenkov et al., "Neutron Spectrum of ^{248}Cm Spontaneous Fission", At. Energ. **71**, 566–568 (1991) [Sov. At. Energy **71**, 1031–1033 (1991)]. Additional details published in Vopr. At. Nauk. Tech., Ser. Yad. Konst., **Issue 1**, p.16 (1992), Russia.

[116] Bao Shanglian, Liu Wenlong, Wen Chenlin, Fan Tieshuan, O.I. Batenkov, M. Majorov "Measurement of ^{248}Cm/^{252}Cf spontaneous prompt fission neutron spectrum", High Energy Phys.& Nucl. Physics (Chinese ed.) **25**, p.304 (2001).

[117] N. V. Kornilov, I. Fabry, S. Oberstedt, F.-J. Hambsch, "Total characterization of neutron detectors with a ^{252}Cf(sf) source and a new light output determination", Nucl. Inst.& Meth. **A599**, 226–233, (2009).

[118] I. Fabry, "GENDARC code", JRC Technical Notes **GE/NP/01/2008/01/13**, JRC-IRMM, Geel, 2008.

[119] "MCNP—A General Monte Carlo Code for Neutron and Photon Transport, Version 5", LANL report **LA-UR-05-8617**, Los Alamos, USA (2005).

[120] A. S. Vorobyev, O. A. Shcherbakov et al., "Measurements of angular and energy distributions of prompt neutrons from thermal neutron-induced fission", Nucl. Instr. & Meth. in Phys. Res. **A598**, 795–801, 2009.

[121] A. S. Vorobyev, O. A. Shcherbakov et al., "Angular and energy distribution of prompt neutrons from thermal neutron-induced fission of ^{233,235}U(n,f)", pp. 60–69, in *Proc. XVII Int. Seminar on Interaction of Neutrons with Nuclei (ISSIN-17), Dubna, May 27-29, 2009*, A.M. Sukhovoj (Ed.), JINR report **E3-2010-36**, Dubna, Russia, 2010.

[122] M. Divadeenam, J. R. Stehn, "A least-squares fit of thermal data for fissile nuclei", Ann. Nucl. Energy **11**, 375–404, 1984.

[123] J. Terrell, "Neutron Yields from Individual Fission Fragments", sc Phys. Rev. **127**, 880–904 (1962).

[124] D. G. Madland, "Theoretical Descriptions of Neutron Emission", pp.201–232 in Ref. [29].

[125] F. H. Frohner, "Evaluation of 252Cf Prompt Fission Neutron Data from 0 to 20 MeV by Watt Spectrum Fit", Nucl. Sci. Eng. **106**, 345–352 (1990).

[126] G. S. Boykov, V. I. Yurevich, "An evaluation of the shape of the spontaneous fission prompt neutron spectrum of ^{252}Cf", Vopr. At. Nauk. Tech., Ser. Yad. Konst. **Issue 1**, 41–57 (1985). (in Russian)

[127] A. S. Vorobyev, O.A. Shcherbakov et al., "Investigation of the prompt neutron emission mechanism in low energy fission of ^{233,235}U($\mathrm{n_{th}}$,f) and ^{252}Cf(sf)", EPJ Web of Conf. **8** 1–7, 2010.

[128] V. E. Bunakov, L. S. Guseva, S. G. Kadmensky, G. A. Petrov, "Angular anisotropy of neutrons evaporated from fission fragments", pp.293–300 in *Proc. XIII Internat. Seminar on Interaction of Neutrons with Nuclei (ISINN-13), Dubna, May 25-28, 2005*, A. M. Sukhovoj (Ed.), JINR report **E3-2006-7**, Dubna, Russia (2006).

[129] J. Randrup, R. Vogt , "Inclusion of angular momentum in FREYA", Phys. Procedia **64**, 19–27 (2015).

[130] U. Brosa, H.-H. Knitter,"The scission neutron spectrum of ^{252}Cf(sf)", Z. Phys. **343**, 39–42 (1992).

[131] N. V. Kornilov, A. B. Kagalenko, F.-J. Hambsch, “Scission neutrons for fission of ^{235}U and ^{252}Cf”, Yad. Fiz. **64**, 1451–1462 (2001) (in Russian).

[132] N. V. Kornilov, A. B. Kagalenko, “Scission neutron emission and prompt fission neutron spectrum”, Report **INDC(CCP)-435**, pp.61–72, IAEA, Vienna, Austria (2002).

[133] T. Ohsawa, “Physics-based calculation of the prompt fission neutron spectrum”, in Report **INDC(NDS)-0571**, pp. 30–33 of Ref. [49].

[134] V. E. Sokolov, G. A. Petrov et al., “Investigation of the angular dependences of neutron-neutron coincidences from 252Cf, 235U, 233U and 239Pu fission in search of scission neutrons”, pp.108–118 in *Proc. XVIII Internat. Seminar on Interaction of Neutrons with Nuclei (ISSIN-18), Dubna, May 26-29, 2010*, A.M. Sukhovoj (Ed.), JINR report **E3-2011-26**, Dubna, Russia (2011).

[135] P. Singh et al., “Status report on the folded tandem ion accelerator at BARC”, Pramana, **59**, 739, (2002).

[136] N. V. Kornilov, A. B. Kagalenko, F.-J. Hambsch, “Computing the spectra of prompt fission neutrons on the basis of a new systematic of experimental data”, Phys. At. Nucl. **62**, 173–185 (1999).

[137] M. W. Herman, R. Capote, B. V. Carlson, P. Oblozinský, M. Sin, A. Trkov, H. Wienke and V. Zerkin, “EMPIRE: Nuclear Reaction Model Code System for Data Evaluation”, Nucl. Data Sheets **108**, 2655–2715 (2007).

[138] M. Herman et al., “EMPIRE-3.2 Malta User’s Manual”, Report **INDC(NDS)-0603**, IAEA, Vienna, Austria (2013). Available online at *www-nds.iaea.org/publications/indc/indc-nds-0603.pdf*

[139] S. Agostinelli et al., “Geant4a simulation toolkit”, Nucl. Inst. Meth. Phys. Res. **506**, 250–303 (2003).

[140] D. Neudecker, T. N. Taddeucci, R. C. Haight, H. Y. Lee, J. P. Lestone, J. M. O’Donnell, B. A. Perdue, M. E. Rising, P. Talou, M. C. White, “Compilation of ^{239}Pu PFNS Experimental Covariance Matrices”, LANL report **LA-UR-13-24743**, Los Alamos, USA (2013).

[141] D. L. Smith, D. Neudecker, R. Capote, “Prompt Fission Neutron Spectrum Evaluation Techniques”, Report **INDC(NDS)-0678**, IAEA, Vienna, Austria (2015); LANL report **LA-UR-15-20961**, Los Alamos, USA (2015).

[142] W. Mannhart, “A Small Guide to Generating Covariances of Experimental Data”, Report **INDC(NDS)-0588**, IAEA, Vienna, Austria (2011).

[143] D. L. Smith, N. Otuka, “Experimental Nuclear Reaction Data Uncertainties: Basic Concepts and Documentation”, Nucl. Data Sheets **113**, 3006–3053 (2012).

[144] W. Mannhart, “Data Fitting and Evaluation Techniques for Neutron Spectra”, pp.247–256 in *Proc. Int. Symp. on Nuclear Data Evaluation Methodology: Brookhaven National Laboratory, Upton, NY, USA, 12–16 October 1992*, World Scientific (1993).

[145] R. C. Haight et al., “Accuracies in the Planned Measurements of Prompt Neutron Output in Neutron-Induced Fission of ^{239}Pu: The Chi-Matrix”, LANL report **LA-UR-11-05576**, Los Alamos, USA (2011).

[146] J. W. Boldeman, “Review of Measurements of the Prompt Fission Neutron Spectrum from the Spontaneous Fission of Cf-252”, Report **IAEA-TECDOC-410**, pp.129–143 IAEA, Vienna, Austria (1987).

[147] D. Neudecker, R. Capote, D. L. Smith, T. Burr, P. Talou, “Impact of the Normalization Condition and Model Information on Evaluated Prompt Fission Neutron Spectra and Associated Uncertainties”, Nucl. Sc. Eng. **179**, 381–397 (2015).

[148] M. B. Chadwick *et al*, “ENDF/B-VII.1 Nuclear Data for Science and Technology: Cross Sections, Covariances, Fission Product Yields and Decay Data”, Nucl. Data Sheets **112**, 2887–2996 (2011).

[149] K. Shibata et al., JENDL-4.0: A New Library for Nuclear Science and Engineering, J. Nucl. Sci. Tech. **48**, 1 (2011).

[150] F. Weisskopf, “Statistics and Nuclear Reactions”, Phys. Rev. **52**, 295–303 (1937).

[151] A. C. Wahl, “Nuclear-Charge Distribution and Delayed-Neutron Yields for Thermal-Neutron-Induced Fission of U-235, U-233 and Pu-239 and for Spontaneous Fission of Cf-252”, At. Data & Nucl. Data Tables **39**, 1–156 (1988).

[152] C. Manailescu, A. Tudora, F.-J. Hambsch, C. Moraraiu, S. Oberstedt, “Possible reference method of the total excitation energy partition between complementary fission fragments”, Nucl. Phys. **A867**, 12–40 (2011).

[153] F.-J. Hambsch, A. Tudora, G. Vladuca, S. Oberstedt , “Prompt fission neutron spectrum evaluation for ^{252}Cf(sf) in the frame of the multi-modal fission model”, Ann. Nucl. Eng. **32**, 1032–1046 (2005).

[154] G. S. Boikov, V. D. Dmitriev, G. A. Kudyaev, Yu. B. Ostapenko, M. I. Svirin, G. N. Smlrenkin, “New Data on Prefission Neutrons”, pp.189–200 in Ref. [29].

[155] V. M. Maslov, Yu. V. Porodzinskij, M. Baba, A. Hasegawa, N. V. Kornilov, A. B. Kagalenko, N. A. Tetereva, “Prompt fission neutron spectra of ^{238}U and ^{232}Th above emissive fission threshold”, Phys. Rev. **C 69**, 34607 (2004).

[156] V. M. Maslov, N. V. Kornilov, A. B. Kagalenko, N. A. Tetereva, “Prompt fission neutron spectra of ^{235}U above emissive fission threshold”, Nucl. Phys. **A760**, 274–302 (2005).

[157] T. Ethvignot, M. Devlin, H. Duarte, T. Granier, R. C. Haight, B. Morillon, R. O. Nelson, J. M. ODonnell, and D. Rochman “Neutron Multiplicity in the Fission of ^{238}U and ^{235}U with Neutrons up to 200 MeV”, Phys. Rev. Lett. **94**, 052701 (2005).

[158] A. Tudora, B. Morillon, F.-J. Hambsch, G. Vladuca, S. Oberstedt, “A refined model for ^{235}U(n,f) prompt fission neutron multiplicity and spectrum calculation with validation in integral benchmarks”, Nucl. Phys. **A756**, 176–191 (2005).

[159] A. Tudora, G. Vladuca, B. Morillon,“Prompt fission neutron multiplicity and spectrum model for 30–80 MeV neutron incident on^{238}U”, Nucl. Phys. **A740**, 33–58 (2004).

[160] G. Vladuca, A. Tudora, B. Morillon, D. Filipescu, “Inner barrier symmetries in ^{237}Np neutron data evaluation up to 40 MeV incident energy”, Nucl. Phys. **A767**, 112–137 (2006).

[161] U. Brosa, S. Grossmann, A. Müller,“Nuclear scission”, Phys. Rep. **197**, 167–262 (1990).

[162] F. Vivès, F.-J. Hambsch, H. Bax, S. Oberstedt, “Investigation of the fission fragment properties of the reaction ^{238}U(n,f) at incident neutron energies up to 5.8 MeV”, Nucl. Phys. **A662**, 63–92 (2000).

[163] E. Birgersson, A. Oberstedt, S. Oberstedt, F.-J. Hambsch, “Properties of the reaction ^{238}U(n,f) at the vibrational resonances”, NUCL. PHYS. **A817**, 1–34 (2009).

[164] F.-J. Hambsch, F. Vivès, P. Siegler, S. Oberstedt, “Study of the ^{237}Np(n,f) reaction at MeV neutron energies”, NUCL. PHYS. **A679**, 3–24 (2000).

[165] F.-J. Hambsch, S. Oberstedt, A. Tudora, G. Vladuca, I. Ruskov, “Prompt fission neutron multiplicity and spectra evaluations for ^{235}U(n,f) in the frame of the multi-modal fission model ”, NUCL. PHYS. **A726**, 248–264 (2003).

[166] P. Schillebeeckx, C. Wagemans, A. Deruytter, R. Barthélémy, “Comparative study of the fragments’ mass and energy characteristics in the spontaneous fission of ^{238}Pu, ^{240} and ^{242}Pu and in the thermal-neutron-induced fission of 239Pu”, NUCL. PHYS. **A542**, 623 (1992).

[167] L. Demattè, C. Wagemans, R. Barthélémy, P. D’Hondt, and A. Deruytter, “Fragments’ mass and energy characteristics in the spontaneous fission of ^{236}Pu, ^{238}Pu, ^{240}Pu, ^{242}Pu, and ^{244}Pu”, NUCL. PHYS. **A617**, 331 (1997)

[168] L. Demattè, PhD thesis, University of Gent, Belgium (1997).

[169] P. Siegler, F.-J. Hambsch, S. Oberstedt, J. P. Theobald, “Fission modes in the compound nucleus ^{238}Np”, NUCL. PHYS. **A594**,45–56 (1995).

[170] T. Ohsawa, T. Horiguchi, H. Hayashi “Multimodal analysis of prompt neutron spectra for ^{237}Np(n,f)”, NUCL. PHYS. **A653**, 17–26 (1999).

[171] T. Ohsawa, T. Horiguchi, M. Mitsuhashi, “Multimodal analysis of prompt neutron spectra for ^{238}Pu(sf), ^{240}Pu(sf), ^{242}Pu(sf) and ^{239}Pu($\mathrm{n_{th}}$,f)”, NUCL. PHYS. **A665**, 3–12 (2000).

[172] G. Vladuca, A. Tudora, “Improved Los Alamos model applied to the neutron induced fission of ^{235}U and ^{237}Np”, ANN. NUCL. ENERGY **28**, 419–435 (2001).

[173] F.-J. Hambsch, S. Oberstedt, G. Vladuca, A. Tudora, “Prompt fission neutron multiplicity and spectra evaluations in the frame of the multi-modal fission model for ^{237}Np(n,f) and ^{238}U(n,f)”, NUCL. PHYS. **A709**, 85–102 (2002).

[174] T. Ohsawa, “Monte Carlo Simulation of Prompt Neutron Emission During Acceleration of Fission Fragments”, in Report **INDC(NDS)-0608**, pp. 23–26 of Ref. [50].

[175] A. Matsumoto, H. Taninaka, K. Hashimoto, T. Ohsawa, “Monte-Carlo simulation of prompt neutron emission during acceleration in fission”, J. NUCL. SCI. TECH. **49**, 782–792 (2012).

[176] T. Ericson, “The statistical model and nuclear level densities” ADV. PHYS. **9**, 425–511 (1960).

[177] V. P. Eismont, “Neutrons from the fission of excited nuclei”, ATOM. ENERG. **19**, 113–115 (1965) [SOV. AT. ENERGY **19**, 1000–1003 (1965)].

[178] R. L. Walsh, “Spin-dependent calculation of fission spectra and fission spectrum integrals for six fissioning systems”, NUCL. SCI. ENG. **102**, 119–133 (1999).

[179] A. Tudora, “Systematic behavior of the average parameters required for the Los Alamos model of prompt neutron emission”, ANN. NUCL. ENERGY **36**, 72–84 (2009).

[180] The JEFF-3.2 Evaluated Data Library, OECD, March 2014. Available online at *www.oecd-nea.org/dbforms/data/eva/evatapes/jeff_32/*.

[181] A. J. Koning, S. Hilaire, M. C. Duijvestijn, in *Proc. Int. Conf. on Nucl. Data for Sci. Tech.*, ND-2007, April 22-27, 2007, Nice, France.

[182] RIPL-3 database [184]: Segment 1 *Nuclear masses and deformations* Audi and Wapstra mass tables [185, 186]. Möller and Nix FRDM masses and deformations [198]. Segment 5 *Nuclear densities* Shell correction prescription, database of shell corrections calculated with the Myers-Swiatecki mass formula.

[183] RIPL-3 database [184]: Segment 4, *Optical model parameters*, Becchetti-Greenlees IREF=100 [328] and Koning-Delaroche IREF= 1422–1463 [232].

[184] R. Capote et al., “RIPL–Reference Input Parameter Library for Calculation of Nuclear Reactions and Nuclear Data Evaluations”, NUCL. DATA SHEETS **110**, 3107–3214 (2009) (see *www-nds.iaea.org/RIPL-3/*).

[185] G. Audi, A. H. Wapstra, “The 1995 update to the atomic mass evaluation”, NUCL. PHYS. **A595**, 409–480 (1995).

[186] G. Audi, A. H. Wapstra, C. Thibault, “The AME2003 atomic mass evaluation (II). Tables, graphs and references”, NUCL. PHYS. **A729**, 337–676 (2003).

[187] A. Tudora, F.-J. Hambsch, G. Giubega, I. Visan, “Even-odd effects in prompt emission in fission”, NUCL. PHYS. **A933**, 165–188 (2015).

[188] A. Tudora, F.-J. Hambsch, G. Giubega, I. Visan, “Even-odd effects in prompt emission of spontaneously fissioning even-even Pu isotopes”, NUCL. PHYS. **A929**, 260–292 (2014).

[189] A. Tudora, “Point-by-Point model description of experimental average prompt neutron multiplicity as a function of total kinetic energy of fission fragments”, ANN. NUCL. ENERGY **53**, 507–518 (2013).

[190] A. Tudora,“Prompt neutron and gamma-ray emission calculations for ^{232}Th(n,f)”, NUCL. PHYS. **A916**, 79–101 (2013).

[191] A. Tudora, F.-J. Hambsch, S. Oberstedt, “Prompt fission neutron emission calculations and description of sub-barrier fission cross section resonances for ^{234}U(n,f)”, NUCL. PHYS. **A917**, 43–70 (2013).

[192] A. Tudora, F.-J. Hambsch, S. Oberstedt, G. Giubega, I. Visan, “Correlation between the prompt neutron multiplicity and prompt gamma-ray energy in the frame of the Point-by-Point model”, PHYS. PROCEDIA **59**, 95–100 (2014).

[193] C. Wagemans, “The Nuclear Fission Process”, (Ed. F. Göhnnewein), CRC Press Boca Raton, 1991, **Chapter 8**.

[194] C. Morariu, A. Tudora, F.-J. Hambsch, S. Oberstedt, C. Manailescu, “Modeling of the total excitation energy partition including fragment deformation and excitation energy at scission ”, J. PHYS. G: NUCL. PART. PHYS. **39**, 055103 (2012).

[195] N. Carjan, F.-J. Hambsch, F. A. Ivanyuk, P. Talou, “Scission configurations for St.I and St.II fission modes in the reaction ^{235}U($\mathrm{n_{th}}$,f)”, PHYS. PROCEDIA **59**, 173–180 (2014).

[196] A. V. Ignatyuk, G. N. Smirenkin, A. S. Tishin, "Phenomenological description of the energy dependence of the level density parameter", YAD. FIZ.**21**, 485 (1975) [SOV. J. NUCL. PHYS. **21**, 255 (1975)].

[197] A. Ignatyuk, IAEA-RIPL1 TECDOC-1034 **Segment V** Chapter 5.1.4, IAEA, Vienna, Austria (1998).

[198] P. Möller, J. R. Nix, W. D. Myers, W. J. Swiatecki, "Nuclear ground-state masses and deformations", AT. DATA NUCL. DATA TABLES **59**, 185–381 (1995).

[199] O. Bersillon, "SCAT2 optical model code", NEA-Data Bank, Computer Program Service, Package NEA 0829/07 version 2010 (V. Manea, University of Bucharest).

[200] G. Vladuca, A. Tudora, "Improved Los Alamos model applied to the neutron induced fission of ^{239}Pu and ^{240}Pu and to the spontaneous fission of Pu isotopes", ANN. NUCL. ENERGY **28**, 689–700 (2001).

[201] G. Vladuca, A. Tudora, "Prompt fission neutron multiplicity and spectrum evaluation for n+^{238}U reaction", ANN. NUCL. ENERGY **28**, 1653–1665 (2001).

[202] W. Hauser, H. Feshbach, "The Inelastic Scattering of Neutrons", PHYS. REV. **87**, 366–373 (1952).

[203] G. Vladuca, A. Tudora, "Prompt fission neutron spectrum calculation for n+^{238}U reaction using the multi-modal model", ANN. NUCL. ENERGY **28**, 1643–1652 (2001).

[204] H. R. Bowman, J. C. D. Milton, S. G. Thompson, W. J. Swiatecki, "Further Studies of the Prompt Neutrons from the Spontaneous Fission of ^{252}Cf", PHYS. REV. **129**, 2133–2146 (1963), USA

[205] V. P. Zakharova, D. K. Ryazanov, "Neutron Yields from Spontaneous Fission of ^{252}Cf", YAD. FIZ. **30**, 36 (1979) [SOV. J. NUCL. PHYS. **30**, 19 (1979)], EXFOR 40420002.

[206] R. Muller, A. A. Naqvi, F. Käppeler, F. Dickmann, "Fragment velocities, energies, and masses from fast neutron induced fission of ^{235}U", PHYS. REV. **C29**, 885–905 (1984), EXFOR 21834009 and 21834010.

[207] Ding Shengyao, et al., "Research of Prompt Neutrons from ^{252}Cf Spontaneous Fission Fragments", CHINESE J.OF NUCL. PHYS. (BEIJING) **6**, 201 (1984) [CHINESE PHYS. **5**, 678 (1985)], EXFOR 30719.

[208] C. Budtz-Jørgensen, H.-H. Knitter, "Simultaneous investigation of fission fragments and neutrons in ^{252}Cf(sf)", NUCL. PHYS. **A490**, 307-328 (1988), EXFOR 23175008, 23175009.

[209] A. Vorobyev, A. Laptev, O. Shcherbakov, V. Kalinin, V. Dushin, B. Petrov, "Distribution of prompt neutron emission probability for fission fragments in spontaneous fission of ^{252}Cf and ^{244,248}Cm", in *Proc. of the Int. Conf. on Nucl. Data for Sc. Tech., ND2004, Santa Fe, NM, USA* (Eds. M. B. Chadwick, R. C. Haight, T. Kawano, P. Talou), AIP CONF. PROC. **769**, 613 (2005), EXFOR 41425014.

[210] H. Nifenecker, C. Signarbieux, R. Babinet, J. Poitou, "Neutron and gamma emission in fission", pp.117–178 in Ref. [25]).

[211] A. Tudora, "Multi-parametric prompt neutron and fission fragment experimental data described by the Point-by-Point model", ANN. NUCL. ENERGY **35**, 1–10 (2008).

[212] A. Tudora, "Experimental prompt fission neutron "sawtooth" data described by the Point-by-Point model", ANN. NUCL. ENERGY **33**, 1030–1038 (2006).

[213] A. Tudora, F.-J. Hambsch, S. Oberstedt, "Sub-barrier resonance fission and its effects on fission fragment properties", NUCL. PHYS. **A890-891**, 77–101 (2012).

[214] K. Nishio, Y. Nakagome, H. Yamamoto, I. Kimura, "Multiplicity and energy of neutrons from ^{235}U($n_{\rm th}$,f) fission fragments", NUCL. PHYS. **A632**, 540–558 (1998).

[215] E. E. Maslin, A. L. Rodgers, W. G. F. Core, "Prompt Neutron Emission from U235 Fission Fragments", PHYS. REV. **164**, 1520–1527 (1967).

[216] F. Pleasonton, R. L. Ferguson, H. Schmitt, "Prompt gamma rays emitted in the thermal-neutron-induced fission of ^{235}U", PHYS. REV. **C6**, 1023–1039 (1972).

[217] K.-H. Schmidt, B. Jurado, "Entropy-driven excitation-energy sorting in superfluid fission dynamics", PHYS. REV. LETT. **104**, 212501 (2010).

[218] M. Mirea, "Energy partion in low energy fission", PHYS. REV. **C83**, 054608 (2011).

[219] M. C. Duijvestijn, A. J. Koning, "Mass distribution in nucleon-induced fission at intermediate energies", PHYS. REV. **C64**, 014607 (2001).

[220] Liu Ting-Jin, Sun Zheng-Jun, Shu Neng-Chuan, "Systematics on fission fragment mass distribution of neutron induced ^{235}U fission", CHIN. PHYS. **C32**, 556–560 (2008).

[221] K.-H. Schmidt, B. Jurado, et al., "General description of observables in low-energy fission", NUCL. DATA SHEETS, this volume.

[222] P. Talou, B. Becker, T. Kawano, M. B. Chadwick, Y. Danon, "Advanced Monte Carlo Modeling of Prompt Fission Neutrons for Thermal and Fast Neutron-Induced Fission Reaction on Pu-239", PHYS. REV. **C83**, 064612 (2011).

[223] T. Kawano, P. Talou, M. B. Chadwick, T. Watanabe, "Monte Carlo Simulation for Particle and Gamma-Ray Emissions in Statistical Hauser-Feshbach Model", J. NUCL. SCI. TECH. **47**, 462 (2010).

[224] P. Talou, T. Kawano, I. Stetcu, "`CGMF` Documentation, Release 1.0.5", Report **LA-UR-14-24031**, Los Alamos, USA (2014).

[225] R. Yanez, L. Yao, J. King, W. Loveland, "Excitation Energy Dependence of the Total Kinetic Energy Release in ^{235}U (n, f)", PHYS. REV. **C89**, 051604(R) (2014).

[226] J. Randrup, P. Möller, "Brownian Shape Motion on Five-Dimensional Potential-Energy Surfaces: Nuclear Fission-Fragment Mass Distributions", PHYS. REV. LETT. **106**, 132503 (2011).

[227] J. Randrup, P. Möller, "Energy dependence of fission-fragment mass distributions from strongly damped shape evolution", PHYS. REV. **C88**, 064606 (2013).

[228] A. J. Sierk, "Dynamical model for fission fragment properties", presentation at FIESTA 2014 Workshop on "Fission Theory and Experimental Advances", Santa Fe, NM, Sep. 8–12, 2014.

[229] W. Younes, D. Gogny, N. Schunck, “A microscopic theory of low energy fission fragment properties”, pp.605 in *Proc. of the 5th International Conference on Fission and Properties of Neutron-Rich Nuclei (ICFN5), 4–10 Nov. 2010, Sanibel Island, FL, USA* AIP, USA (2013).

[230] I. Stetcu, P. Talou, T. Kawano, M. Jandel, “Isomer production ratios and the angular momentum distribution of fission fragments”, Phys. Rev. **C88**, 044603 (2013).

[231] I. Stetcu, P. Talou, T. Kawano, M. Jandel, “Properties of Prompt Fission Gamma Rays”, Phys. Rev. **C90**, 024617 (2014).

[232] A. J. Koning, J. P. Delaroche, “Local and global nucleon optical models from 1 keV to 200 MeV”, Nucl. Phys. **A713**, 231–310 (2003).

[233] J. Kopecky, M. Uhl, “Test of gamma-ray strength functions in nuclear reaction model calculations”, Phys. Rev. **C41**, 1941 (1990).

[234] D. M. Brink, “Some aspects of the interaction of fields with matter”, D. Ph. Thesis, Oxford (1955).

[235] P. Axel, “Electric dipole ground state transition width strength function and 7-MeV photon interactions”, Phys. Rev. **126**, 671 (1962).

[236] A. Gilbert, A. G. W. Cameron, Can. J. Phys. **43**, 1446 (1965).

[237] O. Litaize, O. Serot, “Investigation of phenomenological models for the Monte Carlo simulation of the prompt fission neutron and γ-emission”, Phys. Rev. **C82**, 054616 (2010).

[238] D. Regnier, O. Litaize, O. Serot, “Monte Carlo Simulation of Prompt Fission Gamma Emission”, Phys. Procedia **31**, 59–65 (2012).

[239] D. Regnier, O. Litaize, O. Serot, “Preliminary Results of a Full Hauser-Feshbach Simulation of the Prompt Neutron and Gamma Emission from Fission Fragments”, Phys. Procedia **47**, 47–52 (2013).

[240] D. Regnier, O. Litaize, O. Serot, to be submitted to Computer Physics Communications.

[241] A. C. Wahl, “Systematics of Fission products Yields”, LANL report **LA-13928**, Los Alamos, USA (2002).

[242] C. Wagemans, E. Allaert, A. Deruytter, R. Barthélémy, P. Schillebeeckx, “Comparison of the energy and mass characteristics of the ^{239}Pu($n_{\rm th}$,f) and the ^{240}Pu(sf) fragments”, Phys. Rev. **C30**, 218 (1984).

[243] F.-J. Hambsch, H.-H. Knitter, C. Budtz-Jørgensen, J. P. Theobald, “Fission mode fluctuations in the resonances of 235U(n,f)”, Nucl. Phys. **A491**, 56–90 (1989).

[244] N. Varapai, F.-J. Hambsch, S. Oberstedt, O. Serot, G. Barreau, N. Kornilov, S. Zeinalov, “Development Of A Digital Technique For The Determination Of Fission Fragments And Emitted Prompt Neutron Characteristics”, in *Proc. Int. Workshop on Nuclear Fission and Fission Product Spectroscopy, 11–14 May, Cadarache, France*, AIP Conf. Proc. **798**, 369–372 (2005).

[245] T. Ohsawa, “Representation of fission neutron spectrum by a non-equitemperature Madland-Nix model”, pp.71–80 in Ref. [29].

[246] V. V. Verbinski, H. Weber, R. E. Sund, “Prompt Gamma Rays from ^{235}U(n,f), ^{239}Pu(n,f), and Spontaneous Fission of ^{252}Cf”, Phys. Rev. **C7**, 1173–1185 (1973).

[247] O. Litaize, O. Serot, D. Regnier, C. Manailescu, “Investigation of n+^{238}U Fission Observables”, Nucl. Data. Sheets **118**, 216–219 (2014).

[248] J. Verbeke, R. Vogt, J. Randrup, “Fission Reaction Event Yield Algorithm `FREYA` for event-by-event simulation of fission”, Comp. Phys. Comm. **191**, 178–202 (2015).

[249] R. Vogt, J. Randrup, J. Pruet, W. Younes, “Event-by-event study of prompt neutrons from ^{239}Pu(n,f)”, Phys. Rev. **C80**, 044611 (2009).

[250] J. Randrup, R. Vogt, “Calculation of fission observables through event-by-event simulation”, Phys. Rev. **C80**, 024601 (2009).

[251] R. Vogt, J. Randrup, D. A. Brown, M. A. Descalle, W. E. Ormand, “Event-by-event evaluation of the prompt fission neutron spectrum from ^{239}Pu(n,f)”, Phys. Rev. **C85**, 024608 (2012).

[252] R. Vogt, J. Randrup, “Event-by-event study of neutron observables in spontaneous and thermal fission”, Phys. Rev. **C84**, 044621 (2011).

[253] R. Vogt, J. Randrup, “Event-by-event study of photon observables in spontaneous and thermal fission”, Phys. Rev. **C87**, 044602 (2013).

[254] J. Randrup, R. Vogt “Refined treatment of angular momentum in the event-by-event fission model `FREYA`”, Phys. Rev. **C89**, 044601 (2014).

[255] R. Vogt, J. Randrup, “Neutron angular correlations in spontaneous and neutron-induced fission”, Phys. Rev. **C90** 064623 (2014).

[256] nuclear.llnl.gov/simulation/main.html.

[257] W. J. Swiatecki, K. Siwek-Wilczynska, J. Wilczynski, “Ratios of disintegration rates for distinct decay modes of an excited nucleus”, Phys. Rev. **C78**, 054604 (2008).

[258] E. Gadioli, P. E. Hodgson, “Pre-equilibrium Nuclear Reactions”, Oxford Science Publications, Clarendon Press (1992).

[259] A. J. Koning, M. C. Duijvestijn, “A global pre-equilibrium analysis from 7 to 200 MeV based on the optical model potential”, Nucl. Phys. **A744**, 15–76 (2004).

[260] J. Dobeš, E. Běták, “Two component exciton model”, Z. Phys. **A310**, 329–338 (1983).

[261] W. Younes et al., “Transition from asymmetric to symmetric fission in the ^{235}U(n,f) reaction”, Phys. Rev. **C64**, 054613 (2001).

[262] U. Brosa, “Sawtooth curve of neutron multiplicity”, Phys. Rev. **C32**, 1438–1441 (1985).

[263] T. R. England, B. F. Rider, “Evaluation and Compilation of Fission Yields”, LANL report **LA-UR-94-3106**, Los Alamos,

USA (1994).

[264] L. E. Glendenin, J. E. Gindler, D. J. Henderson, J. W. Meadows, “Mass distributions for monoenergetic-neutron-induced fission of ^{235}U”, PHYS. REV. **C24**, 2600–2605 (1981).

[265] J. E. Gindler, L. E. Glendenin, D. J. Henderson, J. W. Meadows, “Mass distributions in monoenergetic-neutron-induced fission of ^{239}Pu”, PHYS. REV. **C27**, 2058 (1983).

[266] W. Reisdorf, J. P. Unik, H. C. Griffin, L. E. Glendenin, “Fission fragment K X-ray emission and nuclear charge distribution for thermal neutron fission of ^{233}U, ^{235}U, ^{239}Pu and spontaneous fission of ^{252}Cf”, NUCL. PHYS. **A 177**, 337–378 (1971).

[267] T. Kawano, private communication (2008).

[268] S. Lemaire, P. Talou, T. Kawano, M. B. Chadwick, D.G. Madland, “Monte Carlo approach to sequential neutron emission from fission fragments”, PHYS. REV. **C72**, 024601 (2005).

[269] H. Koura, M. Uno, T. Tachibana, M. Yamada, “Nuclear mass formula with shell energies calculated by a new method”, NUCL. PHYS. **A674**, 47–76 (2000).

[270] N. V. Kornilov, “Fission neutrons: Experiments, evaluation, modeling and open problems”, **ISBN 978-3-319-07132-9** (Springer e-book, 2015).

[271] K.-H. Schmidt et al., “Relativistic radioactive beams: A new access to nuclear-fission studies”, NUCL. PHYS. **A665**, 221–267 (2000).

[272] C. Böckstiegel et al., “Nuclear-fission studies with relativistic secondary beams: analysis of fission channels”, NUCL. PHYS. **A802**, 12–25 (2008).

[273] M. Caamano, F. Rejmund, K.-H. Schmidt, “Evidence for the predominant influence of the asymmetry degree of freedom on the even-odd structure in fission-fragment yields”, J. PHYS. G: NUCL. PART. PHYS. **38**, 035101 (2011).

[274] F. Giacoppo et al., “Level densities and thermodynamical properties of Pt and Au isotopes”, PHYS. REV. **C90**, 054330 (2014).

[275] U. Mosel, H. W. Schmitt, “Potential energy surfaces for heavy nuclei in the two-center model”, NUCL. PHYS. **A165**, 73–96 (1971).

[276] W. D. Myers, W. J. Swiatecki, “Nuclear properties according to the Thomas-Fermi model”, NUCL. PHYS. **A601**, 141–167 (1996).

[277] K.-H. Schmidt, A. Kelic, M. V. Ricciardi, “Experimental evidence for the separability of compound-nucleus and fragment properties in fission”, EUROPH. LETT. **83**, 32001 (2008).

[278] K.-H. Schmidt, B. Jurado, “Inconsistencies in the description of pairing effects in nuclear level densities”, PHYS. REV. **C86**, 044322 (2012).

[279] B. Jurado, K.-H. Schmidt, “Influence of complete energy sorting on the characteristics of the odd-even effect in fission-fragment element distributions”, J. PHYS. G: NUCL. PART. PHYS. **42**, 055101 (2015).

[280] K.-H. Schmidt, B. Jurado, Ch. Amouroux, *General description of fission observables*, JEFF Report **24**, Nuclear Energy Agency, OECD, Paris (2014).

[281] W. D. Myers, W. J. Swiatecki, “Thomas-Fermi fission barriers”, PHYS. REV. **C 60**, 014606 (1999).

[282] K.-H. Schmidt, B. Jurado, “Final excitation energy of fission fragments”, PHYS. REV. **C83**, 061601 (2011).

[283] J. R. Huizenga, R. Vandenbosch, “Interpretation of isomeric cross-section ratios for (n,gamma) and (gamma,n) reactions”, PHYS. REV. **120**, 1305–1312 (1960).

[284] A. R. Junghans, G. Rusev, R. Schwengner, A. Wagner, E. Grosse, “Photon data shed new light upon the GDR spreading width in heavy nuclei”, PHYS. LETT. **B670**, 200–204 (2008).

[285] Ch. Straede, C. Budtz-Jørgensen, H. H. Knitter, “^{235}U(n,f) fragment mass-, kinetic energy- and angular distributions for incident neutron energies between thermal and 6 MeV”, NUCL. PHYS. **A462** 85–108 (1987).

[286] A. Al-Adili, F.-J. Hambsch, S. Pomp, S. Oberstedt, “Impact of prompt neutron corrections on final fission fragment distributions”, PHYS. REV. **C86**, 054601 (2012).

[287] F .Göennenwein in “The Nuclear Fission Process”, CRC-Press, C. Wagemans (Ed.), p.323 (1991).

[288] N. V. Kornilov, “Scale Method for Evaluation of Fission Neutron Spectra”, NUCL. SC. ENG. **169**, 290–295 (2011).

[289] W. P. Poenitz, “Evaluation Methods for Neutron Cross Section Standards”, in *Proc. Conf. Nucl. Data Evaluation Methods and Procedures*, BNL report **BNL-NCS-51363**, Vol.1, p. 249 (1981). Codes and documentation available online at *www-nds.iaea.org/standards/codes.html*.

[290] B. Marcinkevicius, S. Simakov, V. G. Pronyaev, “Short User Guide of Generalized Least Squares Code GMAP”. Available online at *www-nds.iaea.org/standards/Codes/GMA-User-Guide.pdf*.

[291] D. W. Muir, “Global Assessment of Nuclear Data Requirements”, IAEA, Vienna, Austria (2001). Code and documentation available online (see *www-nds.iaea.org/gandr/*).

[292] D. L. Smith, PROBABILITY, STATISTICS AND DATA UNCERTAINTIES IN NUCLEAR SCIENCE AND TECHNOLOGY, American Nuclear Society, LaGrange Park, IL (1991).

[293] D. L. Smith, “A Least-Squares Computational Tool Kit”, ANL report **ANL/NDM-128**, Argonne, USA, 1993.

[294] D. L. Smith, “A Unified Monte Carlo Approach to Fast Neutron Cross Section Data Evaluation”, pp.736–743 in *Proc. 8th Int. Topical Meet. on Nucl. Appl. and Utilization of Accelerators, Pocatello, July 29-August 2*, American Nuclear Society, USA (2007)

[295] R. Capote, D. L. Smith, “An Investigation of the Performance of the Unified Monte Carlo Method of Neutron Cross Section Data Evaluation”, NUCL. DATA SHEETS **109**, 2768–2773 (2008).

[296] R. Capote, D. L. Smith, A. Trkov, M. Meghzifene, “A New Formulation of the Unified Monte Carlo Approach (UMC-B) and Cross-Section Evaluation for the Dosimetry Reaction ^{55}Mn(n,γ)^{56}Mn”, J. ASTM INTERNAT. **9**, JAI104115 (2012).

[297] D. Neudecker, P. Talou, D. L. Smith, R. Capote, M. E. Rising, A. C. Kahler, “Evaluation of the ^{239}Pu Prompt Fission

Neutron Spectrum Induced by Neutrons of 500 keV and Associated Covariances", Nucl. Inst. Meth. Phys. Res. **A791**, 80–92 (2015).

[298] M. E. Rising, P. Talou, T. Kawano, A. K. Prinja, "Evaluation and uncertainty quantification of prompt fission neutron spectra of uranium and plutonium isotopes", Nucl. Sci. Eng. **175**, 81–93 (2013).

[299] R. Capote, D. L. Smith, A. Trkov, "Nuclear Data Evaluation Methodology Including Estimates of Covariances", EPJ Web of Conf. **8**, 04001 (2010).

[300] D. Neudecker, R. Capote, H. Leeb, "Impact of model defect and experimental uncertainties on evaluated output", Nucl. Inst.& Meth. Phys. Res. **A723**, 163–172 (2013).

[301] V. G. Pronyaev, A. Mengoni, A. D. Carlson (Eds), "International Neutron Cross Section-Standards: Measurements and Evaluation Techniques", Report **INDC(NDS)-0540**, IAEA, Vienna, Austria (2008).

[302] V. G. Pronyaev, A. D. Carlson, R. Capote Noy (Eds), "Toward a New Evaluation of Neutron Standards", Report **INDC(NDS)-0641**, IAEA, Vienna, Austria (2013).

[303] V. G. Pronyaev, A. D. Carlson, R. Capote Noy (Eds), "Current Status of Neutron Standards", Report **INDC(NDS)-0677**, IAEA, Vienna, Austria (2015).

[304] A. Wallner et al., "Precise measurement of the ^{27}Al(n,2n)^{26g}Al excitation function near threshold and its relevance for fusion-plasma technology", Eur. Phys. J. **A17**, 285–296 (2003).

[305] W. Mannhart, "Validation of Differential Cross Sections with Integral Data", Report **INDC(NDS)-0435**, pp.59–64, IAEA, Vienna, Austria (2002).

[306] W. Mannhart, "Status of the Evaluation of the Neutron Spectrum of 235U + n-th", Report **INDC(NDS)-0540**, presentation link in Appendix C, IAEA, Vienna, Austria (2008).

[307] W. Mannhart, "Response of activation reactions in the neutron field of Cf-252(sf)", in textitInternational Reactor Dosimetry File 2002 (IRDF-2002), IAEA Technical Reports Series **No. 452**, pp.30–45 IAEA, Vienna, Austria (2006). Available online at *www-pub.iaea.org/MTCD/publications/PDF/TRS452_web.pdf*.

[308] K. Kobayashi, "Measurement of ^{233}U fission spectrum-averaged cross sections for some threshold reactions" in *Proc. 8th ASTM-EURATOM Symposium on Reactor Dosimetry, Vail, CO, USA, Aug.29–Sept.3, 1993*, ASTM STP 1228, 720–726 (1994).

[309] K. Kobayashi, I. Kimura, "Fission spectrum averaged cross sections with standard neutron fields" in *Proceedings of the 3rd ASTM-EURATOM Symposium on Reactor Dosimetry, Ispra, Varese, Italy, 1–5 Oct. 1979*, Brussels and Luxembourg, EUR 6813 EN, 1004–1015 (1980).

[310] O. Horibe, Y. Mizumoto, T. Kusakabe, H. Chatani, "U-235 Fission Neutron Spectrum Averaged Cross Sections Measured for Some Threshold Reactions on Mg, Al, Ca, Sc, Ti, Fe, Co, Ni, Zn, Sr, Mo, Rh, In and Ce", pp. 923-930 in *Proc. Conf. 50 Years with Nuclear Fission, 25-28 April 1989, Gaithersburg, USA*, J. W. Behrens and A. D. Carlson (Eds), Vol. 2, American Nuclear Society, Inc., USA (1989).

[311] K. Kobayashi et al., "The ^{235}U Fission Neutron Spectrum Adjusted With Multi-Foil Activation Data", EUR 14356 EN, pp.263–270 in *Reactor Dosimetry: Proc. 7th ASTM-EURATOM Symposium on Reactor Dosimetry, Strasbourg, France, 27-31 August 1990*, Dordrecht, Boston and London, Kluwer Academics Publisher (1992).

[312] K. Kobayashi et al., "Measurement of ^{235}U fission spectrum-averaged cross sections and neutron spectrum adjusted with the activation data", Ann. Rep. Res. React. Inst. Kyoto Univ. **25**, 21–35 (1992).

[313] D. Neudecker, P. Talou, D. L. Smith, R. Capote, M. E. Rising, A. C. Kahler, "Preliminary Evaluation and Uncertainty Quantification of the Prompt Fission Neutron Spectrum of ^{239}Pu", Nucl. Data Sheets **123**, 146–152 (2015).

[314] P. Talou, T. Kawano, D. G. Madland, A. C. Kahler, D. K. Parsons, M. C. White, R. C. Little, M. B. Chadwick, "Uncertainty Quantification of Prompt Fission Neutron Spectrum for n(0.5 MeV)+^{239}Pu", Nucl. Sc. Eng. **166**, 254–266 (2010).

[315] T. N. Taddeucci et al., "Multiple-scattering Corrections to Measurements of the Prompt Fission Neutron Spectrum", Nucl. Data Sheets **123**, 135–139 (2015).

[316] D. G. Madland, "Total Prompt Energy Release in the Neutron-induced Fission of ^{235}U, ^{238}U and ^{239}Pu", Nucl. Phys. **A772**, 113–137 (2006).

[317] J. P. Lestone, T. T. Strother, "Energy Dependence of Plutonium and Uranium Average Fragment Total Kinetic Energies", Nucl. Data Sheets **118**, 208–210 (2014).

[318] M. E. Rising, F. R. Brown, D. Neudecker, A. C. Kahler, P. Talou, "Impact of New Prompt Fission Neutron Spectrum Evaluations and the Associated Cross-Correlations on Critical Assemblies using MCNP6", LANL report **LA-UR15-24045**, Los Alamos, USA (2015).

[319] R. E. Kalman, "A New Approach to Linear Filtering and Prediction Problems", Trans. of the ASME–J. Basic Engin. **82** (Series D), 35–45 (1960).

[320] T. Kawano, "Estimation of energy dependence of the optical potential parameters for Bi-209", Nucl. Sci. Eng. **131**, 107–115 (1999).

[321] P. Talou, P. G. Young, T. Kawano, M. E. Rising, M. B. Chadwick, "Quantification of uncertainties for evaluated neutron-induced reactions on actinides in the fast energy range", Nucl. Data Sheets **112**, 3054–3074 (2011).

[322] M. E. Rising, A. K. Prinja, P. Talou, "Prompt fission neutron spectrum uncertainty propagation using polynomial chaos expansion", Nucl. Sci. Eng. **175**, 188–203 (2013).

[323] A. Tudora, F.-J. Hambsch, G. Giubega, I. Visan, "Even-odd effects in the prompt emission of ^{234}U(n,f) at incident neutron energy ranging from 0.2 MeV to 5 MeV", submitted to Nucl. Phys. A (March 2015).

[324] A. Tudora, F.-J. Hambsch, S. Oberstedt, G. Giubega, I. Visan, "How sensitive is the prompt neutron multiplicity to the fission fragment characteristics?", Nucl. Sci. Eng. 2015 in press (accepted for publication in February 2015).

[325] F.-J. Hambsch, S. Oberstedt, et al. , "Fission Fragment Yield, Cross Section and Prompt Neutron and Gamma Emission

Data from Actinide Isotopes", NUCL. DATA SHEETS **119**, 38–41 (2014).

[326] V. M. Surin, A. I. Sergachev, N. I. Rezchikov, B. D. Kuzminov, "Yields and Kinetic Energies of Fragments in the Fission of ^{233}U and ^{239}Pu by 5.5- and 15-MeV Neutrons", YAD. FIZ. **14**, 935 (1971), EXFOR 40112004.

[327] A. I. Sergachev, V. G. Vorobyeva, B. D. Kuzminov, V. B. Mikhailov, M. Z. Tarasko, "Influence of Intermediate States of Fissioning Th233 Nucleus on the Mass and Kinetic Energy Distributions of the Fragments", YAD. FIZ. **7**, 778 (1968) [Sov. J. Nucl. Phys. 7, 475 (1968)], EXFOR 40173.

[328] F. D. Becchetti, Jr., G. W. Greenlees, "Nucleon-nucleus optical-model parameters, $A > 40$, $E < 50$ MeV", PHYS. REV. **182**, 1190–1209 (1969).

[329] D. Wilmore, P. E. Hodgson, "The calculation of neutron cross-sections from optical potentials", NUCL. PHYS. **55**, 673–694 (1964).

[330] O. Iwamoto, "Systematics of Prompt Fission Neutron Spectra", J. NUCL. SCI. TECH. **45**, 910–919 (2008).

[331] A. Tarantola, "Inverse Problem Theory", SIAM press (2005).

[332] M. B. Chadwick et al., "ENDF/B-VII.0: Next Generation Evaluated Nuclear Data Library for Nuclear Science and Technology", NUCL. DATA SHEETS **107**, 2931–3060 (2006).

[333] M. D. McKay, R. J. Beckman, W. J. Conover, "A comparison of three methods for selecting values of input variables in the analysis of output from a computer code", TECHNOMETRICS **21**, 239–245 (1979).

[334] R. L. Iman, J. C. Helton, J. E. Campbell, "An approach to sensitivity analysis of computer models: Part I – Introduction, input variable selection and preliminary variable assessment", J. QUAL. TECH. **13**, 174–183 (1981).

[335] P. G. Young et al., "Evaluation of Neutron Reactions for ENDF/B-VII: $^{232--241}$U and ^{239}Pu", NUCL. DATA SHEETS **108**, 2589–2654 (2007).

[336] R. Brun, F. Rademakers, "ROOT - An Object Oriented Data Analysis Framework", NUCL. INST. METH **A389**, 81–86 (1997). See also *root.cern.ch/*.

[337] R. E. MacFarlane, D. W. Muir, R. M. Boicourt, A. C. Kahler, "The NJOY Nuclear Data Processing System, Version 2012", LANL report **LA-UR-12-27079**, Los Alamos, USA (2012).

[338] A. Trkov, RR_UNC code: calculates uncertainties in reaction rates and cross sections. Available online at *www-nds.iaea.org/IRDFF/rr_unc.for*.

[339] ICSBEP 2006: INTERNATIONAL HANDBOOK OF EVALUATED CRITICALITY SAFETY BENCHMARK EXPERIMENTS, Report **NEA/NSC/DOC(95)03**, Nuclear Energy Agency, OECD, Paris (2006).

[340] A. Koning et al., The JEFF-3.1 Nuclear Data Library, REPORT JEFF **21**, Nuclear Energy Agency, OECD, Paris (2006).

[341] V. M. Maslov et al., "^{235}U(n,f), ^{233}U(n,f) and ^{239}Pu(n,f) Prompt Fission Neutron Spectra", J. KOREAN PHYS. SOC. **59**, 1337–1342 (2011).

[342] E. Bauge et al., "Coherent investigation of nuclear data at CEA DAM: Theoretical models, experiments and evaluated data", EUR. PHYS. J. **A48**, 113–152 (2012).

[343] F. Tovesson, T. S. Hill, "Cross Sections for ^{239}Pu(n,f) and ^{241}Pu(n,f) in the Range $E_n = 0.01$ eV to 200 MeV", NUCL. SCI. ENG. **165**, 224–231 (2010), EXFOR 14271002.

[344] R. L. Reed, R. W. Hockenbury, R. C. Block, "Prompt neutron multiplicity measurements for neutron-induced fission of ^{233}U and ^{235}U", CHICAGO OPERATIONS OFFICE, A.E.C. CONTRACT REPORT **Vol.39, No.3058**, p.9, Chicago, USA (1973).

[345] A. J. Plompen, T. Kawano, R. Capote (Eds), "Technical Meeting on Inelastic Scattering and Capture Cross-section Data of Major Actinides in the Fast Neutron Region", Report **INDC(NDS)-0597**, IAEA, Vienna, Austria (2011).

[346] M. B. Chadwick et al., "The CIELO Collaboration: Neutron Reactions on 1H, 16O, 56Fe, 235;238U, and 239Pu", NUCL. DATA SHEETS **118**, 1–25 (2014).

[347] A. Wallner, T. Belgya, M. Bichler, K. Buczak, I. Dillmann, F. Kaeppeler, C. Lederer, A. Mengoni, F. Quinto, P. Steier, L. Szentmiklosi, "Novel Method to Study Neutron Capture of ^{235}U and ^{238}U Simultaneously at keV Energies", PHYS. REV. LETT. **112**, 192501 (2014).

[348] R. Capote, A. Trkov, M. Sin, M.W. Herman, A. Daskalakis, Y. Danon, "Physics of Neutron Interactions with ^{238}U: New Developments and Challenges", NUCL. DATA SHEETS **118**, 26–31 (2014).

[349] K. I. Zolotarev, "Evaluation and Improvement of Cross-Section Accuracy for Most Important Dosimetry Reactions Including Covariance Data", Report **INDC(NDS)-0431**, IAEA, Vienna, Austria (2002).

[350] K. I. Zolotarev, "Evaluation and Improvement of Cross Section Accuracy for Most Important Dosimetry Reactions 27Al(n,p), 56Fe(n,p) and 237Np(n,f) including Covariance Data", Report **INDC(NDS)-0438**, IAEA, Vienna, Austria (2004).

[351] K. I. Zolotarev, "Re-evaluation of microscopic and integral cross-section data for important dosimetry reactions", Report **INDC(NDS)-0526**, IAEA, Vienna, Austria (2008).

[352] K. I. Zolotarev, "Evaluation of cross section data from threshold to 40-60 MeV for specific neutron reactions important for neutron dosimetry applications", Report **INDC(NDS)-0546**, IAEA, Vienna, Austria (2009).

[353] K. I. Zolotarev, "Evaluation of cross section data from threshold to 40 MeV for some neutron reactions important for fusion dosimetry applications, Part 2", Report **INDC(NDS)-0584**, IAEA, Vienna, Austria (2010).

[354] K. I. Zolotarev, "Evaluation of some (n,n'), (n,γ), (n,p), (n,2n) and (n,3n) excitation functions for fission and fusion reactor dosimetry applications", Report **INDC(NDS)-0657**, IAEA, Vienna, Austria (2013).

[355] N. Carjan, M. Rizea, "Similarities between calculated scission-neutron properties and experimental data on prompt fission neutrons", PHYS. LETT. **B747** 178–181 (2015).

APPENDIX I: TERMINOLOGY FOR UNCERTAINTY QUANTIFICATION

An "uncertainty" measures the dispersion of possible and often (to some extent) unknown errors pertinent to the measured values, see e.g., Refs. [46, 47]. An "error" is the difference between the true value of an observable, here the PFNS, and the actual measured value. These errors can be of statistical and systematic nature. Corresponding statistical uncertainties quantify the possible dispersion of an uncorrelated random error for a specific data point which is independent of any other data point, while systematic uncertainties correspond to the dispersion of correlated errors which might affect part or all of one or even multiple data sets. Here, we provide uncertainties and correlations between uncertainties of different data points in the form of covariances. A covariance matrix element $\text{Cov}(x_i, x_j)$ for variables x_i and x_j is formerly defined as,

$$\text{Cov}(x_i, x_j) = \langle (x_i - \langle x_i \rangle)(x_j - \langle x_j \rangle) \rangle \,, \tag{116}$$

where $\langle . \rangle$ signifies an expectation value. It is the second moment of the probability distribution function of the variables x_i and x_j, while the mean value $\langle x_i \rangle$ corresponds to the first moment. The diagonal of a covariance matrix,

$$\text{Cov}(x_i, x_i) = \left\langle (x_i - \langle x_i \rangle)^2 \right\rangle = \text{var}(x_i), \tag{117}$$

corresponds to the variance $\text{var}(x_i)$ of the variable x_i. The correlation matrix element $\text{Cor}(x_i, x_j)$ associated with $\text{Cov}(x_i, x_j)$ is given by,

$$\text{Cor}(x_i, x_j) = \frac{\text{Cov}(x_i, x_j)}{\text{var}(x_i)\text{var}(x_j)}. \tag{118}$$

The diagonal elements of $\text{Cor}(x_i, x_j)$ must always be 1, while the off-diagonal elements can assume values between -1 and 1, $-1 \leq \text{Cor}(x_i, x_j) \leq 1$ for $i \neq j$. The off-diagonal elements measure the linear dependence of x_i and x_j; for independent variables, it is zero, 1 for exact positive linear dependence. However generally, $\text{Cor}(x_i, x_j) = 0$ does not indicate that x_i and x_j are independent, because $\text{Cor}(x_i, x_j)$ and $\text{Cov}(x_i, x_j)$ only measure the "linear" dependence and have no contribution from higher-order expansion terms. A covariance matrix is not a physical quantity. It is a measure of belief into the data set either assigned by the experimentalists of the respective data sets themselves or at a later point by evaluators, and are consequently subjective. In particular, systematic uncertainties are often obtained by expert judgment quantifying a possible error that cannot be completely determined, and are thus only an estimate on that possible error. In addition, to this "uncertainty on the known uncertainty", there can be unknown errors or unrecognized uncertainties affecting the data. One should keep also in mind that mean values and covariances might not sufficiently describe the whole probability distribution function. Hence, evaluations using only mean values and covariances might bias the results.